Universität Rostock Traditio et Innovatio

LEIBNIZ-INSTITUTE OF ATMOSPHERIC PHYSICS IAP

Doctoral Thesis

Universität Rostock

Mathematisch-Naturwissenschaftliche Fakultät
Institute: Leibniz-Institut für Atmosphärenphysik

Long-term studies and variability of the mesosphere and lower thermosphere summer wind dynamics at middle and high latitudes

a cumulative dissertation by

Juliana María Jaen

from Argentina

Reviewers:

Prof. Dr. Jorge L Chau
Leibniz Institute of Atmospheric Physics at the University of Rostock, Germany

Prof. Dr. Huixin Liu
Department of Earth and Planetary Science, Kyushu University, Japan

Prof. Dr. Christian von Savigny
Institute of Physics, University of Greifswald, Germany

Date of submission: 12.04.2024
Date of defense: 28.06.2024

https://doi.org/10.18453/rosdok_id00004845

Abstract

The mesosphere and lower thermosphere constitute a dynamic and complex system characterized by strong winds and varying temperatures due to a combination of solar radiation, Earth's geodesic shape, composition, and rotation. The middle and lower part of the atmosphere serves as the source, medium for propagation, and sink for multiple waves. In the course of the year, the winds in the mesosphere and lower thermosphere undergo drastic changes from winter to summer resulting in the filtering of different waves. The winter season is particularly active due to strong polar vortex and wave activity. In contrast, the summer season is relatively calmer due to the lesser contribution of the solar tides and wave filtering by the stratosphere. Significant changes are also observed from year to year due to the influences of multiyear oscillation phenomena as a result of coupling from lower layers, and the solar radiation. Moreover, anthropogenic activity has an impact on the atmosphere. In the pursuit of investigating the long-term wind dynamics, the focus is set on the summer season. By combining specular meteor radars and partial reflection radars at middle and high latitudes, it is possible to obtain wind measurements from 60 to 110 km altitude and a time series length of 17-33 years, depending on the instrument.

Comparing the two definitions of the summer length, the one defined by the first wind reversal from eastward to westward (in March-April), depicted more variability and significant trends than the definition of wind reversal from westward to eastward that occurs at higher altitudes and later in the year (April-May). Both definitions showed that the variability is mostly coming from the winter and the ending of the summer remains within a week with no significant changes over the years. The significant trends obtained from the former definition of summer length indicate longer summers due to an earlier onset of the summer by approximately half a day per year (2004-2020). At middle latitudes, with an extended time series, the summer length definition revealed a breakpoint in the trends (1990-2008, and 2008-2020), which could be the evidence of decadal oscillations or even the consequence of anthropogenic changes.

Motivated by the observed summer length trends, the summer wind intensity over the years was investigated. Considering only the monthly maxima, the lower thermospheric eastward wind, the mesopause southward wind, and the mesospheric westward wind were investigated at middle and high latitudes. This study revealed a significant trend indicating the weakening of lower thermospheric eastward wind in July at high latitudes (2004-2022) of approximately -0.5 m/s per year. While at middle latitudes, the mesospheric westward wind is increasing approximately by 0.4-0.6 m/s/year (1990-2022) while the mesopause southward wind is decreasing by about 0.2-0.3 m/s/year (2004-2022). Moreover, the time series revealed oscillations that could be connected to external forcing such as the solar cycle, the quasi-biennial oscillation, and El Niño-southern oscillation. Additionally, the influence of the geomagnetic activity on the winds and the possible impact on the trends was studied.

Zusammenfassung

Die Mesosphäre und die untere Thermosphäre stellen als Teil der mittleren Atmosphäre ein dynamisches und komplexes System dar, welches durch starke Winde und variierende Temperaturen aufgrund einer Kombination aus Sonnenstrahlung, der Gestalt und Form der Erde, ihrer Zusammensetzung und Rotation gekennzeichnet ist. Die mittlere und untere Atmosphäre dienen somit als Quelle, Medium für die Ausbreitung und Senke verschiedener Wellen. Im Laufe des Jahres unterliegen die Winde in der Mesosphäre und unteren Thermosphäre drastischen Veränderungen von Winter bis Sommer, was zur Filterung verschiedener Wellen führt. Die Wintersaison ist aufgrund des starken Polarwirbels und der Wellenaktivität besonders aktiv, während die Sommersaison durch den geringeren Beitrag solarer Gezeiten und der Wellenfilterung durch die Stratosphäre relativ ruhig ist. Auch von Jahr zu Jahr werden signifikante Veränderungen beobachtet, die auf den Einfluss von mehrjährigen Oszillationsphänomenen als Folge der Kopplung aus unteren Schichten und der Sonnenstrahlung zurückzuführen sind. Darüber hinaus hat die anthropogene Aktivität einen Einfluss auf die Atmosphäre. Bei der Untersuchung der langzeitlichen Winddynamik liegt der Fokus auf der Sommersaison. Durch die Kombination von spekularen Meteor- und partiellen Reflexionsradaren in mittleren und hohen Breiten ist es möglich, Windmessungen in 60 bis 110 km Höhe mit einer Gesamtlänge von 17-33 Jahren, je nach Instrument, zu erhalten. Sie werden verwendet, um die langfristige Sommerlänge und die Windmaxima sowie deren Variabilitäten zu untersuchen.

Beim Vergleich der beiden Definitionen der Sommerlänge zeigt die erste Windumkehr (ostwärts nach westwärts im März-April) eine größere Variabilität und signifikantere Trends als die zweite Definition zur späteren Frühjahrswindumkehr (April-Mai) von westwärts nach ostwärts in größeren Höhen. Beide Definitionen zeigen, dass die Variabilität größtenteils aus dem Winter stammt und das Ende des Sommers zwischen hohen und mittleren Breiten innerhalb einer Woche auftritt, ohne signifikante Veränderungen im Laufe der Jahre. Die signifikanten Trends der ersten Definition der Sommerlänge deuten auf längere Sommer hin, bedingt durch einen früheren Beginn des Sommers von etwa einem halben Tag pro Jahr (2004-2020). In mittleren Breiten, mit einer erweiterten Zeitreihe, zeigte die Definition der Sommerlänge einen Knick in den Trends (1990-2008 und 2008-2020), was auf dekadische Oszillationen oder sogar auf die Folgen anthropogener Veränderungen hinweisen könnte.

Angeregt durch die beobachteten Sommerlängentrends wurden die Intensität der Sommerwindmaxima in der Mesosphäre und unteren Themosphäre für mittlere und hohe Breiten näher untersucht. Diese Studie zeigte rückläufige signifikante Trends im ostwärtigen Wind in der unteren Thermosphäre im Juli in hohen Breiten (2004-2022) von etwa -0,5 m/s pro Jahr. Während in mittleren Breiten der westwärtige Wind in der Sommermesosphäre etwa 0,4-0,6 m/s/Jahr (1990-2022) zunimmt und der südwärtige Wind in der Sommermesopause die Geschwindigkeit um etwa 0,2-0,3 m/s/Jahr (2004-2022) reduziert. Darüber hinaus zeigten die Zeitreihen Oszillationen, die mit externen Einflüssen wie dem Sonnenzyklus, der stratosphärischen

quasi-biennalen Oszillation und El Niño-Southern Oscillation verbunden sein könnten. Zusätzlich wurde der Einfluss der geomagnetischen Aktivität auf die Winde und die möglichen Auswirkungen auf die Trends untersucht.

Acknowledgements

I am deeply grateful to my advisors, Prof. Jorge L. Chau, Dr Toralf Renkwitz, and Prof. Dr Huixin Liu, for their exceptional guidance throughout my doctoral studies. A special appreciation goes to Prof. J. L. Chau for giving me the opportunity to come to Germany, providing me with such an interesting topic, and helping me during my PhD journey. Special thanks to my informal supervisor, Dr Toralf Renkwitz who walked through my entire PhD with me, sharing my excitement and stumbles. Additional thanks to Prof. Dr Huixin Liu, who invited me to visit Japan and Kyushu University. During my two weeks there, I felt welcome and I really enjoyed our interactions.

I extend my thanks to all the members at the Institute of Atmospheric Physics, Kühlungsborn, past and present, who helped me during my time there. From sharing a simple beer to a long scientific discussion. Many of them have become life friends.

I extend my heartfelt thanks to my parents, my brother, sister-in-law, and nephews for their boundless love and support throughout my life. Additionally, I want to express my deepest gratitude to my partner, Kesava Ramachandran, for his love and unwavering encouragement during this journey.

My gratitude wouldn't be complete without mentioning the guidance of the late Dr Peter Hoffmann, who accompanied me during the first couple of years of my Ph.D. and continues to teach me through his papers to this day.

Contents

List of Figures

List of Abbreviations

DJF December-January-February

DOY Day Of the Year

ENSO El Niño Southern Oscillation

EP Eliassen-Palm

Es Sporadic E

GW Gravity Wave

HF High-Frequency

JJA June-July-August

MLT Mesosphere and Lower Thermosphere

MLT-SL Mesospheric and Lower Thermospheric Summer Length

M-SL Mesospheric Summer Length

MAM March-April-May

MSSW Major Sudden Stratospheric Warming

MLS Microwave Limb Sounder

NAM Northern Annular Mode

NAO North Atlantic Oscillation

NO Nitric Oxide

OH Hydroxyl

ONI Oceanic Niño Index

PCA Principal Component Analysis

PRR Partial Reflection Radar

QBO Quasi-Biennial Oscillation

SABER Sounding of the Atmosphere using Broadband Emission Radiometry

SMR Specular Meteor Radar

SON September-October-November

SSW Sudden Stratospheric Warming

sPJO Strong Polar-night Jet Oscillations

TEM Transformed Eulerian Mean

TIMEGCM Thermosphere Ionosphere Mesosphere Electrodynamic General Circulation Model

UV Ultraviolet

This thesis is dedicated to my family,
they are my rock.

Chapter 1

Introduction

The atmosphere of Earth is a dynamic system driven by many complex processes. The region of Earth's atmosphere between 50 and 110 km is known as the Mesosphere and Lower Thermosphere (MLT), defined by its temperature profile, where the neutral and ionized atmosphere coexist. In the thermosphere, the absorption of solar extreme ultraviolet radiation causes ionization (i.e., ionosphere), while in the lower region of the thermosphere, along with the mesosphere, winds and wave interactions strongly dominate. The dynamical activity in the neutral atmosphere produces chemical mixing and temperature changes. Whereas, the Ultraviolet (UV) radiation is absorbed in the stratosphere, which is located below the mesosphere.

Historically the ozone layer has been of great importance since it marked a starting point in the relevance of the human activity footprint in the atmosphere. With it, the beginning of the long-term and trends studies became highly important, not only for science but also for society. In 1984, researchers discovered that the atmosphere was evidencing a depletion of ozone in spring, especially in the Antarctic region (Farman et al., 1985). The study led to the conclusion that halocarbons ($CFCl_3$ and CF_2Cl_2) were responsible for this effect. Nowadays gases like Carbon dioxide (CO_2), Methane (CH_4), Nitrous Oxide (N_2O), Chlorofluorocarbons (CFCs), Hydrofluorocarbons (HFCs), Sulphuric Hexafluoride (SF_4), and water vapor (H_2O) are also considered Greenhouse gases due to the global effect of retaining the heat in the atmosphere and not allowing it to escape (Ohara, 2022). An extreme situation of these effects is present in Venus, with a dense atmosphere that retains the high temperatures of a highly active volcanic surface plus the radiation from the Sun. The rise of greenhouse gases in the Earth's atmosphere can lead to an increase in the global temperature (e.g. Lindsey and Dahlman, 2020), with extreme weather conditions that can disrupt normal human life. Human activity like fossil fuel burning, agriculture, usage of propellants and aerosols for various applications, etc. can lead to an increase in the concentration of greenhouse gases in the atmosphere. Consequently, in 1987 the Montreal Protocol was signed to stop the emission of ozone-depleting substances. Subsequent studies show a positive shift in the stratospheric ozone trends in 1995 at equatorial latitudes and in 2000 at high latitudes (e.g., Weber et al., 2022). Due to the necessity to understand the changes in the atmosphere and the human impact on the environment, scientists have been studying the long-term compositions, temperature changes, and the dynamics of middle atmosphere for several decades (Bremer and Berger, 2002; Bremer and Peters, 2008; Yue et al., 2015; Peters and Entzian, 2015; Qian et al., 2017; Peters et al., 2017; Karagodin-Doyennel et al., 2021, etc.).

The middle atmospheric dynamics are governed by the interaction of waves of many different scales namely, from planetary waves to Gravity Waves (GWs). The mean

winds are crucial for wave propagation and over the year the mesospheric winds depict an annual behavior. In winter, the zonal winds are eastward, reversing to westward in summer. The middle atmospheric wind changes facilitate different scenarios for wave propagation, tides, and changes in temperatures. The MLT is also affected by other external processes like the Quasi-Biennial Oscillation (QBO) which alters the direction of the equatorial stratospheric zonal winds over 26-28 months, and equatorial ocean-atmospheric warming (and cooling) that occurs during the northern hemisphere winter season. This is known as El Niño Southern Oscillation (ENSO) whose periods are not precisely defined but are thought to span around three to six years (Baldwin et al., 2001; Jacobi and Kürschner, 2002; Wang and Picaut, 2004; Espy et al., 2011; Offermann et al., 2015; French et al., 2020). Not only from below, but also from above the MLT is sensitive to external forcing. As mentioned before, the thermosphere is directly affected by solar radiation, characterized by an 11-year periodicity of sunspot activity, coronal mass ejection, and solar wind. The latter is responsible for transporting particles that, upon reaching Earth, can precipitate and may interact with the atmosphere, significantly altering its ionization state and chemistry.

It is possible to observe the MLT winds with satellites and ground-based instruments, such as lidars and radars. While satellites, though constrained to their orbit, are good for monitoring global parameters, lidars, on the other hand, have good resolution but depend on the weather conditions of their location to obtain measurements. Radars have the advantage of being able to measure independently of the weather conditions. The radars used in this study are sensitive to atmospheric irregularities with scales of 3 to 30 meters and these irregularities serve as tracers within the observing volumes. For Partial Reflection Radars (PRRs), the observing volumes in MLT regions are around a few kilometers while for Specular Meteor Radars (SMRs), a few hundred kilometers. Consequently, it is possible to build homogeneous time series for long-term studies. Their limitation relies on the length of their measurements (i.e. when they were built) and the continuity of these measurements. The length of the instrument's measurements is one of the most challenging aspects, among many that the long-term community faces (e.g., Laštovička and Jelínek, 2019).

The objective of this thesis is to investigate the long-term dynamics of the MLT at middle and high latitudes, especially the long-term variability of the neutral winds. The focus is set on the northern hemisphere summer due to the comparably low wave activity from the troposphere and stratosphere, in order to establish proxies and study in a non-traditional way (e.g., a traditional method is a multiple regression analysis) the long-term behavior. Additionally, with collaborative projects, the wind trends over all the seasons, the ionospheric F, E and Sporadic E (Es) layers residual trends are investigated at middle latitudes, and the D-region high latitude electron density climatology is explored.

This dissertation is organized as follows. Chapter 2 provides a brief introduction to middle and upper atmospheric terminologies used in the articles and the wind dynamics of the MLT. The instruments and methods used are explained in Chapter 3. The published papers on summer length and summer winds are introduced in Chapters 4 and 5, respectively. The collaboration papers are introduced in Chapter 6. Finally, Chapter 7 contains the conclusions and open question related to this topic.

Chapter 2

Middle and Upper Atmosphere

The Earth's atmosphere is dynamically active throughout the year with the Sun as its main source of energy. This energy interacts with the atmosphere in several regions due to absorption, reflection, ionization, convection, conduction, radiative cooling, etc. Depending on the composition, temperature, and ionization level, the atmosphere is divided into different layers. Figure 2.1 shows the temperature profile for summer and winter for two different years. Traveling from the lowermost region of the Earth's atmosphere which is the troposphere where the daily weather pattern directly affects human life, through the stratosphere where the maximum ozone concentration is localized (i.e. 18-35 km), we reach the MLT at an altitude of 50 km. Around 60 km, the concentration of electrons begins to increase in a region still predominantly influenced by waves and neutral winds, extending up to approximately 90 km, known as the ionospheric D-layer (Hargreaves, 1992). The mesopause which marks a transition between two distinct atmospheric regions, varies between 84-90 km depending on the season and is characterized by the increasing significance of molecular diffusion which provides a medium for the breaking and dissipation of waves. One of the limiting regions is strongly dominated by neutral winds, neutral species, and wave activity (i.e., the mesosphere), while the other region is known

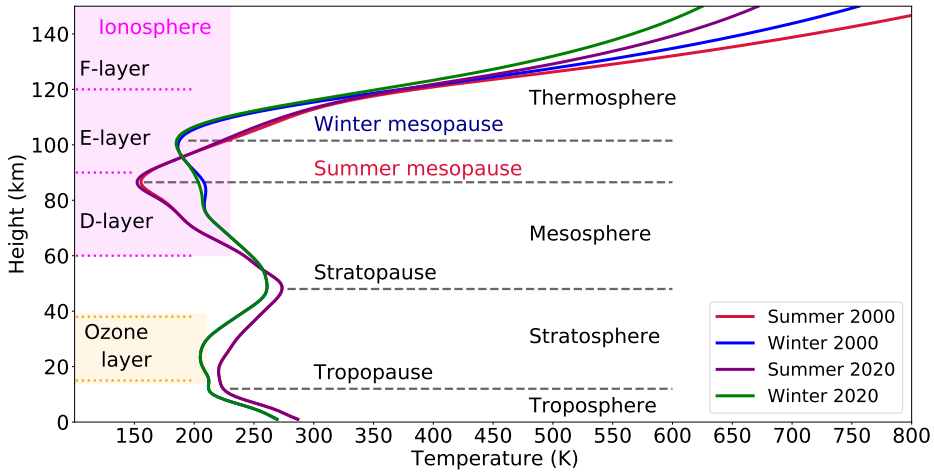

FIGURE 2.1: Structure of the atmosphere at middle latitudes (54°N, 13°E) with summer and winter temperature profiles for 2000 and 2020 from the NRLMSISE-2.0 model. Daytime layers of the ionosphere and ozone layer are indicated in the figure.

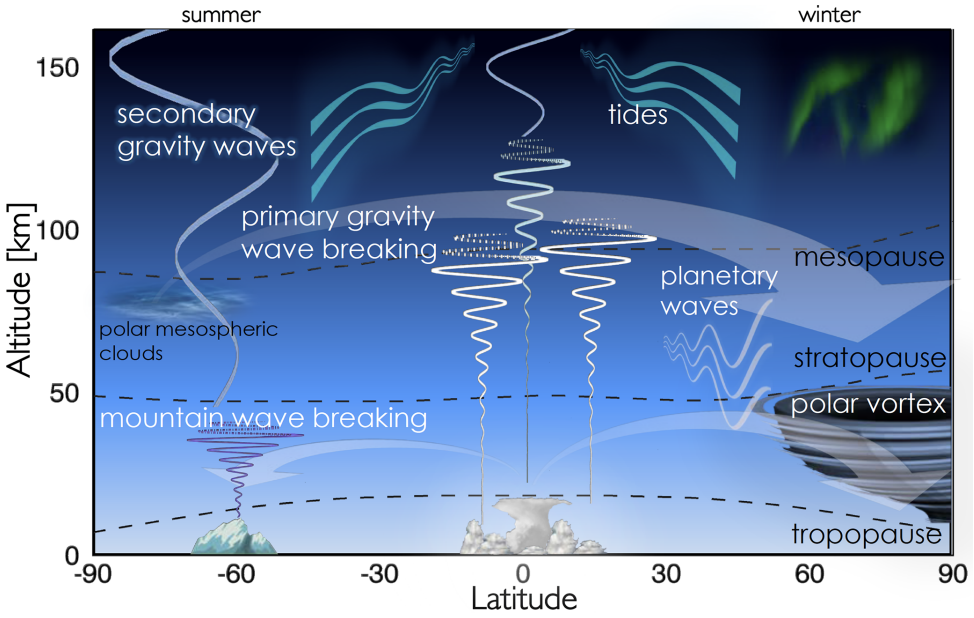

FIGURE 2.2: Scheme of wave sources affecting the MLT (Figure from McCormack et al., 2021).

as the lower thermosphere, which includes the ionospheric E layer. In this region, under special circumstances, the Es layer is formed due to the combination of wind shears and the conversion of material deposited by sporadic meteors (e.g., Whitehead, 1989; Mathews, 1998). The lower thermosphere has more ionized species and electrons, with decreasing density and increasing temperature with height while the F-layer, which is above 120 km, is divided into two layers, F1 and F2, depending on the day and under direct solar radiation (Hargreaves, 1992).

The MLT temperature profiles depict an important difference between the solstices (see Fig. 2.1). The temperature changes drastically in the mesopause and in summer due to adiabatic cooling its altitude reduces (e.g., Smith, 2012). The nature of the coldest place on Earth (i.e. summer mesopause) is due to MLT dynamics. To understand the whole system, a short explanation of the types of waves (Section 2.1), the MLT dynamics with the one definition of the residual mean meridional circulation (Section 2.2), and different effects that contribute to the complexity of this system are described in this chapter.

2.1 Waves

There are several sources of wave activity in the atmosphere. The main wave components that contribute to the MLT are depicted in Figure 2.2. The waves mentioned in this cumulative dissertation are described below.

Gravity (Buoyancy) Waves: GWs are short periods (from minutes to a few hours) oscillations, with a restorative property due to buoyancy. Generated by orographic forcing, convection, wind shear, or wave interactions (e.g secondary gravity waves), most gravity waves originate in the troposphere and propagate upward and horizontally, increasing their amplitude with decreasing density

until they reach critical levels, where they break, dissipate and dump the energy into the background wind (Fritts and Alexander, 2003).

Tides: The atmospheric thermal tides are global-scale daily oscillations, primarily forced by the solar UV absorption by atmospheric water vapor and ozone. These waves have components that can propagate vertically and reach the thermosphere (Chapman and Lindzen, 1969). The tides can be divided into non-migrating and migrating tides, the latter moves following the direction of the Sun's apparent movement. The migrating tides are divided into 24 h (diurnal), 12 h (semidiurnal), 8 h (terdiurnal), etc, depending on their periods. However, tides with periods less than 12 h have smaller amplitudes and are not extensively studied as the diurnal and semidiurnal tides. While at low (equatorial) latitudes, the predominant tidal amplitude is the diurnal tide, at middle and high latitudes the semidiurnal tide is more relevant (Holton, 2004; Smith, 2011).

Planetary (Rossby) Waves: These waves are large-scale oscillations with periods above 2 days. Their restoring force is the conservation of angular momentum. Planetary waves play an important role in the winter MLT dynamics, however, in summer their activity is limited by the background wind conditions (Andrews et al., 1987; Smith, 2011; Smith, 2012). The quasi-two-day wave is the only planetary wave that maximizes in the summer mesosphere (Salby, 1981; Pancheva et al., 2018; Iimura et al., 2021).

2.2 Dynamics

The dynamics of the atmosphere are describe by equations of fluid motions. The most effective theoretical framework is the Navier-Stokes equations:

$$\rho\left(\frac{\partial \mathbf{u}}{\partial t} + (\mathbf{u}\cdot\nabla)\mathbf{u}\right) = -\nabla p + \mu\nabla^2\mathbf{u} + \mathbf{F} \tag{2.1}$$

where $\mathbf{u}$ is the velocity vector field of the fluid, ρ is the density, p is the pressure, μ is the dynamic viscosity, and t is time. The term $\mathbf{F}$ represents any external forces acting on the fluid, such as gravity, or electromagnetic forces. The left term of the eq. 2.1 represents the convective acceleration of the velocity change rate with respect to time, describing the changes in the fluid velocity in time and space. The first term on the right represents the pressure gradient force and describes the changes in pressure spatially and the induction of motion from high to low-pressure regions. The second term describes the viscous forces and changes in the velocity field due to internal friction.

Numerical approximations and parameterizations are necessary to apply to Navier-Stokes equation in order to study large-scale atmospheric dynamics. This process allows arriving at a set of primitive equations that describe: 1) horizontal and vertical momentum, 2) mass continuity, and 3) thermodynamic equation, which describes the energy conservation. From these sets of equations and assuming large-scale motion in fluids, is possible to arrive at the Transformed Eulerian Mean (TEM) equations. These equations consider the division of variables into mean and disturbed parts, which provide an easy understanding of the zonal mean flow response to the change in the physical properties (Andrews et al., 1987; Holton, 2004). This way, any quantity can be described as: $a\,(\text{total}) = \bar{a}\,(\text{Eulerian mean}) + a'\,(\text{deviation, eddy})$. Following this

approach, the *residual mean meridional circulation* is defined as $(\bar{v}^*, \bar{\omega}^*)$, where:

$$\bar{v}^* \equiv \bar{v} - \frac{R}{\rho_o H}\frac{\partial}{\partial z}\left(\frac{\rho_o \overline{v'T'}}{N^2}\right), \quad \bar{\omega}^* \equiv \bar{\omega} - \frac{R}{H}\frac{\partial}{\partial y}\left(\frac{\overline{v'T'}}{N^2}\right),$$

and the TEM equations:

Zonal-mean momentum
$$\frac{\partial \bar{u}}{\partial t} - f_c\,\bar{v}^* = \frac{1}{\rho_o}\nabla \bullet \overline{F} + \overline{X} \equiv \overline{G} \tag{2.2}$$

Mass continuity
$$\frac{\partial \bar{v}^*}{\partial y} + \frac{1}{\rho_o}\frac{\partial}{\partial z}(\rho_o \bar{\omega}^*) = 0 \tag{2.3}$$

Thermodynamic eq.
$$\frac{\partial \overline{T}}{\partial t} + \frac{N^2 H}{R}\,\bar{\omega}^* = \frac{\overline{J}}{c_p} \tag{2.4}$$

Thermal wind eq.
$$f_c \frac{\partial \bar{u}}{\partial z} + \frac{R}{H}\frac{\partial \overline{T}}{\partial y} = 0 \tag{2.5}$$

where

N	Brunt–Väisälä (buoyancy) frequency	N^2	$\equiv \frac{R}{H}\left(\frac{\kappa T}{H} + \frac{dT}{dz}\right)$
$\bar{u}$	Zonal velocity	ϕ	Latitude
$\bar{v}$	Meridional velocity	g	Acceleration due to gravity
$\bar{w}$	Vertical velocity	T	Temperature
z	Altitude	t	Time
Ω	Angular velocity of Earth	f_c	Coriolis parameter $= 2\Omega \sin\phi$
H	Constant scale height	ρ_o	Basic state of density $\propto e^{-z/H}$
R	Universal gas constant	c_p	Specific heat capacity (p=cte)
κ	Specific heat ratio $= R/c_p \approx 2/7$		

In this context, $\overline{J}$ is the zonal-mean diabatic heating rate per unit mass, and $\overline{X}$ is the zonal force due to small-scale eddies or GW drag. $\overline{F}$ represents the Eliassen-Palm (EP) flux, a vector in the meridional plane ($\overline{F} = \check{j}F_y + \check{k}F_z$), which for large-scale quasi-geostrophic (i.e. equilibrium between the pressure gradient force and the Coriolis force) eddies, has the components,

$$F_y = -\rho_o\,\overline{u'v'}, \quad F_z = \frac{\rho_o f_c R}{N^2 H}\,\overline{u'T'}.$$

The resultant of these components is the total zonal force per unit mass $\overline{G}$.

Particularly with this set of equations, it is possible to identify the energy sources in the wind circulation and the restorative motions for equilibrium. Some results from the TEM equations explain the meridional circulation and mass transport in connection with the upwelling in the summer and downwelling in the winter hemisphere with maxima during the solstice. Figure 2.3 depicts the meridional mass stream function obtained with TEM equation for the summer solstice at the northern hemisphere (adapted from Garcia et al., 1984).

The downwelling in winter and upwelling in summer is the result of the approximation of $\overline{G} = -f_c\bar{v}^*$. It is expected that $\bar{v}^*$ is directed from the summer to winter hemisphere at the mesopause altitudes, then the mass continuity requires that:

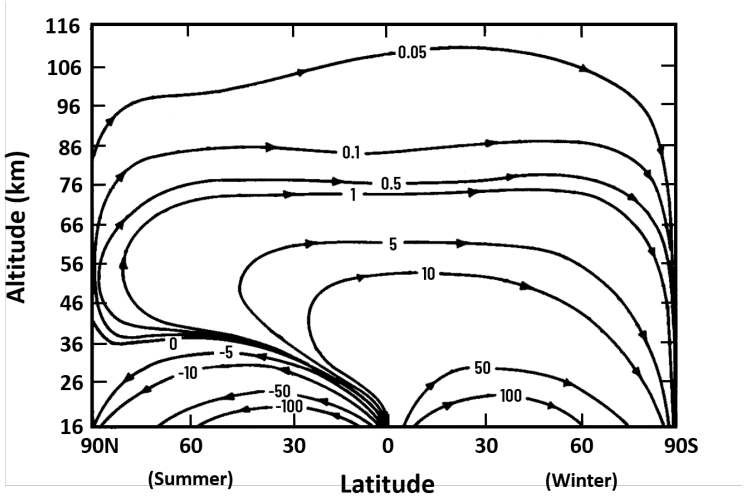

FIGURE 2.3: Representation of the meridional mass stream function for the northern hemisphere summer solstice, demonstrating the Brewer-Dobson circulation. Units are in $\mathrm{kgm^{-1}s^{-1}}$, adapted from Garcia et al. (1984).

$(\rho_o \bar{w}^*)_z > 0$ in winter and $(\rho_o \bar{w}^*)_z < 0$ in summer. The last requirement is that $\bar{w}^*$ does not vary rapidly over pressure scale-height or alternatively that $\bar{v}^* = 0$ (Andrews et al., 1987).

The mean winds over the seasons were thought to be symmetrical over the hemispheres (Andrews et al., 1987). However, ocean-land distribution and orography that differentiates the two hemispheres contribute to global differences in the wind pattern. Figure 2.4 shows latitudinal mean-zonal winds for January, April, July, and October by pressure height and geometric height (adapted from Fleming et al., 1990). The red colored areas depict the eastward wind and the blue the westward winds. The difference between the equinoxes (April and October), and the solstice (January and July) are clearly evident. During the solstices, the westward winds extend from the extratropical stratosphere to the mesopause in summer, while in winter, eastward winds prevail.

Historically it was thought that the temperatures in the middle atmosphere were due to pure geostrophic balance, but the wind reversal in the summer mesopause would not occur under these conditions. GWs provide the main part of the necessary forcing ($\overline{G}$, from Eq. 2.2) in the upper mesosphere. They grow in amplitude as they propagate from tropospheric and lower stratosphere sources up into the rarefied mesosphere, where they break and deposit their momentum which leads to turbulence, small-scale mixing, and dissipation. Under the GWs linear theory, the net contribution to the forcing $\overline{G}$ associated with GWs tends to drag the mean flow towards the horizontal phase speed of the waves. Since GWs are absorbed at or near critical levels, where the local horizontal wind speed equals their horizontal-phase speed, only the GWs reaching the mesosphere from below are expected to have phase speeds outside the range of horizontal wind speed. When the winter eastward winds are present in the stratosphere, the GWs within a range of westward phase speeds will exist in the mesosphere and break there. Above the mesospheric eastward jet, the GW contribution to $\overline{G}$ is negative. On the other hand, when the summer westward winds are present in the stratosphere, GWs with eastward phase speeds would be

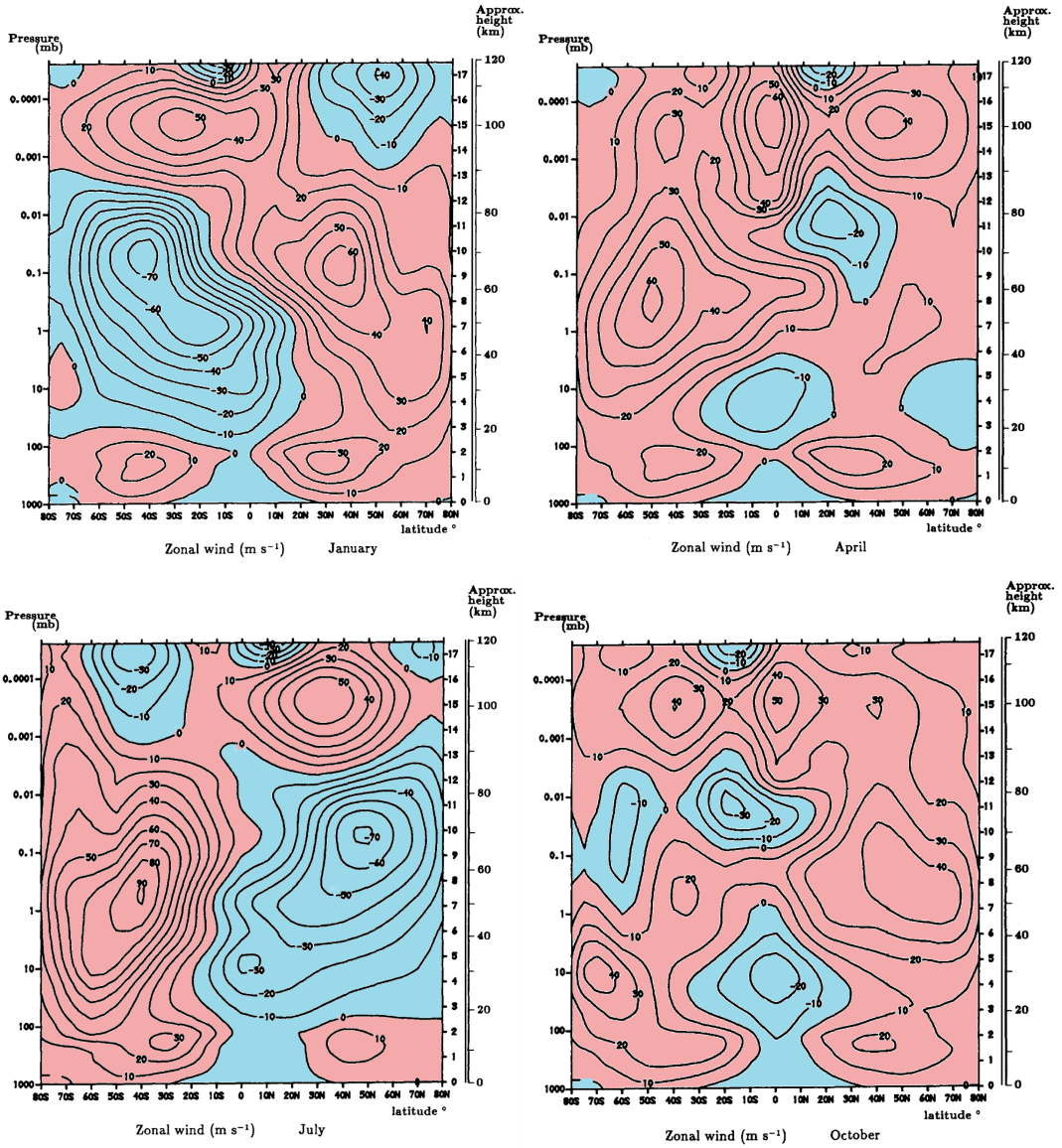

FIGURE 2.4: Latitudinal monthly mean zonal wind during the solstice (left column) and equinoxes (right column) by pressure height and geometric height (Fleming et al., 1990).

expected to propagate, reaching the mesosphere and break in the region where the contribution to $\overline{G}$ is positive, above the peak of the mesospheric westward jet.

Some studies have shown that above the region of strong wind jets, the GW spectrum has significant anisotropies (e.g., Ern et al., 2011). These regions are sources of GW breaking and transferring energy to the mean flow (Yiğit and Medvedev, 2017). This highlights the limitations of the linear theory and the atmospheric dynamic complexity.

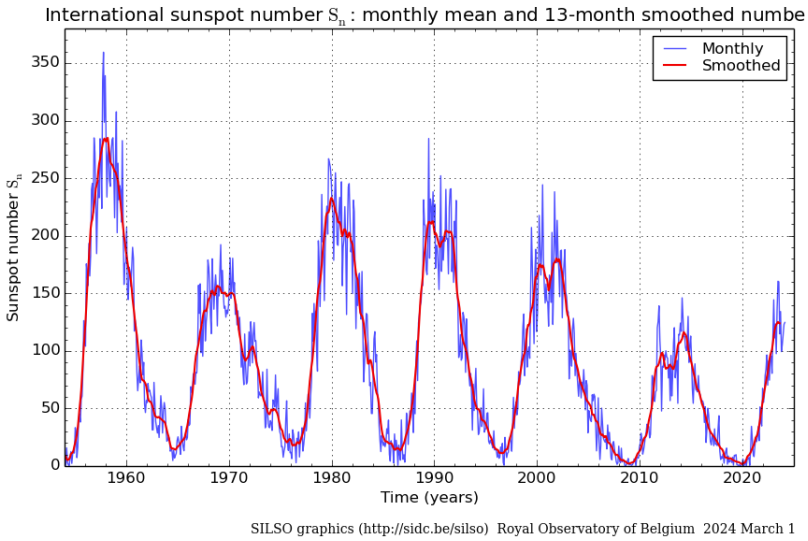

FIGURE 2.5: Solar activity: sunspot numbers (1956-2024). Obtained from the Royal Observatory of Belgium.

2.3 External Sources of Forcing

The dynamics of the Earth's atmosphere vary through seasons and years. To study the MLT and their long-term variations, it is necessary to consider this region as a coupled system along with the lower atmosphere (stratosphere and troposphere), which absorbs most of the solar radiation, and the upper thermosphere along with the geomagnetic field, which serves as the first filter from solar radiation. Strong climate phenomena, multi-year oscillations, and the Sun are some external sources of forcing considered in this thesis. A brief overview of them is provided in this section.

2.3.1 Solar Cycle and Lyman α

The Sun's magnetic rotation period is 22 years (also known as the Hale cycle), during which the internal magnetic dynamo polarization changes (Mursula et al., 2002). Throughout this period, the Sun experiences alternating phases of low and high activity, as evidenced by the appearance of sunspots, which are quantified using the sunspot number. This number is directly correlated with solar activity. Figure 2.5 shows the monthly mean sunspot number (blue) and the 13-month smoothed monthly sunspot number (red) from 1956 until 2024.

Under periods of higher sunspot numbers, the probability of solar activity affecting the Earth is higher. One way of measuring the solar activity directly at around 90 km is the Lyman α line. This line belongs to the UV region of the electromagnetic spectrum and depicts the energy jump between level 2 to 1 of the Hydrogen, 121.56 nanometres after being excited by solar radiation (Machol et al., 2019).

The solar activity is one of the most utilized factors modulating long-term studies. The complex dynamics that are in play depend on the altitudes and latitudes. However, their effects on the MLT temperatures and winds have been investigated with contradicting results (e.g., Jacobi, 1998; Singer et al., 2013; Li et al., 2021; Gan et al., 2017; Wilhelm et al., 2019; Noble et al., 2024). Several studies show an anticorrelation between solar activity and wind speed (highly dependent on season and height)

until the new millennium. With the change of the millennium, this anticorrelation has disappeared or been obscured with low statistical significance. The reason for this change remains open.

2.3.2 Geomagnetic Activity

The geomagnetic activity represents the Earth's magnetic field's response to extraterrestrial forcing, with the Sun being its primary source. Several indices provide information on the status of the geomagnetic field. The one relevant to this dissertation is the daily Ap index, calculated as the Earth's planetary index from a network of magnetic observatories. The Ap index varies between 0 and 400 and is the product of a conversion of the daily average of the 3 h mean Kp index (Matzka et al., 2021).

Several studies have shown changes in the neutral winds during geomagnetic storms. Li et al. (2019) and Li et al. (2023) studied the response of the MLT during a geomagnetic storm with the Thermosphere Ionosphere Mesosphere Electrodynamic General Circulation Model (TIMEGCM) at middle and high latitudes, respectively. During the initial phase of a geomagnetic storm, the upper thermosphere winds at middle latitudes undergo greater changes and occur earlier than in the MLT. These changes generate downward vertical winds that, due to adiabatic heating and heat advection generate a temperature increase in the MLT. Consequently the pressure gradient and the Coriolis force, due to the temperature changes, drive changes in the meridional wind. As the temperature is increased, it produces upward vertical winds that lead to a reduction of temperatures (Li et al., 2019). Sun et al. (2022) compared the simulation with TIMEGCM and Sounding of the Atmosphere using Broadband Emission Radiometry (SABER) and found that the storm effects penetrate down to 80 km, and the model agrees with the observation but overestimates increase and underestimates decrease in temperatures at high and middle latitudes. Jacobi et al. (2021) found significant eastward wind changes at middle latitudes comparing 5 years of measurements divided into low and high geomagnetic activity. In the study it was also found that the meridional wind component becomes disturbed during high geomagnetic conditions.

2.3.3 Stratospheric Quasi-Biennial Oscillation

The QBO is an atmospheric phenomenon that occurs in the tropical stratosphere. The distinct characteristic is the quasi-periodic horizontal wind reversal of approximately 28 to 29 months on average. Figure 2.6 shows the stratospheric zonal wind at equatorial latitudes between 1987 and 2022. The oscillation between these periods changes the zonal wind between eastward and westward. This oscillation is contained between 15 to 30 km, however, the troposphere can have downstream effects on the weather patterns and climate variability like tropical cyclone activity (e.g. Collimore et al., 2003; Jaramillo et al., 2021). Extensive research have shown that QBO affects the MLT (e.g. Baldwin et al., 2001). Espy et al. (2011) showed QBO modulation on the summer mesospheric Hydroxyl (OH) temperatures at 60°N. Ford et al. (2009) demonstrated a dynamical link between QBO and mesospheric zonal wind over Antarctica. The QBO mechanism is not fully understood, however, the main drivers are inertia-gravity waves and planetary waves acting in the tropical stratosphere.

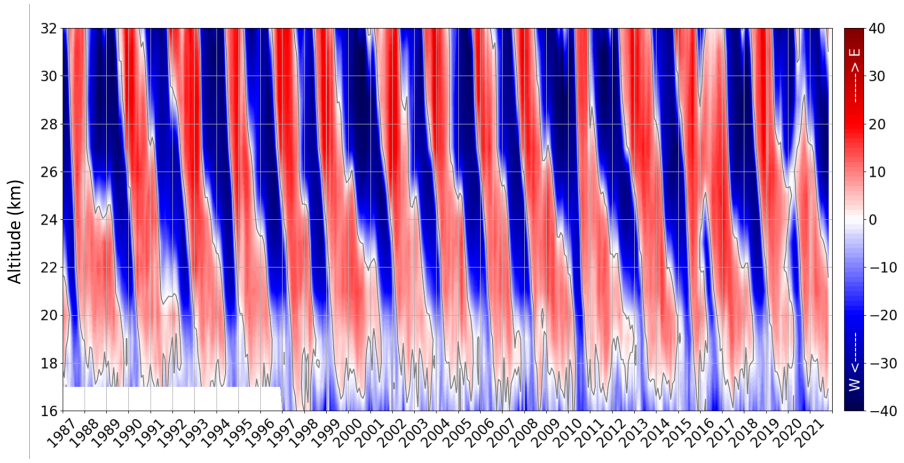

FIGURE 2.6: Equatorial zonal stratospheric wind and the Quasi-Biennial Oscillation (QBO) from 1987 to 2022. Winds obtained from the Freie Universität Berlin.

2.3.4 El Niño - Southern Oscillation

ENSO is a climate phenomenon characterized by the periodic warming (El Niño) and cooling (La Niña) of sea surface temperatures in the tropical eastern Pacific Ocean. With the temperature changes, a variation in winds is associated. The period oscillated between 2 to 7 years and it is characterized by these two phases (i.e., El Niño and La Niña). Figure 2.7 depicts the normal conditions and the two extreme phases of ENSO. The normal conditions (Fig. 2.7 middle) is a convective circulation from east to west in the tropical Pacific Ocean, winds, and tropical precipitations. The extreme condition where there is a cooling (below the $-0.5°$C in the Oceanic Niño Index (ONI) is La Niña phase. The warming phase (temperature above $+0.5°$C in the ONI) is when the circulation weakens or reverses, leading to an ocean-warm water band that approaches the South American coast. The warm water and atmospheric convection move eastward. In the ocean, the upwelling of cold water is reduced (limited by the thermocline or thermal layer, which delimits the well-mixed layer from the calm deep water below). These extreme conditions generate an increase in rainfall and flooding in the eastern Pacific region during El Niño phase, or the opposite conditions, droughts, during La Niña phase, with increased rainfall over the western Pacific region.

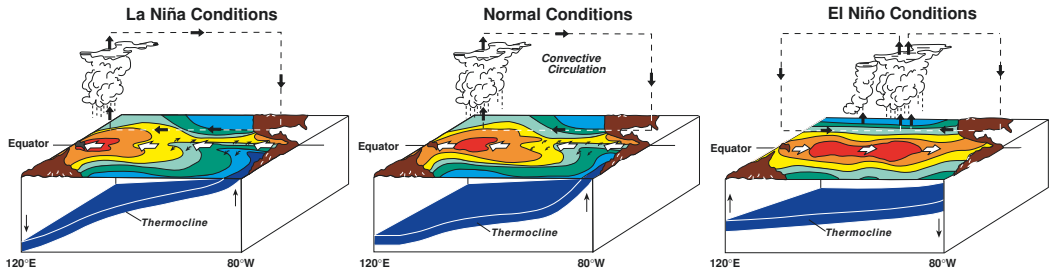

FIGURE 2.7: ENSO phases: La Niña, normal and El Niño conditions. Troposphere and ocean changes in temperature and the circulation patterns (source: NOAA/PMEL/TAO Project Office, 2023).

Even when ENSO is a tropospheric-ocean phenomenon at equatorial latitudes, the effects are observed globally. In the MLT, several studies have shown the effects of ENSO. García-Herrera et al. (2006) found a delay of a few months between ENSO extreme phase and the temperature response in the stratosphere at high latitudes. Jacobi and Kürschner (2002) found a negative correlation of about one month delay between ENSO and the middle latitudes summer zonal winds (1983-1998). Later on, Jacobi et al. (2017) reported that ENSO had a negative correlation in summer with the winds, which remained until 1990. Afterwards, the correlation decreased and reversed. Sundararajan (2020) found strong correlation with ENSO extremes and tides, temperatures and MLT winds with satellite data (2002-2018). Other studies identified oscillations of 3–4 years in OH and oxygen airglow at 96 and 87 km at 35°S, and OH temperatures at 56°N, 2000–2016 (Reid et al., 2014; Perminov et al., 2018).

2.3.5 Major Sudden Stratospheric Warming

A Sudden Stratospheric Warming (SSW) is a dramatic winter event that occurs in the Earth's polar stratosphere. It is characterized by a rapid and significant increase in temperatures, accompanied by deceleration or reversal from eastward to westward wind (Butler et al., 2015; Butler et al., 2017; Zülicke et al., 2018). During a Major Sudden Stratospheric Warming (MSSW) event, the polar vortex can be disrupted or weakened suddenly, which leads to a split or displacement of the polar vortex. Figure 2.8 shows a 3D temperature representation of the polar vortex in its normal conditions, with a displacement and split scenario. The split of the polar vortex can create multiple smaller vortices leading to a more chaotic stratospheric circulation. The displacement of the polar vortex is a shift of position, from the typical location over the pole, moving toward another polar region or lower latitudes. Particularly the events characterized by a complete reversal of the zonal-mean winds are categorized as MSSWs, while a minor warming is the consequence of a deceleration of the zonal mean wind, without the wind reversal (e.g., Charlton and Polvani, 2007).

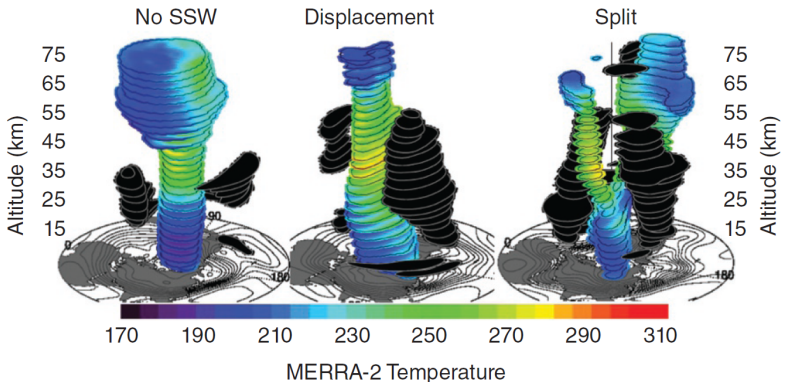

FIGURE 2.8: Arctic polar vortex representation: normal conditions, displacement and split. The 3D representation is generated with MERRA-2 temperatures (source: Goncharenko et al., 2021).

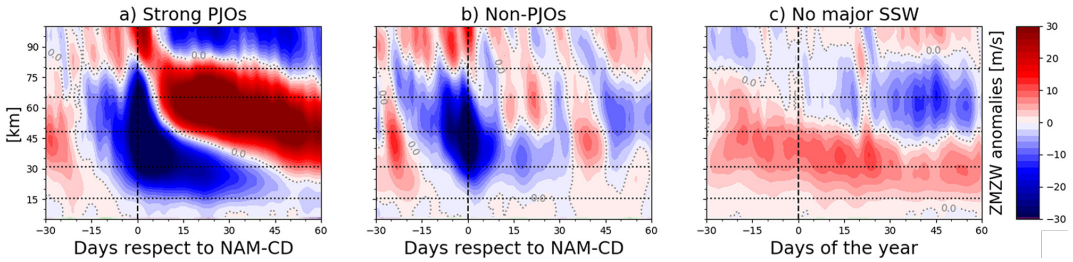

FIGURE 2.9: Strong polar-night jet oscillations: comparison with non-PJOs and no MSSW. (source: Conte et al., 2019).

2.3.6 Strong Polar-night Jet Oscillations

Strong Polar-night Jet Oscillations (sPJO) is described as the anomalous warmer stratospheric condition, that can persist for long periods of time after certain MSSWs. During this event, warmer temperatures propagate downward and can reach the troposphere altering the normal conditions (e.g., Kuroda and Kodera, 2004). Particularly the sPJO are those events where the events exceed three standard deviations (see Peters et al., 2018; Conte et al., 2019). Figure 2.9 depicts the zonal mean zonal winds and the Northern Annular Mode (NAM) index central day (CD), indicating the NAM index exceeds a threshold value of -2.3 at 10 hPa (Peters et al., 2018; Conte et al., 2019).

Chapter 3

Instruments and Methods

This Chapter provides a brief overview of the instruments utilized in this thesis, alongside the analytical methods employed for data analysis.

3.1 Instruments

The MLT is monitored by several instruments such as radars, lidars, rockets, cameras, imagers, and satellites, each with its advantages and disadvantages. While satellites have a large coverage, the timespan between transit over the same region makes it difficult to observe events of shorter timescales. Furthermore, long-term studies bring an extra complication as measurements of more than one decade are necessary to investigate the underlying dynamical processes. Even though satellites could orbit the planet for several years, maintaining them is difficult (due to their designed lifetime and unforeseen failures or damages to the onboard instruments, etc.) and hence their replacement is necessary. Moreover, for long-term observations, an overlap of satellites for a certain duration is essential for a consistent time series measurement (Weatherhead et al., 2017), which is difficult to achieve due to planning, projects, and funding. Insitu measurements of temperature, density, winds, and composition of gases are accomplished by instrumented rockets. However, they are sporadically launched and are highly dependent on campaigns (Lübken, 1999). Airglow imagers have a wide field of view coverage and measure chemical species emission, namely $O(^1S)$, O_2, and OH emissions between 87-97 km (Garcia and Sassi, 1999). On the other hand, Rayleigh, Sodium (Na), Potassium (K), and Iron (Fe) lidars cover the altitude range between 50-90 km (Rayleigh), 80-110 km (Na and K), and 80-150 km (Fe). From these instruments, it is possible to obtain temperature and wind measurements. However, the disadvantage of these instruments is that they require clear-sky conditions (e.g., Measures, 1984; She et al., 2021). On the other hand, radars and satellites are not dependent on weather conditions and thus can be operated at all times. Furthermore, ground-based radar installations are easy to maintain as well.

This thesis focuses on the measurements from specular meteor radars and partial reflection radars and complemented by the Microwave Limb Sounder (MLS) - Aura satellite and ionosonde.

3.1.1 Specular Meteor Radars

SMRs detect the plasma trails created by the meteors entering the atmosphere between 75 and 110 km. The typical operation of the system is such that the radio wave from the radar is reflected at the meteor plasma trail and received back at the interferometer on the ground. Figure 3.1 shows a schematic of this signal interaction

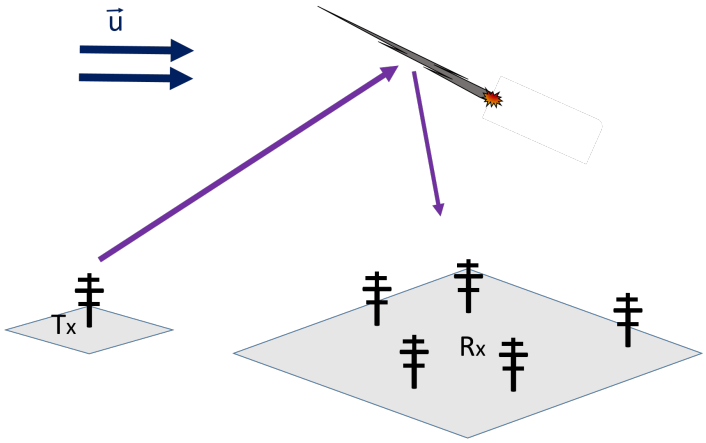

FIGURE 3.1: Schematic diagram of a specular meteor radar (not scaled). The meteors are sufficiently distant to allow for the consideration of parallel vectors between received signals.

between the transmission antenna (Tx) and the receiver antennas (Rx). The meteor trail is displaced by the background wind ($\vec{u}$) which measures the corresponding Doppler shift (f_d) or the radial velocity component (v_{rad}). From the difference between incident and scattering wave vectors, we can obtain the Bragg vector ($\vec{k}_{Bi}$),

$$2\pi f_{di} = \vec{u} \cdot \vec{k}_{Bi} + \varepsilon_i, \tag{3.1}$$

where ε_i are the uncertainties. The mean winds are estimated with the Doppler frequencies in a grid of time and height by least-square fitting. To perform this calculation is necessary to assume horizontal homogeneity over the observed area.

To determine the horizontal winds, a sufficient number of meteors spread across altitude and time intervals is required. By knowing the position and radial velocity of each meteor, the mean zonal and meridional wind within the specified window can be calculated (Hocking et al., 2001). To construct a homogeneous time series, we have adopted a comprehensive methodology that amalgamates detections originating from two closely located SMRs. This methodology works by clustering quasi-simultaneous detections, emulating the approach employed in a singular radar mode's data collection strategy (Chau et al., 2017). This combination of measured volumes aims to mitigate observation gaps, which is highly valuable for long-term studies.

For middle latitudes, the network is composed of two SMRs in Germany at Juliusruh and Collm. At high latitudes, the SMRs are located in northern Norway at Andenes and Tromsø. Andenes and Juliusruh SMRs were upgraded in 2021 to operate in a coded continuous wave and multiple-input multiple-output mode (e.g., Huyghebaert et al., 2022; Poblet et al., 2023). However, for this thesis, measurements from one

SMR	Latitude and longitude	Frequency (MHz)	Peak power (kW)
Andenes	69.3°N, 16.0°E	32.55	12
Tromsø	69.6°N, 19.2°E	30.25	7.5
Juliusruh	54.6°N, 13.4°E	32.55	12
Collm	51.3°N, 13.0°E	36.2	6

TABLE 3.1: Specular meteor radar system parameters.

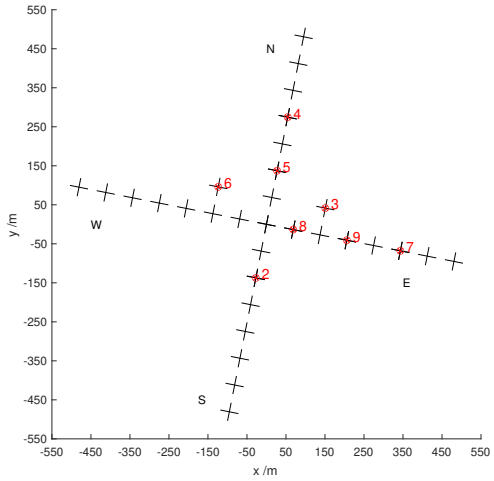

FIGURE 3.2: Schematic diagram of Saura PRR antenna array. Marked antennas are connected to individual receiver channels used for interferometry. Figure taken from Renkwitz et al. (2023), Fig. 1.

receiving station located close to each transmitter are used. Table 3.1 contains the main parameters of the radar systems used in this thesis' manuscripts.

3.1.2 Partial Reflection Radars

PRRs use the mechanism of partial reflection at gradients in the electron density profile through the ionized component in the lower ionosphere as a tracer for the neutral motions in the MLT between 50 and 90 km (Singer et al., 2005; Renkwitz and Latteck, 2017). Table 3.2 lists the system's location and parameters.

The Saura PRR is located in Northern Norway, 14 km south of the Andenes SMR, and has been in operation since 2004 (e.g. Singer et al., 2005; Renkwitz and Latteck, 2017). Figure 3.2 shows a sketch of the antenna distribution with the connected antennas and positions marked for individually sampled antennas lately used for interferometry (see e.g. Fukao and Hamazu, 2014; Reid, 2015).

The Juliusruh PRR is located in Juliusruh, Germany, co-located with the SMR and has been in operation since 2004. (Hoffmann et al., 2010). The predecessor system, with a different configuration and measurement technique, was in place from 1990 to 2003, which complements the time series (Keuer et al., 2007).

PRR	Latitude and longitude	Frequency (MHz)	Peak power (kW)
Saura	69.1°N, 16.0°E	3.17	116
Juliusruh	54.6°N, 13.4°E	3.18	64

TABLE 3.2: Partial reflection radar system parameters.

3.1.3 Ionosondes

The ionosonde is an ionospheric sounder that sweeps frequencies between 0.5 MHz to 30 MHz, which correspond to the High-Frequency (HF) band in the radio spectrum. The ionosonde emits a radio wave signal at a given frequency, which penetrates the

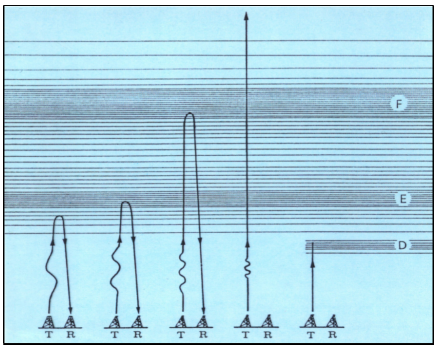

FIGURE 3.3: Ionosonde frequency diagram: the transmitter (T) emits a signal, reflected by the ionosphere and it is captured by the receiver (R). The F, E, and D denote the ionospheric layers, with different reflection indexes (Zolesi and Cander, 2014).

neutral atmosphere and is reflected back by the ionospheric layers. This process repeats until the signal reaches the F2 layer, at which point, upon reaching the critical frequency, the wave refracts and eventually exits the ionosphere. This is where the maximum electron density is found. Although the density at higher altitudes from this point decreases, the sounder cannot measure this decrease because the frequency required for measurement should be lower than what has been achieved to determine the upper part of the density profile. Thus, it remains masked by the lower layers. Consequently, the sounder can only provide information about the electron density profile in the lower part of the density profile. Figure 3.3 shows a diagram of the ionosonde, where the transmitter (T) emits a signal in a determined frequency that is reflected by the ionospheric layer and it is captured by the receiver (R). Every layer obtained from the ionosonde is the critical plasma frequencies (f_o), which represent the maximum frequency for total wave reflection for each layer, along with their corresponding heights. In particular, Juliusruh ionosonde is one of the oldest from Europe, with a data records since July 1957 and one of the most continuos around the globe.

3.1.4 AURA Satellite

The Aura EOS satellite flies in a Sun-synchronous, near polar (98.2 degrees inclination) orbit at 705 km above the Earth's surface with a 16-day repeat cycle and 233 revolutions per cycle. It was launched in 2004 and carries a passive microwave limb-sounding radiometer and spectrometer that measures thermal emission from the atmospheric limb. The MLS instrument operates by pointing its sensors toward the limb of the Earth, which allows it to capture the spectrum of microwave radiation emitted by the atmosphere. By analyzing this radiation, it is possible to determine the concentration of different gases and temperatures from the troposphere up to 90 km (e.g. Waters et al., 2006; Livesey et al., 2015). From the temperature measurements, it is possible to calculate geostrophic zonal winds from geopotential height profiles (Rüfenacht et al., 2018). It is important to point out that geostrophic balance is considered here, and when comparing the geometrical heights and winds at the mesopause with the geostrophic winds, the errors remain under 2%. The zonal mean geostrophic zonal wind represents an average across longitudes, and it is comparable to the mean zonal winds obtained in a specific location from radars.

3.2 Methods

This cumulative dissertation uses mainly statistical analysis and Principal Component Analysis (PCA). The following sections explain the implementation of the PCA and the statistical Student-t test under the adaptation from Behrens-Fisher.

3.2.1 Principal Component Analysis

The PCA is a technique that transforms high-dimension data into lower-dimension while retaining as much information as possible (Jolliffe and Jackson, 1993; Jolliffe, 2002). The main points of the method are:

1. Calculate the mean ($\bar{A}$) over the n-dimensional matrix A.
2. Subtract the mean matrix from the matrix A.
3. Calculate the covariance matrix ($cov(X, Y)$), where X and Y are two elements of the matrix A.
4. Calculate the eigenvectors and corresponding eigenvalues.
5. Sorting the eigenvectors by decreasing eigenvalues and keeping m eigenvectors with the largest eigenvalues. This results in a matrix of $n \times m$ dimension.

Finally, the expression obtained is:

$$A = UDV \tag{3.2}$$

where U are the eigenvectors of $(A \times A^T)$, V are the eigenvectors of $(A^T \times A)$, and D are the eigenvalues of the square root of $(A^T \times A)(A \times A^T)$.

In Jaen et al. (2022), the time series is built from the first Day Of the Year (DOY) of the first year until the last day of the last year as one dimension, altitude as a second dimension and the wind velocity as the third dimension. Then it is smoothed with a 16-day window, concluding with the matrix A. The smoothing technique mitigates transient oscillations, arising from factors such as gravity waves, tides, and instrumental impacts. The mean over altitude ($\bar{A}$) is subtracted from the matrix A and then divided into years and using the DOY between 100-280, the covariance, eigenvectors, and eigenvalues are calculated. As a result, the initial two principal components capture a significant proportion, ranging from 97.6 to 99.5%, of the overall variance.

Figure 3.4 depicts an example with the calculation for one year for easy comparison of each component and reconstruction. The first row shows the one year after smoothing (Fig. 3.4a), the matrix reconstructed with the first and second eigenvalues (Fig. 3.4b), and the reconstruction with the first three eigenvalues. The second row shows the independent eigenvalues (Fig. 3.4d, e, f). The last row depicts the variability over the DOY for the first three eigenvalues (Fig. 3.4g), their altitude variability (Fig. 3.4h), and the variances for all the eigenvalues (Fig. 3.4i).

3.2.2 Statistical Student-t Test

The field of long-term studies is based on assuming mostly linear trends. To calculate linear trends and correctly assume that there is a significant tendency or trend, there are several statistical tests. In this thesis, the Student-t test is implemented to investigate the significance of the linear tendencies. A linear function can be fitted by

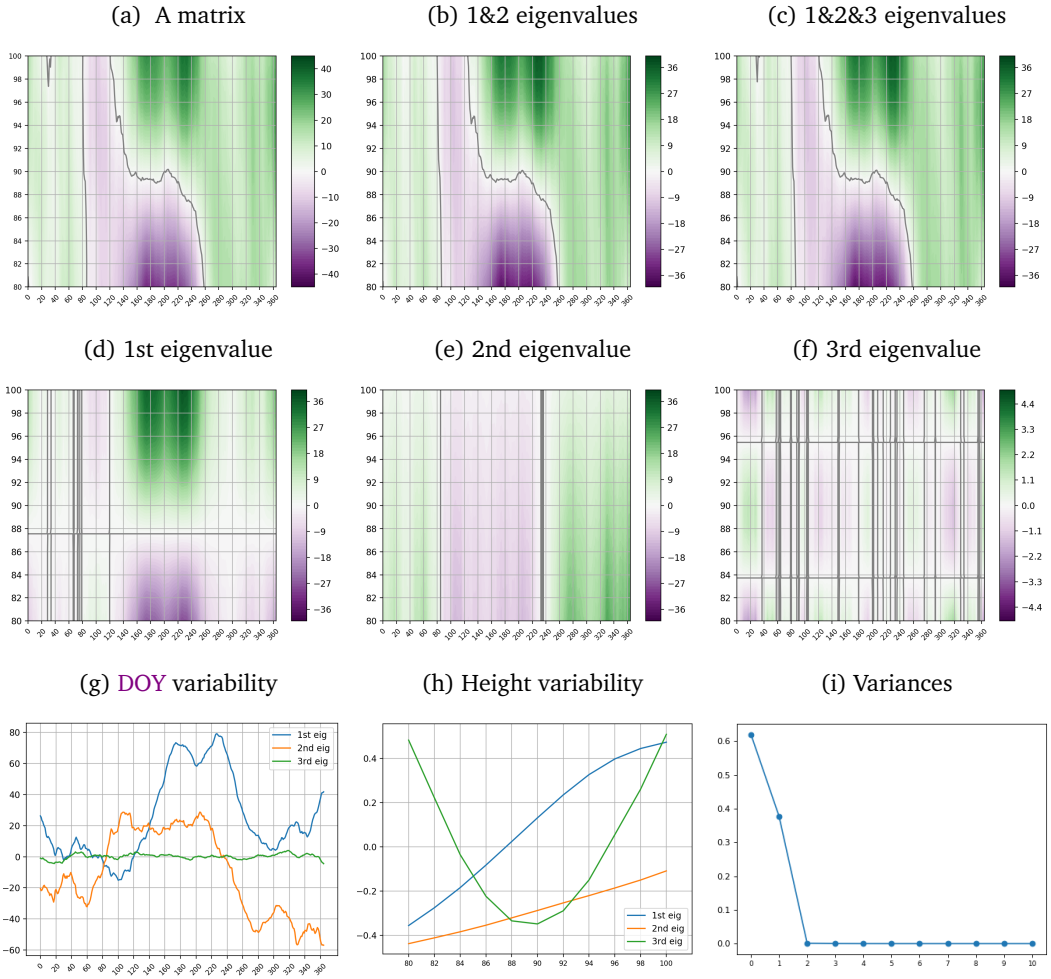

FIGURE 3.4: PCA eigenvalues and reconstructions of the zonal-mean winds of Andenes SMR, year 2015. Figures (a)-(f) are DOY, height (km) and the colorbar is velocity (m/s). Figures (g)-(i) are the variabilities of DOY, heigh (km) and component, respectively.

least-squares, for example, $v = m \cdot yr + b$, where v is our target measurement (e.g., velocity, summer length), m is the slope, yr is the year and b is the v-intercept.

The significance of the slope is tested by the Student's t-test, which is used to reject the null hypothesis: $H_o : m = 0$, which means the assumption of no trends.

Then, the statistical t is defined as,

$$t = \frac{m}{s_e / \sqrt{\sum_{i=1}^{n}(v_i - \bar{v})^2}}, \quad df \geq n - 2 \tag{3.3}$$

where n is the number of data points in the time series, df is the degree of freedom of the t-distribution associated with the case of study, $\bar{v}$ represents mean value of the measurements, s_e corresponds to the residual standard error ($s_e = \sqrt{SSE/(n-2)}$) and SSE is the sum of squared errors, determined as the sum of the squared differences between the measurements (v) and the predicted values ($\hat{v} = m \cdot yr + b$), $SSE = \sum_{i=1}^{n}(v_i - \hat{v}_i)^2$. The confidence interval for the slope parameter is:

$$\left(m - \frac{T_{95\%} \cdot s_e}{\sqrt{\sum_{i=1}^{n}(v_i - \bar{v})^2}} \, , \; m + \frac{T_{95\%} \cdot s_e}{\sqrt{\sum_{i=1}^{n}(v_i - \bar{v})^2}} \right), \tag{3.4}$$

where $T_{95\%}$ is the statistical T value at 95% of significance for the Student distribution (Storch and Zwiers, 1984). By comparing the T value at the corresponding degrees of freedom with the calculated statistical t for the problem, the null hypothesis is rejected ($t > T_{95\%}$) in the case of significant trends.

The student-t test assumes three conditions: 1) Sampling: every realization x (or y) occurs independently of all other realizations. 2) Distribution: the distribution that generates the realization x (or y) is the same for each observation sampled. 3) Normal distribution with equal variances. In Jaen et al. (2023), when testing for the geomagnetic wind differences, the last hypothesis is not fulfilled. The Behrens-Fisher Student-t test circumvents this problem by adjusting the degrees of freedom by comparing the first and second moments of the distribution to the chi-squared distribution. The result is calculating the degrees of freedom as,

$$df = \frac{(S_x^2/n_x + S_y^2/n_y)^2}{\frac{(S_x^2/n_x)^2}{n_{x-1}} + \frac{(S_y^2/n_y)^2}{n_{y-1}}}, \tag{3.5}$$

where S is the sampled variance (Robinson, 1976; Storch and Zwiers, 1984).

Chapter 4

Long-term Changes in the MLT Summer Lengths

Summary of:

Jaen, J., Renkwitz, T., Chau, J. L., He, M., Hoffmann, P., Yamazaki, Y., Jacobi, C., Tsutsumi, M., Matthias, V., and Hall, C.: Long-term studies of mesosphere and lower-thermosphere summer length definitions based on mean zonal wind features observed for more than one solar cycle at middle and high latitudes in the Northern Hemisphere, Ann. Geophys., 40, 23–35, https://doi.org/10.5194/angeo-40-23-2022, 2022.

Throughout the year the MLT changes over seasons drastically. Dynamics during the equinoxes are completely different from the solstice seasons, leading to opposite conditions during winter and summer (see Chapter 2). Temperature studies in the mesopause showed that over the years the summer duration has been extended. One of them is Offermann et al. (2010), which shows a tendency of longer summers with a rate of 1.21 day/year between 1988 and 2008 at 87 km, obtained with OH at middle latitudes. Kalicinsky et al. (2016) extended the study between 1988 and 2015 identifying a breakpoint in 2008 ($\pm$ 1.7 years) with negative temperature trends of -0.24 ($\pm$ 0.07 K/yr) and 0.64 ($\pm$ 0.33 K/yr) before and after the breakpoint. Anthropogenic changes or the ozone recovery are proposed as possible explanations for this breakpoint. Considering only the wind reversal, Jaen et al. (2022) proposed two definitions to investigate the long-term behavior and variability over the years at high and middle latitudes. The combination of SMRs at Andenes (69.3°N, 16.0°E) and Tromsø (69.6°N, 19.2°E), complemented by the Saura PRR (69.1°N, 16.0°E) at high latitudes, is also used for comparison with MLS satellite geostrophic winds at 70°N. Similarly, the Juliusruh (54.6°N, 13.4°E) and Collm (51.3°N, 13.0°E) SMRs, along with the PRR located at Juliusruh (54.6°N, 13.4°E) and MLS satellite geostrophic winds at 55°N, serve as instruments representing the middle latitude. The length of the time series varies between 2004/2005 and 2020, depending on the instruments. Additionally, a 31-year time series from 1990 to 2020, obtained from Juliusruh PRR, is also investigated.

The spring transition of the MLT wind occurs slowly over several days due to the active winter wave activity. Facing this long reversal time set, a sixteen-day sliding window and a principal component analysis were used to identify the two primary eigenvectors to rebuild the winds and identify the reversal day. The definitions are established with the main conditions; i) the wind changes from one direction to the

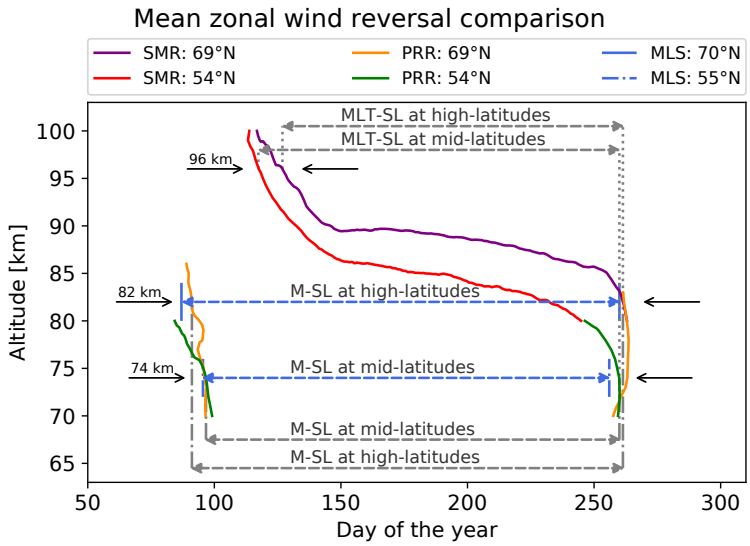

FIGURE 4.1: Summer length definitions in the MLT wind reversal. Each color line represents the zero wind line by instrument. SMRs, PRRs and Aura satellite (MLS) at each latitude are marked with color and line styles. The arrows denote the altitude where the day of the wind reversal is taken for the summer length definition. Figure taken from Jaen et al. (2022), Fig. 2.

opposite, ii) the wind reversal must occur at several kilometers in a short time, ideally, the same day. This selection is constrained by altitude and latitude, due to the latitudinal differences in the dynamics. Figure 4.1 depicts the climatological zero wind line (i.e. zero wind velocity) at middle and high latitudes, with the different instruments differentiated by colors. The arrows indicate the chosen height for the summer beginning and summer end at both latitudes.

The two definitions are as follows:

Mesospheric and Lower Thermospheric Summer Length (MLT-SL) is defined by the second wind reversal after the spring equinox at a fixed altitude. The summer beginning DOY is the day when the westward wind reverses to eastward at 96 km. The summer end is analogous, but with an altitude change, at 82 and 74 km for high and middle latitudes, respectively.

Mesospheric Summer Length (M-SL) is defined by the first and second wind reversal after the spring equinox at the same height. The summer beginning day of the year is the day when the eastward wind reverses to westward at 82 and 74 km for high and middle latitudes, respectively. The summer end is considered at the same altitude as the summer beginning when the westward wind reverses to eastward around the fall equinox.

Figures 4.2 and 4.3 depict the time series of the summer beginning, end, and length in the first three rows, for both definitions, at high and middle latitudes, respectively. The time series include their respective error-bar, the linear regression in a solid line and in dashed lines the slope variation (only when there was a significant slope for the time series). The fourth row is a composite of different indexes that could contribute as an external forcing agent to the wind reversal date. These indexes are listed below and explained in Section 2.3.

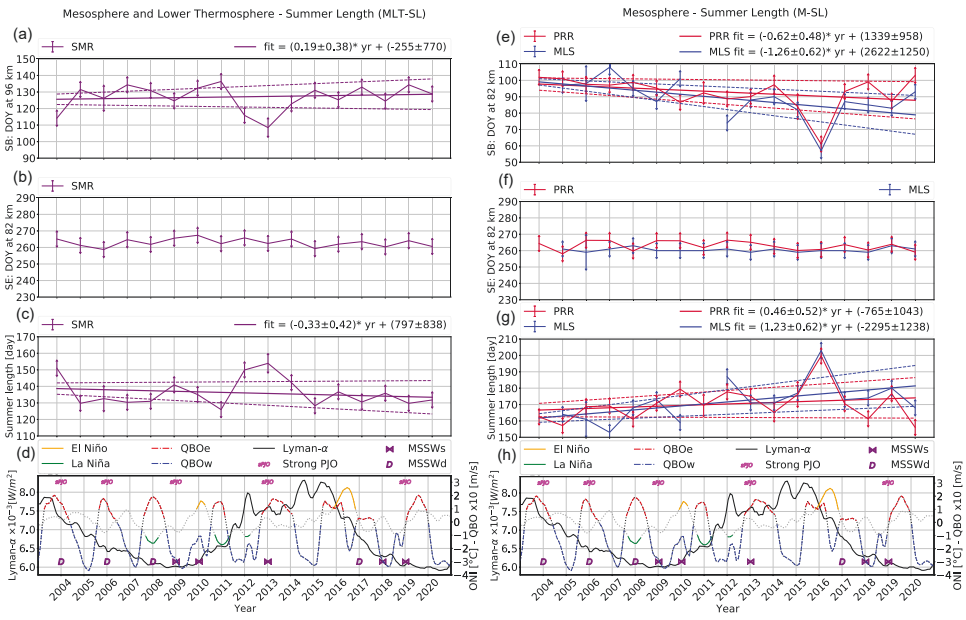

FIGURE 4.2: Summer beginning(a, e), summer end (b, f), summer length (c, g) at high latitudes. The last row (d, h) show different proxies for external processes. Figure taken from Jaen et al. (2022), Fig. 3.

sPJO Represents the strong polar-night jet oscillations.

MSSW Major sudden stratospheric warmings that ends in a split ($\bowtie$) or a displacement (D) of the polar vortex.

El Niño Extreme positive values of the ONI (i.e. ONI $\geq$ 1°C).

La Niña Extreme negative values of the ONI (i.e. ONI $\leq$ -1°C).

QBOw Quasi-biennial oscillation westward phase at 30 hpa.

QBOe Quasi-biennial oscillation eastward phase at 30 hpa.

Lyman-α Irradiance of the UV emission line of the hydrogen atom resulting from the transition from the second to the first energy level (1215.67 Å), measured at an altitude of 90 km.

The interaction of all these phenomena are quite complex and the simple correlations are insignificant. Nevertheless, for the year 2016, the earlier summer beginning is explained by an earlier final warming reported by Yamazaki and Matthias (2019) and the earlier summer beginning observed in 2013 is explained by a late strong planetary wave activity (Fiedler et al., 2015)

At middle latitudes, the PRR located in Juliusruh provided with an extended time series of 31 years. Figure 4.4 shows the mesospheric summer length and the periodograms for the summer length and summer end. Particularly this time series depict a breakpoint around 2008 $\pm$ 2 years.

From this study, the main findings are summarized below.

- The summer beginning is the most variable, transferring the variability to the summer length. This is the case for both summer definitions. However, the

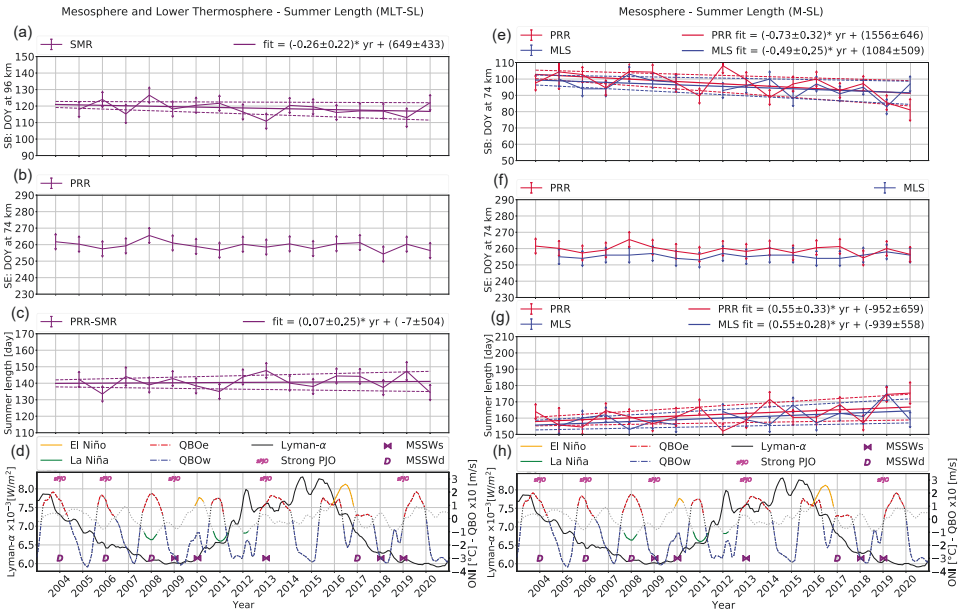

FIGURE 4.3: Same as Fig. 4.2 at middle latitudes. Figure taken from Jaen et al. (2022), Fig. 4.

length depends on the chosen latitude and altitude, having the highest variability at high latitudes. The summer end occurs for all latitudes in the same week, before the autumn equinox and presents no significant linear trend across latitudes.

⋆ In the MLT-SL definition, summer starts around 7 May at high latitudes (SL=136 days) and approximately 29 April at mid-latitudes (SL=141 days), indicating a shorter duration of summer at higher latitudes. This definition exhibits no significant trends, and the compared events (MSSW, strong polar-night jet oscillations, ENSO, QBO, and Lyman-α) do not show a consistent impact on the summer length. However, there is strong evidence of abnormal behaviour in the years 2004, 2012 and 2013, also observed by Hall and Tsutsumi (2020). During

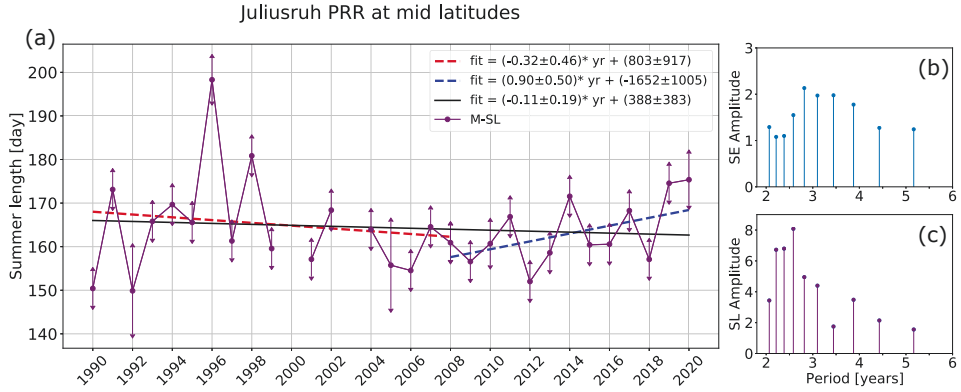

FIGURE 4.4: Mesospheric summer length at middle latitudes (a). The panel (b, c) depict the periodograms in years for the summer end and mesospheric summer length, respectively. Figure taken from Jaen et al. (2022), Fig. 5.

the winter of 2013, as reported by Fiedler et al. (2015), a heightened planetary wave activity occurring later than usual induced an earlier mean zonal wind reversal.

⋆ The M-SL definition is the most variable definitions due to it being more susceptible to winter conditions. The summer starts between the end of March and the beginning of April for high-latitudes and one week later for mid-latitudes. This definition presents significant trends indicating longer summer of around 0.55 days per year. The years 2012 and 2016 displayed extreme values. However, in the latter, the earlier summer beginning was a consequence of a final warming (Yamazaki and Matthias, 2019).

⋆ A comparison with the length of the plants' growing season shows a difference of around 10 days with respect to M-SL at middle latitudes.

⋆ The periodograms of the 31-year time series show periods of approximately 2.21-2.58 and 2.82-3.87 years, which could be attributed to QBO and ENSO, respectively (e.g., Offermann et al., 2015).

Chapter 5

Long-Term Changes of the MLT Summer Wind Velocity Maxima

Summary of

Jaen, J., Renkwitz, T., Liu, H., Jacobi, C., Wing, R., Kuchař, A., Tsutsumi, M., Gulbrandsen, N., and Chau, J. L.: Long-term studies of the summer wind in the mesosphere and lower thermosphere at middle and high latitudes over Europe, Atmos. Chem. Phys., 23, 14871–14887, https://doi.org/10.5194/acp-23-14871-2023, 2023.

The winds over the years exhibit a distinct characteristic pattern with seasons. During the equinoxes, the winds change direction and there is an enhancement of semidiurnal tides, which are stronger away from the tropics. The winter is a particular high activity season for the diurnal tide and planetary waves. The extratropical summer displays a weak secondary maximum of the diurnal tides, a minimum of the semidiurnal tides and strong winds that filter gravity waves reaching the MLT. These gravity waves break at the mesopause dumping their energy, which slows down the winds contributing to a wind reversal in lower thermosphere, above ∼86 km. Part of the dumped energy contributes to a change in wind direction due to the Coriolis torque inducing the meridional equatorward wind, contributing to the residual meridional circulation (e.g., Andrews et al., 1987; Holton, 2004). Under these conditions, the MLT summer horizontal winds display three main components: 1) the lower thermospheric eastward wind, 2) the mesospheric westward wind, and 3) the mesopause southward (equatorward) wind. Considering only the maxima of the wind in each month, independently from the altitude, Jaen et al. (2023) investigated the long-term intensity of the winds at high and middle latitudes over Europe with a selection of radars. At high latitudes the combination of SMRs at Andenes (69.3°N, 16.0°E) and Tromsø (69.6°N, 19.2°E), complemented by Saura PRR (69.1°N, 16.0°E), were used to investigate the eastward, westward and southward wind components. Similarly, at middle latitudes the combination of Juliusruh (54.6°N, 13.4°E) and Collm (51.3°N, 13.0°E) SMRs, along with the PRR located at Juliusruh (54.6°N, 13.4°E), was employed. The latter with an extended time series of 33 years (1990 - 2022) and the remaining instruments provided 19 years (2004 - 2022) of measurements.

Figure 5.1 depicts the horizontal wind climatologies calculated for both latitudes. In these figures, the wind components are represented as the mean over the years after being smoothed with a 16-day sliding window. In the summer, the wind maxima occurs during June, July and August. By calculating the monthly median per year

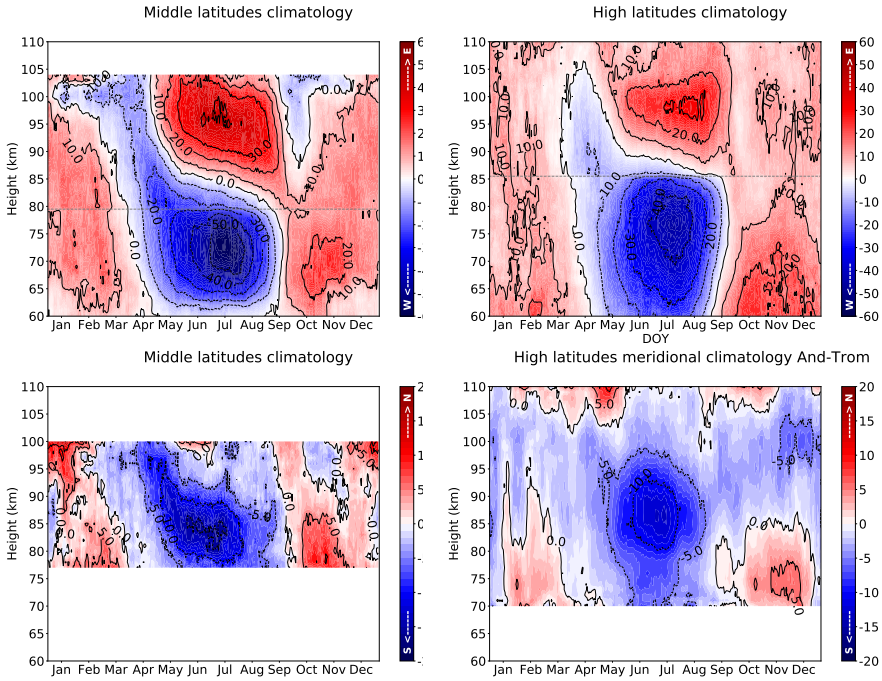

FIGURE 5.1: Middle and high latitudes horizontal winds climatologies. Sub-figures (a) and (b) show the zonal wind climatology were the red represents the eastward wind and the blue is the westward component for middle and high latitudes, respectively. The horizontal grey dotted line marks the change on the instruments, above are obtained from SMR and below PRRs. The (c) and (d) sub-figures depict the meridional wind over the years obtained from SMRs. The meridional wind with northward (poleward) is shown in red and the southward (equatorward) in blue. Figure taken from Jaen et al. (2023), Fig. 1.

and selecting the highest value in the altitude range for each wind component, the resultant time series are depicted in Figure 5.2. The time series are displayed with the difference between the third and first quartiles in a lighter color, along with their linear fit. The slopes with significant tendencies are shown in dashed line (i.e. $\geq$ 95%), while the dotted lines depict the non significant trends. From this figure, the significant results shows a decreasing lower thermospheric eastward wind speed at high latitudes in July. Another significant result comes from the middle latitudes, where significant increase of the mesospheric wind speed is accompanied with a significant decrease of the mesopause southward wind speed. The strengthening of the westward component tied to the weakening of the southward wind, could be an indicator of the wind circulation being affected.

Even that several studies have shown evidence of the MLT shrinking due to diabatic cooling (e.g., Peters et al., 2017; Yuan et al., 2019), the heights from the wind maxima show yearly variability with no significant long-term change. Figure 5.3 depict the height for the wind component at middle and high latitudes, respectively. In the middle latitudes, the westward wind component (33-year time series) depict an altitude jump between 2002 and 2004. The reason for this change in the heights is due to a replacement of the system; therefore, the height before the 2004 are considered to be non-reliable.

Investigating the variability of the time series, the periodograms show significant

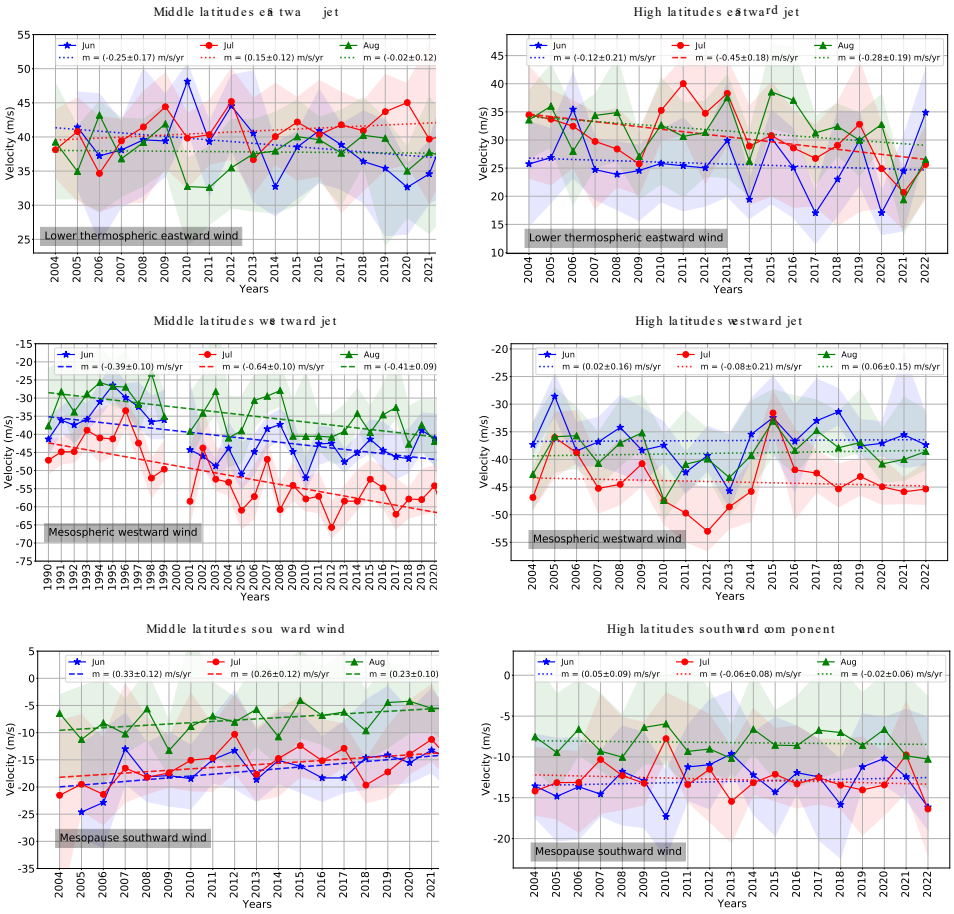

FIGURE 5.2: MLT wind maxima time series at middle (a, c, e) and high (b, d, f) latitudes. The eastward (a, b), westward (c, d), and southward (e, f) velocity maxima calculated yearly from a monthly median with their respective quartile difference (i.e., 75th and 25th quartiles). June (blue stars), July (red dots), and August (green triangles) with the linear fit where m represents the slope. The dashed lines depict the trends with 95 % significance. Figure taken from Jaen et al. (2023), Fig. 2.

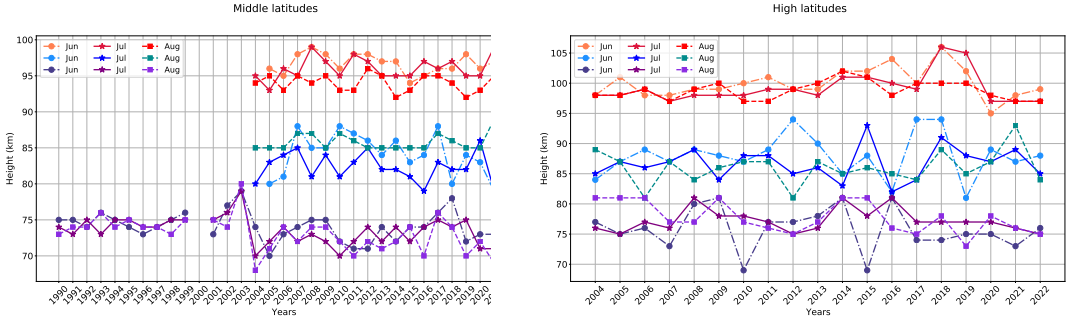

FIGURE 5.3: Altitude of the summer wind maxima over the years at middle (left) and high (right) latitudes. Circles, stars, and squares are the altitudes of the wind maxima for June, July and August, respectively. Red colors represent the height of the lower thermospheric eastward wind maxima. Blue/green colors are the altitude of the mesopause southward wind maxima and purple colors depict the altitude over the years of the mesosphere westward maxima. [Figure not published in the manuscript]

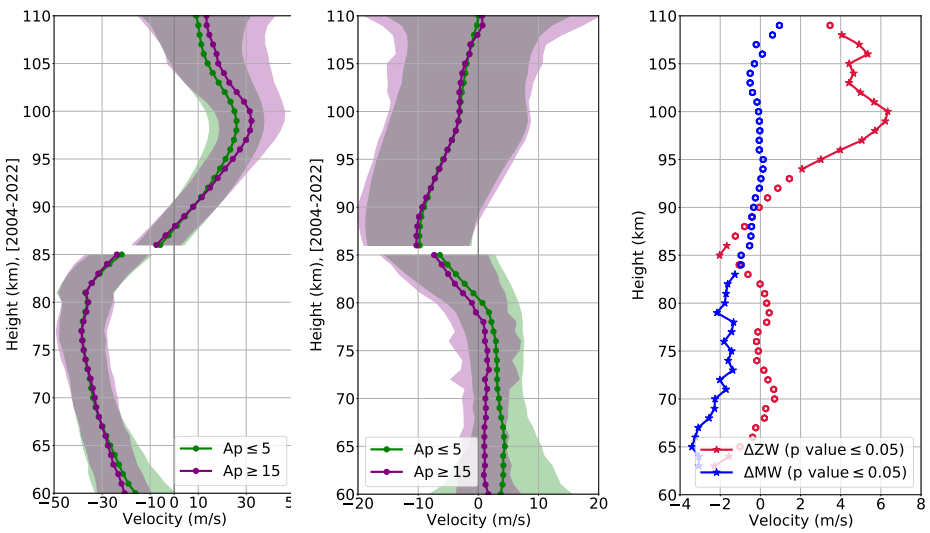

FIGURE 5.4: Differences between mean velocity profiles for low and high geomagnetic activity for middle (left) and high (right) latitudes. The differences for the zonal component are shown in blue, while the meridional differences are depicted in red. Stars represent significant differences, while circles depict nonsignificant differences. The figures are taken from Jaen et al. (2023), Fig. 6 and 5, respectively.

oscillation of 2-3, 4-6 and 10-12 years. However, these oscillation are not consistent across the months for the same wind component.

Another important aspect that has been shown to change the MLT wind speed is the geomagnetic activity. Jacobi et al. (2021) identified significant wind changes in the lower thermospheric eastward wind (2015-2020) dividing the days with the Ap index. As a result of the study, the authors found that the zonal wind becomes weaker during disturbed geomagnetic conditions. These results raise the question of whether geomagnetic activity could be involved in the identified significant trends. By dividing the summer days into low (Ap $\leq$ 5) and high geomagnetic activity (Ap $\geq$ 20, 15 at middle and high latitudes, respectively), Figure 5.4 depicts these summer mean differences, with significance indicated by different symbols based on the Behrens-Fisher Student's t test. Red depicts the zonal wind differences, while blue represents the meridional wind differences for middle (left) and high (right) latitudes. Stars indicate significant differences, whereas circles denote nonsignificant ones. From this figure, it becomes evident that geomagnetic activity weakens the MLT winds, except at high latitudes for the lower thermospheric eastward component, which becomes stronger. The reason for these changes in the wind speed are explained by Li et al. (2019) and Li et al. (2023). The authors found that while Joule heating warms the thermosphere, its effect is small compared to air movement (vertical heat advection) and temperature changes (adiabatic heating/cooling) in the MLT. The storm causes temperature changes and wind shifts, with these wind changes influencing pressure gradients.

Given that geomagnetic activity demonstrates appreciable effects on the wind, the next step is to investigate their potential impact on trends. Figure 5.5 shows a histogram with the distribution of days of high (purple) and low (green) geomagnetic activity across all years, overlaid is the Lyman α (red), which serves as a proxy for the solar activity. A clear difference is observed between the first and second half

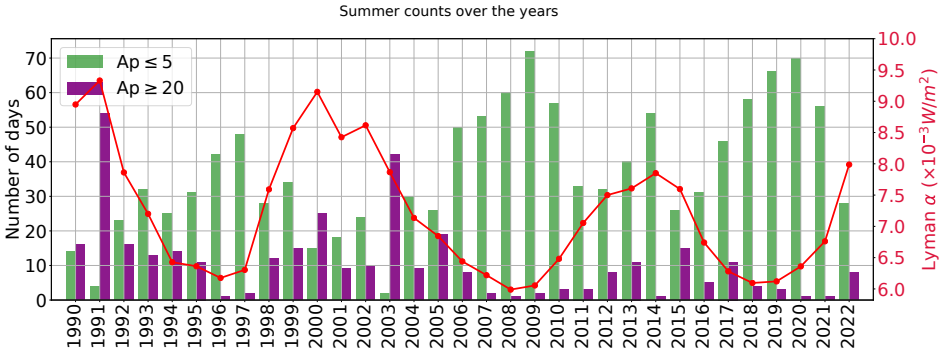

FIGURE 5.5: Low (green) and high (purple) geomagnetic activity summer days over the years. In red is depicted the Lyman α with a summer mean. Figure taken from Jaen et al. (2023), Fig. 7.

of the time series (i.e. 1990-2005 and 2006-2022). High solar activity typically correlates with more days of high geomagnetic activity. Despite covering more than one cycle, solar cycle 24 is weaker than its predecessor (i.e., solar cycle 23), resulting in fewer days of high geomagnetic activity in the second half of the time series. The observed difference may influence wind speed and trends. Specifically, the trends in the mesospheric westward winds might be partially due to recent geomagnetically quiet period. However, upon analysis of only the quiet periods, the summer mean wind trend remains significant, suggesting the influence of other factors on wind changes.[12]

The main findings of Jaen et al. (2023) are summarized as follows:

- In July at high latitudes, the lower thermospheric eastward summer maximum exhibits a significant decreasing trend of 0.45±0.18 m/s per year. The wind maxima occurs between June and August, ranging from 25 to 32 m/s at an altitude of 98-99 km.
- At middle latitudes, the mesospheric westward summer maximum has intensified over the past 33 years (1990-2022), exhibiting a significant trend of 0.64 $\pm$ 0.10 m/s per year (July). This trend is independent of geomagnetic activity.
- The mesopause southward wind maxima at middle latitudes, exhibits a significant weakening across the three studied months over the years. The most substantial decrease is in June and July, reaching negative slopes of 0.33 $\pm$ 0.12 and 0.26 $\pm$ 0.12 m/s per year, respectively.
- Among the analyzed components, only the mesospheric summer westward maxima exhibits signatures of the solar cycle (8.6-11.3 years) during the three months. The remaining time series show additional oscillations around 2.3-2.8 years and 3.2-4.4 years, potentially linked to modulations from the QBO, ENSO, or the quasi-quadrennial oscillation.
- Geomagnetic activity weakens the horizontal winds except at high latitudes, where it strengthens the lower thermospheric eastward winds above 94 km.
- The meridional wind component, under high geomagnetic activity, exhibits a disturbed pattern with reduced velocities below 84 km at high latitudes and below 78 km at middle latitudes.

Chapter 6

Collaborative Papers

In parallel to my own research during my PhD, I collaborated with colleagues which led to the following publications.

- Jacobi, C., Kuchar, A., Renkwitz, T., and Jaen. J.: Long-term trends of midlatitude horizontal mesosphere/lower thermosphere winds over four decades, Adv. Radio Sci., 21, 1–11, https://doi.org/10.5194/ars-21-111-2023, 2023.
- Sivakandan, M., Mielich, J., Renkwitz, T., Chau, J. L., Jaen, J., & Laštovička, J.: Long-term variations and residual trends in the E, F, and sporadic E (Es) layer over Juliusruh, Europe, J. Geophys. Res. Space Phys., 128, e2022JA031097, https://doi.org/10.1029/2022JA031097, 2023.
- Renkwitz, T., Sivakandan, M., Jaen, J., and Singer, W.: Ground-based noontime D-region electron density climatology over northern Norway, Atmos. Chem. Phys., 23, 10823–10834, https://doi.org/10.5194/acp-23-10823-2023, 2023.

Engaging in these investigations has immensely enriched my research focus and has played an important role in the evolution of my doctoral journey. Below, I present concise summaries of these studies.

6.1 Long-Term Trends of Midlatitude MLT Winds over Four Decades

This paper combines low frequency measurements from 1978 to 2008, and the very high frequency meteor radar winds from 2004 to 2021 from Collm at 90 km, which are compared with Juliusruh partial reflection radar mean winds at 81-85 km from 1990-2021. These MLT wind time series obtained are among the longest globally, offering insight into potential climate change effects on the MLT. In this study, long-term trends and trend changes over Collm are presented, and a comparison of long-term linear trends over both sites is conducted. Due to variations in observation methods, the considered altitudes differ by several kilometers, leading to differences in summer climatological mean zonal winds between Juliusruh and Collm. Despite these variations, long-term trends over Collm and Juliusruh generally agree qualitatively, particularly in September-October-November (SON) and December-January-February (DJF), although differences emerge in March-April-May (MAM). Particularly, Collm winds show indications of a potential trend change in the 1990s, especially prominent in June-July-August (JJA) with zonal trend values of 0.50 m $s^{-1}yr^{-1}$ before 1998 $\pm$ 4.4 yr and after -0.04 m $s^{-1}yr^{-1}$. This change could be connected to the ozone turnaround after 1995 or lower atmosphere climate change (Jacobi et al.,

2015). The comparison between Collm and Juliusruh winds shows considerable variability at timescales of a few years, possibly influenced by lower/middle atmosphere circulation patterns like QBO, North Atlantic Oscillation (NAO), and ENSO. These patterns may impact middle atmosphere winds up to the mesosphere, but their effects decrease or reverse near the mesopause region. The height difference of the wind time series analyzed here may contribute to the observed variability at these timescales. A significant difference is observable in May for both sites, nevertheless, a correlation coefficient of r = 0.7 indicates variability at both sites is consistent even with the altitude differences and latitude sets of the wind reversal already studied in Jaen et al. (2022).

6.2 Long-Term Variations and Residual Trends in the E, F, and Es Layers at Middle Latitudes

Sivakandan et al. (2023) investigates the long-term variations and linear residual trends in the ionospheric E, Es, and F2 and corresponding altitudes of the layers over Juliusruh, Germany. The study combines traditional regression analysis with a new method to estimate trends. In addition, the study uses Lomb-Scargle analysis to identify predominant oscillations in the ionospheric parameters, demonstrating the significant influence of annual and solar cycle oscillations on the F2 layer's critical plasma frequencies and altitudes. The 11-year solar cycle oscillation is more significant than the annual oscillation in daytime foF2 and nighttime hmF2, while the opposite relation is observed in the daytime foE and foEs. The height (hmF2) exhibits a negative trend (-413 $\pm$ 47 m yr^{-1} daytime and -574 $\pm$ 75 m yr^{-1} nighttime), suggesting a hydrostatic contraction in the ionospheric peak altitudes, possibly caused by the greenhouse cooling effects. The corresponding critical frequency depicts negative trends (-4.44 $\pm$ 1.78 kHz yr^{-1} daytime and -4.30 $\pm$ 1.63 kHz yr^{-1} nighttime) that once divided before and after 1996, the significant trend from before 1996, becomes positive, but insignificant in the second period (i.e., 1997-2019). In the E-region, the foE has no significant trend. However, the foEs depict negative trends (-2.00 $\pm$ 0.61 kHz yr^{-1}), with a similar behavior to the foF2, where the divided time series showed weak trends after 1997.

6.3 D-Region Noontime Electron Density Climatology at High Latitudes

This study presents local noontime climatologies of electron density in the middle atmosphere at high latitudes during periods of quiet and geomagnetic active periods. The data is collected using the high-frequency Saura radar experiment applying dedicated signal processing and interferometry techniques to localize the scattering structures. Furthermore, the Faraday-International Reference Ionosoheric model is also used to remove the outliers in the data. The electron density climatologies show an unexplained asymmetry between spring and fall, which is not related to the solar zenith angle, as well as a significant decrease in electron densities around the autumn equinox. The electron density pattern of spring-fall asymmetry and the October decrease is found for all analyzed nine years (2004-2022). A possible explanation is proposed that the meridional circulation during fall and winter, along with the transport of Nitric Oxide (NO) from the lower thermosphere, could be responsible

for enhanced electron density. In contrast, increased meridional winds and tidal activity at lower altitudes might explain a sudden reduction in electron density in early October. Observed changes in temperature and tidal activity could also contribute to electron density variations.

Chapter 7

Conclusions and Outlook

This cumulative dissertation aimed to investigate the long-term dynamics of the summer MLT at middle and high latitudes, with the main objective being the study of the long-term variability of the neutral winds. The MLT is the region where the neutral and ionized atmosphere coexist, contributing to the complexity of the system. Furthermore, it is a significant portion of Earth's atmosphere, which makes it essential for understanding the full system and its evolution.

The dynamics that drive the middle atmosphere are due to motion, mixing, heating, and propagation of waves. The Earth's geodesic shape and the ocean-land distribution produce asymmetries over the two hemispheres (e.g. Shepherd, 2008). These differences are observed in the winds, temperatures, and composition. Ozone, one of the main absorbers of solar radiation, shows these asymmetries when depleting at polar latitudes in spring and has a higher concentration in the Northern than the Southern polar summer hemisphere. Venkateswara Rao et al. (2015) found a significant correlation between the Southern hemisphere ozone gradients in spring with the stratospheric wind and a significant anticorrelation with mesospheric wind residuals. The authors also explained that due to strong winter conditions and strong eastward wind persisting into late spring in the stratosphere, as a consequence of an increase in stratospheric ozone gradients, a poleward residual circulation is expected in the upper mesosphere extending the winter time. The opposite effect is observed in the polar mesospheric summer echo occurrence, as was shown by Latteck et al. (2021). In their study, the authors found significant trends of longer polar mesospheric summer echoes of half a day per year in the past two decades in the Northern Hemisphere. This result agrees with the studied trends in this thesis. At high latitudes, the summer length, defined by the mesospheric eastward to westward wind reversal, depicted a significant trend of earlier summer onset of about half a day per year.

Between many limitations faced by the long-term community in this field of study (see Laštovička and Jelínek, 2019; Laštovička, 2023), the length of the measurements represents one of the more important aspects. Phenomena like the multi-year oscillations and its underlying mechanism, as well as the potentially multi-decadal oscillations, are not fully understood (e.g., Offermann et al., 2021). Evidence of these phenomena arises when breakpoints appear in the time series (Lauter and Entzian, 1983; Offermann et al., 2006; Liu et al., 2010; Jacobi et al., 2015; Hall and Tsutsumi, 2020). The middle latitudes' summer length of 31-year time series, studied in this thesis, evidenced one of these breakpoints. Moreover, the significant trends in the zonal and meridional components for different seasons studied in Jacobi et al. (2023), also evidenced breakpoints in the 40 years of measurements. Portnyagin et al. (2006) tested more than one degree polynomial to fit the trends, concluding that the

MLT winds have non-uniform trends. To understand the breakpoints, it is necessary to study atmospheric dynamics as a whole system and identify where these changes originate. Possible sources of the change in the atmospheric parameters could be due to external causes, such as the ozone depletion recovery (Weber et al., 2022) or even major volcanic eruptions (Savigny et al., 2020; Wallis et al., 2023).

The contribution of advanced global circulation models is key to understanding the underlying physics occurring in the atmosphere. Particularly, accurate modeling of the MLT region is challenging due to the importance of GWs in the summer mesopause and especially the GW drag occurring in the lower thermospheric spring. The westward wind pattern observed at lower thermospheric altitudes in spring, a product of GW drag, is not reproduced by most models (e.g., Stober et al., 2021). One exception is the KMCM (K"uhlungsborn Mechanistic General Circulation Model), which successfully accomplished the spring wind reversal through GWs parameterizations (Hoffmann et al., 2010).

GWs have a crucial role in the global MLT dynamics and have the characteristic of traveling long distances away from their sources, and introducing forcing in the middle atmosphere which affects the global winds. Ern et al. (2011) suggested that GWs produced by deep convection in the subtropical monsoon regions could contribute to the mesospheric wind reversal at middle and high latitudes. Additionally, they indicated that there could be an anticorrelation between solar flux and GW momentum flux. With increasing GW activity, it is possible to expect higher energy deposition in the mesopause and an increase in the southward winds due to the residual meridional mean circulation. However, this contradicts the results from the wind maxima studied in this thesis. While at high latitudes, the southward wind showed non-significant trends, at middle latitudes this wind component showed a weakening trend. On the other hand, the zonal mesospheric wind depicted a significant strengthening over the past 33 years, which could indicate that the breaking of GWs is occurring below the mesopause giving energy to the mean zonal winds. Hoffmann et al. (2011), Liu et al. (2017) and Luo et al. (2021) are some of the studies that have shown significant increasing GW trends that could contribute to this explanation. Another explanation could arise from investigating atmospheric tidal waves. The semidiurnal tides, which are maximized in extratropical regions and during the equinoxes, have less probability of contributing to the summer wind trends. On the other hand, the diurnal tide, which maximizes during the solstices and at low latitudes, could contribute to the wind trends. However, McLandress (2002) showed that with strong wind shears, there is a weakening of the tides and an amplification of the quasi-two-day waves, which still need to be investigated as a possible source for the trends.

Shifting the focus from the neutral aspect of the MLT region to the ionized one, in this thesis a significant influence of the solar activity on the neutral wind maxima was observed. As a part of this thesis, the electron density climatology for both quiet and disturbed periods was studied (Renkwitz et al., 2023). This investigation revealed asymmetries between the periods around the equinoxes, which agree with the different processes mentioned in this thesis (i.e. residual mean meridional circulation, tides, and temperature changes). However, their mechanism and changes over the years remain to be investigated.

The advantage of looking into the long-term parameters of the ionosphere is the access to longer time series. This is the case for 56-year datasets of the F2 critical frequency measurements studied here. The trends obtained by Sivakandan et al. (2023) also revealed a breakpoint in 1996. Additionally, the ionospheric F-region proved to

have a strong positive correlation with the solar cycle (sunspot number in this study) and the E-region showed a positive correlation until the 23rd solar cycle and a weak correlation afterward, which has already been reported before by the ionospheric community (e.g., Danilov, 2021; Laštovička, 2023). The *disappearing* anticorrelation with the solar cycle is also observed in the MLT winds (Portnyagin et al., 2006; Fiedler et al., 2011; DeLand and Thomas, 2015). The mesospheric westward wind maxima showed oscillation between 10.2 to 11.3 years that could be associated with the solar cycle. However, a direct correlation with Lyman α showed it to be non-significant considering the 33-year time series. On the other hand, by dividing the time series into two periods (1990-2004 and 2004-2022), the same analysis shows significant anticorrelation ($\rho = 0.69$) for the first period. The second period remains with non-significant correlations between the mesospheric westward wind maxima and Lyman α. These changes are evidence on the evolution over the years of the MLT which stills needs to be investigated. A possible explanation was recently provided by Vellalassery et al. (2023), who studied the water vapor response to Lyman α variability for the periods 1992 to 2018 and found that the amplitude of Lyman α variation decreased by about 40% after 2005.

In contemporary times, models specializing in replicating the middle atmosphere are imperative for comprehending the physics, composition, coupling, and dynamics. Essentially, the models provide information on how the atmosphere changes, whether due to intrinsic natural factors or anthropogenic contributions. Consequently, long-term studies employing models contribute to understanding how the changes impact the atmosphere, predicting its future evolution. However, they still fall short of faithfully reproducing the observed atmosphere. Instrumental measurements, on the other hand, provide evidence of the atmospheric evolution from past to present. Simultaneously, prolonged investigations utilizing consistent and extended measurements facilitate the study and monitoring of atmospheric evolution, which makes it imperative to maintain instruments for long-term studies. Through the implementation of theories in models, a more profound comprehension of observed phenomena becomes possible. Both facets, modeling studies, and extended empirical analyses, collaboratively enhance our comprehension of the characteristics of the atmosphere.

Bibliography

Andrews, David G., James R. Holton, and Conway B. Leovy (1987). *Middle atmosphere dynamics*. Vol. 40. ISBN: 0120585766.

Baldwin, Mark P, Lesley J. Gray, T. J. Dunkerton, Kevin Hamilton, P. H. Haynes, W. J. Randel, James R. Holton, M Joan Alexander, I. Hirota, T. Horinouchi, D. B. A. Jones, J. S. Kinnersley, C. Marquardt, K. Sato, and M. Takahashi (2001). "The quasi-biennial oscillation". In: *Reviews of Geophysics* 39.2, pp. 179–229. ISSN: 87551209. DOI: 10.1029/1999RG000073.

Bremer, J. and U. Berger (2002). "Mesospheric temperature trends derived from ground-based LF phase-height observations at mid-latitudes: Comparison with model simulations". In: *Journal of Atmospheric and Solar-Terrestrial Physics* 64.7, pp. 805–816. ISSN: 13646826. DOI: 10.1016/S1364-6826(02)00073-1.

Bremer, J. and Dieter H.W. Peters (2008). "Influence of stratospheric ozone changes on long-term trends in the meso- and lower thermosphere". In: *Journal of Atmospheric and Solar-Terrestrial Physics* 70.11-12, pp. 1473–1481. ISSN: 1364-6826. DOI: 10.1016/J.JASTP.2008.03.024.

Butler, Amy Hawes, Dian J. Seidel, Steven C. Hardiman, Neal Butchart, Thomas Birner, and Aaron Match (2015). "Defining sudden stratospheric warmings". In: *Bulletin of the American Meteorological Society* 96.11, pp. 1913–1928. ISSN: 00030007. DOI: 10.1175/BAMS-D-13-00173.1.

Butler, Amy Hawes, Jeremiah P. Sjoberg, Dian J. Seidel, and Karen H. Rosenlof (2017). "A sudden stratospheric warming compendium". In: *Earth System Science Data* 9.1, pp. 63–76. ISSN: 18663516. DOI: 10.7289/V5NS0RWP.

Chapman, Sydney and Richard S. Lindzen (1969). *Atmospheric Tides*. Springer Netherlands. ISBN: 9789401033992. DOI: 10.1007/978-94-010-3399-2.

Charlton, Andrew J. and Lorenzo M. Polvani (2007). "A New Look at Stratospheric Sudden Warmings. Part I: Climatology and Modeling Benchmarks". In: *Journal of Climate* 20.3, 449–469. ISSN: 0894-8755. DOI: 10.1175/jcli3996.1.

Chau, Jorge L., Gunter Stober, Chris M. Hall, Masaki Tsutsumi, Fazlul I. Laskar, and Peter Hoffmann (2017). "Polar mesospheric horizontal divergence and relative vorticity measurements using multiple specular meteor radars". In: *Radio Science* 52.7, pp. 811–828. ISSN: 00486604. DOI: 10.1002/2016RS006225.

Collimore, Christopher C., David W. Martin, Matthew H. Hitchman, Amihan Huesmann, and Duane E. Waliser (2003). "On The Relationship between the QBO and Tropical Deep Convection". In: *Journal of Climate* 16.15, 2552–2568. ISSN: 1520-0442. DOI: 10.1175/1520-0442(2003)016<2552:otrbtq>2.0.co;2.

Conte, J. Federico, Jorge L. Chau, and Dieter H.W. Peters (2019). "Middle- and High-Latitude Mesosphere and Lower Thermosphere Mean Winds and Tides in Response to Strong Polar-Night Jet Oscillations". In: *Journal of Geophysical Research: Atmospheres* 124.16, pp. 9262–9276. ISSN: 2169-897X. DOI: 10.1029/2019JD030828.

Danilov, A.D. (2021). "Behavior of F2-layer parameters and solar activity indices in the 24th cycle". In: *Advances in Space Research* 67.1, 102–110. ISSN: 0273-1177. DOI: 10.1016/j.asr.2020.09.042.

DeLand, Matthew T. and Gary E. Thomas (2015). "Updated PMC trends derived from SBUV data". In: *Journal of Geophysical Research: Atmospheres* 120.5, pp. 2140–2166. ISSN: 2169897X. DOI: 10.1002/2014JD022253.

Delgado-Osorio, Ximena, Marco Gierke, Juliana Jaen, Johnson Kansiime, Dominik Lonken, Emilio Pérez-Bosch Quesada, Kesava Ramachandran, Tommaso Rizzi, and Pankhuri Saxena (2023). *Being a Doctoral Researcher in the Leibniz Association: 2021 Leibniz PhD Network Survey Report*. DOI: 10.13140/RG.2.2.29723.44320. URL: https://rgdoi.net/10.13140/RG.2.2.29723.44320.

Ern, M., P. Preusse, J. C. Gille, C. L. Hepplewhite, M. G. Mlynczak, J. M. Russell, and M. Riese (2011). "Implications for atmospheric dynamics derived from global observations of gravity wave momentum flux in stratosphere and mesosphere". In: *Journal of Geophysical Research Atmospheres* 116.19. ISSN: 01480227. DOI: 10.1029/2011JD015821.

Espy, P. J., S. Ochoa Fernández, P. Forkman, D. Murtagh, and J. Stegman (2011). "The role of the QBO in the inter-hemispheric coupling of summer mesospheric temperatures". In: *Atmospheric Chemistry and Physics* 11.2, pp. 495–502. DOI: 10.5194/acp-11-495-2011.

Farman, J. C., B. G. Gardiner, and J. D. Shanklin (1985). "Large losses of total ozone in Antarctica reveal seasonal ClOx/NOx interaction". In: *Nature* 315.6016, 207–210. ISSN: 1476-4687. DOI: 10.1038/315207a0.

Fiedler, J., G. Baumgarten, U. Berger, P. Hoffmann, N. Kaifler, and F. J. Lübken (2011). "NLC and the background atmosphere above ALOMAR". In: *Atmospheric Chemistry and Physics* 11.12, pp. 5701–5717. ISSN: 16807324. DOI: 10.5194/ACP-11-5701-2011.

Fiedler, Jens, Gerd Baumgarten, Uwe Berger, Axel Gabriel, Ralph Latteck, and Franz-Josef Lübken (2015). "On the early onset of the NLC season 2013 as observed at ALOMAR". In: *Journal of Atmospheric and Solar-Terrestrial Physics* 127, pp. 73–77. ISSN: 13646826. DOI: 10.1016/j.jastp.2014.07.011.

Fleming, Eric L., Sushil Chandra, J.J. Barnett, and M. Corney (1990). "Zonal mean temperature, pressure, zonal wind and geopotential height as functions of latitude". In: *Advances in Space Research* 10.12, pp. 11–59. ISSN: 0273-1177. DOI: https://doi.org/10.1016/0273-1177(90)90386-E.

Ford, E. A. K., R. E. Hibbins, and M. J. Jarvis (2009). "QBO effects on Antarctic mesospheric winds and polar vortex dynamics". In: *Geophysical Research Letters* 36.20. ISSN: 1944-8007. DOI: 10.1029/2009gl039848.

French, W. John R., Andrew R. Klekociuk, and Frank J. Mulligan (2020). "Analysis of 24 years of mesopause region OH rotational temperature observations at Davis, Antarctica-Part 2: Evidence of a quasi-quadrennial oscillation (QQO) in the polar mesosphere". In: *Atmospheric Chemistry and Physics* 20.14, pp. 8691–8708. DOI: 10.5194/ACP-20-8691-2020.

Fritts, David C. and M Joan Alexander (2003). "Gravity wave dynamics and effects in the middle atmosphere". In: *Reviews of Geophysics* 41.1, p. 1003. ISSN: 8755-1209. DOI: 10.1029/2001RG000106.

Fukao, Shoichiro and Kyosuke Hamazu (2014). *Radar for Meteorological and Atmospheric Observations*. Vol. 9784431543. Tokyo: Springer Japan, pp. 1–537. ISBN: 978-4-431-54333-6. DOI: 10.1007/978-4-431-54334-3.

Gan, Quan, J Du, Victor I. Fomichev, William E. Ward, Stephen R. Beagley, Shaodong Zhang, and Jia Yue (2017). "Temperature responses to the 11 year solar cycle in the mesosphere from the 31 year (1979–2010) extended Canadian Middle Atmosphere Model simulations and a comparison with the 14 year (2002–2015) TIMED/SABER

observations". In: *Journal of Geophysical Research: Space Physics* 122.4, pp. 4801–4818. ISSN: 21699402. DOI: 10.1002/2016JA023564.

Garcia, Rolando R. and Fabrizio Sassi (1999). "Modulation of the mesospheric semiannual oscillation by the quasibiennial oscillation". In: *Earth, Planets and Space* 51.7-8, pp. 563–569. ISSN: 18805981. DOI: 10.1186/BF03353215/METRICS.

Garcia, Rolando R., Susan Solomon, Raymond G. Roble, and David W. Rusch (1984). "A numerical response of the middle atmosphere to the 11-year solar cycle". In: *Planetary and Space Science* 32 (4). ISSN: 00320633. DOI: 10.1016/0032-0633(84)90121-1.

García-Herrera, R., Natalia Calvo, R. R. Garcia, and M. A. Giorgetta (2006). "Propagation of ENSO temperature signals into the middle atmosphere: A comparison of two general circulation models and ERA-40 reanalysis data". In: *Journal of Geophysical Research Atmospheres* 111.6. ISSN: 01480227. DOI: 10.1029/2005JD006061.

Goncharenko, Larisa P., V. Lynn Harvey, Huixin Liu, and Nicholas M. Pedatella (2021). *Sudden Stratospheric Warming Impacts on the Ionosphere–Thermosphere System: A Review of Recent Progress*. DOI: 10.1002/9781119815617.ch16.

Gularte, Erika, Daniel D. Carpintero, and Juliana Jaen (2018). "Upgrading CCIR's f o F2 maps using available ionosondes and genetic algorithms". In: *Advances in Space Research* 61.7, pp. 1790–1802. ISSN: 18791948. DOI: 10.1016/j.asr.2017.08.019.

Hall, Chris M. and Masaki Tsutsumi (2020). "Neutral temperatures at 90 km altitude over Svalbard (78°N 16°E), 2002–2019, derived from meteor radar observations". In: *Polar Science* 24.May, p. 100530. ISSN: 18739652. DOI: 10.1016/j.polar.2020.100530.

Hargreaves, John Keith (1992). *The Solar-Terrestrial Environment: An Introduction to Geospace - the Science of the Terrestrial Upper Atmosphere, Ionosphere, and Magnetosphere*. Cambridge University Press. ISBN: 9780511628924. DOI: 10.1017/cbo9780511628924.

Hocking, Wayne K, Ryan A. Fuller, and B. Vandepeer (2001). "Real-time determination of meteor-related parameters utilizing modern digital technology". In: *Journal of Atmospheric and Solar-Terrestrial Physics* 63.2-3, pp. 155–169. ISSN: 13646826. DOI: 10.1016/S1364-6826(00)00138-3.

Hoffmann, Peter, Erich Becker, Werner Singer, and Manja Placke (2010). "Seasonal variation of mesospheric waves at northern middle and high latitudes". In: *Journal of Atmospheric and Solar-Terrestrial Physics* 72.14-15, pp. 1068–1079. ISSN: 1364-6826. DOI: 10.1016/j.jastp.2010.07.002.

Hoffmann, Peter, Markus Rapp, Werner Singer, and D. Keuer (2011). "Trends of mesospheric gravity waves at northern middle latitudes during summer". In: *Journal of Geophysical Research* 116.15, D00P08. ISSN: 0148-0227. DOI: 10.1029/2011JD015717.

Holton, James R. (2004). *An Introduction to Dynamic Meteorology*. 4th. Elsevier. ISBN: 0123540151.

Huyghebaert, Devin, Matthias Clahsen, Jorge L. Chau, Toralf Renkwitz, Ralph Latteck, Magnar G. Johnsen, and Juha Vierinen (2022). "Multiple E-Region Radar Propagation Modes Measured by the VHF SIMONe Norway System During Active Ionospheric Conditions". In: *Frontiers in Astronomy and Space Sciences* 9.May, pp. 1–16. ISSN: 2296-987X. DOI: 10.3389/fspas.2022.886037.

Iimura, Hiroyuki, David C Fritts, Ruth S Lieberman, Diego Janches, Nicholas J Mitchell, Steven J Franke, Werner Singer, Wayne K Hocking, Michael J Taylor, and Tracy Moffat-griffin (2021). "Journal of Atmospheric and Solar-Terrestrial Physics Climatology of quasi-2-day wave structure and variability at middle latitudes in the

northern and southern hemispheres". In: *Journal of Atmospheric and Solar-Terrestrial Physics* 221.March, p. 105690. ISSN: 1364-6826. DOI: 10.1016/j.jastp.2021.105690.

Jacobi, Christoph (1998). "On the solar cycle dependence of winds and planetary waves as seen from mid-latitude D1 LF mesopause region wind measurements". In: *Annales Geophysicae* 16.12, pp. 1534–1543. ISSN: 09927689. DOI: 10.1007/S00585-998-1534-3.

Jacobi, Christoph, Tatiana Ermakova, Daniel Mewes, and Alexander I. Pogoreltsev (2017). "El Niño influence on the mesosphere/lower thermosphere circulation at midlatitudes as seen by a VHF meteor radar at Collm (51.3°N, 13°E)". In: *Advances in Radio Science* 15, 199–206. ISSN: 1684-9973. DOI: 10.5194/ars-15-199-2017.

Jacobi, Christoph, Ales Kuchar, Toralf Renkwitz, and Juliana Jaen (2023). "Long-term trends of midlatitude horizontal mesosphere/lower thermosphere winds over four decades". In: *Advances in Radio Science* 21, 111–121. ISSN: 1684-9973. DOI: 10.5194/ars-21-111-2023.

Jacobi, Christoph and D. Kürschner (2002). "A possible connection of mid-latitude mesosphere/lower thermosphere zonal winds and the southern oscillation". In: *Physics and Chemistry of the Earth* 27.6-8, pp. 571–577. ISSN: 14747065. DOI: 10.1016/S1474-7065(02)00039-6.

Jacobi, Christoph, Friederike Lilienthal, Christoph Geißler, and Amelie Krug (2015). "Long-term variability of mid-latitude mesosphere-lower thermosphere winds over Collm (51°N, 13°E)". In: *Journal of Atmospheric and Solar-Terrestrial Physics* 136, pp. 174–186. ISSN: 13646826. DOI: 10.1016/j.jastp.2015.05.006.

Jacobi, Christoph, Friederike Lilienthal, Dmitry Korotyshkin, Evgeny Merzlyakov, and Gunter Stober (2021). "Influence of geomagnetic disturbances on mean winds and tides in the mesosphere/lower thermosphere at midlatitudes". In: *Adv. Radio Sci* 19, pp. 185–193. DOI: 10.5194/ars-19-185-2021.

Jaen, Juliana, Toralf Renkwitz, Jorge L. Chau, Maosheng He, Peter Hoffmann, Yosuke Yamazaki, Christoph Jacobi, Masaki Tsutsumi, Vivien Matthias, and Chris M. Hall (2022). "Long-term studies of mesosphere and lower-thermosphere summer length definitions based on mean zonal wind features observed for more than one solar cycle at middle and high latitudes in the Northern Hemisphere". In: *Annales Geophysicae* 40.1, pp. 23–35. ISSN: 1432-0576. DOI: 10.5194/angeo-40-23-2022.

Jaen, Juliana, Toralf Renkwitz, Huixin Liu, Christoph Jacobi, Robin Wing, Aleš Kuchař, Masaki Tsutsumi, Njål Gulbrandsen, and Jorge L. Chau (2023). "Long-term studies of the summer wind in the mesosphere and lower thermosphere at middle and high latitudes over Europe". In: *Atmospheric Chemistry and Physics* 23.23, 14871–14887. ISSN: 1680-7324. DOI: 10.5194/acp-23-14871-2023.

Jaen, Juliana M., A. Erika Gularte Scarone, and Daniel D. Carpintero (2017). "Aplicación de algoritmos genéticos en mapas ionosféricos de foF2 para América del Sur". In: ISBN: 978-950-34-1471-2. URL: http://sedici.unlp.edu.ar/handle/10915/60848.

Jaramillo, Alejandro, Christian Dominguez, Graciela Raga, and Arturo I. Quintanar (2021). "The Combined QBO and ENSO Influence on Tropical Cyclone Activity over the North Atlantic Ocean". In: *Atmosphere* 12.12, p. 1588. ISSN: 2073-4433. DOI: 10.3390/atmos12121588.

Jolliffe, Ian T. (2002). *Principal Component Analysis*. Springer Series in Statistics. New York: Springer-Verlag, pp. XXX–488. ISBN: 978-0-387-22440-4. DOI: https://doi.org/10.1007/b98835.

Jolliffe, Ian T. and J. Edward Jackson (1993). "A User's Guide to Principal Components." In: *The Statistician* 42.1, p. 76. ISSN: 00390526. DOI: 10.2307/2348121.

Kalicinsky, Christoph, Peter Knieling, Ralf Koppmann, Dirk Offermann, Wolfgang Steinbrecht, and Johannes Wintel (2016). "Long-term dynamics of OH temperatures over central Europe: Trends and solar correlations". In: *Atmospheric Chemistry and Physics* 16.23, pp. 15033–15047. DOI: 10.5194/ACP-16-15033-2016.

Karagodin-Doyennel, A., E. Rozanov, A. Kuchar, W. Ball, P. Arsenovic, E. Remsberg, P. Jöckel, M. Kunze, D. A. Plummer, A. Stenke, D. Marsh, D. Kinnison, and T. Peter (2021). "The response of mesospheric H_2O and CO to solar irradiance variability in models and observations". In: *Atmospheric Chemistry and Physics* 21.1, pp. 201–216. DOI: 10.5194/acp-21-201-2021.

Keuer, D, P Hoffmann, W Singer, and J Bremer (2007). "Long-term variations of the mesospheric wind field at mid-latitudes". In: *Annales Geophysicae*, pp. 1779–1790. DOI: 10.5194/angeo-25-1779-2007.

Kuroda, Yuhji and Kunihiko Kodera (2004). "Role of the Polar-night Jet Oscillation on the formation of the Arctic Oscillation in the Northern Hemisphere winter". In: *Journal of Geophysical Research: Atmospheres* 109.D11. ISSN: 0148-0227. DOI: 10.1029/2003jd004123.

Laštovička, Jan (2023). "Progress in investigating long-term trends in the mesosphere, thermosphere, and ionosphere". In: *Atmospheric Chemistry and Physics* 23.10, pp. 5783–5800. ISSN: 1680-7324. DOI: 10.5194/acp-23-5783-2023.

Laštovička, Jan and Š. Jelínek (2019). "Problems in calculating long-term trends in the upper atmosphere". In: *Journal of Atmospheric and Solar-Terrestrial Physics* 189, pp. 80–86. ISSN: 13646826. DOI: 10.1016/j.jastp.2019.04.011.

Latteck, Ralph, Toralf Renkwitz, and Jorge L. Chau (2021). "Two decades of long-term observations of polar mesospheric echoes at 69°N". In: *Journal of Atmospheric and Solar-Terrestrial Physics* 216. ISSN: 13646826. DOI: 10.1016/J.JASTP.2021.105576.

Lauter, E.A. and Günter Entzian (1983). "Peculiarities of the middle atmosphere in winter and during the transitional seasons". In: *HHI-STP-Report* 17, pp. 57–64.

Li, Jingyuan, Wenbin Wang, Jianyong Lu, Jia Yue, Alan G. Burns, Tao Yuan, Xuetao Chen, and Wenjun Dong (2019). "A Modeling Study of the Responses of Mesosphere and Lower Thermosphere Winds to Geomagnetic Storms at Middle Latitudes". In: *Journal of Geophysical Research: Space Physics* 124.5, pp. 3666–3680. ISSN: 21699402. DOI: 10.1029/2019JA026533.

Li, Jingyuan, Guanchun Wei, Wenbin Wang, Qinshun Luo, Jianyong Lu, Yufeng Tian, Shiping Xiong, Meng Sun, Fuzhen Shen, Tao Yuan, Xiaoping Zhang, Shuai Fu, Zheng Li, Hua Zhang, and Chaolei Yang (2023). "A Modeling Study on the Responses of the Mesosphere and Lower Thermosphere (MLT) Temperature to the Initial and Main Phases of Geomagnetic Storms at High Latitudes". In: *Journal of Geophysical Research: Atmospheres* 128.10, pp. 1–14. DOI: 10.1029/2022JD038348.

Li, Tao, Jia Yue, James M. Russell, and Xi Zhang (2021). "Long-term trend and solar cycle in the middle atmosphere temperature revealed from merged HALOE and SABER datasets". In: *Journal of Atmospheric and Solar-Terrestrial Physics* 212, p. 105506. ISSN: 1364-6826. DOI: 10.1016/J.JASTP.2020.105506.

Lindsey, Rebecca and LuAnn Dahlman (2020). "Climate change: Global temperature". In: *Climate. gov* 16.

Liu, R. Q., Christoph Jacobi, Peter Hoffmann, G. Stober, and E. G. Merzlyakov (2010). "A piecewise linear model for detecting climatic trends and their structural changes with application to mesosphere/lower thermosphere winds over Collm, Germany". In: *Journal of Geophysical Research Atmospheres* 115.22, pp. 1–10. ISSN: 01480227. DOI: 10.1029/2010JD014080.

Liu, Xiao, Jia Yue, Jiyao Xu, Rolando R. Garcia, James M. Russell, Martin Mlynczak, Dong L. Wu, and Takuji Nakamura (2017). "Variations of global gravity waves derived from 14 years of SABER temperature observations". In: *Journal of Geophysical Research* 122.12, pp. 6231–6249. ISSN: 21562202. DOI: 10.1002/2017JD026604.

Livesey, N. J., Read, W. G., P. A. Wagner, L. Froidevaux, A. Lambert, G. L. Manney, and et al. (2015). "EOS MLS Version 4.2x Level 2 data quality and description document." In: URL: https://mls.jpl.nasa.gov/data/v4-2_data_quality_document.pdf.

Luo, Jia, Jialiang Hou, and Xiaohua Xu (2021). "Variations in stratospheric gravity waves derived from temperature observations of multi-gnss radio occultation missions". In: *Remote Sensing* 13.23, pp. 1–20. ISSN: 20724292. DOI: 10.3390/rs13234835.

Lübken, F.-J. (1999). "Thermal structure of the Arctic summer mesosphere". In: *Journal of Geophysical Research: Atmospheres* 104.D8, pp. 9135–9149. DOI: 10.1029/1999JD900076.

Machol, J., M. Snow, D. Woodraska, T. Woods, R. Viereck, and O. Coddington (2019). "An Improved Lyman-Alpha Composite". In: *Earth and Space Science* 6.12, pp. 2263–2272. ISSN: 23335084. DOI: 10.1029/2019EA000648.

Mathews, J.D. (1998). "Sporadic E: current views and recent progress". In: *Journal of Atmospheric and Solar-Terrestrial Physics* 60.4, 413–435. ISSN: 1364-6826. DOI: 10.1016/s1364-6826(97)00043-6.

Matzka, J., C. Stolle, Y. Yamazaki, O. Bronkalla, and A. Morschhauser (2021). "The Geomagnetic Kp Index and Derived Indices of Geomagnetic Activity". In: *Space Weather* 19.5. ISSN: 15427390. DOI: 10.1029/2020SW002641.

McCormack, John P., V. Lynn Harvey, Cora E. Randall, Nicholas Pedatella, Dai Koshin, Kaoru Sato, Lawrence Coy, Shingo Watanabe, Fabrizio Sassi, and Laura A. Holt (2021). "Intercomparison of middle atmospheric meteorological analyses for the Northern Hemisphere winter 2009–2010". In: *Atmospheric Chemistry and Physics* 21.23, 17577–17605. ISSN: 1680-7324. DOI: 10.5194/acp-21-17577-2021.

McLandress, Charles (2002). "The Seasonal Variation of the Propagating Diurnal Tide in the Mesosphere and Lower Thermosphere. Part II: The Role of Tidal Heating and Zonal Mean Winds". In: *Journal of the Atmospheric Sciences* 59.5, 907–922. ISSN: 1520-0469. DOI: 10.1175/1520-0469(2002)059<0907:tsvotp>2.0.co;2.

Measures, Raymond M. (1984). *Laser remote sensing: fundamentals and applications*. Wiley New York. ISBN: 978-0471081937.

Mursula, K., I.G. Usoskin, and G.A. Kovaltsov (2002). "A 22-year cycle in sunspot activity". In: *Advances in Space Research* 29.12, 1979–1984. ISSN: 0273-1177. DOI: 10.1016/s0273-1177(02)00244-2.

NOAA/PMEL/TAO Project Office Dr. Michael J. McPhaden, Director. (2023). *ENSO figure*. http://www.pmel.noaa.gov/tao/proj_over/diagrams/index.html [Accessed: (22.01.2024)].

Noble, Phoebe E., Neil P. Hindley, Corwin J. Wright, Chihoko Cullens, Scott England, Nicholas Pedatella, Nicholas J. Mitchell, and Tracy Moffat-Griffin (2024). "Interannual Variability of Winds in the Antarctic Mesosphere and Lower Thermosphere Over Rothera (67°S, 68°W) During 2005–2021 in Meteor Radar Observations and WACCM-X". In: *Journal of Geophysical Research: Atmospheres* 129.4. ISSN: 2169-8996. DOI: 10.1029/2023jd039789.

Offermann, Dirk, O. Goussev, Ch Kalicinsky, R. Koppmann, K. Matthes, Hauke Schmidt, W. Steinbrecht, and J. Wintel (2015). "A case study of multi-annual temperature oscillations in the atmosphere: Middle Europe". In: *Journal of Atmospheric and Solar-Terrestrial Physics* 135, pp. 1–11. ISSN: 1364-6826. DOI: 10.1016/j.jastp.2015.10.003.

Offermann, Dirk, Peter Hoffmann, P. Knieling, R. Koppmann, J. Oberheide, and W. Steinbrecht (2010). "Long-term trends and solar cycle variations of mesospheric temperature and dynamics". In: *Journal of Geophysical Research Atmospheres* 115.18, p. D18127. ISSN: 0148-0227. DOI: 10.1029/2009JD013363.

Offermann, Dirk, M. Jarisch, M. Donner, W. Steinbrecht, and A.I. Semenov (2006). "OH temperature re-analysis forced by recent variance increases". In: *Journal of Atmospheric and Solar-Terrestrial Physics* 68.17, pp. 1924–1933. ISSN: 13646826. DOI: 10.1016/j.jastp.2006.03.007.

Offermann, Dirk, Christoph Kalicinsky, Ralf Koppmann, and Johannes Wintel (2021). "Very long-period oscillations in the atmosphere (0-110km)". In: *Atmospheric Chemistry and Physics* 21.3, pp. 1593–1611. DOI: 10.5194/ACP-21-1593-2021.

Ohara, Kieran (2022). "Physical drivers of climate change". In: *Climate Change in the Anthropocene*. Elsevier, 19–41. DOI: 10.1016/b978-0-12-820308-8.00011-8.

Pancheva, Dora, Plamen Mukhtarov, and David E. Siskind (2018). "Climatology of the quasi-2-day waves observed in the MLS/Aura measurements (2005–2014)". In: *Journal of Atmospheric and Solar-Terrestrial Physics* 171, 210–224. ISSN: 1364-6826. DOI: 10.1016/j.jastp.2017.05.002.

Perminov, V.I., A.I. Semenov, N.N. Pertsev, I.V. Medvedeva, P.A. Dalin, and V.A. Sukhodoev (2018). "Multi-year behaviour of the midnight OH temperature according to observations at Zvenigorod over 2000-2016". In: *Advances in Space Research* 61.7, pp. 1901–1908. ISSN: 02731177. DOI: 10.1016/j.asr.2017.07.020.

Peters, Dieter H.W., Günter Entzian, and Philippe Keckhut (2017). "Mesospheric temperature trends derived from standard phase-height measurements". In: *Journal of Atmospheric and Solar-Terrestrial Physics* 163.February, pp. 23–30. ISSN: 13646826. DOI: 10.1016/j.jastp.2017.04.007.

Peters, Dieter H.W. and Günter Entzian (2015). "Long-term variability of 50 years of standard phase-height measurement at Kühlungsborn, Mecklenburg, Germany". In: *Advances in Space Research* 55.7, pp. 1764–1774. ISSN: 0273-1177. DOI: 10.1016/j.asr.2015.01.021.

Peters, Dieter H.W., Andrea Schneidereit, and Alexey Karpechko (2018). "Enhanced Stratosphere/Troposphere Coupling During Extreme Warm Stratospheric Events with Strong Polar-Night Jet Oscillation". In: *Atmosphere* 9.12, p. 467. ISSN: 2073-4433. DOI: 10.3390/atmos9120467.

Poblet, Facundo L., Juha Vierinen, Victor Avsarkisov, J. Federico Conte, Harikrishnan Charuvil Asokan, Christoph Jacobi, and Jorge L. Chau (2023). "Horizontal Correlation Functions of Wind Fluctuations in the Mesosphere and Lower Thermosphere". In: *Journal of Geophysical Research: Atmospheres* 128.6, e2022JD038092. ISSN: 2169-897X. DOI: 10.1029/2022JD038092.

Portnyagin, Yu I., E. G. Merzlyakov, T. V. Solovjova, Christoph Jacobi, D. Kürschner, Alan H Manson, and C. Meek (2006). "Long-term trends and year-to-year variability of mid-latitude mesosphere/lower thermosphere winds". In: *Journal of Atmospheric and Solar-Terrestrial Physics* 68.17, pp. 1890–1901. ISSN: 13646826. DOI: 10.1016/j.jastp.2006.04.004.

Qian, Liying, Alan G. Burns, Stanley C. Solomon, and Wenbin Wang (2017). "Carbon dioxide trends in the mesosphere and lower thermosphere". In: *Journal of*

Geophysical Research: Space Physics 122.4, pp. 4474–4488. ISSN: 21699402. DOI: 10.1002/2016JA023825.

Reid, Iain M., Andrew J. Spargo, and Jonathan M. Woithe (2014). "Seasonal variations of the nighttime O(1S) and OH (8-3) airglow intensity at Adelaide, Australia". In: *Journal of Geophysical Research* 119.11, pp. 6991–7013. ISSN: 21562202. DOI: 10.1002/2013JD020906.

Reid, Iain Murray (2015). "MF and HF radar techniques for investigating the dynamics and structure of the 50 to 110 km height region: a review". In: *Progress in Earth and Planetary Science* 2.1. DOI: 10.1186/s40645-015-0060-7.

Renkwitz, T., M. Sivakandan, J. Jaen, and W. Singer (2023). "Ground-based noontime D-region electron density climatology over northern Norway". In: *Atmospheric Chemistry and Physics* 23, 10823–10834. DOI: 10.5194/acp-23-10823-2023.

Renkwitz, Toralf and Ralph Latteck (2017). "Variability of virtual layered phenomena in the mesosphere observed with medium frequency radars at 69°N". In: *Journal of Atmospheric and Solar-Terrestrial Physics* 163, pp. 38–45. ISSN: 13646826. DOI: 10.1016/j.jastp.2017.05.009.

Robinson, G. K. (1976). "Properties of student's t and of the Behrens-Fisher solution to the two means problem". In: *Annals of Statistics* 4.5, pp. 963–971. DOI: 10.1214/aos/1176343594.

Rüfenacht, Rolf, Gerd Baumgarten, Jens Hildebrand, Franziska Schranz, Vivien Matthias, Gunter Stober, Franz-Josef Lübken, and Niklaus Kämpfer (2018). "Intercomparison of middle-atmospheric wind in observations and models". In: *Atmospheric Measurement Techniques* 11.4, pp. 1971–1987. ISSN: 18678548. DOI: 10.5194/amt-11-1971-2018.

Salby, Murry L. (1981). "The 2-day wave in the middle atmosphere: Observations and theory". In: *Journal of Geophysical Research: Oceans* 86.C10, 9654–9660. ISSN: 0148-0227. DOI: 10.1029/jc086ic10p09654.

Savigny, Christian von, Claudia Timmreck, Stefan A. Buehler, John P. Burrows, Marco Giorgetta, Gabriele Hegerl, Akos Horvath, Gholam Ali Hoshyaripour, Corinna Hoose, Johannes Quaas, Elizaveta Malinina, Alexei Rozanov, Hauke Schmidt, Larry Thomason, Matthew Toohey, and Bernhard Vogel (2020). "The Research Unit VolImpact: Revisiting the volcanic impact on atmosphere and climate – preparations for the next big volcanic eruption". In: *Meteorologische Zeitschrift* 29.1, 3–18. ISSN: 0941-2948. DOI: 10.1127/metz/2019/0999.

She, Chiao-Yao, Alan Z. Liu, Tao Yuan, Jia Yue, Tao Li, Chao Ban, and Jonathan S. Friedman (2021). *MLT Science Enabled by Atmospheric Lidars*. DOI: 10.1002/9781119815631.ch20.

Shepherd, Theodore G. (2008). "Dynamics, stratospheric ozone, and climate change". In: *Atmosphere-Ocean* 46.1, 117–138. ISSN: 1480-9214. DOI: 10.3137/ao.460106.

Singer, Werner, Peter Hoffmann, G Kishore Kumar, Nicholas J Mitchell, and Vivien Matthias (2013). *Climate and Weather of the Sun-Earth System (CAWSES)*. Ed. by Franz-Josef Lübken. Springer Atmospheric Sciences. Dordrecht: Springer Netherlands, pp. 409–427. ISBN: 978-94-007-4347-2. DOI: 10.1007/978-94-007-4348-9.

Singer, Werner, Ralph Latteck, M. Friedrich, P. Dalin, S. Kirkwood, N. Engler, and David A. Holdsworth (2005). "D-region electron densities obtained by differential absorption and phase measurements with a 3-MHz-Doppler radar". In: *ESA Symposium on European Rocket and Balloon Programmes and Related Research*. 17th, pp. 233–238. ISBN: 9783540773405.

Sivakandan, Mani, Jens Mielich, Toralf Renkwitz, Jorge L. Chau, Juliana Jaen, and Jan Lastovicka (2023). "Long-term variations and residual trends in the E, F, and

sporadic E (Es) layer over Juliusruh, Europe". In: *Journal of Geophysical Research: Space Physics*, e2022JA031097. ISSN: 2169-9402. DOI: 10.1029/2022JA031097.

Smith, Anne K. (2011). "Interactions Between the Lower, Middle and Upper Atmosphere". In: *Space Science Reviews* 168.1–4, 1–21. ISSN: 1572-9672. DOI: 10.1007/s11214-011-9791-y.

– (2012). "Global Dynamics of the MLT". In: *Surveys in Geophysics* 33.6, 1177–1230. ISSN: 1573-0956. DOI: 10.1007/s10712-012-9196-9.

Stober, Gunter, Ales Kuchar, Dimitry Pokhotelov, Huixin Liu, Han-Li Liu, Hauke Schmidt, Christoph Jacobi, Kathrin Baumgarten, Peter Brown, Diego Janches, Damian Murphy, Alexander Kozlovsky, Mark Lester, Evgenia Belova, Johan Kero, and Nicholas Mitchell (2021). "Interhemispheric differences of mesosphere-lower thermosphere winds and tides investigated from three whole-atmosphere models and meteor radar observations". In: *Atmos. Chem. Phys* 21, pp. 13855–13902. DOI: 10.5194/acp-21-13855-2021.

Storch, Hans von and Francis W. Zwiers (1984). *Statistical Analysis in Climate Research*. Cambridge University Press. ISBN: 9780511612336. DOI: 10.1017/cbo9780511612336.

Sun, Meng, Zheng Li, Jingyuan Li, Jianyong Lu, Chunli Gu, Mengbin Zhu, and Yufeng Tian (2022). "Responses of Mesosphere and Lower Thermosphere Temperature to the Geomagnetic Storm on 7-8 September 2017". In: *Universe* 8.2, p. 96. ISSN: 2218-1997. DOI: 10.3390/universe8020096.

Sundararajan, Sridharan (2020). "Equatorial upper mesospheric mean winds and tidal response to strong El Niño and La Niña". In: *Journal of Atmospheric and Solar-Terrestrial Physics* 202, p. 105270. ISSN: 1364-6826. DOI: 10.1016/j.jastp.2020.105270.

Vellalassery, A., G. Baumgarten, M. Grygalashvyly, and F.-J. Lübken (2023). "Greenhouse gas effects on the solar cycle response of water vapour and noctilucent clouds". In: *Annales Geophysicae Discussions* 2023, pp. 1–35. DOI: 10.5194/angeo-2023-3.

Venkateswara Rao, N., P. J. Espy, R. E. Hibbins, D. C. Fritts, and A. J. Kavanagh (2015). "Observational evidence of the influence of Antarctic stratospheric ozone variability on middle atmosphere dynamics". In: *Geophysical Research Letters* 42.19, 7853–7859. ISSN: 1944-8007. DOI: 10.1002/2015gl065432.

Wallis, Sandra, Hauke Schmidt, and Christian von Savigny (2023). "Impact of a strong volcanic eruption on the summer middle atmosphere in UA-ICON simulations". In: *Atmospheric Chemistry and Physics* 23.12, 7001–7014. ISSN: 1680-7324. DOI: 10.5194/acp-23-7001-2023.

Wang, Chunzai and Joël Picaut (2004). "Understanding ENSO physics—a review". In: *Geophysical Monograph Series* 147, pp. 21–48. ISSN: 23288779. DOI: 10.1029/147GM02.

Waters, Joe W., Lucien Froidevaux, Robert S. Harwood, Robert F. Jarnot, Herbert M. Pickett, William G. Read, Peter H. Siegel, Richard E. Cofield, Mark J. Filipiak, Dennis A. Flower, James R. Holden, Gary K. Lau, Nathaniel J. Livesey, Gloria L. Manney, Hugh C. Pumphrey, Michelle L. Santee, Dong L. Wu, David T. Cuddy, Richard R. Lay, Mario S. Loo, Vincent S. Perun, Michael J. Schwartz, Paul C. Stek, Robert P. Thurstans, Mark A. Boyles, Kumar M. Chandra, Marco C. Chavez, Gun Shing Chen, Bharat V. Chudasama, Randy Dodge, Ryan A. Fuller, Michael A. Girard, Jonathan H. Jiang, Yibo Jiang, Brian W. Knosp, Remi C. Labelle, Jonathan C. Lam, Karen A. Lee, Dominick Miller, John E. Oswald, Navnit C. Patel, David M. Pukala, Ofelia Quintero, David M. Scaff, W. Van Snyder, Michael C. Tope, Paul A. Wagner, and Marc J. Walch (2006). "The Earth Observing System Microwave Limb Sounder

(EOS MLS) on the aura satellite". In: *IEEE Transactions on Geoscience and Remote Sensing* 44.5, pp. 1075–1092. ISSN: 01962892. DOI: 10.1109/TGRS.2006.873771.

Weatherhead, Elizabeth C., Jerald Harder, Eduardo A. Araujo-Pradere, Greg Bodeker, Jason M. English, Lawrence E. Flynn, Stacey M. Frith, Jeffrey K. Lazo, Peter Pilewskie, Mark Weber, and Thomas N. Woods (2017). "How long do satellites need to overlap? Evaluation of climate data stability from overlapping satellite records". In: *Atmospheric Chemistry and Physics* 17 (24). ISSN: 16807324. DOI: 10.5194/acp-17-15069-2017.

Weber, Mark, Carlo Arosio, Melanie Coldewey-Egbers, Vitali E. Fioletov, Stacey M. Frith, Jeannette D. Wild, Kleareti Tourpali, John P. Burrows, and Diego Loyola (2022). "Global total ozone recovery trends attributed to ozone-depleting substance (ODS) changes derived from five merged ozone datasets". In: *Atmospheric Chemistry and Physics* 22.10, pp. 6843–6859. ISSN: 1680-7324. DOI: 10.5194/ACP-22-6843-2022.

Whitehead, J.D. (1989). "Recent work on mid-latitude and equatorial sporadic-E". In: *Journal of Atmospheric and Terrestrial Physics* 51.5, 401–424. ISSN: 0021-9169. DOI: 10.1016/0021-9169(89)90122-0.

Wilhelm, Sven, Gunter Stober, and Peter Brown (2019). "Climatologies and long-term changes in mesospheric wind and wave measurements based on radar observations at high and mid latitudes". In: *Annales Geophysicae* 37.5, pp. 851–875. ISSN: 1432-0576. DOI: 10.5194/angeo-37-851-2019.

Yamazaki, Yosuke and Vivien Matthias (2019). "Large-Amplitude Quasi-10-Day Waves in the Middle Atmosphere During Final Warmings". In: *Journal of Geophysical Research: Atmospheres* 124.17-18, pp. 9874–9892. ISSN: 2169-897X. DOI: 10.1029/2019JD030634.

Yiğit, Erdal and Alexander S. Medvedev (2017). "Influence of parameterized small-scale gravity waves on the migrating diurnal tide in Earth's thermosphere". In: *Journal of Geophysical Research: Space Physics* 122.4, pp. 4846–4864. ISSN: 2169-9402. DOI: 10.1002/2017JA024089. eprint: 1704.07401.

Yuan, Tao, S. C. Solomon, C. Y. She, D. A. Krueger, and H. L. Liu (2019). "The Long-Term Trends of Nocturnal Mesopause Temperature and Altitude Revealed by Na Lidar Observations Between 1990 and 2018 at Midlatitude". In: *Journal of Geophysical Research: Atmospheres* 124.12, pp. 5970–5980. ISSN: 21698996. DOI: 10.1029/2018JD029828.

Yue, Jia, James Russell, Yongxiao Jian, Ladislav Rezac, Rolando Garcia, Manuel Lõpez-Puertas, and Martin G. Mlynczak (2015). "Increasing carbon dioxide concentration in the upper atmosphere observed by SABER". In: *Geophysical Research Letters* 42.17, pp. 7194–7199. ISSN: 19448007. DOI: 10.1002/2015GL064696.

Zolesi, Bruno and Ljiljana R. Cander (2014). *Ionospheric prediction and forecasting*, pp. 1–240. ISBN: 9783642384301. DOI: 10.1007/978-3-642-38430-1.

Zülicke, Christoph, Erich Becker, Vivien Matthias, Dieter H. W. Peters, Hauke Schmidt, Han-Li Liu, Laura de la Torre Ramos, and Daniel M. Mitchell (2018). "Coupling of Stratospheric Warmings with Mesospheric Coolings in Observations and Simulations". In: *Journal of Climate* 31.3, pp. 1107–1133. DOI: 10.1175/jcli-d-17-0047.1.

Appendix A

Jaen et al. (2022)

Jaen, J., Renkwitz, T., Chau, J. L., He, M., Hoffmann, P., Yamazaki, Y., Jacobi, C., Tsutsumi, M., Matthias, V., and Hall, C.: Long-term studies of mesosphere and lower-thermosphere summer length definitions based on mean zonal wind features observed for more than one solar cycle at middle and high latitudes in the Northern Hemisphere, Ann. Geophys., 40, 23–35, https://doi.org/10.5194/angeo-40-23-2022, 2022.

Ann. Geophys., 40, 23–35, 2022
https://doi.org/10.5194/angeo-40-23-2022

Annales Geophysicae Open Access EGU

Long-term studies of mesosphere and lower-thermosphere summer length definitions based on mean zonal wind features observed for more than one solar cycle at middle and high latitudes in the Northern Hemisphere

Juliana Jaen[1], Toralf Renkwitz[1], Jorge L. Chau[1], Maosheng He[1], Peter Hoffmann[1,†], Yosuke Yamazaki[2], Christoph Jacobi[3], Masaki Tsutsumi[4], Vivien Matthias[5], and Chris Hall[6,†]

[1]Leibniz Institute of Atmospheric Physics at the University of Rostock, Schloss-Strasse 6, 18225 Kühlungsborn, Germany
[2]GFZ German Research Centre for Geosciences, Potsdam, Germany
[3]Institute Meteorology, Leipzig University, Stephanstr. 3, 04103 Leipzig, Germany
[4]National Institute of Polar Research, Tokyo, Japan
[5]Institute for Solar-Terrestrial Physics, German Aerospace Center (DLR), Neustrelitz, Germany
[6]Tromsø Geophysical Observatory, Arctic University of Norway, Tromsø, Norway
[†]deceased, Peter Hoffmann on 29 October 2020 and Chris Hall on 9 August 2021

Correspondence: Juliana Jaen (jaen@iap-kborn.de)

Received: 31 August 2021 – Discussion started: 13 September 2021
Revised: 21 November 2021 – Accepted: 2 December 2021 – Published: 20 January 2022

Abstract. Specular meteor radars (SMRs) and partial reflection radars (PRRs) have been observing mesospheric winds for more than a solar cycle over Germany (∼ 54° N) and northern Norway (∼ 69° N). This work investigates the mesospheric mean zonal wind and the zonal mean geostrophic zonal wind from the Microwave Limb Sounder (MLS) over these two regions between 2004 and 2020. Our study focuses on the summer when strong planetary waves are absent and the stratospheric and tropospheric conditions are relatively stable. We establish two definitions of the summer length according to the zonal wind reversals: (1) the mesosphere and lower-thermosphere summer length (MLT-SL) using SMR and PRR winds and (2) the mesosphere summer length (M-SL) using the PRR and MLS. Under both definitions, the summer begins around April and ends around middle September. The largest year-to-year variability is found in the summer beginning in both definitions, particularly at high latitudes, possibly due to the influence of the polar vortex. At high latitudes, the year 2004 has a longer summer length compared to the mean value for MLT-SL as well as 2012 for both definitions. The M-SL exhibits an increasing trend over the years, while MLT-SL does not have a well-defined trend. We explore a possible influence of solar activity as well as large-scale atmospheric influences (e.g., quasi-biennial oscillation (QBO), El Niño–Southern Oscillation (ENSO), major sudden stratospheric warming events). We complement our work with an extended time series of 31 years at middle latitudes using only PRR winds. In this case, the summer length shows a breakpoint, suggesting a non-uniform trend, and periods similar to those known for ENSO and QBO.

1 Introduction

As Earth orbits around the Sun, the duration of the four seasons is well defined at ground level at middle latitudes. Higher up between 50 and 100 km in the mesosphere and lower thermosphere (MLT), the separation is not well defined. Earth's atmosphere is a complex system governed by several processes that are continuously evolving (e.g., radiative heating, coupling, mixing processes). The dynamics of the MLT are forced mainly by solar radiation and the wave activities arising in the lower atmosphere, such as planetary

waves, gravity waves, and tides (e.g., Yiğit et al., 2016). Circulation patterns such as the stratospheric quasi-biennial oscillation (QBO, Baldwin et al., 2001) and El Niño–Southern Oscillation (ENSO, Wang and Picaut, 2004) also influence the MLT dynamics at middle latitudes. During winter conditions strong planetary wave activity is present and, later on, in the transition from winter to summer, a reduction of the planetary activity occurs (Lauter and Entzian, 1983; Hoffmann et al., 2002). With the transition, every year the zonal wind circulation in the MLT displays the final reversal of the wind direction from eastward to westward, in part produced by the wave dissipation generated by gravity wave activity (see Hoffmann et al., 2010; Laskar et al., 2017). In connection with this wind reversal, the mesopause experiences a decrease in temperature resulting in the appearance of ice particles, due to the water vapor present in the atmosphere. The presence of charged ice particles is observed through radar echoes known as polar mesospheric summer echoes (PMSE; see, e.g., Rapp et al., 2003). Between 80 and 90 km and on nanometer scales, a congregation of ice particles is called noctilucent clouds or polar mesospheric clouds (e.g., Hervig et al., 2001; Baumgarten et al., 2008; Fiedler et al., 2015).

The above-mentioned summer characteristics exhibit interannual variabilities and interactions with adjacent layers, highlighting the importance of studying this season as well as its long-term behavior. Previous works, like Lauter and Entzian (1983), used the mean zonal wind reversal at around 25 km altitude to study long-term behavior between 1958 and 1982, obtaining an increase in the summer duration of 0.52 days per year ($\mathrm{d\,yr^{-1}}$). Nevertheless, the authors suggested a possible change in the trends after 1980 and reported a connection between the QBO and the wind reversal dates during 1958–1967 and again after 1977. Under the name of *equivalent summer duration*, defined by a threshold of 198 K at 87 km at middle latitudes, the temperature variations during summer were investigated by Offermann et al. (2010). This study covered the years 1988 to 2008, obtaining a change rate of $1.21\,\mathrm{d\,yr^{-1}}$. The authors also compared the obtained values with the zonal wind reversal in the stratosphere (20 hPa) that showed a decrease in the summer duration of $0.99\,\mathrm{d\,yr^{-1}}$. Later on, French et al. (2020) studied the hydroxyl nightglow rotational temperatures in the Antarctic region and compared them with satellite winds and temperatures at 86 km. The authors found a correlation between temperature and meridional winds but no significant correlation with the mean zonal winds. Offermann et al. (2005) characterized the summer duration, referring to the stratospheric zonal wind reversal in broad ranges of latitude and altitude between 1948 and 2003. They found a dependency on latitude and altitude, with longer summer duration at higher altitudes and high latitudes for the Northern Hemisphere. However, in all the cases they detected a breakpoint around 1978–1980, obtaining an increase in summer duration before the breakpoint and negative trends after 1978/1980.

For several years, long-term studies aimed to investigate the anthropogenic influence in the atmosphere. Having in mind the atmosphere as a whole and considering that the temperature changes affect life at ground level, we can compare the summer length with the vegetation growing season. The normalized difference vegetation index (NDVI) is obtained from CO_2 satellite measurements (e.g., Zhou et al., 2001). During the vegetation growing season there is an exchange of CO_2 between the plants and the soil due to the process of photosynthesis and decomposition (Fung et al., 1987). In these studies the summer season starts around April/May and ends in September/October at middle latitudes, which appears to be comparable with the time interval for the mean zonal wind reversal investigated in this paper.

The middle-atmosphere studies, mentioned above, were made before 2010. Since the beginning of the 21st century, new radar systems have been deployed in Germany and Norway. After more than one solar cycle of system operations, we are able to look into the long-term trends. In this study, we aim to analyze the long-term variability of the mean zonal wind reversal, which occurs around March and in September by implementing two different definitions of summer length. Both definitions applied to radar wind measurements are related to different processes and regions in MLT and incorporate altitude and latitude features. With these definitions we search for possible correlations with known forcing events from above or below the MLT, like, e.g., solar activity measured by the Lyman α line, major sudden stratospheric warming (MSSW, Butler et al., 2015), and strong polar-night jet oscillations (sPJO, Peters et al., 2018; Conte et al., 2019). The Lyman α line is a good representation of the solar activity in the MLT, as a consequence of the hydrogen absorption that occurred by the Sun's ultraviolet light, maximizing at around 90 km (Machol et al., 2019).

To study the MLT summer length, we combine MLT winds from specular meteor radars (SMRs) and mesospheric winds from partial reflection radars (PRR, Wilhelm et al., 2017; Hoffmann et al., 2010). These systems are located in Germany and northern Norway. Our ground-based observations are complemented with similar years of satellite observations, specifically from the Microwave Limb Sounder (MLS) on board the Earth Observing System Aura satellite (e.g., Waters et al., 2006; Wu et al., 2008).

The paper is organized as follows. Section 2 contains the description of the database and instruments used as well as a brief description of the applied data-processing methods for the individual systems. Section 3 gives a description of the climatology and the applied summer length definitions. The final time series and a brief description of the results are given in Sect. 4. This is followed by the discussion for the individual latitudes and a comparison between the definitions in Sect. 5 and, finally, a summary and conclusions are found in Sect. 6.

2 Database

Considering the difficulties in obtaining a homogeneous data set, which are well known in long-term studies (e.g., Laštovička and Jelínek, 2019), we used a combination of closely located SMRs at two selected latitudes. This combination allows us to reduce the number of data gaps and provides a highly reliable wind estimation for the regions under investigation. To study the mean zonal wind reversal at lower altitudes, namely below 80 km, we have included data from PRRs and the MLS on board the Aura Earth Observing System (Aura EOS). Both types of radars, SMRs and PRRs, have a good agreement between 80 and 90 km (e.g., Hoffmann et al., 2010; Wilhelm et al., 2017). In the next subsections we briefly describe each of these systems and the methodology of the processed radar data.

2.1 Specular meteor radars

SMRs detect meteor trails between mostly 75 and 110 km altitude, measuring their position in space and radial velocity to derive the mean background winds (e.g., Hocking et al., 2001). To generate a homogeneous time series without gaps, we use a combination of detections from two closely located SMRs, using quasi-simultaneous detections binned in the same way as a single radar mode does to obtain the hourly winds (for details, see Chau et al., 2017). This combination helps us to reduce the observation gaps for the high- and middle-latitude regions we have selected. At middle latitudes we combine two SMRs located in Germany, specifically Juliusruh (54.6° N, 13.4° E) and Collm (51.3° N, 13.0° E) (e.g., Hoffmann et al., 2010; Jacobi et al., 2015). At high latitudes we use two SMRs in northern Norway: Andenes (69.3° N, 16.0° E) and Tromsø (69.6° N, 19.2° E) (e.g., Singer et al., 2004; Hall et al., 2005). The covered years at middle and high latitudes are 2005–2020 and 2004–2020, respectively.

Given the inherent variability within the radar measurements, the wind data set of 1 h resolution was first smoothed by a 16 d-width sliding window. The smoothing suppresses short-term fluctuations, which are caused by, e.g., gravity waves and tides as well as instrumental effects, which are not within the focus of this study. For this long-term study dealing with a length of up to 31 years, the principal component analysis (PCA, Jolliffe and Jackson, 1993; Jolliffe, 2002) proved to be a useful tool to compress the data. At each station and for each year, the zonal wind between DOY 100–280 and 82–98 km in the time–altitude depiction is arranged into a two-dimensional matrix and decomposed as a linear combination of principal components. The first two principal components capture 97.6 %–99.5 % of the total variance and are used to reconstruct the two-dimensional matrix used for this study and effectively reduce its short-term variability. The principal components representing the data set are planned to be investigated in more detail with respect to their temporal evolution in a subsequent study.

2.2 Partial reflection radars

PRRs use the mechanism of partial reflection through the ionized component in the atmosphere as a tracer for the neutral motions in the MLT between 50 and 100 km altitude, depending on the instrument configuration and by means of the solar and geomagnetic conditions (see, e.g., Fukao and Hamazu, 2014; Reid, 2015). The Saura PRR, located in Andøya (69.1° N, 16.0° E), has been in operation since 2004 (e.g., Singer et al., 2005; Renkwitz and Latteck, 2017). For the middle latitudes, we use measurements from Juliusruh PRR (54.6° N, 13.4° E) that were obtained between 2004 and 2020 with a comparable system and method (e.g., Hoffmann et al., 2010). To complement our work, we also include data from the Juliusruh PRR predecessor system, using a different configuration and technique between 1990 and 2003. More details on this data set can be found in Keuer et al. (2007).

Equivalently to the descriptions given for the SMR data, we implemented a 16 d sliding window and the principal component analysis capturing 98.2 %–99.3 % of the total variance with the first two principal components. The time window implemented in the principal component analysis is DOY 50–280 and 70–95 km.

2.3 Microwave Limb Sounder

On board the Aura EOS satellite is the MLS instrument, sensing atmospheric temperatures from the troposphere up to 90 km (e.g., Waters et al., 2006; Livesey et al., 2015). From these measurements one can calculate the zonal mean geostrophic zonal winds and geopotential heights (e.g., Yamazaki and Matthias, 2019). In this work, we use MLS zonal mean zonal winds at middle and high latitudes between 2005 and 2020. It is important to consider that the zonal mean geostrophic zonal wind is a longitude average, while the radars are located at a specific longitude. These time series are extracted with a 16 d sliding window at 74 km (55° N) and at 82 km (70° N).

3 MLT mean zonal wind climatologies and summer length definitions

A mean zonal wind climatology for both latitudes and combinations of stations is shown in Fig. 1. The high-latitude climatology (Fig. 1a) is generated from the combination of Andenes and Tromsø SMRs above 81 km and below from the Saura PRR. An equivalent approach is used for the middle latitudes (Fig. 1b), where between 81 and 100 km observations from Juliusruh and Collm SMRs are used and, for altitudes below 81 km, from the Juliusruh PRR wind climatology (years 2004–2020). During summer months, the mean

zonal wind over these sites is expected to be equivalent to the zonal mean zonal wind (e.g., Hoffmann et al., 2010).

Both climatologies depict a reversal of the wind (grey line) around March–April, when the wind reverses from eastward (red) to westward (blue) at all altitudes. Between April and May at high altitudes, the wind changes from westward to eastward (grey line), and the temporal evolution of this reversal occurs rapidly from 100 km down to around 90 km (86 km for middle latitudes). From early June, the mean zonal wind reverses slowly with decreasing altitude until 85 km (78 km at middle latitudes) until middle September. Later on, the wind direction reverses rapidly from westward to eastward from these altitudes downwards, indicating the end of the summer in the MLT in middle September, around 1 week before the autumnal equinox. The dynamics of the mean zonal wind displays a clear dependence of altitude with respect to latitude (e.g., Laskar et al., 2017; Conte et al., 2018; Wilhelm et al., 2019). Given this latitudinal dependence, we adjust the selected altitudes in the summer length definitions (described below) accordingly.

Figure 2 displays a climatological mean of the mean zonal wind reversal for all data sets. We are indicating the altitudes used in this work for the different summer definitions (see below). At 69° N, the mean zonal wind reversal from the combination of SMRs is depicted in purple and from PRR in orange lines, while for 54° N the combination of SMRs is shown in red and the PRR in green lines. The climatological zonal mean geostrophic zonal wind value is also represented at 82 km for 70° N (solid blue lines) and at 74 km height for 55° N (dash-dotted blue lines).

3.1 Mesosphere and lower-thermosphere summer length

The MLT-SL definition is established by the mean zonal wind reversal from westward to eastward at both the upper and lower altitudes. The altitudes depend primarily on the temporal evolution of the mean zonal wind reversal and in consequence on the latitude. These altitudes are chosen where the mean zonal wind reversal occurs rapidly and simultaneously for several kilometers. Considering these characteristics, at high latitudes the MLT summer beginning (SB) is chosen at 96 km height and the MLT summer end (SE) at 82 km (Fig. 2, purple line). At middle latitudes, the MLT-SB altitude is the same as at high latitudes (i.e., 96 km), but the MLT-SE was chosen at 74 km, using PRR data (see the combination of the red and green lines in Fig. 2). In both definitions, the summer length is the difference between the summer end and summer beginning.

3.2 Mesosphere summer length

The M-SL is selected at the same altitude, varying only by latitude. The summer beginning and summer ending are considered when the final mean zonal wind reversal occurs from eastward to westward and later from westward to eastward, for high latitudes at 82 km and for middle latitudes at 74 km (see Fig. 2, orange and green lines, respectively). The same altitudes are taken for the MLS (see Fig. 2 blue lines, solid lines at high latitudes and dash-dotted lines at middle latitudes). M-SL has been selected to allow a direct comparison between the MLS and radar observations and other definitions. Moreover, this definition can also be compared with models since most of them are able to reproduce the observed wind field below 90 km during April and May (e.g., Hoffmann et al., 2010; Conte et al., 2018; Pokhotelov et al., 2018).

4 Results

Here we briefly describe how the radar data have been processed and the results are obtained. We first calculate the daily mean of hourly winds for each altitude and site. Then the mean is smoothed by a 16 d running window, shifted by 1 d. In order to compress the data and to further reduce its variability and to be able to focus on the long-term changes, we implemented a principal component analysis (see details in Sect. 2). With the first two components of principal component analysis, we are able to reconstruct the mean zonal winds year by year and, considering only the altitudes of interest, we extract the day of the year (DOY) on which the reversal occurs. Following this analysis, we obtain three different time series for each latitude and definition (summer beginning, summer end, and summer length). Each time series is treated with a default standard deviation error from the size of the smoothing window plus an extra consideration for the years where the mean zonal wind reversal is particularly difficult to assess due to an unclear transition. In these cases, the sum of days during the unclear reversal period is divided by 2 and manually implemented as an error for the particular value.

Figure 3 presents the detected wind reversal dates at high latitudes, i.e., MLT-SL (left column, purple lines) and M-SL (right column) for the previously introduced altitude definitions. Note that for M-SL, both MLS (blue lines) and PRR (red lines) results are included. The first three panels for both definitions (Fig. 3a, b, c and e, f, g) depict the DOY (ordinate) when the mean zonal wind reversal occurs for every year (abscissa) for summer beginning, summer end, and summer length, respectively.

To explore the long-term behavior, we fit a linear function and apply the Student's t test (with null hypothesis being the slope equal to zero) to investigate whether there is a significant slope incorporating the standard deviation error propagation (e.g., Santer et al., 2000). The linear regression (solid line in the same color) is only shown for the summer beginning and summer length (first and third panels, respectively), and enclosed in dashed lines (same color) is shown the expected variability. In the case of summer end for both

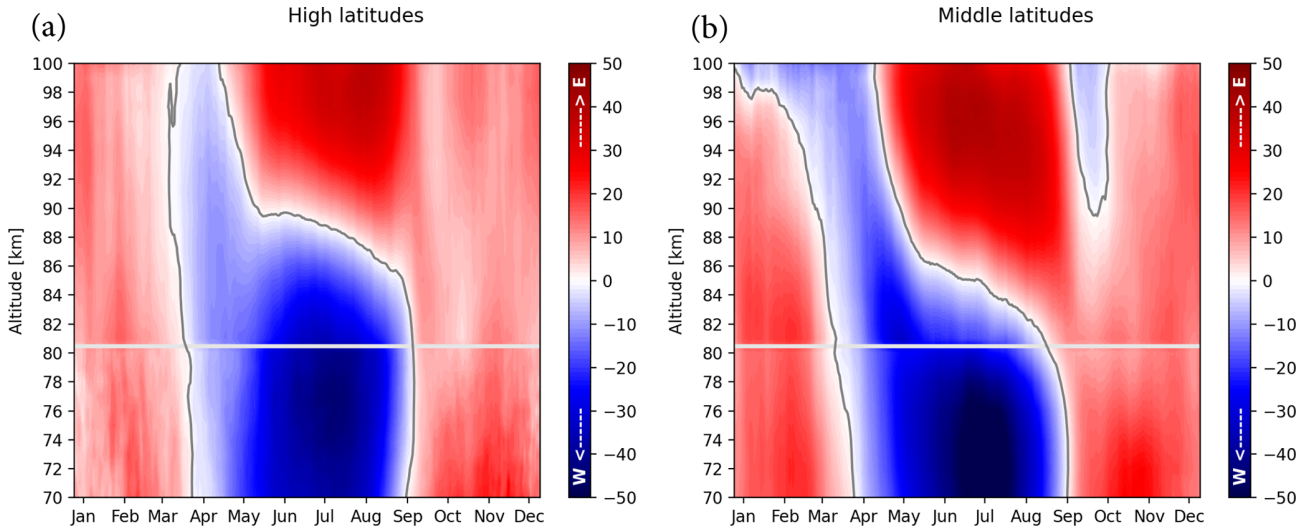

Figure 1. Combined mean zonal wind climatologies at **(a)** high and **(b)** middle latitudes. High-latitude values above 81–100 km depict the combination of SMRs at Andenes and Tromsø, while below (i.e., 70–80 km) the climatology comes from the Saura PRR. The middle-latitude values are divided in the same altitude range with SMRs at Juliusruh and Collm (81–100 km) and Juliusruh PRR for lower altitudes (70–80 km). The grey line shows the zero wind line.

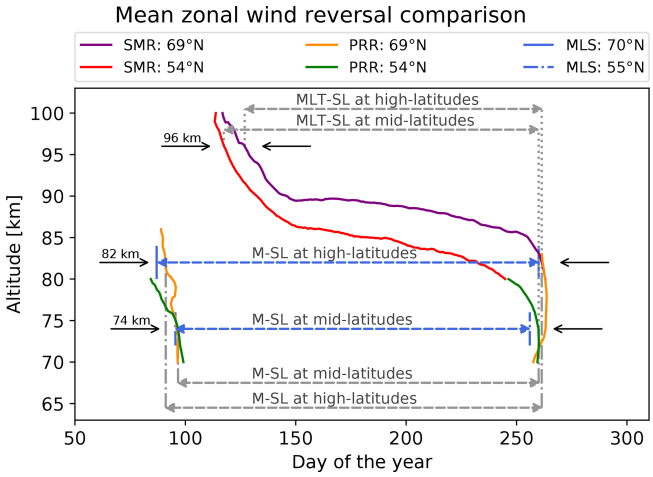

Figure 2. Mean zonal wind reversal comparison and summer length definitions (MLT-SL and M-SL) at high and middle latitudes. The mean zonal wind reversal ($0\,\mathrm{m\,s^{-1}}$) extracted from the climatologies from SMRs (purple) and PRR (orange) at 69° N and SMRs (red) and PRR (green) at 54° N. In addition, the specific geopotential heights with the zero zonal mean geostrophic zonal wind values from the MLS (blue) are shown at 70° N (solid line) and at 55° N (dash-dotted line). The black arrows indicate the altitude taken for the mean zonal wind reversal used in the individual definitions.

definitions, the linear regression is not shown since we were not able to reject the null hypothesis.

The M-SL (Fig. 3g) for the high latitudes is found to be 170 ± 11 d long using PRR measurements (173 ± 12 d for the MLS) with a tendency of $0.46 \pm 0.52\,\mathrm{d\,yr^{-1}}$ (1.23 ± 0.62 d for the MLS). Most of the variability and trend is introduced by the summer beginning (Fig. 3a) occurring at DOY 93 ± 10 d for PRR (3 April) and DOY 88 ± 12 d for the MLS (29 March), with a tendency to start earlier, -0.62 ± 0.48 and -1.26 ± 0.62 d, respectively. For the MLT-SL (Fig. 3c) we found 136 ± 8 d but with no significant trend starting around 7 May (see Table 1 for more details).

The last row for both definitions (Fig. 3d, h) represents proxies of possible forcing in the MLT region that occurred during the corresponding previous winter (for MSSW and strong polar-night jet oscillations) or centered in the mean value for the summer beginning (March, April, and May) for Lyman α line (black line), QBO and ENSO. ENSO is represented by the Oceanic Niño Index (ONI), where the values over 1 °C are considered an El Niño phase (orange) and under −1 °C a La Niña (green) (see, e.g., Pedatella and Liu, 2012). The QBO is represented by the winds at 10 hPa from Singapore (scaled by $10\,\mathrm{m\,s^{-1}}$). QBO eastward (QBOe) is shown in red, and QBO westward (QBOw) is blue. The MSSWs are represented (in purple) as follows: when a displacement of the polar vortex occurred is indicated by a "*D*", and in case of a split it is indicated by the bow tide symbol. The pink "sPJO" shows the year when strong polar-night jet oscillations occurred.

The middle-latitude results are shown in Fig. 4 in a similar format. The main difference is that the altitude for the summer end in both definitions is 74 km. There, the M-SL (Fig. 4g) is found to be 162 ± 7 d long using PRR measurements (160 ± 6 d for the MLS), with an almost identical tendency of $0.55 \pm 0.3\,\mathrm{d\,yr^{-1}}$ for the PRR and MLS. Equivalently to the high latitudes, this mostly corresponds to the summer beginning (Fig. 4a) occurring at DOY 95 ± 5 d for PRR and DOY 97 ± 7 d for the MLS (between 5 and 7 April)

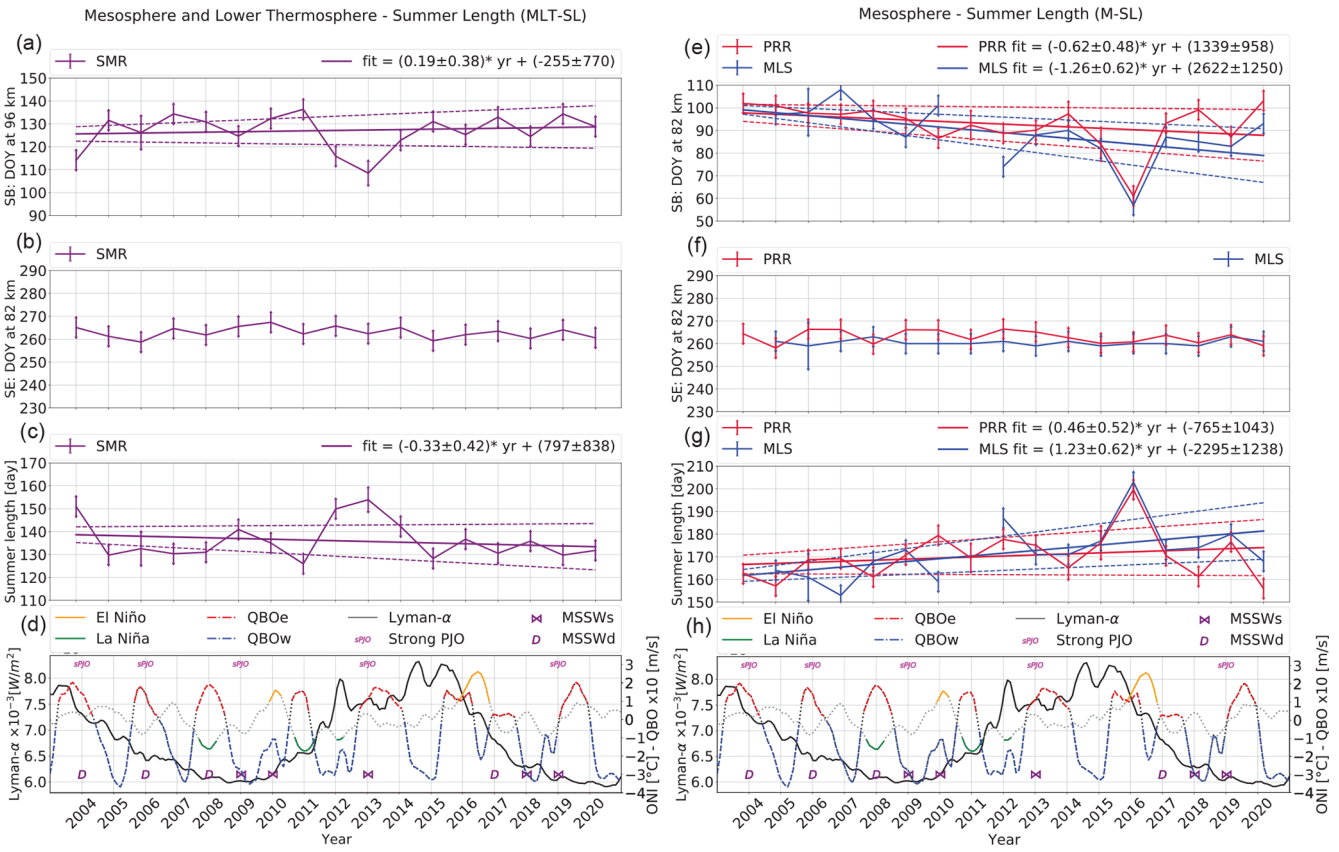

Figure 3. Summer length at high latitudes: on the left is shown MLT-SL and M-SL on the right: panel **(a)** represents the summer beginning at 96 km (MLT-SB) and panel **(e)** 82 km (M-SB) for each year (abscissa) and the DOY when the mean zonal wind reversal occurs (ordinate). The summer end is measured at 82 km for both **(b)** MLT-SE and **(f)** M-SE. Panels **(c)** and **(g)** depict the summer length as the difference between summer end and summer beginning, i.e., MLT-SL and M-SL, respectively. For each time series a linear fit is shown in the same color with the standard deviation of the slope in the same color with dashed lines. The panels in the last row **(d, h)** show proxies of lower and extraterrestrial atmospheric forcing (see text for details).

Table 1. Summary of the mean values and their standard deviations for each time series with the corresponding values of the slope from the linear fit and confidence values (cv) divided into three categories: less than 80 % without a star, greater than 90 % with one star and greater than 95 % with two stars.

Def.	Lat. (° N)	Alt. (SB, SE) (km)	System	SL	SB	SE	SL-Slope	SB-Slope
MLT	High (69)	(96, 82)	SMR	136 ± 8	127 ± 8	263 ± 3	-0.33 ± 0.42	0.19 ± 0.38
	Middle (54)	(96, 74)	SMR, PRR	141 ± 4	119 ± 4	259 ± 3	0.08 ± 0.25	-0.26 ± 0.21
M	High (70)	(82, 82)	MLS	173 ± 12	88 ± 12	260 ± 1	$1.23 \pm 0.62^{**}$	$-1.26 \pm 0.62^{**}$
	High (69)	(82, 82)	PRR	170 ± 11	93 ± 10	263 ± 3	$0.46 \pm 0.52^{*}$	$-0.62 \pm 0.48^{**}$
	Middle (55)	(74, 74)	MLS	160 ± 6	95 ± 5	255 ± 1	$0.55 \pm 0.28^{**}$	$-0.49 \pm 0.25^{**}$
	Middle (54)	(74, 74)	PRR	162 ± 7	97 ± 7	259 ± 3	$0.55 \pm 0.33^{**}$	$-0.72 \pm 0.32^{**}$

Confidence value: **cv > 95 %, *cv > 90 %.

with tendencies of -0.49 ± 0.25 and -0.72 ± 0.32 d, respectively. For the MLT-SL (Fig. 4c) we found 141 ± 4 d, but again with no significant trend, starting on 29 April.

The mean values, with the standard deviations from Figs. 3 and 4, are summarized in Table 1, as well as the slopes for the summer beginning and summer length with their standard deviations. The slopes are classified from the result of the Student's t-test, as follows. The slopes with less than 80 % of confidence have no stars, more than 90 % have one star, and more than 95 % have two stars.

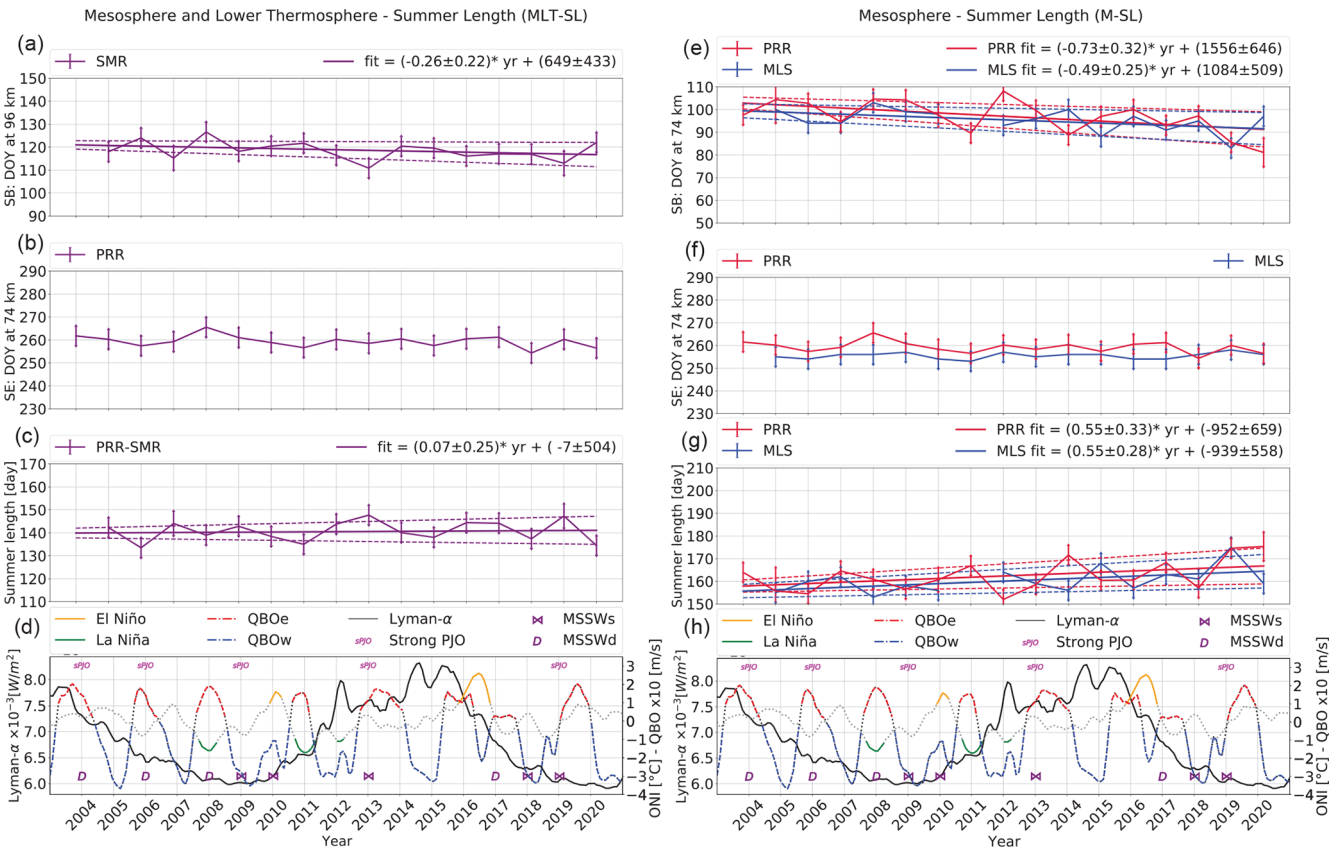

Figure 4. Summer length at middle latitudes: similar to Fig. 3, but in this case, the altitude of MLT-SE **(b)** is 74 km as well as for M-SB **(e)** and M-SE **(g)**. At this latitude the MLT-SL is obtained from a combination of SMRs and PRR.

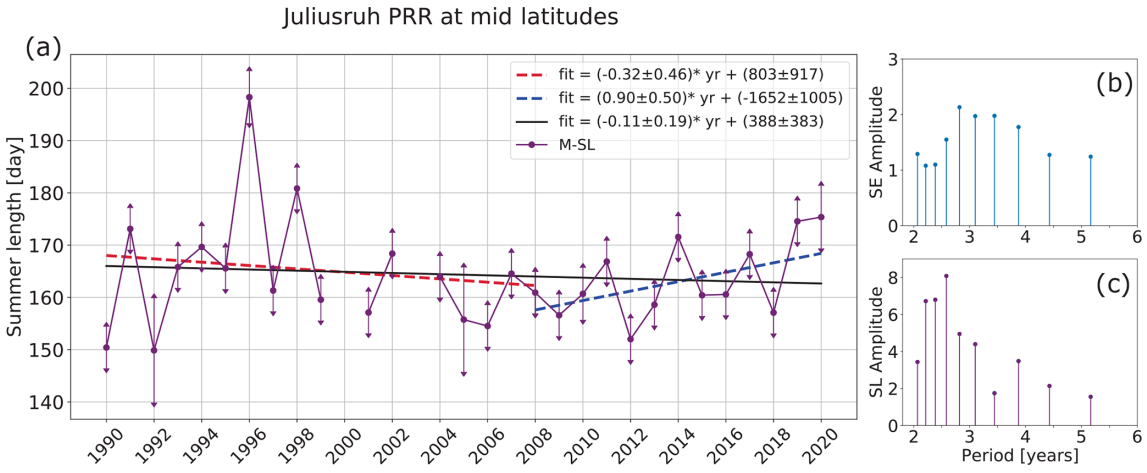

Figure 5. (a) Mesosphere summer length at middle latitudes for 31 years of measurements from Juliusruh PRR. The points show the M-SL obtained from the difference between summer end (SE) and summer beginning (SB) at 74 km. The dashed lines show the linear fit for each interval, from 1990 to 2008 in red and from 2008 to 2020 in blue. The black line denotes the linear fit for the complete time series. On the right, the summer end **(b)** and summer length **(c)** periods in years obtained by the Fourier transformation.

As mentioned previously, in the case of middle latitudes one can extend the study of the M-SL using the Juliusruh PRR to 31 years by combining zonal winds obtained at the same place but with different partial reflection radar systems and measuring techniques. Figure 5 depicts the M-SL values from this combined data set covering the period 1990–2020. In this case, we show a linear function for the entire time series in black. Due to an apparent breakpoint around 2008, we include two linear regressions according to this breakpoint, i.e., 1990–2008 in dashed red line and 2008–2020 in dashed blue line. The breakpoint was obtained by a second-degree polynomial fitted by the least square method.

5 Discussion

In this section we discuss the obtained result. Noteworthy, for both latitudes and definitions, is that the variability of the summer lengths is dominated by the summer beginning and, thus, by the winter conditions. Since our results display a latitudinal dependency, we also divided our discussion by latitude. In addition, we discuss the results of our summer definitions with respect to other definitions used in earlier studies. The long-term behavior of our results, including the 31-year analysis, is discussed separately.

5.1 High latitudes

As both definitions represent different processes from the different altitudes (in the summer beginning) and therefore times in the year, there is also a significant difference observed in the variability. The observed variability is higher in M-SB due to the proximity to the winter conditions, which is modulated by the planetary wave activity, final warmings, etc. (Lauter and Entzian, 1983; Hoffmann et al., 2002; Savenkova et al., 2012).

The MLT-SL shows peculiar values for the years 2004, 2012 and 2013, with an earlier MLT-SB. The 2013 winter-to-summer transition was reported by Fiedler et al. (2015) as an uncommon year with extreme conditions showing lower temperatures (~ 6 K below the mean) and a higher concentration of water vapor at 83 km. In their study, they found strongly enhanced planetary wave activity uncommon for the time of the year (see Fiedler et al., 2015, Fig. 5).

A similar period was recently studied at the MLT Northern Hemisphere high latitudes by Hall and Tsutsumi (2020). The authors reported on temperatures at 90 km over Svalbard (78° N), calculating monthly mean values and fitting trends using December as a representation of winter trends. The authors found lower temperature values in the winters 2003/2004 and 2012/2013 and reported 2012 as a change point detected by their algorithm (see Hall and Tsutsumi, 2020, Fig. 3). Even though both data sets are different (December monthly mean temperature at 78° N and mean zonal wind reversal in May at 69° N), these data "outliers" appear to be connected.

In the case of M-SL the years 2012 and 2016 strongly deviate from the mean behavior of the M-SL. In 2012 the satellite data show an early M-SB (DOY 74), while the radar (DOY 89) depicts a value not far from the mean (DOY 92). At high latitudes, in the Northern Hemisphere the winter is dominated by the behavior of the polar vortex and its temporal dependence on the position. Considering the satellite zonal mean geostrophic zonal winds are an average in longitude and the radar only shows the mean zonal wind at a fixed longitude, it is reasonable to find differences between these individual observations. Thus, here we can see the complexity of understanding the winter time in a localized position (radar site) compared with the average in longitude (obtained from satellite). In contrast to this example, 2016 has an earlier M-SB for both instruments (DOY 61 PRR and DOY 57 MLS) as a consequence of the event categorized as a final warming (Yamazaki and Matthias, 2019). In contrast to this categorization, Manney and Lawrence (2016) described 2016 as a major final sudden stratospheric warming.

In the time series we were not able to find a relation to Lyman α. In the case of ENSO and QBO, we also do not find a clear connection with the mean zonal wind reversal dates. A similar result is obtained analyzing the MSSW, strong polar-night jet oscillation years and the summer beginning time series. We can only find two particular clear cases where the summer beginning is affected by a final warming.

5.2 Middle latitudes

As we move far away from the polar vortex and approach the middle latitudes, the summer beginning displays less variability than at high latitudes, and there is a clear time–latitude difference in the time series (also indicated in Fig. 2). The mean zonal wind reversal occurs earlier at high latitudes and later on at middle latitudes. Towards the end of the summer, the westward wind velocity decreases and finally reverses again to the eastward direction at middle latitudes and later on at higher latitudes. Thus, the summer length difference is dependent on the latitude as a consequence of the residual mesospheric wind circulation (e.g., Andrews et al., 1987; Hoffmann et al., 2002). The mean zonal wind reversals for both latitudes exhibit a comparable profile, while the mean zonal wind reversal at high latitudes occurs at about 5 km higher altitudes (see Figs. 1 and 2). Thus, for the use of the same upper altitude (96 km), the mean zonal wind reversal occurs earlier at middle latitudes. Furthermore, small differences in the profile steepness are visible; i.e., the wind reversal does not occur simultaneously at several altitudes. However, near and especially above 100 km altitude, the meteor count rates decrease substantially, introducing larger uncertainties, which restrain us from selecting a higher altitude (e.g., Younger et al., 2009), where we exactly want to observe the mean zonal wind reversal and MLT-SB.

Looking into the unusual years seen at high latitudes, the reversal during 2012 (Fig. 4a) occurs on DOY = 116, representing an earlier start but within the variability. However, the reversal occurs on the same day at both latitudes, raising the question of what kind of event might produce a reversal of the wind on the same day at 15° latitude difference. 2013 shows a deviation of 8 d apart (DOY 111) from the mean behavior in the MLT-SB but well outside of the mean standard deviation of 4 d. This difference shows again evidence of latitudinal difference and the earlier starts, which once more could be representing an unusually strong planetary wave activity for this time of the year (Fiedler et al., 2015). The M-SB (Fig. 4e) depicts a higher variability than MLT-SB, but the only year with a slight deviation from the mean behavior is 2012 with a late final warming. In addition, this late final warming and the difference between the satellite and the radar could be indicating the displaced polar vortex near the radar site.

Once more, similarly to high latitudes, the mean zonal wind reversal dates do not depict a connection to the solar activity or the other events (i.e., ENSO, QBO, strong polar-night jet oscillation or MSSW).

5.3 Comparisons with other definitions

Comparing the definitions proposed in this work with the one made by Offermann et al. (2004), we can find a big difference for the summer end. While Offermann et al. (2010) showed opposite sign slopes retrieved from a threshold in temperature in the beginning and end, we have found a variability dependence on the summer beginning. This difference is attributed to the rapid wind changes in September; meanwhile, the temperature appears to change with a weaker gradient. The summer duration obtained in their works is comparable with the values obtained for M-SL at middle latitudes, with a difference of around 10 d.

Inspired by the comparison between the summer duration in the MLT and that at ground level made by Offermann et al. (2004), we investigate the summer length through the vegetation growing season length. A recent study on the topic was performed by Hurdebise et al. (2019) with the tree *Fagus sylvatica* in eastern Belgium between the years 1997 and 2014, obtaining a "leafed period length" (or growing season length) of 165 ± 7 d and a slope of $-0.62\,\mathrm{d\,yr^{-1}}$ with high significance (statistical p-value < 0.05). Chen et al. (2019) studied three different species of trees (among them the *Fagus sylvatica*, presenting less change rate between the studied species) common in central Europe (47–55° N) between 1950 and 2013. They found that since 2000 the length of the growing season has not increased, and their mean value is around 174 d. These studies show a connection between the temperatures and the leaf unfolding and folding periods at ground level for middle latitudes. The Zhou et al. (2001) extrapolated value gives us a mean of the vegetation growing season length of 160 ± 4 d (maintaining their own standard error), comparable with M-SL at middle latitudes ($160–162 \pm 7$ d). In the case of Hurdebise et al. (2019) the resulting length of the vegetation growing season is 169 ± 7 d, and for Chen et al. (2019) it is 174 with an apparent variability of around 3 d. In these cases, the M-SL is more similar to the length obtained at high latitudes ($170–173 \pm 12$ d), even though their studies were performed for middle latitudes.

5.4 Long-term analysis

A linear regression was implemented for all the time series and the result proven with a Student's t-test. Since in all the summer ending times series we were not able to reject the null hypothesis, we only show the significance levels for the summer beginnings and summer lengths. However, the MLT-SL definition shows no significant linear change over the years and, thus, we consider this definition to be not sensible to a possible long-term change. On the other hand, the M-SL and M-SB show linear tendencies with confidences greater than 95 % in most of the cases. The only exception is in M-SL at high latitudes (Saura PRR), where the slope shows a confidence greater than 90 % (see Table 1). In none of the time series did we apply a correction by QBO or solar activity as they were used in other works (e.g., Offermann et al., 2010; Keuer et al., 2007). In the case of QBO, the influence is not clear or seen in the mean zonal wind reversal dates, probably due to the short time series. Pursuing this concept, we extended M-SL at middle latitudes with the available data, obtaining a 31-year time series (see Fig. 5a). The summer beginning revealed periods of 2.21–2.58 years and the summer end periods of 2.82–3.87 years. Due to the low amplitude in the summer end, the summer length only reveals those found in the summer beginning (see Fig. 5b and c). These periods are associated with QBO and ENSO, 2.2–2.4 and 3.5 years, respectively (e.g., Offermann et al., 2015).

The slope of the 31-year linear regression (negative) shows an opposite direction (positive) to the shorter version (17-year time series, Fig. 4g), which made us speculate about a non-uniform trend. An inflection point is detected around 2008 ± 2 years, and the high variability occurs mostly because of the higher uncertainties in the earlier years of the data set, where the radar experienced several changes (see Sect. 2). These uncertainties may influence the determination of the breakpoint year, and we might be in the presence of another breakpoint around 1992–1995. Moreover, the results from the spectra of the individual time series (i.e., 1990–2007 and 2008–2020) are similar to the ones in Fig. 5b and c. Particularly in the 2008–2020 time series, we identify periods around 2.25–2.57 years for the summer end, while in the summer beginning 3-year and 4.5-year periodicities are identified. Nevertheless, the 4.5-year amplitude is not as relevant as the 3-year one, but it could be associated with a quasi-quadrennial oscillation (French et al., 2020).

Evidence of breakpoints in the long-term studies has been reported by several authors. Lauter and Entzian (1983) speculated a period of 10–20 years after finding a breakpoint

in 1980. The same year was identified by Offermann et al. (2004, 2005), and Offermann et al. (2006) reported an additional one in 2001/2002. Studying the amplitudes of the mean zonal winds during different seasons, Liu et al. (2010) and Jacobi et al. (2015) described a breakpoint in the summer months around 1995–2000 in Collm observations. Later on, Hall and Tsutsumi (2020) detected a breakpoint in 2012 ± 1 year. Portnyagin et al. (2006) found a breakpoint in 1980 and adjusted two different linear functions and parabolas, concluding that at middle latitudes, the MLT winds have non-uniform trends. With our initial time series (2004–2020), we cannot see a clear indication of a breakpoint. Nevertheless, it is detected within 31 years of measurements. Considering the numerous studies and our findings, we can only assume that a more robust trend analysis might require a longer time series.

6 Summary and conclusions

Smoothed mean zonal winds between 2004/2005 and 2020 from different radars located at high and middle latitudes (Andenes SMR–Tromsø SMR, Saura PRR, Juliusruh SMR–Collm SMR and Juliusruh PRR), as well as MLS measurements, are used to study two different summer length definitions (see Sect. 3). The MLT-SL definition is taken when the last wind reversal occurred from westward to eastward at 96 km (MLT-SB) and 82 km at high latitudes (74 km for middle latitudes) as MLT-SE. On the other hand, the M-SL definition is taken at the same altitude (M-SB and M-SE) but depending on the latitude (82 km at high latitudes and 74 km at middle latitudes), when the mean zonal wind reverses from eastward to westward (M-SB) and, again, from westward to eastward (M-SE).

With the obtained time series, we analyzed the summer length and studied the variability and the linear tendency. We looked into the dates and the different events occurring in the upper and lower atmosphere to understand the events modifying the summer length. Furthermore, we compared the summer length to the growing season length. The results are summarized as follows.

- The summer length is determined by the mean zonal wind reversal, which depends on the actual latitude and altitude. High latitudes showed more variability than middle latitudes for both definitions. The summer beginning presents most of the variability that is transferred to the summer length. The summer end occurs for all latitudes in the same week before the autumn equinox and presents no significant linear trend.

- MLT-SL definition: the summer starts around 7 May at high latitudes (SL = 136 d) and around 29 April at middle latitudes (SL = 141 d), showing a shorter summer length at high latitudes. This definition presents no significant trends, and the events studied (MSSW, strong polar-night jet oscillations, ENSO, QBO and Lyman α) do not seem to affect the duration of the summer. Nevertheless, we have found strong evidence of abnormal behavior in the years 2004, 2012 and 2013, also observed by Hall and Tsutsumi (2020). Particularly the year 2013 has been reported by Fiedler et al. (2015) as presenting high planetary wave activity later than the usual time, producing an earlier mean zonal wind reversal.

- M-SL definition: this is more variable than the MLT-SL due to the higher variability in the summer beginning, which is more prone to the winter conditions. The summer starts between the end of March and the beginning of April for high latitudes and 1 week later at middle latitudes (see Table 1). In this case, linear trends were found for summer beginning and summer length with 90 % or more confidence. The years 2012 and 2016 displayed extreme values. However, in the latter, the earlier summer beginning was a consequence of a final warming (Yamazaki and Matthias, 2019).

- At middle latitudes, the length of the growing season at ground level is similar or has around 10 d difference (depending on the author) to the M-SL.

- After analyzing the time series and trying to relate it to other events (solar activity, QBO, ENSO, strong polar-night jet oscillations, and MSSW), we were not able to find a direct influence on the summer length or summer beginning. Only for the M-SL did we find 1 year (with a strong MSSW and 2016 final warming) being directly affected. The 17-year time series are short for studying the period related to QBO or ENSO. On the other hand, with the 31-year time series (see Fig. 5), we detected periodicities of around 2.21–2.58 and 2.82–3.87 years that we could attribute to QBO and ENSO, respectively (e.g., Offermann et al., 2015).

Data availability. The data to produce the figures are available in HDF5 format at https://doi.org/10.22000/513 (Jaen et al., 2022). The QBO winds were obtained from the Free University of Berlin repository (https://www.geo.fu-berlin.de/en/met/ag/strat/produkte/qbo/index.html, Free University of Berlin, 2021; Naujokat, 1986). The ENSO index (ONI) was acquired from the NOAA/National Weather Service (https://origin.cpc.ncep.noaa.gov/products/analysis_monitoring/ensostuff/ONI_v5.php, Climate Prediction Center, 2021; Huang et al., 2017). Lyman-α values were retrieved from NASA (https://omniweb.gsfc.nasa.gov/form/dx1.html, NASA, 2021).

Author contributions. JJ, TR, JLC and PH developed the idea and helped in the interpretation of results. MH assisted in the implementation and interpretation of PCA. VM and YY provided the wind analysis used for the Microwave Limb Sounder values. CH and MT ensured the operation of the Tromsø specular meteor radar

and CJ of the Collm specular meteor radar. Furthermore, JJ wrote the manuscript with input from all the coauthors.

Competing interests. Christoph Jacobi is editor-in-chief and topical editor of *Annales Geophysicae*.

Disclaimer. Publisher's note: Copernicus Publications remains neutral with regard to jurisdictional claims in published maps and institutional affiliations.

Acknowledgements. We acknowledge use of NASA/GSFC's Space Physics Data Facility's OMNIWeb service, and OMNI data. We thank the Free University of Berlin for the provision of the QBO data. We thank the NOAA/National Weather Service, Climate Prediction Center for the ENSO index.

Financial support. This research has been supported by the Deutsche Forschungsgemeinschaft (VACILT, grant nos. PO 2341/2-1 and JA 836/47-1) and the Bundesministerium für Bildung und Forschung (TIMA, grant no. 01 LG 1902A).

The publication of this article was funded by the Open Access Fund of the Leibniz Association.

Review statement. This paper was edited by Andrew J. Kavanagh and reviewed by two anonymous referees.

References

Andrews, D. G., Holton, J. R., and Leovy, C. B.: Middle Atmosphere Dynamics, vol. 40 – 1st edn., Academic Press, ISBN 0-12-058576-6, 1987.

Baldwin, M. P., Gray, L. J., Dunkerton, T. J., Hamilton, K., Haynes, P. H., Randel, W. J., Holton, J. R., Alexander, M. J., Hirota, I., Horinouchi, T., Jones, D. B. A., Kinnersley, J. S., Marquardt, C., Sato, K., and Takahashi, M.: The quasi-biennial oscillation, Rev. Geophys., 39, 179–229, https://doi.org/10.1029/1999RG000073, 2001.

Baumgarten, G., Fiedler, J., Lübken, F.-J., and von Cossart, G.: Particle properties and water content of noctilucent clouds and their interannual variation, J. Geophys. Res., 113, D06203, https://doi.org/10.1029/2007JD008884, 2008.

Butler, A. H., Seidel, D. J., Hardiman, S. C., Butchart, N., Birner, T., and Match, A.: Defining sudden stratospheric warmings, B. Am. Meteorol. Soc., 96, 1913–1928, https://doi.org/10.1175/BAMS-D-13-00173.1, 2015.

Climate Prediction Center: Cold & Warm Episodes by Season, NOAA/National Weather Service, National Centers for Environmental Prediction [data set], available at: https://origin.cpc.ncep.noaa.gov/products/analysis_monitoring/ensostuff/ONI_v5.php, last access: 20 July 2021.

Chau, J. L., Stober, G., Hall, C. M., Tsutsumi, M., Laskar, F. I., and Hoffmann, P.: Polar mesospheric horizontal divergence and relative vorticity measurements using multiple specular meteor radars, Radio Sci., 52, 811–828, https://doi.org/10.1002/2016RS006225, 2017.

Chen, L., Huang, J., Ma, Q., Hänninen, H., Tremblay, F., and Bergeron, Y.: Long-term changes in the impacts of global warming on leaf phenology of four temperate tree species, Glob. Change Biol., 25, 997–1004, https://doi.org/10.1111/gcb.14496, 2019.

Conte, J. F., Chau, J. L., Laskar, F. I., Stober, G., Schmidt, H., and Brown, P.: Semidiurnal solar tide differences between fall and spring transition times in the Northern Hemisphere, Ann. Geophys., 36, 999–1008, https://doi.org/10.5194/angeo-36-999-2018, 2018.

Conte, J. F., Chau, J. L., and Peters, D. H.: Middle- and High-Latitude Mesosphere and Lower Thermosphere Mean Winds and Tides in Response to Strong Polar-Night Jet Oscillations, J. Geophys. Res.-Atmos., 124, 9262–9276, https://doi.org/10.1029/2019JD030828, 2019.

Fiedler, J., Baumgarten, G., Berger, U., Gabriel, A., Latteck, R., and Lübken, F.-J.: On the early onset of the NLC season 2013 as observed at ALOMAR, J. Atmos. Sol.-Terr. Phy., 127, 73–77, https://doi.org/10.1016/j.jastp.2014.07.011, 2015.

Free University of Berlin: QBO winds [data set], available at: https://www.geo.fu-berlin.de/en/met/ag/strat/produkte/qbo/index.html, last access: 20 July 2021.

French, W. J. R., Klekociuk, A. R., and Mulligan, F. J.: Analysis of 24 years of mesopause region OH rotational temperature observations at Davis, Antarctica – Part 2: Evidence of a quasi-quadrennial oscillation (QQO) in the polar mesosphere, Atmos. Chem. Phys., 20, 8691–8708, https://doi.org/10.5194/acp-20-8691-2020, 2020.

Fukao, S. and Hamazu, K.: Radar for Meteorological and Atmospheric Observations, Springer Japan, Tokyo, ISBN 978-4-431-54333-6, https://doi.org/10.1007/978-4-431-54334-3, 2014.

Fung, I. Y., Tucker, C. J., and Prentice, K. C.: Application of Advanced Very High Resolution Radiometer vegetation index to study atmosphere-biosphere exchange of CO_2, J. Geophys. Res., 92, 2999–3015, https://doi.org/10.1029/JD092iD03p02999, 1987.

Hall, C. M. and Tsutsumi, M.: Neutral temperatures at 90 km altitude over Svalbard (78° N 16° E), 2002–2019, derived from meteor radar observations, Polar Sci., 24, 100530, https://doi.org/10.1016/j.polar.2020.100530, 2020.

Hall, C. M., Aso, T., Tsutsumi, M., Nozawa, S., Manson, A. H., and Meek, C. E.: A comparison of mesosphere and lower thermosphere neutral winds as determined by meteor and medium-frequency radar at 70°N, Radio Sci., 40, RS4001, https://doi.org/10.1029/2004RS003102, 2005.

Hervig, M., Thompson, R. E., McHugh, M., Gordley, L. L., Russell, J. M., and Summers, M. E.: First confirmation that water ice is the primary component of polar mesospheric clouds, Geophys. Res. Lett., 28, 971–974, https://doi.org/10.1029/2000GL012104, 2001.

Hocking, W., Fuller, B., and Vandepeer, B.: Real-time determination of meteor-related parameters utilizing modern digital technology, J. Atmos. Sol.-Terr. Phy., 63, 155–169, https://doi.org/10.1016/S1364-6826(00)00138-3, 2001.

Hoffmann, P., Singer, W., and Keuer, D.: Variability of the mesospheric wind field at middle and Arctic latitudes in winter and its relation to stratospheric circulation disturbances, J. Atmos. Sol.-Terr. Phy., 64, 1229–1240, https://doi.org/10.1016/S1364-6826(02)00071-8, 2002.

Hoffmann, P., Becker, E., Singer, W., and Placke, M.: Seasonal variation of mesospheric waves at northern middle and high latitudes, J. Atmos. Sol.-Terr. Phy., 72, 1068–1079, https://doi.org/10.1016/j.jastp.2010.07.002, 2010.

Huang, B., Thorne, P. W., Banzon, V. F., Boyer, T., Chepurin, G., Lawrimore, J. H., Menne, M. J., Smith, T. M., Vose, R. S., and Zhang, H.: Extended Reconstructed Sea Surface Temperature, Version 5 (ERSSTv5): Upgrades, Validations, and Intercomparisons, J. Climate, 30, 8179–8205, https://doi.org/10.1175/JCLI-D-16-0836.1, 2017.

Hurdebise, Q., Aubinet, M., Heinesch, B., and Vincke, C.: Increasing temperatures over an 18-year period shortens growing season length in a beech (Fagus sylvatica L.)-dominated forest, Ann. For. Sci., 76, 75, https://doi.org/10.1007/s13595-019-0861-8, 2019.

Jacobi, C., Lilienthal, F., Geißler, C., and Krug, A.: Long-term variability of mid-latitude mesosphere-lower thermosphere winds over Collm (51° N, 13° E), J. Atmos. Sol.-Terr. Phy., 136, 174–186, https://doi.org/10.1016/j.jastp.2015.05.006, 2015.

Jaen, J., Renkwitz, T., Chau, J. L., He, M., Hoffmann, P., Yamazaki, Y., Jacobi, C., Tsutsumi, M., Matthias, V., and Hall, C.: JaenANGEO2021, Leibniz Institute of Atmospheric Physics at the University of Rostock [data set], https://doi.org/10.22000/513, 2022.

Jolliffe, I. T.: Principal Component Analysis, Springer Series in Statistics, Springer-Verlag, New York, https://doi.org/10.1007/b98835, 2002.

Jolliffe, I. T. and Jackson, J. E.: A User's Guide to Principal Components., Statistician, 42, 76–77, https://doi.org/10.2307/2348121, 1993.

Keuer, D., Hoffmann, P., Singer, W., and Bremer, J.: Long-term variations of the mesospheric wind field at mid-latitudes, Ann. Geophys., 25, 1779–1790, https://doi.org/10.5194/angeo-25-1779-2007, 2007.

Laskar, F. I., Chau, J. L., St.-Maurice, J. P., Stober, G., Hall, C. M., Tsutsumi, M., Höffner, J., and Hoffmann, P.: Experimental Evidence of Arctic Summer Mesospheric Upwelling and Its Connection to Cold Summer Mesopause, Geophys. Res. Lett., 44, 9151–9158, https://doi.org/10.1002/2017GL074759, 2017.

Laštovička, J. and Jelínek, Š.: Problems in calculating long-term trends in the upper atmosphere, J. Atmos. Sol.-Terr. Phy., 189, 80–86, https://doi.org/10.1016/j.jastp.2019.04.011, 2019.

Lauter, E. and Entzian, G.: Peculiarities of the middle atmosphere in winter and during the transitional seasons, HHI-STP-Report, 17, 57–64, 1983.

Liu, R. Q., Jacobi, C., Hoffmann, P., Stober, G., and Merzlyakov, E. G.: A piecewise linear model for detecting climatic trends and their structural changes with application to mesosphere/lower thermosphere winds over Collm, Germany, J. Geophys. Res., 115, D22105, https://doi.org/10.1029/2010JD014080, 2010.

Livesey, N. J., Read, G., W., Wagner, P. A., Froidevaux, L., Lambert, A., Manney, G. L., Millán Valle, L. F., Pumphrey, H. C., Santee, M. L., Schwartz, M. J., Wang, S., Fuller, R. A., Jarnot, R. F., Knosp, B. W., Martinez, E., and Lay, R. R.: EOS MLS Version 4.2x Level 2 data quality and description document, available at: https://mls.jpl.nasa.gov/data/v4-2_data_quality_document.pdf (last access: 10 May 2021), 2015.

Machol, J., Snow, M., Woodraska, D., Woods, T., Viereck, R., and Coddington, O.: An Improved Lyman-Alpha Composite, Earth Space Sci., 6, 2263–2272, https://doi.org/10.1029/2019EA000648, 2019.

Manney, G. L. and Lawrence, Z. D.: The major stratospheric final warming in 2016: dispersal of vortex air and termination of Arctic chemical ozone loss, Atmos. Chem. Phys., 16, 15371–15396, https://doi.org/10.5194/acp-16-15371-2016, 2016.

NASA: OMNIWeb, available at: https://omniweb.gsfc.nasa.gov/form/dx1.html, last access: 17 March 2021.

Naujokat, B.: An Update of the Observed Quasi-Biennial Oscillation of the Stratospheric Winds over the Tropics, J. Atmos. Sci., 43, 1873–1877, https://doi.org/10.1175/1520-0469(1986)043<1873:AUOTOQ>2.0.CO;2, 1986.

Offermann, D., Donner, M., Knieling, P., and Naujokat, B.: Middle atmosphere temperature changes and the duration of summer, J. Atmos. Sol.-Terr. Phy., 66, 437–450, https://doi.org/10.1016/j.jastp.2004.01.028, 2004.

Offermann, D., Jarisch, M., Donner, M., Oberheide, J., Wohltmann, I., Garcia, R., Marsh, D., Naujokat, B., and Winkler, P.: Middle atmosphere summer duration as an indicator of long-term circulation changes, Adv. Space Res., 35, 1416–1422, https://doi.org/10.1016/j.asr.2005.02.065, 2005.

Offermann, D., Jarisch, M., Donner, M., Steinbrecht, W., and Semenov, A.: OH temperature re-analysis forced by recent variance increases, J. Atmos. Sol.-Terr. Phy., 68, 1924–1933, https://doi.org/10.1016/j.jastp.2006.03.007, 2006.

Offermann, D., Hoffmann, P., Knieling, P., Koppmann, R., Oberheide, J., and Steinbrecht, W.: Long-term trends and solar cycle variations of mesospheric temperature and dynamics, J. Geophys. Res.-Atmos., 115, D18 127, https://doi.org/10.1029/2009JD013363, 2010.

Offermann, D., Goussev, O., Kalicinsky, C., Koppmann, R., Matthes, K., Schmidt, H., Steinbrecht, W., and Wintel, J.: Journal of Atmospheric and Solar-Terrestrial Physics A case study of multi-annual temperature oscillations in the atmosphere : Middle Europe, J. Atmos. Sol.-Terr. Phy., 135, 1–11, https://doi.org/10.1016/j.jastp.2015.10.003, 2015.

Pedatella, N. M. and Liu, H.-L.: Tidal variability in the mesosphere and lower thermosphere due to the El Niño-Southern Oscillation, Geophys. Res. Lett., 39, 1–7, https://doi.org/10.1029/2012GL053383, 2012.

Peters, D. H., Schneidereit, A., and Karpechko, A.: Enhanced Stratosphere/Troposphere Coupling During Extreme Warm Stratospheric Events with Strong Polar-Night Jet Oscillation, Atmosphere, 9, 467, https://doi.org/10.3390/atmos9120467, 2018.

Pokhotelov, D., Becker, E., Stober, G., and Chau, J. L.: Seasonal variability of atmospheric tides in the mesosphere and lower thermosphere: meteor radar data and simulations, Ann. Geophys., 36, 825–830, https://doi.org/10.5194/angeo-36-825-2018, 2018.

Portnyagin, Y. I., Merzlyakov, E. G., Solovjova, T. V., Jacobi, C., Kürschner, D., Manson, A., and Meek, C.: Long-term trends and year-to-year variability of mid-latitude mesosphere/lower thermosphere winds, J. Atmos. Sol.-Terr. Phy., 68, 1890–1901, https://doi.org/10.1016/j.jastp.2006.04.004, 2006.

Rapp, M., Lübken, F.-J., and Blix, T.: The role of charged ice particles for the creation of PMSE: A review of recent developments,

Adv. Space Res., 31, 2033–2043, https://doi.org/10.1016/S0273-1177(03)00226-6, 2003.

Reid, I. M.: MF and HF radar techniques for investigating the dynamics and structure of the 50 to 110 km height region: a review, Prog. Earth Planet. Sci., 2, 33, https://doi.org/10.1186/s40645-015-0060-7, 2015.

Renkwitz, T. and Latteck, R.: Variability of virtual layered phenomena in the mesosphere observed with medium frequency radars at 69°N, J. Atmos. Sol.-Terr. Phy., 163, 38–45, https://doi.org/10.1016/j.jastp.2017.05.009, 2017.

Santer, B. D., Wigley, T. M., Boyle, J. S., Gaffen, D. J., Hnilo, J. J., Nychka, D., Parker, D. E., and Taylor, K. E.: Statistical significance of trends and trend differences in layer-average atmospheric temperature time series, J. Geophys. Res.-Atmos., 105, 7337–7356, https://doi.org/10.1029/1999JD901105, 2000.

Savenkova, E., Kanukhina, A., Pogoreltsev, A., and Merzlyakov, E.: Variability of the springtime transition date and planetary waves in the stratosphere, J. Atmos. Sol.-Terr. Phy., 90-91, 1–8, https://doi.org/10.1016/j.jastp.2011.11.001, 2012.

Singer, W., von Zahn, U., and Weiß, J.: Diurnal and annual variations of meteor rates at the arctic circle, Atmos. Chem. Phys., 4, 1355–1363, https://doi.org/10.5194/acp-4-1355-2004, 2004.

Singer, W., Latteck, R., Friedrich, M., Dalin, P., Kirkwood, S., Engler, N., and Holdsworth, D.: D-region electron densities obtained by differential absorption and phase measurements with a 3-MHz-Doppler radar, in: 17th ESA Symposium on European Rocket and Balloon Programmes and Related Research, 30 May–2 June 2005, Sandefjord, Norway, edited by: Warmbein, B., ESA SP-590, ESA Publications Division, Noordwijk, ISBN 92-9092-901-4, 233–237, 2005.

Wang, C. and Picaut, J.: Understanding ENSO physics—a review, Geophys. Monogr. Ser., 147, 21–48, https://doi.org/10.1029/147GM02, 2004.

Waters, J. W., Froidevaux, L., Harwood, R. S., Jarnot, R. F., Pickett, H. M., Read, W. G., Siegel, P. H., Cofield, R. E., Filipiak, M. J., Flower, D. A., Holden, J. R., Lau, G. K., Livesey, N. J., Manney, G. L., Pumphrey, H. C., Santee, M. L., Wu, D. L., Cuddy, D. T., Lay, R. R., Loo, M. S., Perun, V. S., Schwartz, M. J., Stek, P. C., Thurstans, R. P., Boyles, M. A., Chandra, K. M., Chavez, M. C., Chen, G. S., Chudasama, B. V., Dodge, R., Fuller, R. A., Girard, M. A., Jiang, J. H., Jiang, Y., Knosp, B. W., Labelle, R. C., Lam, J. C., Lee, K. A., Miller, D., Oswald, J. E., Patel, N. C., Pukala, D. M., Quintero, O., Scaff, D. M., Van Snyder, W., Tope, M. C., Wagner, P. A., and Walch, M. J.: The Earth Observing System Microwave Limb Sounder (EOS MLS) on the aura satellite, IEEE T. Geosci. Remote, 44, 1075–1092, https://doi.org/10.1109/TGRS.2006.873771, 2006.

Wilhelm, S., Stober, G., and Chau, J. L.: A comparison of 11-year mesospheric and lower thermospheric winds determined by meteor and MF radar at 69° N, Ann. Geophys., 35, 893–906, https://doi.org/10.5194/angeo-35-893-2017, 2017.

Wilhelm, S., Stober, G., and Brown, P.: Climatologies and long-term changes in mesospheric wind and wave measurements based on radar observations at high and mid latitudes, Ann. Geophys., 37, 851–875, https://doi.org/10.5194/angeo-37-851-2019, 2019.

Wu, D. L., Schwartz, M. J., Waters, J. W., Limpasuvan, V., Wu, Q., and Killeen, T. L.: Mesospheric doppler wind measurements from Aura Microwave Limb Sounder (MLS), Adv. Space Res., 42, 1246–1252, https://doi.org/10.1016/j.asr.2007.06.014, 2008.

Yamazaki, Y. and Matthias, V.: Large-Amplitude Quasi-10-Day Waves in the Middle Atmosphere During Final Warmings, J. Geophys. Res.-Atmos., 124, 9874–9892, https://doi.org/10.1029/2019JD030634, 2019.

Yiğit, E., Koucká Knížová, P., Georgieva, K., and Ward, W.: A review of vertical coupling in the Atmosphere-Ionosphere system: Effects of waves, sudden stratospheric warmings, space weather, and of solar activity, J. Atmos. Sol.-Terr. Phy., 141, 1–12, https://doi.org/10.1016/j.jastp.2016.02.011, 2016.

Younger, P. T., Astin, I., Sandford, D. J., and Mitchell, N. J.: The sporadic radiant and distribution of meteors in the atmosphere as observed by VHF radar at Arctic, Antarctic and equatorial latitudes, Ann. Geophys., 27, 2831–2841, https://doi.org/10.5194/angeo-27-2831-2009, 2009.

Zhou, L., Tucker, C. J., Kaufmann, R. K., Slayback, D., Shabanov, N. V., and Myneni, R. B.: Variations in northern vegetation activity inferred from satellite data of vegetation index during 1981 to 1999, J. Geophys. Res.-Atmos., 106, 20069–20083, https://doi.org/10.1029/2000JD000115, 2001.

Appendix B

Jaen et al. (2023)

Jaen, J., Renkwitz, T., Liu, H., Jacobi, C., Wing, R., Kuchař, A., Tsutsumi, M., Gulbrandsen, N., and Chau, J. L.: Long-term studies of the summer wind in the mesosphere and lower thermosphere at middle and high latitudes over Europe, Atmos. Chem. Phys., 23, 14871–14887, https://doi.org/10.5194/acp-23-14871-2023, 2023.

Atmos. Chem. Phys., 23, 14871–14887, 2023
https://doi.org/10.5194/acp-23-14871-2023

Atmospheric Chemistry and Physics
Open Access
EGU

Long-term studies of the summer wind in the mesosphere and lower thermosphere at middle and high latitudes over Europe

Juliana Jaen[1], Toralf Renkwitz[1], Huixin Liu[2], Christoph Jacobi[3], Robin Wing[1], Aleš Kuchař[4], Masaki Tsutsumi[5], Njål Gulbrandsen[6], and Jorge L. Chau[1]

[1]Leibniz-Institute of Atmospheric Physics at the University of Rostock, Kühlungsborn, Germany
[2]Department of Earth and Planetary Science, Kyushu University, Fukuoka, Japan
[3]Institute for Meteorology, Leipzig University, Leipzig, Germany
[4]Institute for Meteorology and Climatology, University of Natural Resources and Life Sciences (BOKU), Vienna, Austria
[5]National Institute of Polar Research, Tokyo, Japan
[6]Tromsø Geophysical Observatory, UiT - The Arctic University of Norway, Tromsø, Norway

Correspondence: Juliana Jaen (jaen@iap-kborn.de) and Huixin Liu (liu.huixin.295@m.kyushu-u.ac.jp)

Received: 30 June 2023 – Discussion started: 11 July 2023
Revised: 5 October 2023 – Accepted: 18 October 2023 – Published: 1 December 2023

Abstract. Continuous wind measurements using partial-reflection radars and specular meteor radars have been carried out for nearly 2 decades (2004–2022) at middle and high latitudes over Germany (∼ 54° N) and northern Norway (∼ 69° N), respectively. They provide crucial data for understanding the long-term behavior of winds in the mesosphere and lower thermosphere. Our investigation focuses on the summer season, characterized by the low energy contribution from tides and relatively stable stratospheric conditions. This work presents the long-term behavior, variability, and trends of the maximum velocity of the summer eastward, westward, and southward winds. In addition, the geomagnetic influence on the summer zonal and meridional wind is explored at middle and high latitudes. The results show a mesospheric westward summer maximum located around 75 km with velocities of 35–54 m s^{-1}, while the lower-thermospheric eastward wind maximum is observed at ∼ 97 km with wind speeds of 25–40 m s^{-1}. A weaker southward wind peak is found around 86 km, ranging from 9 to 16 m s^{-1}. The findings indicate significant trends at middle latitudes in the westward summer maxima with increasing winds over the past decades, while the southward winds show a decreasing trend. On the other hand, only the eastward wind in July has a decreasing trend at high latitudes. Evidence of oscillations around 2–3, 4, and 6 years modulate the maximum velocity of the summer winds. In particular, a periodicity between 10.2 and 11.3 years found in the westward component is more significant at middle latitudes than at high latitudes, possibly due to solar radiation. Furthermore, stronger geomagnetic activity at high latitudes causes an increase in eastward wind velocity, whereas the opposite effect is observed in zonal jets at middle latitudes. The meridional component appears to be disturbed during high geomagnetic activity, with a notable decrease in the northward wind strength below approximately 80 km at both latitudes.

Published by Copernicus Publications on behalf of the European Geosciences Union.

1 Introduction

The Earth's atmosphere constitutes a complex and dynamic system. The mesosphere and lower thermosphere (MLT) spanning between 50 and 110 km is a region where the neutral and ionized atmosphere coexist. The ionization process due to the absorption of solar irradiance governs the thermosphere, whereas the neutral atmosphere is subjected to active winds and wave interactions, leading to chemical mixing and temperature regulation. The stratosphere, which is located below the mesosphere, is the region where ozone mainly absorbs the ultraviolet (UV) radiation from the Sun.

In the 1980s, the ozone hole was discovered, which led to the awareness of health problems due to UV radiation. In 1987, the Montreal Protocol was implemented to stop the emission of ozone-depleting substances, and studies show a positive shift in the trends of stratospheric ozone in 1995 at equatorial latitudes and in 2000 at high latitudes (e.g., Weber et al., 2022). Since then, researchers have been studying long-term compositions, temperatures, and dynamics to understand the behavior of the atmosphere and the human footprint on the environment. Greenhouse gases, including CH_4, H_2O, O_3, and CO_2, are studied as tracers to monitor the evolution of the atmosphere (Bremer and Berger, 2002; Bremer and Peters, 2008; Yue et al., 2015; Peters and Entzian, 2015; Qian et al., 2017; Peters et al., 2017; Karagodin-Doyennel et al., 2021, etc.). At an altitude of 96 km, atomic oxygen is formed through the photo-dissociation of O_2 and O_3 in the mesopause. The atomic oxygen then interacts with CO_2 through collisions, resulting in a radiative cooling effect that leads to hydrostatic contraction of the atmosphere (Gu et al., 2022; Akmaev, 2002; Li et al., 2021; Pisoft et al., 2021; Dawkins et al., 2023, etc.). As a consequence, carbon dioxide serves as a reliable indicator of cooling in the middle atmosphere, even during periods of disturbed geomagnetic activity (e.g., Liu et al., 2020).

The dynamics of the MLT are governed by the interaction of mean winds and waves, from large-scale planetary waves to small-scale gravity waves. The latter are driven by gravity and buoyancy in the atmosphere and are generated by orographic forcing, convection, wind shear, or wave interactions (Fritts and Alexander, 2003). Most gravity waves are generated in the troposphere and propagate upward and horizontally, breaking already in the troposphere and lower stratosphere. During winter, the zonal-mean zonal wind in the stratosphere and mesosphere is eastward and reverses in summer to be westward. The mean wind flow is crucial for the propagation of gravity waves. The linearized theory explains that gravity waves with an eastward velocity phase filtered by the westward wind reach the mesopause, where they break and deposit the momentum that decelerates the mean flow. This deceleration causes a wind reversal from westward to eastward in the summer lower thermosphere. As a consequence of the injection of energy from the breaking of the gravity waves and under the Coriolis force, a mean meridional circulation is induced from the summer hemisphere to the winter hemisphere, generating an upwelling in summer and a downwelling in winter. This circulation is the cause of the cold (warm) summer (winter) mesopause (Andrews et al., 1987; Holton and Alexander, 2000; Holton, 2004). In a nonlinear regime, the contribution of anisotropic gravity waves has been proven to deposit a significant amount of momentum to the mean flow at lower altitudes (Medvedev et al., 1998). Furthermore, regions characterized by intense wind jets exhibit significant anisotropy, particularly in the upper area of a strong wind jet (Warner et al., 2005; Gong et al., 2008), which is a characteristic of the summer MLT. Additionally, the MLT exhibits sensitivity to external phenomena such as the stratospheric quasi-biennial oscillation (QBO), which alters the direction of the zonal winds over a span of 26–28 months, and the equatorial ocean–atmospheric warming (and cooling) that occurs during the Northern Hemisphere's winter season. This phenomenon, referred to as the El Niño–Southern Oscillation (ENSO), has periods that are not precisely defined but generally span around 3 to 6 years (Baldwin et al., 2001; Jacobi and Kürschner, 2002; Wang and Picaut, 2004; Espy et al., 2011; Offermann et al., 2015; French et al., 2020; Jaen et al., 2022).

Sprenger and Schminder (1969) studied the wind at 95 km during winter at middle latitudes and identified changes in the wind due to solar activity. The eastward component would reach 30–40 $m\,s^{-1}$ during solar maximum but around 23 $m\,s^{-1}$ during low solar activity. On the other hand, the meridional component shifted from 0 to 15 $m\,s^{-1}$ in the southward direction during solar maximum and minimum, respectively. Later on, Bremer et al. (1997) identified weakly negative correlations with solar activity during most months (1964–1994) in the zonal component but with low significance, although the authors identified significant non-solar trends. Jacobi (1998) identified weaker eastward winds during solar maximum between 1972 and 1996. Portnyagin et al. (2006) studied the annual winds at middle latitudes between 1964 and 2004 and reported that zonal winds exhibited a decreasing trend, while meridional winds increased until 1980. However, after this time period, no significant trends were observed. The authors also identified different trends for the summer winds, specifically an increase in the summer zonal component in the 90s, as well as in the summer meridional component in the 70s, and concluded that these trends are non-uniform. Keuer et al. (2007) also found a correlation between solar activity and the MLT winds during summer, and the trend shows an increase in the zonal wind and a decrease in the meridional component during 1990–2005. Later on, Jacobi et al. (2015) reported an increase with weaker tendencies in the eastward winds, with a decrease in the southward component (1979–2014).

Hoffmann et al. (2010) compared 1 year of measurements from radars with the Kühlungsborn Mechanistic General Circulation Model (KMCM), showing the role of gravity wave drag in the summer MLT and the differences between middle

and high latitudes and the interaction with waves between 12 and 72 h. Later on, Hoffmann et al. (2011) studied the long-term behavior of the winds and gravity wave activity from kinetic energy over Germany and Norway and showed differences between the intensity of these two. Particularly, they found trends in the westward wind increasing around 75 km and a corresponding increase in gravity wave activity of 3–6 h above 80 km (1990–2010) at middle latitudes, while this was not the behavior observed at high latitudes by Hibbins et al. (2007). Offermann et al. (2011) also identified trends in the eastward wind due to an increase in gravity waves at 87 km with hydroxyl (OH) measurements.

Considering all the mentioned studies, the MLT exhibits varying trends over time, with distinct behavior during winter and summer due to differences in the seasonal wind dynamics inherent to the wind field properties. Additionally, many studies have focused solely on wind velocities at fixed altitudes. However, as mentioned before, research suggests that the MLT height has been decreasing over the past decades (e.g., Peters et al., 2017; Vincent et al., 2019; Yuan et al., 2019; Dawkins et al., 2023). In light of this, the present study examines the maximum velocity of the horizontal winds independent of their altitude, their variability, and their trends over 19 years at high and middle latitudes over Europe during summer. In addition, the mesospheric time series at middle latitudes is extended to 33 years. Therefore, an introduction to the radar system and analysis methods implemented to extract the time series and analyze the trends is in Sect. 2. Section 3 describes the results obtained, while Sects. 4 and 5 provide the discussion and concluding remarks, respectively.

2 Instruments and methods

2.1 Radar observations

The observational data used in this work are entirely from two types of radars: partial-reflection radars (PRRs, also called MF radars) and specular meteor radars (SMRs). The PRR typically covers between 60 and 90 km altitude. Saura (69.14° N, 16.02° E) is located on Andøya, Norway, and has been in operation since 2004. This particular system operates with a peak power of 116 kW at a frequency of 3.17 MHz, having a Mills cross array that is composed of 29 crossed half-wave dipoles and thus offers a narrow beam for measurements (more information in Singer et al., 2005; Renkwitz and Latteck, 2017). A slightly smaller system which also has a Mills cross shape is located in Juliusruh (54.63° N 13.37° E), Germany, having an altitude coverage between 60 and 90 km. It has only 13 antennas and operates at a frequency of 3.18 MHz with a peak power of 64 kW. Starting as a frequency-modulated continuous wave radar in 1990, it was modernized into a modular pulsed system (more details on the Juliusruh PRR systems can be found in Keuer et al., 2007; Singer et al., 1992).

The SMRs use the plasma trails left by meteors disintegrating in the atmosphere to retrieve the MLT winds by measuring their position and Doppler shift (e.g., Hocking et al., 2001). These systems are capable of measuring winds between 70 and 110 km (depending on the number of meteor detections). Particularly for this work, we have combined detections from two closely located SMRs. This combination allows us to estimate the MLT mean winds, reducing data gaps and improving the precision and continuity of the time series. The latter is especially useful for long-term studies (e.g., Jaen et al., 2022).

At high latitudes, the Andenes SMR (69.27° N, 16.04° E) and Tromsø SMR (69.58° N, 19.22° E) are combined for measurements between 2004 and 2022, with a 4 km–4 h resolution to derive winds from 70 up to 110 km. In the case of middle latitudes, winds with 1 km–1 h resolution have been obtained by combining meteor detections from Collm SMR (51.3° N, 13.0° E) and Juliusruh SMR (54.63° N, 13.37° E), both operating in a pulsed mode. Note that both Andenes and Juliusruh SMR systems were upgraded in 2021 to operate in a coded continuous wave (CW) and multiple-input–multiple-output mode (e.g., Huyghebaert et al., 2022; Poblet et al., 2023, for details of the upgrades in Andenes and Juliusruh). In this work, measurements from only one receiving station located close to each coded-CW transmitter are used.

The SMR systems cover a volume spanning from a 250 km radius around a single system to 500 km or more, depending on the number of systems in the network. The winds used in the study are representative of the entire volume covered by the systems. While the SMR winds measure a larger volume than the PRR winds, the mean zonal wind is not affected by this difference in volume. However, the meridional wind presents a relatively larger latitudinal and longitudinal dependence, and these differences are more important. It has been studied and debated that PRRs underestimate the wind velocity above 80 km (Hall et al., 2005; Reid et al., 2018; Nozawa et al., 2002; Jacobi et al., 2009). Particularly for Saura PRR, the winds are corrected based on the angle of arrival statistics and compared to mesospheric very high frequency (VHF) wind measurements (Renkwitz et al., 2018).

2.2 Data analysis

In this study, most of the measurements have a length of 19 years (2004–2022), except for Juliusruh PRR with 33 years (1990–2022) at middle latitudes, from which we studied the mesospheric westward jet. To study the long-term behavior of the summer winds and their variability, we focus on the maximum median velocity per month as a proxy of the MLT dynamics. The different altitude ranges in the zonal and meridional data used for the climatologies aim to capture the maximum wind velocity. The zonal component is built with the combination of two datasets from different instruments, while the meridional component is only from SMRs since it captures the maximum wind velocity during summer. To

obtain the time series, we calculated monthly median values and extracted the maximum velocity between a range of altitudes corresponding to the peak and latitude (i.e., westward jet: 65–96 km, southward wind: 75–95 km, and eastward jet: 80–106 km). With the maximum wind velocity per month v, we implemented a linear function to fit by least squares, $v = m \cdot \mathrm{yr} + b$, where m is the slope, yr is the year, and b is the v intercept. To test the slope of the linear fit, we implemented Student's t test to reject the null hypothesis ($H_o : m = 0$) and calculated the confidence interval with 95 % confidence for the slope.

In order to study the variability of the time series, we implemented a generalized Lomb–Scargle (LS) periodogram analysis, with the difference between the 75 % and 25 % quartiles (third minus first) being an indication of the variability (since this is bigger than the measurements uncertainties), taken as the signal error (Czesla et al., 2019). The periodograms give the periods in years and the normalized power provided by PyAstronomy (Zechmeister and Kürster, 2009). With this implementation, it is possible to obtain the false-alarm probability (FAP) that responds to the question of what the probability is that a signal with no periodic component would lead to a peak of this magnitude over the highest peak, but it does not give information on the remaining peaks (VanderPlas, 2018). Even though the data are evenly spaced, one of the time series has a missing year (2000 in the Juliusruh PRR), which presents a complication in implementing the classical Fourier transform. In addition, Mossad et al. (2023) compared the Fourier transform to LS and found that LS is slightly more accurate for estimating the amplitude of a single frequency in the presence of minor gaps. The only disadvantage is the computation time, which, in this study, is not of importance given the number of data points.

It is widely known that there are many indices to categorize the atmosphere's external or internal forcing. In this case, we use the daily Ap index calculated from a network of magnetic observatories around the world. The Ap index varies between 0 and 400 and is the product of a conversion of the daily average of the 3 h mean Kp index (Matzka et al., 2021). Following the study at middle latitudes by Jacobi et al. (2021), we extend the work to 33 years below 82 km at middle latitudes and to high latitudes with the 19-year time series and investigate the response to disturbed and undisturbed geomagnetic conditions during summer. We divided the days of the years with low geomagnetic activity, $\mathrm{Ap} \leq 5$, and high geomagnetic activity, $\mathrm{Ap} \geq 20$, for middle latitudes and $\mathrm{Ap} \geq 15$ for high latitudes. The reason for the distinction comes from the nature of the behavior of the geomagnetic field with the change in latitudes. Juliusruh is located at 52° N geomagnetic latitude, while Andenes is located at 67° N. Renkwitz and Latteck (2017) showed that the majority of the particle precipitation events already occur at $\mathrm{Kp} = 3$ ($\mathrm{Ap} \geq 15$), which allows us to have a more robust time series considering the low geomagnetic activity in the last 19 years. In the case of middle latitudes, we use the limits already established by Jacobi et al. (2021). The time period used for the summer mean is 2004–2022, except for the zonal vertical profile (below 82 km) and the meridional profile (below 80 km) at middle latitudes, where the time period used is 1990–2022. Considering this selection, the total number of days between 2004 and 2022 is 888, 171, and 115 for $\mathrm{Ap} \leq 5$, $\mathrm{Ap} \geq 15$, and $\mathrm{Ap} \geq 20$, respectively. In the case of 1990–2022, it is 1228 ($\mathrm{Ap} \leq 5$) and 355 d ($\mathrm{Ap} \geq 20$)

The summer mean vertical wind profile is determined by utilizing the time series from the selected Ap index. The difference between high and low geomagnetic activity in the summer winds is computed, and then a Behrens–Fisher Student's t test is calculated since the variance hypothesis is not satisfied (i.e., the variances of the samples are not assumed to be equal), and a combined degree of freedom is calculated for this objective (Robinson, 1976).

3 Results

3.1 Seasonal variations of winds

Figure 1a and b depict the climatologies of the mean zonal winds between 60 and 110 km at middle and high latitudes, respectively. The climatologies are the mean of all the years (2004–2021) after a 16 d smoothing window shifted by 1 d. The horizontal lines at 79.5 km at middle latitudes and at 85.5 km at high latitudes indicate the transition between the SMR and PRR measurements. Colors represent wind direction and intensity, while contour lines indicate wind velocity levels. Between January and March, the mean winds remain eastward until the springtime when the wind reversal occurs and the summertime begins (Jaen et al., 2022). During the summer months, the vertical wind profile (60–100 km) depicts the formation of the summer wind jets, with an increase in the wind velocity in May and reaching the maximum velocities between June and August (see Fig. 1a and b in blue). As a result of the eastward wind in the lower thermosphere and the westward wind in the mesosphere, a strong wind shear around 83–86 km at middle latitudes (87–90 km at high latitudes) is located at the mesopause. The intensity of the wind jets differs quantitatively: at middle latitudes, they are stronger than at high latitudes due to the mesospheric wind circulation. Below the zonal wind shear height and between 72 and 76 km (75 and 78 km), the westward wind velocity maxima reach a mean of approximately 54 $\mathrm{m\,s^{-1}}$ (45 $\mathrm{m\,s^{-1}}$). Above the strong wind shear and in the range of 93–98 km (97–100 km), the eastward jet mean is approximately 40 $\mathrm{m\,s^{-1}}$ (32 $\mathrm{m\,s^{-1}}$). As August progresses, the maximum velocity of the wind reduces, and by the end of the summer (middle of September), the wind reversal occurs below 85 km (88 km), leaving eastward wind during the winter in the MLT (Jaen et al., 2022).

In terms of the meridional wind climatologies, Fig. 1c and d were obtained similarly to the zonal component, with the difference of using only the SMRs since the maximum

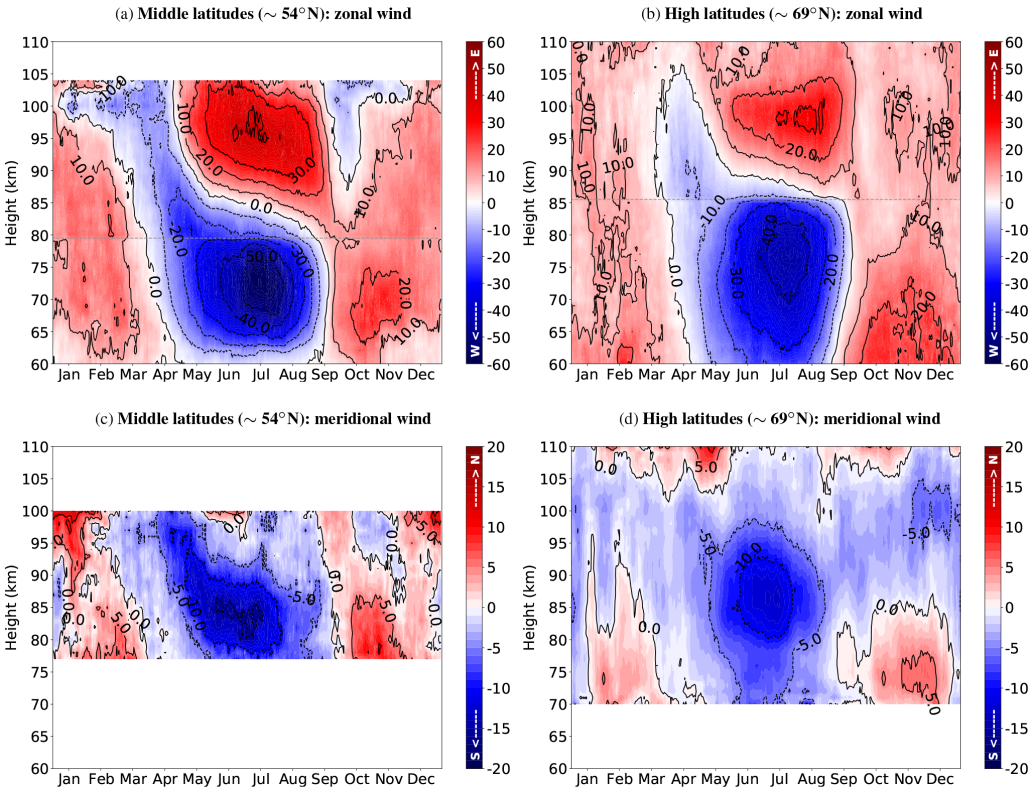

Figure 1. Horizontal wind height–time cross-section of the annual variation at middle **(a, c)** and high **(b, d)** latitudes. The upper row depicts the zonal **(a, b)** component with eastward (red) and westward (blue) wind velocity ($m\,s^{-1}$) by means of the color bar and the contour lines. The horizontal gray lines mark the change in the instrument. Similarly, the bottom row depicts the meridional component **(c, d)** with the northward (red) and southward (blue) wind velocity. Note that the meridional wind climatologies are only from SMR.

summer wind altitude range is well captured by these radars. The meridional wind is less intense than the zonal wind. The velocity is quite variable in the observed range of 75–100 km. The velocity during the winter remains in the range of −5 to 5 $m\,s^{-1}$. The time period between June and July depicts the strongest southward wind throughout the year and is located between 82 and 86 km at middle latitudes (85–89 km at high latitudes), with a median of 16 $m\,s^{-1}$ (13 $m\,s^{-1}$).

3.2 Trend in the horizontal winds

Figure 2 shows the time series peak velocity of the wind. Figure 2a and b are the eastward lower-thermospheric jets per year for June, July, and August (blue stars, red dots, and green triangles) at middle and high latitudes, respectively. For each time series, the shaded area represents the interval between the first and the third quartiles (25th and 75th empirical quartiles), and the linear fit is displayed in the corresponding color. Through the implementation of Student's t test and rejecting the null hypothesis (i.e., null slope, as discussed in Sect. 2.2), we obtain a statistical p value. The color lines are the possible trends where m is the slope, wherein a dashed colored line indicates a significance level exceeding 95 %. Conversely, a dotted line suggests that Student's t test did not reject the null hypothesis, implying that the slope could potentially be zero and thus that no significant trend exists. As a summary, the median height, the median velocity of the wind maxima, the slopes, and the 95 % confidence interval for the individual fit are listed in Table 1. In addition, the slopes with more than 95 % significance are highlighted in bold.

The eastward jets at middle latitudes (Fig. 2a) show no significant trends. However, at high latitudes, July depicts a significant trend with more than 98 % (see Fig. 2b), indicating weaker eastward winds over the years. In the case of the mesospheric westward jet at high latitudes, Student's t test does not reject the null-slope hypothesis, but the westward jet at middle latitudes depicts significant trends with more than 99.9 % for all the months, indicating a tendency for stronger westward winds since 1990 (Fig. 2c).

Figure 2e and f depict the southward winds at middle and high latitudes, respectively. In both cases, the jets are stronger during June and July than during August. While the southward maximum wind velocity remains approximately constant at high latitudes, at middle latitudes a significant trend (more than 95 % confidence) is visible, indicating a weakening of the meridional wind component over the years.

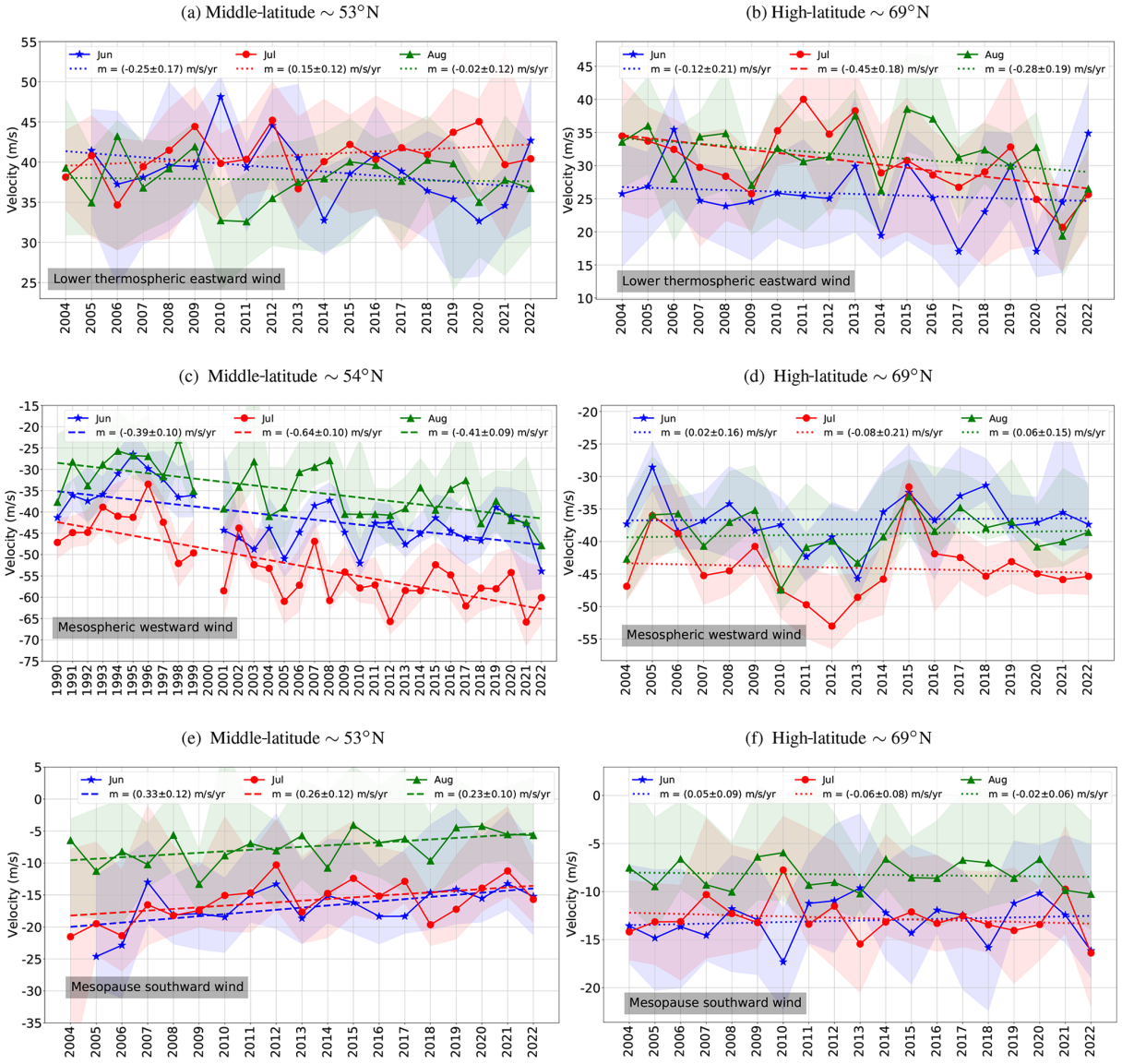

Figure 2. Middle-latitude **(a, c, e)** and high-latitude **(b, d, f)** zonal and meridional wind maxima for every year. The eastward **(a, b)**, westward **(c, d)**, and southward **(e, f)** velocity maxima. Each wind component has the yearly velocity maxima obtained with a monthly median and their respective quartile difference (i.e., 75th and 25th quartiles). June (blue stars), July (red dots), and August (green triangles) with the linear fit where m represents the slope. The dashed lines depict the trends with 95 % significance.

The altitude of the wind maxima fluctuates from year to year while consistently maintaining its mean height (see Table 1) without any significant trends between 2004 and 2022.

3.3 Interannual variability of winds

The time series in Fig. 2 reveals year-to-year variability, which motivated us to investigate the interannual variability of the time series through periodogram analyses. Figure 3 depicts the Lomb–Scargle periodograms of winds for each summer month. The upper row corresponds to middle latitudes, while the bottom row refers to high latitudes. The columns from left to right represent the lower-thermospheric eastward, mesospheric westward, and mesopause southward winds, respectively

Table 2 summarizes the corresponding periods. At high latitudes, the eastward wind exhibits significant (over 90 % confidence level) periodicities of 2–3 years in June and August and of 12 years in July. At middle latitudes, significant periodicities are seen in the eastward wind around 6 years in June, in the westward wind around 10–11 years in June and August, and 2–4 years in the southward wind in July and August.

Table 1. Summary of the wind maxima characteristics with the respective latitude, the range of years, median height, median velocity, monthly slope with standard deviation, and the 95 % confidence interval. Highlighted in bold are the significant trends with more than 95 % confidence.

Wind proxy	Latitude (° N), years	Month	Height (km)	Velocity ($m\,s^{-1}$)	Slope ($m\,s^{-1}\,yr^{-1}$)	95 % confidence interval
Eastward	High (69)	June	99 ± 2	25 ± 2	-0.12 ± 0.21	$(-0.54, 0.30)$
	2004–2022	July	98 ± 2	30 ± 3	$\mathbf{-0.45 \pm 0.18}$	$(-0.81, -0.09)$
		August	99 ± 2	32 ± 3	-0.28 ± 0.19	$(-0.68, 0.11)$
	Middle (53)	June	97 ± 1	39 ± 2	-0.25 ± 0.17	$(-0.66, 0.16)$
	2004–2022	July	95 ± 1	40 ± 1	0.15 ± 0.12	$(-0.27, 0.56)$
		August	94 ± 1	38 ± 2	-0.02 ± 0.12	$(-0.45, 0.40)$
Westward	High (69)	June	76 ± 2	-37 ± 2	0.02 ± 0.16	$(-0.40, 0.44)$
	2004–2022	July	77 ± 1	-45 ± 2	-0.08 ± 0.21	$(-0.50, 0.34)$
		August	77 ± 3	-39 ± 2	0.06 ± 0.15	$(-0.36, 0.48)$
	Middle (54)	June	74 ± 1	-43 ± 4	$\mathbf{-0.39 \pm 0.10}$	$(-0.64, -0.14)$
	1990–2022	July	74 ± 2	-54 ± 6	$\mathbf{-0.64 \pm 0.10}$	$(-0.84, -0.44)$
		August	74 ± 1	-35 ± 6	$\mathbf{-0.41 \pm 0.09}$	$(-0.64, -0.17)$
Southward	High (69)	June	88 ± 2	-12 ± 2	0.05 ± 0.09	$(-0.36, 0.47)$
	2004–2022	July	87 ± 2	-13 ± 1	-0.06 ± 0.08	$(-0.48, 0.35)$
		August	86 ± 2	-9 ± 1	-0.02 ± 0.06	$(-0.44, 0.40)$
	Middle (53)	June	84 ± 2	-16 ± 2	$\mathbf{0.33 \pm 0.12}$	$(-0.03, 0.70)$
	2004–2022	July	82 ± 1	-16 ± 2	$\mathbf{0.26 \pm 0.12}$	$(-0.13, 0.65)$
		August	85 ± 1	-7 ± 2	$\mathbf{0.23 \pm 0.10}$	$(-0.13, 0.60)$

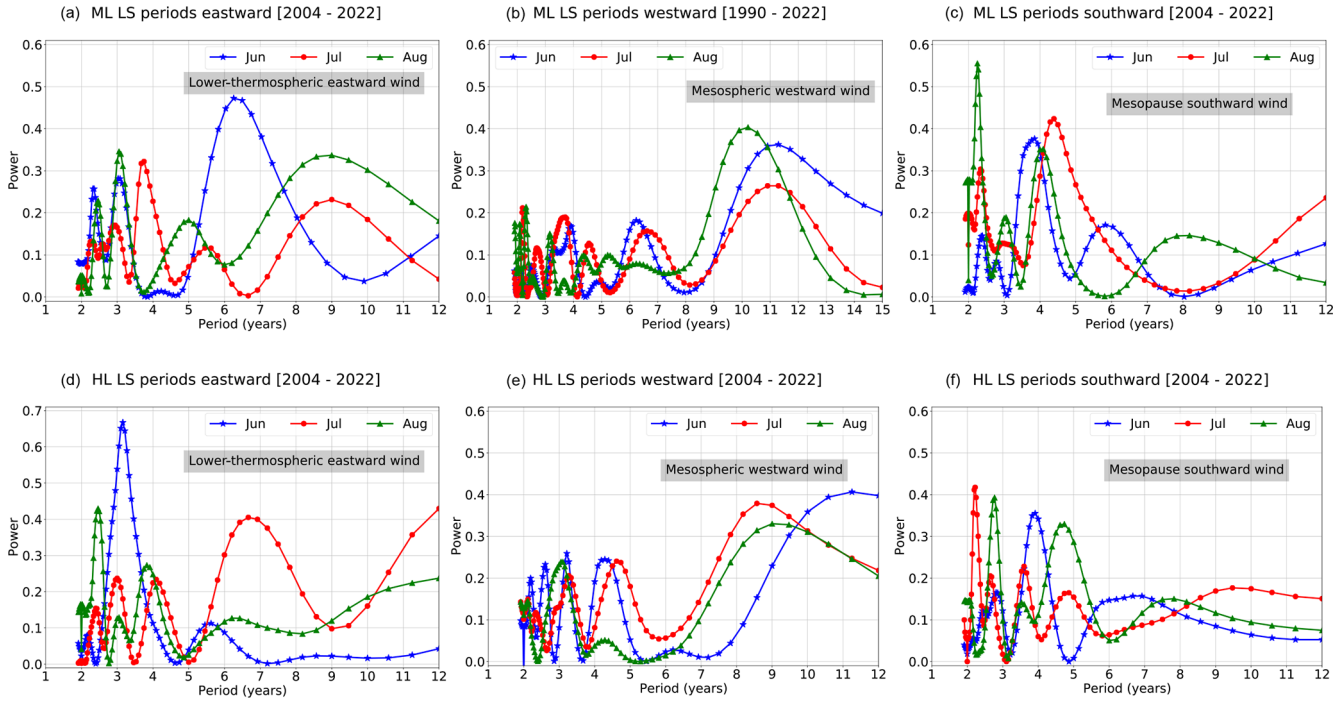

Figure 3. Middle-latitude **(a, b, c)** and high-latitude **(d, e, f)** periodograms calculated with Lomb–Scargle. The left column represents the periodograms from the time series of the eastward maxima **(a, d)**, the middle are the westward maxima **(b, e)**, and the right column is the southward wind maxima **(c, f).**

Table 2. Summary of the periods obtained from LS analysis of monthly time series. The periods in bold are the ones that passed the false-alarm probability of 90 %, and the ones with a star are the ones that passed the false-alarm probability of 95 %.

		Periods (years)		
Latitude (° N)	Wind (mean height)	June	July	August
High (∼ 69)	Eastward (99 km)	**3.2***	6.7, **12.0**	**2.5**, 3.8
	Westward (76 km)	4.3, 11.3	3.3, 4.6, 8.6	3.1, 9.0
	Southward (87 km)	3.9	2.2, 3.6	2.8, 4.7
Middle (∼ 54)	Eastward (95 km)	2.3, 3.1, **6.3**	3.8, 9.0	2.5, 3.1, 9.0
	Westward (74 km)	**11.3***	11.3	**10.2***
	Southward (84 km)	3.8	2.3, **4.4**	**2.3***, 4.1

3.4 Wind response to geomagnetic activity

Figure 4 shows the summer wind at high latitudes under quiet and disturbed geomagnetic conditions over the years. Figure 4a and b depict the yearly median summer zonal wind at low ($Ap \leq 5$) and high ($Ap \geq 15$) geomagnetic activity, respectively. On a simple visual examination, an enhancement in the eastward jet (red) under high geomagnetic activity is evident, while the westward jet (blue) remains in the same velocity range. The meridional component under disturbed geomagnetic conditions (Fig. 4d) displays a more variable velocity than at low geomagnetic activity (Fig. 4c). Note that, for high geomagnetic activity (Fig. 4b and d), the year 2020 depicts significant differences compared to the rest of the years due to the reduced number of days (2) with $Ap \geq 15$.

In order to quantify the possible differences, a summer mean with its standard deviation is calculated. The altitude velocity profiles for the summer mean at high latitudes are shown in Fig. 5 with low (green) and high (purple) geomagnetic activity for the zonal component (Fig. 5a) and the meridional component (Fig. 5b). They show stronger eastward winds under high geomagnetic activity above 92 km, while the rest of the profile does not exhibit a distinct difference between high and low geomagnetic activity.

In the case of the meridional component (Fig. 5b), considerable differences appear below 85 km, with a stronger northward wind under quiet geomagnetic conditions. Figure 5c shows the difference between low and high geomagnetic activity for the zonal (red) and meridional (blue) summer wind components. Significant mean differences beyond 95 % according to the Behrens–Fisher test are denoted by stars, while circles indicate differences where the hypothesis of equal means was not rejected by the test. The summer eastward wind is significantly affected by geomagnetic activity, with 2–6 $m\,s^{-1}$ stronger eastward wind velocities above 94 km and 1–3.5 $m\,s^{-1}$ weaker northward winds below 83 km for strong geomagnetic activity.

A similar analysis is done for mid-latitudes, with the results shown in Fig. 6. Note that the zonal wind between 70 and 82 km and the meridional wind at 70–80 km are obtained between 1990 and 2022, while the winds above are obtained from 2004–2022 due to the use of different systems (see Sect. 2). The selection of the different range of altitudes or systems over the wind components is to avoid the instrument shift over the wind maxima, which is the focus of our study.

Table 3. Wind maxima slopes obtained with the linear fit with days of low geomagnetic activity. Highlighted in bold are the significant trends with more than 95 % confidence.

Latitude	Wind proxy	Slope ($m\,s^{-1}\,y^{-1}$)
∼ 69° N	July eastward (99 km)	$\mathbf{-0.44 \pm 0.15}$
∼ 53° N	Summer westward (74 km)	$\mathbf{-0.41 \pm 0.08}$

As shown in Fig. 6c, higher geomagnetic activity has a significant impact on the middle-latitude zonal wind, decelerating both the eastward jet (by up to $-10\,m\,s^{-1}$) above 95 km altitude and the westward jet below 80 km (by up to $8\,m\,s^{-1}$). Its impact on the meridional wind is mainly seen below 78 km altitude, decelerating the northward wind by up to $-3\,m\,s^{-1}$. Note that there are differences between the meridional winds from Figs. 1d and 4c, d, which are a consequence of different instruments (see Sect. 2.1). Table 3 contains the trends calculated for July eastward and the summer westward maximum at high and middle latitudes, respectively, with only the days of low geomagnetic activity to compare with the significant trends in the zonal wind.

4 Discussion

In this work, we have explored the long-term variability of MLT summer wind using the maximum wind velocity as a proxy. The resulting time series were fitted with linear functions, and the slopes were tested in search of significant trends. In addition, we calculated the periodograms of the time series and explored the response of the wind under disturbed and non-disturbed geomagnetic conditions at high and middle latitudes.

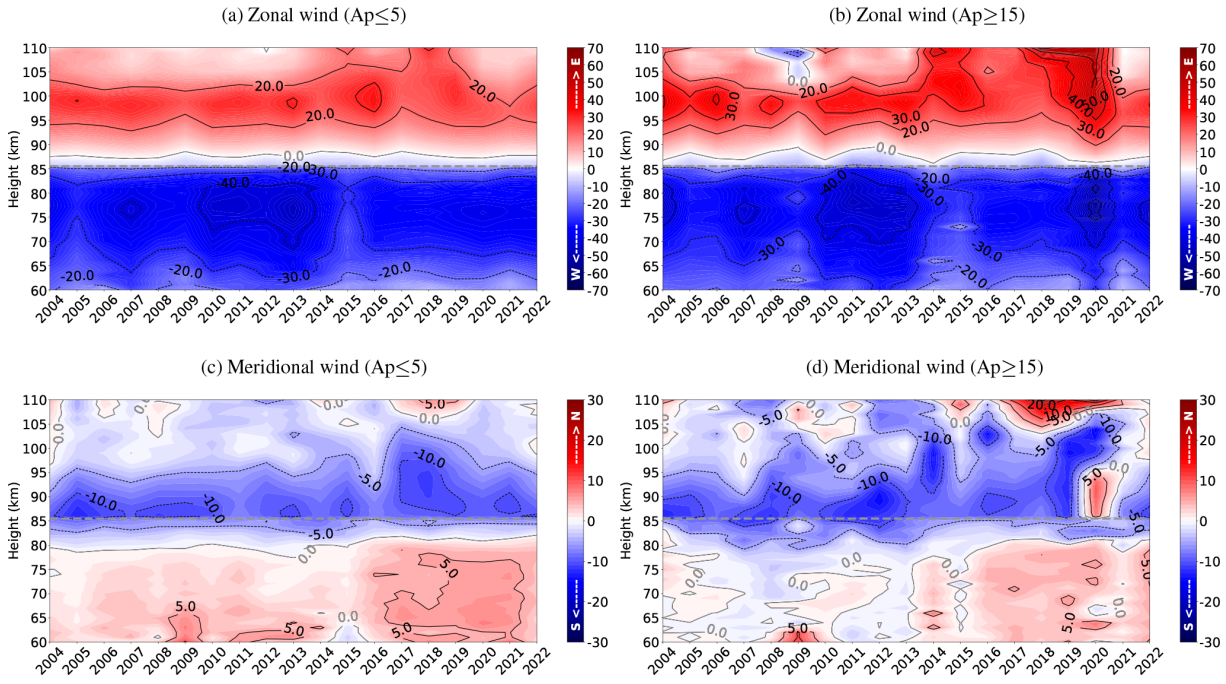

Figure 4. Summer zonal winds at high latitudes over the years with low **(a)** and high **(b)** geomagnetic activity. In the same way, the bottom row depicts the summer meridional mean winds with low **(c)** and high **(d)** geomagnetic activity; this is also the case for high latitudes.

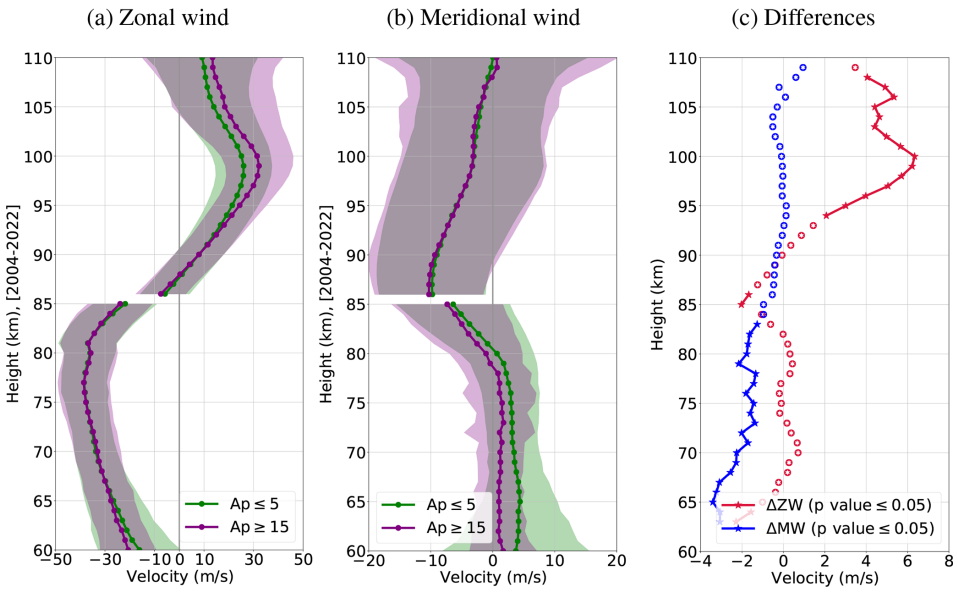

Figure 5. Mean velocity profiles at high latitudes for low (green, Ap ≤ 5) and high (purple, Ap ≥ 15) geomagnetic activity for the summer zonal **(a)** and meridional **(b)** winds. The difference between both profiles under high and low geomagnetic activity **(c)** for the zonal (red) and the meridional (blue) wind component. The stars depict the values with more than 95 % significance, tested with the Behrens–Fisher test, and the circles the values with no significant difference between the means.

4.1 Seasonal wind variations and trends

The wind climatologies are in agreement with previous studies at similar latitudes, considering the differences in height and investigated time lengths (Wilhelm et al., 2019; Hoffmann et al., 2010; Jaen et al., 2022; Schminder et al., 1997; Manson et al., 2004, etc.). However, a comparison with models shows that, in the summer season, WACCM-X(SD) and UA-ICON exhibit a good agreement with radars, while winter is better represented by GAIA (Ground-to-topside model

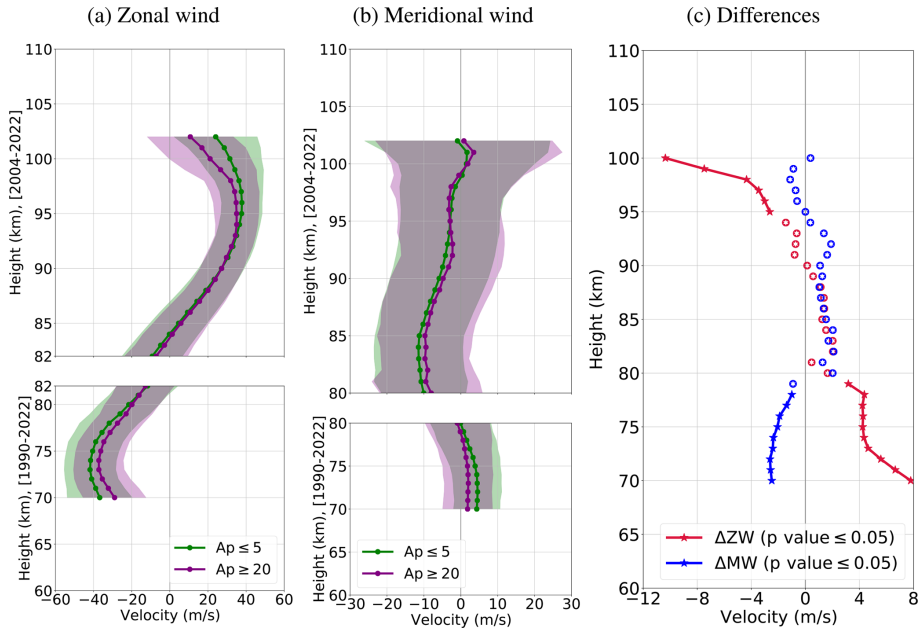

Figure 6. Mean velocity profiles at middle latitudes for low (green, Ap $\leq$ 5) and high (purple, Ap $\geq$ 20) geomagnetic activity for the summer zonal **(a)** and meridional **(b)** winds. In the range of 70–82 (80) km, the zonal (meridional) components are calculated for the years 1990–2022. Above these heights, the analyzed years are 2004–2022. **(c)** The difference between both profiles under high and low geomagnetic activity for the zonal (red) and the meridional (blue) wind components. The stars depict the values with more than 95 % significance, tested with the Behrens–Fisher test, and the circles are the values with no significant difference between the means.

of Atmosphere and Ionosphere for Aeronomy; Stober et al., 2021). Zhou et al. (2022) compared a network of meteor radars located at different latitudes (from middle to low latitudes) with WACCM-X(SD), finding similar results.

The wind trends observed in July for the lower-thermospheric eastward maxima at high latitudes and the southward maxima at middle latitudes are consistent with the study done by Wilhelm et al. (2019). In their work, the authors studied the trends at high latitudes and middle latitudes from 2002 to 2018 with specular meteor radars, and with this limitation, the westward wind maxima are not captured in their study, although a significant westward wind trend is visible below 85 km during the summer months. Hall and Tsutsumi (2013) made a similar study comparing two SMRs at latitudes of 70 and 78° N between 2001 and 2012. The authors identified a strengthening of the summer westward jet, contradicting our results. However, considering the time period during which their results overlap with those of our study (i.e., 2004–2012), it is visible in Fig. 2d that a possible significant trend could be found. On the other hand, Jacobi et al. (2023) analyzed 43 years of the winds near 90 and 81–85 km over Collm and Juliusruh, respectively, obtaining significant trends at Juliusruh for the summer-month eastward wind that do not agree with our findings. The differences can be attributed to the varying heights that were studied, which do not capture the proxies from this study. Hoffmann et al. (2011) studied the trends in the zonal wind for July at middle latitudes and found significant trends at 72 and 76 km, where the lower and upper limits of the westward jet are located. These trends showed stronger westward winds of 1.1 and 0.643 m s^{-1} yr^{-1}, respectively, over the period of 1990–2010. Vincent et al. (2019) studied the trends in the meridional wind over the Antarctic ($\sim$ 69° S) between 1994 and 2018 during the austral summer. While the study shows a descent in the height of the maximum wind velocity by 1.5 km, the strengths of the wind maxima did not change, which agrees with our findings in the Northern Hemisphere.

It is essential to highlight that, while the zonal wind shows a good representation of the global zonal wind behavior, the meridional component has a higher dependence on the region where it is observed, as a consequence of the gravity wave input at the mesopause (e.g., Jacobi et al., 2001). This could also explain the variations in trends across different latitudes and longitudes, as well as the limitations of global models, which often rely on parameterizations. Moreover, different lengths of the time series, their locations, and their parameters may show different trends due to the complex dynamics. Laštovička and Jelínek (2019) listed the main difficulties when studying trends.

4.2 Interannual oscillations

From the periodograms, several periods are identified (Fig. 3). Those periods of around 2–3 years could be associated with modulations from the stratospheric QBO, also called mesospheric QBO (MQBO). Espy et al. (2011)

showed QBO modulation on the summer mesospheric OH temperatures at 60° N. The mesopause southward winds are a result of the eastward-phase gravity waves that reach the mesopause where they break and deposit momentum. Coupled with the Coriolis force, the meridional component of these winds drives the summer-to-winter pole circulation (e.g., Andrews et al., 1987; Holton, 2004). These gravity waves are previously filtered by the stratospheric flow, which is predominantly influenced by QBO (e.g., Baldwin et al., 2001; Lindzen and Holton, 1968). As such, these filtered gravity waves may be the underlying cause of the observed wind oscillations in the mesopause.

The periods between 3 and 4 years have been associated with modulation from ENSO. Reid et al. (2014) obtained oscillations of 3–4 years in OH and O (1 s) airglow at 96 and 87 km at 35° S. Perminov et al. (2018) obtained similar oscillations in OH temperatures at 56° N (2000–2016). García-Herrera et al. (2006) found a lag of a few months between ENSO and the temperature response in the stratosphere at high latitudes. Considering that ENSO's main phase occurs in December and the fact that it is an ocean–atmospheric event at equatorial latitudes, a signal's attenuation with time and space would be expected. While these findings are a result of mesospheric temperature observations, they are intrinsically linked to the mesospheric dynamics as expressed in the thermal-wind equation. Jacobi and Kürschner (2002) identified a possible signature of ENSO with Collm zonal winds in the 1980s and 1990s, and later on, Jacobi et al. (2017) found that this signal changes between the mesosphere and lower thermosphere. However, having common periodicity does not necessarily mean causality, and dedicated work needs to be done to connect these oscillations to QBO and ENSO phenomena.

4.3 Solar cycle dependence

The summer wind also shows a significant periodicity around 6 and 10–12 years, which could be a signature of the solar cycle and its harmonic (see Table 2). Previous works have shown connections between the solar cycle and the winds (e.g., Jacobi and Kürschner, 2006), while other authors have shown that these signatures have disappeared in past solar cycles (Portnyagin et al., 2006; Fiedler et al., 2011; DeLand and Thomas, 2015). For our data, a simple Pearson correlation between the Lyman α and the June westward wind maximum at middle latitudes gives $\rho = -0.11$, with a p value of 0.56, which indicates a non-significant anti-correlation. When considering the periods of 1990–2004 and 2004–2022 separately, we find two different correlations of $\rho = -0.69$ (p value $= 0.01$) and $\rho = -0.17$ (p value $=$ 0.51), respectively. The first one shows a significant ($\geq 95\,\%$) anti-correlation between the westward wind maximum and Lyman α during the time length of 1990 to 2004, while the latter is not significant. Recently, Vellalassery et al. (2023) showed how the attenuation of the solar cycle response with Lyman α is correlated with the increase in water vapor in the mesosphere at polar latitudes.

4.4 Impact of geomagnetic activity on trends

Our results reveal an impact of geomagnetic activity on MLT winds in summer (Figs. 5 and 6), with higher geomagnetic activity weakening the winds at both middle and high latitudes, except for the eastward wind at high latitudes, which strengthens under disturbed conditions. The results at middle latitudes agree with those of Jacobi et al. (2021), who found weaker winds at a higher geomagnetic activity at two mid-latitude stations, Collm and Kazan, during the summers of 2016–2020.

Li et al. (2023, 2019) studied the response of the MLT during a geomagnetic storm with the thermosphere–ionosphere–mesosphere–electrodynamic general circulation model (TIMEGCM) at high and middle latitudes, respectively. While the effects of Joule heating penetrate up to ∼95 km at 70° N, the temperature contribution is minor compared to vertical heat advection and the adiabatic processes. Above 100 km, the Joule heating becomes significant and comparable to the other two processes. In the MLT, the major heating contributions are due to adiabatic heating and cooling and vertical heat advection associated with vertical winds. During a storm, the temperature increases and decreases with the vertical wind advection, and the horizontal advection also contributes to the total heating rate (Li et al., 2023). The meridional winds showed a shift in the direction, from southward to northward, similarly to the decrease in the winds observed below 79 km (Figs. 5b and 6b). These changes are a consequence of the temperature changes leading to downward or upward vertical winds which, together with the Coriolis force, produce a change in the pressure gradient (Li et al., 2019). However, Sun et al. (2022) compared the simulation with TIMEGCM and SABER (Sounding of the Atmosphere using Broadband Emission Radiometry) and found that the storm effects penetrate down to ∼ 80 km, and the model agrees with the observation but overestimates the temperature increase and underestimates the temperature decrease at high and middle latitudes.

The geomagnetic activity could significantly affect long-term trend studies, as demonstrated by Liu et al. (2021). Given the significant geomagnetic activity effect on the mesospheric wind, the long-term variation of the geomagnetic activity could potentially contribute to the wind trend we obtained in Fig. 2. The histogram in Fig. 7 shows the count of days from 1990 to 2022 with $\mathrm{Ap} \leq 5$ (green) and $\mathrm{Ap} \geq 20$ (purple). The right axis shows the scaled Lyman α (red line) to illustrate the solar activity over the investigated time period.

Comparatively, the first half of the time series has more days with high geomagnetic activity than the second half. This could imply that the negative trend in the westward jet can partially be due to more quiet days in the recent

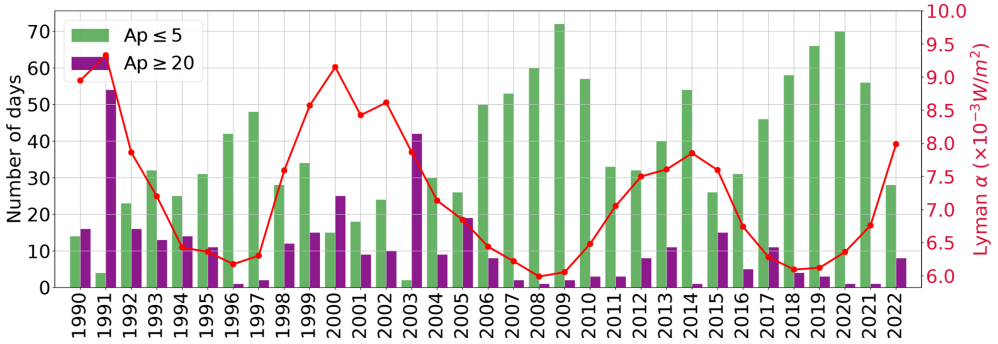

Figure 7. Histogram with the counts of days for Ap ≤ 5 (green) and Ap ≥ 20 (purple). On the right axis is the Lyman α (red) scale with yearly summer mean values.

2 decades. To test this, we calculated the summer mean (June–August averaged) maximum velocity from the yearly summer winds under only quiet conditions. At high latitudes, the eastward jet shows a significant summer trend of $-0.23 \pm 0.13\,\mathrm{m\,s^{-1}\,yr^{-1}}$ and a July eastward trend of $-0.44 \pm 0.08\,\mathrm{m\,s^{-1}\,yr^{-1}}$, in agreement with the complete time series (see Table 1). At middle latitudes, the westward jet also shows a significant trend of $-0.41 \pm 0.08\,\mathrm{m\,s^{-1}\,yr^{-1}}$, which is similar to the summer mean with the complete time series ($-0.49 \pm 0.13\,\mathrm{m\,s^{-1}\,yr^{-1}}$). This result suggests that the winds are getting stronger due to different causes.

As to the cause of the long-term trends in the winds observed here, it could be related to changes in various atmospheric waves, such as planetary waves, tides, and gravity waves, as discussed by Laštovička et al. (2012). However, during summer, the contribution of tides is filtered at lower altitudes in the stratosphere, leaving less of a contribution in the mesosphere (Conte et al., 2017; Wilhelm et al., 2019; Pedatella et al., 2021). Ern et al. (2011) and Alexandre et al. (2021) found evidence of the fact that gravity waves generated in the lower latitudes of the summer hemisphere contribute to the momentum budget of the mesospheric jet in the middle and high latitudes. Hoffmann et al. (2011) found a significant trend of increasing gravity waves above 80 km. Liu et al. (2017) studied the gravity wave potential energy derived from satellite-observed temperatures and also found a positive trend below 80 km during July at 50° N. Furthermore, Luo et al. (2021) found a decreasing gravity wave trend in the stratosphere between 2007 and 2020, derived from temperature observations of GNSS radio occultation. A likely scenario could be a decrease in the stratospheric filtering of gravity waves, allowing them to reach higher altitudes and to deposit momentum flux in the mean westward flow (Medvedev et al., 1998; Yiğit and Medvedev, 2017; Conte et al., 2023). In a similar way, the southward wind is decreasing, and this could be a consequence of less energy reaching the mesopause due to the intense westward flow. In the future, we want to explore this possibility to identify the origin of this long-term trend.

5 Concluding remarks

The current paper examines long-term variations by analyzing the median maximum wind velocity in June, July, and August as an indicator of wind dynamics over the years. Linear functions were fitted to the time series, and the slope was tested using Student's t test; in addition, Lomb–Scargle periodograms were calculated. This study also investigates the relationship between wind patterns and geomagnetic activity by using the Ap index and tests its influence on the identified trends. The results are summarized as follows:

- The lower-thermospheric eastward summer maximum in July shows a significant trend from 2004 to 2022 at high latitudes, with a decrease of $(0.45 \pm 0.18)\,\mathrm{m\,s\,yr^{-1}}$, exceeding 95 % statistical significance. The wind velocity reaches its peak between June and August, ranging from 25 to 32 $\mathrm{m\,s^{-1}}$ at an altitude of 98–99 km.

- The mesospheric westward summer maximum has strengthened over the past 33 years (1990–2022) at middle latitudes. The highest velocity occurs in July, where it exhibits a significant trend of $0.64 \pm 0.10\,\mathrm{m\,s^{-1}}$. The summer mesospheric westward trends are independent of the geomagnetic activity.

- The mesopause southward wind velocity experiences a significant decline during the 3 studied months at middle latitudes between 2004 and 2022, with the most substantial decrease occurring in June and July with slopes of 0.33 ± 0.12 and $0.26 \pm 0.12\,\mathrm{m\,s\,yr^{-1}}$, respectively.

- The summer mesospheric westward wind maxima exhibit an oscillation related to the solar cycle (8.6–11.3 years). This oscillation is significant for the months of June, July, and August during the period from 1990 to 2022. Additionally, other oscillations with periods of 2.3–2.8 and 3.2–4.4 years are present in most of the time series and could be associated with modulation from the QBO or ENSO.

- Geomagnetic activity induces higher lower-thermospheric eastward winds above 94 km at high latitudes and weaker zonal winds at middle latitudes above 95 km and below 79 km.
- The mesopause southward wind displays a disturbed pattern under high geomagnetic activity, reducing the wind velocity below 84 km at high latitudes and below 78 km at middle latitudes.

As the Earth's atmosphere continues evolving, the pursuit of long-term studies becomes increasingly challenging, yielding changing results over the years. Therefore, the acquisition of longer time series becomes imperative in order to truly comprehend the dynamics of the MLT. Although models have made notable improvements in their results, they still encounter certain limitations that need to be addressed. While measurements provide localized insights and show specific latitudinal characteristics, they inherently lack a comprehensive view of the entire system. Additionally, understanding the complexities of gravity waves in the middle atmosphere is crucial as they emerge as a significant energy source in the MLT dynamics.

Data availability. The data to produce the figures are available in HDF5 format at https://doi.org/10.22000/1603 (Jaen, 2023).

Author contributions. JJ, TR, HL, and JC developed the idea and helped in the interpretation of results. NG and MT ensured the operation of the Tromsø specular meteor radar, and CJ ensured the operation of the Collm specular meteor radar. The writing of this paper was done by JJ with the assistance of all the authors, who made contributions to the discussion, draft review, and editing.

Competing interests. The contact author has declared that none of the authors has any competing interests.

Disclaimer. Publisher's note: Copernicus Publications remains neutral with regard to jurisdictional claims made in the text, published maps, institutional affiliations, or any other geographical representation in this paper. While Copernicus Publications makes every effort to include appropriate place names, the final responsibility lies with the authors.

Special issue statement. This article is part of the special issue "Long-term changes and trends in the middle and upper atmosphere". It is a result of the 11th International Workshop on Long-Term Changes and Trends in the Atmosphere, Helsinki, Finland, 23–27 May 2022.

Acknowledgements. Juliana Jaen thanks Axel Gabriel and Federico Conte for the helpful discussions and Matthias Clahsen for the data processing.

Lyman α is obtained from LISIRD (https://lasp.colorado.edu/lisird/, last access: 18 February 2023). Ap index is available from GFZ (https://www.gfz-potsdam.de/en/section/geomagnetism/data-products-services/geomagnetic-kp-index, last access: 25 November 2022).

The authors acknowledge the financial support of the Deutsche Forschungsgemeinschaft and the Bundesministerium für Bildung und Forschung (TIMA). Huixin Liu acknowledges the support of the JSPS KAKENHI and JRPs-LEAD with DFG.

Financial support. This research has been supported by the Deutsche Forschungsgemeinschaft (grant nos. PO 2341/2-1, JA 836/47-1, and JPJSJPR 20181602), the Bundesministerium für Bildung und Forschung (grant no. 01 LG 1902A), and the Japan Society for the Promotion of Science (grant nos. 18H01270, 17KK0095, 20H00197, and 22K21345).

The publication of this article was funded by the Open Access Fund of the Leibniz Association.

Review statement. This paper was edited by John Plane and reviewed by two anonymous referees.

References

Akmaev, R. A.: Modeling the cooling due to CO2 increases in the mesosphere and lower thermosphere, Phys. Chem. Earth, 27, 521–528, https://doi.org/10.1016/S1474-7065(02)00033-5, 2002.

Alexandre, D., Thurairajah, B., England, S. L., and Cullens, C. Y.: A Hemispheric and Seasonal Comparison of Tropospheric to Mesospheric Gravity-Wave Propagation, J. Geophys. Res.-Atmos., 126, e2021JD034990, https://doi.org/10.1029/2021JD034990, 2021.

Andrews, D. G., Holton, J. R., and Leovy, C. B.: Middle Atmosphere Dynamics, Vol. 40, 1st edn., Academic Press, ISBN: 0-12-058576-6, 1987.

Baldwin, M. P., Gray, L. J., Dunkerton, T. J., Hamilton, K., Haynes, P. H., Randel, W. J., Holton, J. R., Alexander, M. J., Hirota, I., Horinouchi, T., Jones, D. B. A., Kinnersley, J. S., Marquardt, C., Sato, K., and Takahashi, M.: The quasi-biennial oscillation, Rev. Geophys., 39, 179–229, https://doi.org/10.1029/1999RG000073, 2001.

Bremer, J. and Berger, U.: Mesospheric temperature trends derived from ground-based LF phase-height observations at mid-latitudes: Comparison with model simulations, J. Atmos. Sol.-Terr. Phy., 64, 805–816, https://doi.org/10.1016/S1364-6826(02)00073-1, 2002.

Bremer, J. and Peters, D. H.: Influence of stratospheric ozone changes on long-term trends in the meso- and lower thermosphere, J. Atmos. Sol.-Terr. Phy., 70, 1473–1481, https://doi.org/10.1016/J.JASTP.2008.03.024, 2008.

Bremer, J., Schminder, R., Greisiger, K. M., Hoffmann, P., Kürschner, D., and Singer, W.: Solar cycle dependence and long-term trends in the wind field of the mesosphere/lower thermosphere, J. Atmos. Sol.-Terr. Phy., 59, 497–509, https://doi.org/10.1016/S1364-6826(96)00032-6, 1997.

Conte, J. F., Chau, J. L., Stober, G., Pedatella, N. M., Maute, A., Hoffmann, P., Janches, D., Fritts, D. C., and Murphy, D. J.: Climatology of semidiurnal lunar and solar tides at middle and high latitudes: Interhemispheric comparison, J. Geophys. Res.-Space, 122, 7750–7760, https://doi.org/10.1002/2017JA024396, 2017.

Conte, J. F., Chau, J. L., Yigit, E., Suclupe, J., and Rodríguez, R. R.: Investigation of mesosphere and lower thermosphere dynamics over central and northern Peru using SIMONe systems, J. Geophys. Res.-Atmos., https://doi.org/10.1029/2009JD012388, 2023.

Czesla, S., Schröter, S., Schneider, C. P., Huber, K. F., Pfeifer, F., Andreasen, D. T., and Zechmeister, M.: PyA: Python astronomy-related packages, https://ui.adsabs.harvard.edu/abs/2019ascl.soft06010C (last access: 23 April 2023), 2019.

Dawkins, E. C. M., Stober, G., Janches, D., Carrillo-Sánchez, J. D., Lieberman, R. S., Jacobi, C., Moffat-Griffin, T., Mitchell, N. J., Cobbett, N., Batista, P. P., Andrioli, V. F., Buriti, R. A., Murphy, D. J., Kero, J., Gulbrandsen, N., Tsutsumi, M., Kozlovsky, A., Kim, J. H., Lee, C., and Lester, M.: Solar Cycle and Long-Term Trends in the Observed Peak of the Meteor Altitude Distributions by Meteor Radars, Geophys. Res. Lett., 50, e2022GL101953, https://doi.org/10.1029/2022GL101953, 2023.

DeLand, M. T. and Thomas, G. E.: Updated PMC trends derived from SBUV data, J. Geophys. Res.-Atmos., 120, 2140–2166, https://doi.org/10.1002/2014JD022253, 2015.

Ern, M., Preusse, P., Gille, J. C., Hepplewhite, C. L., Mlynczak, M. G., Russell, J. M., and Riese, M.: Implications for atmospheric dynamics derived from global observations of gravity wave momentum flux in stratosphere and mesosphere, J. Geophys. Res.-Atmos., 116, D19107, https://doi.org/10.1029/2011JD015821, 2011.

Espy, P. J., Ochoa Fernández, S., Forkman, P., Murtagh, D., and Stegman, J.: The role of the QBO in the inter-hemispheric coupling of summer mesospheric temperatures, Atmos. Chem. Phys., 11, 495–502, https://doi.org/10.5194/acp-11-495-2011, 2011.

Fiedler, J., Baumgarten, G., Berger, U., Hoffmann, P., Kaifler, N., and Lübken, F.-J.: NLC and the background atmosphere above ALOMAR, Atmos. Chem. Phys., 11, 5701–5717, https://doi.org/10.5194/acp-11-5701-2011, 2011.

French, W. J. R., Klekociuk, A. R., and Mulligan, F. J.: Analysis of 24 years of mesopause region OH rotational temperature observations at Davis, Antarctica – Part 2: Evidence of a quasi-quadrennial oscillation (QQO) in the polar mesosphere, Atmos. Chem. Phys., 20, 8691–8708, https://doi.org/10.5194/acp-20-8691-20200, 2020.

Fritts, D. C. and Alexander, M. J.: Gravity wave dynamics and effects in the middle atmosphere, Rev. Geophys., 41, 1003, https://doi.org/10.1029/2001RG000106, 2003.

García-Herrera, R., Calvo, N., Garcia, R. R., and Giorgetta, M. A.: Propagation of ENSO temperature signals into the middle atmosphere: A comparison of two general circulation models and ERA-40 reanalysis data, J. Geophys. Res. Atmos., 111, D06101, https://doi.org/10.1029/2005JD006061, 2006.

Gong, J., Geller, M. A., and Wang, L.: Source spectra information derived from U.S. high-resolution radiosonde data, J. Geophys. Res., 113, D10106, https://doi.org/10.1029/2007JD009252, 2008.

Gu, S., Zhao, H., Wei, Y., Wang, D., and Dou, X.: Atomic Oxygen SAO, AO and QBO in the Mesosphere and Lower Thermosphere Based on Measurements from SABER on TIMED during 2002–2019, Atmosphere, 13, 517, https://doi.org/10.3390/ATMOS13040517, 2022.

Hall, C. M. and Tsutsumi, M.: Changes in mesospheric dynamics at 78° N, 16° E and 70° N, 19° E: 2001–2012, J. Geophys. Res.-Atmos., 118, 2689–2701, https://doi.org/10.1002/jgrd.50268, 2013.

Hall, C. M., Aso, T., Tsutsumi, M., Nozawa, S., Manson, A. H., and Meek, C. E.: A comparison of mesosphere and lower thermosphere neutral winds as determined by meteor and medium-frequency radar at 70° N, Radio Sci., 40, RS4001, https://doi.org/10.1029/2004RS003102, 2005.

Hibbins, R. E., Espy, P. J., Jarvis, M. J., Riggin, D. M., and Fritts, D. C.: A climatology of tides and gravity wave variance in the MLT above Rothera, Antarctica obtained by MF radar, J. Atmos. Sol.-Terr. Phy., 69, 578–588, https://doi.org/10.1016/J.JASTP.2006.10.009, 2007.

Hocking, W. K., Fuller, R. A., and Vandepeer, B.: Real-time determination of meteor-related parameters utilizing modern digital technology, J. Atmos. Sol.-Terr. Phy., 63, 155–169, https://doi.org/10.1016/S1364-6826(00)00138-3, 2001.

Hoffmann, P., Becker, E., Singer, W., and Placke, M.: Seasonal variation of mesospheric waves at northern middle and high latitudes, J. Atmos. Sol.-Terr. Phy., 72, 1068–1079, https://doi.org/10.1016/j.jastp.2010.07.002, 2010.

Hoffmann, P., Rapp, M., Singer, W., and Keuer, D.: Trends of mesospheric gravity waves at northern middle latitudes during summer, J. Geophys. Res., 116, D00P08, https://doi.org/10.1029/2011JD015717, 2011.

Holton, J. R.: An Introduction to Dynamic Meteorology, Elsevier, 4th edn., ISBN 0123540151, 2004.

Holton, J. R. and Alexander, M. J.: The Role of Waves in the Transport Circulation of the Middle Atmosphere, Geoph. Monog. Series, 123, 161–176, https://doi.org/10.1029/GM123p0161, 2000.

Huyghebaert, D., Clahsen, M., Chau, J. L., Renkwitz, T., Latteck, R., Johnsen, M. G., and Vierinen, J.: Multiple E-Region Radar Propagation Modes Measured by the VHF SIMONe Norway System During Active Ionospheric Conditions, Frontiers in Astronomy and Space Sciences, 9, 1–16, https://doi.org/10.3389/fspas.2022.886037, 2022.

Jacobi, C.: On the solar cycle dependence of winds and planetary waves as seen from mid-latitude D1 LF mesopause region wind measurements, Ann. Geophys., 16, 1534–1543, https://doi.org/10.1007/s00585-998-1534-3, 1998.

Jacobi, C. and Kürschner, D.: A possible connection of mid-latitude mesosphere/lower thermosphere zonal winds and the southern oscillation, Phys. Chem. Earth, 27, 571–577, https://doi.org/10.1016/S1474-7065(02)00039-6, 2002.

Jacobi, C. and Kürschner, D.: Long-term trends of MLT region winds over Central Europe, Phys. Chem. Earth, 31, 16–21, https://doi.org/10.1016/j.pce.2005.01.004, 2006.

Jacobi, C., Lange, M., Kürschner, D., Manson, A., and Meek, C.: A long-term comparison of saskatoon MF radar and collm LF

D1 mesosphere-lower thermosphere wind measurements, Phys. Chem. Earth Pt. C, 26, 419–424, https://doi.org/10.1016/S1464-1917(01)00023-X, 2001.

Jacobi, C., Arras, C., Kürschner, D., Singer, W., Hoffmann, P., and Keuer, D.: Comparison of mesopause region meteor radar winds, medium frequency radar winds and low frequency drifts over Germany, Adv. Space Res., 43, 247–252, https://doi.org/10.1016/j.asr.2008.05.009, 2009.

Jacobi, C., Lilienthal, F., Geißler, C., and Krug, A.: Long-term variability of mid-latitude mesosphere-lower thermosphere winds over Collm (51° N, 13° E), J. Atmos. Sol.-Terr. Phy., 136, 174–186, https://doi.org/10.1016/j.jastp.2015.05.006, 2015.

Jacobi, C., Krug, A., and Merzlyakov, E.: Radar observations of the quarterdiurnal tide at midlatitudes: Seasonal and long-term variations,J. Atmos. Sol.-Terr. Phy., 163, 70–77, https://doi.org/10.1016/j.jastp.2017.05.014, 2017.

Jacobi, C., Lilienthal, F., Korotyshkin, D., Merzlyakov, E., and Stober, G.: Influence of geomagnetic disturbances on mean winds and tides in the mesosphere/lower thermosphere at midlatitudes, Adv. Radio Sci., 19, 185–193, https://doi.org/10.5194/ars-19-185-2021, 2021.

Jacobi, C., Kuchar, A., Renkwitz, T., and Jaen, J.: Long-term trends of midlatitude horizontal mesosphere/lowerthermosphere winds over four decades, 2022 Kleinheubach Conference, KHB 2022, 1–11, https://doi.org/10.5194/ars-21-1-2023, 2023.

Jaen, J.: JaenACP2023, Leibniz Institute of Atmospheric Physics at the University of Rostock [data set], https://doi.org/10.22000/1603, 2023.

Jaen, J., Renkwitz, T., Chau, J. L., He, M., Hoffmann, P., Yamazaki, Y., Jacobi, C., Tsutsumi, M., Matthias, V., and Hall, C.: Long-term studies of mesosphere and lower-thermosphere summer length definitions based on mean zonal wind features observed for more than one solar cycle at middle and high latitudes in the Northern Hemisphere, Ann. Geophys., 40, 23–35, https://doi.org/10.5194/angeo-40-23-2022, 2022.

Karagodin-Doyennel, A., Rozanov, E., Kuchar, A., Ball, W., Arsenovic, P., Remsberg, E., Jöckel, P., Kunze, M., Plummer, D. A., Stenke, A., Marsh, D., Kinnison, D., and Peter, T.: The response of mesospheric H_2O and CO to solar irradiance variability in models and observations, Atmos. Chem. Phys., 21, 201–216, https://doi.org/10.5194/acp-21-201-2021, 2021.

Keuer, D., Hoffmann, P., Singer, W., and Bremer, J.: Long-term variations of the mesospheric wind field at mid-latitudes, Ann. Geophys., 25, 1779–1790, https://doi.org/10.5194/angeo-25-1779-2007, 2007.

Laštovička, J. and Jelínek, Š.: Problems in calculating long-term trends in the upper atmosphere, J. Atmos. Sol.-Terr. Phy., 189, 80–86, https://doi.org/10.1016/j.jastp.2019.04.011, 2019.

Laštovička, J., Solomon, S. C., and Qian, L.: Trends in the Neutral and Ionized Upper Atmosphere, Space Sci. Rev., 168, 113–145, https://doi.org/10.1007/s11214-011-9799-3, 2012.

Li, J., Wang, W., Lu, J., Yue, J., Burns, A. G., Yuan, T., Chen, X., and Dong, W.: A Modeling Study of the Responses of Mesosphere and Lower Thermosphere Winds to Geomagnetic Storms at Middle Latitudes, J. Geophys. Res.-Space, 124, 3666–3680, https://doi.org/10.1029/2019JA026533, 2019.

Li, J., Wei, G., Wang, W., Luo, Q., Lu, J., Tian, Y., Xiong, S., Sun, M., Shen, F., Yuan, T., Zhang, X., Fu, S., Li, Z., Zhang, H., and Yang, C.: A Modeling Study on the Responses of the Mesosphere and Lower Thermosphere (MLT) Temperature to the Initial and Main Phases of Geomagnetic Storms at High Latitudes, J. Geophys. Res.-Atmos., 128, 1–14, https://doi.org/10.1029/2022JD038348, 2023.

Li, T., Yue, J., Russell, J. M., and Zhang, X.: Long-term trend and solar cycle in the middle atmosphere temperature revealed from merged HALOE and SABER datasets, J. Atmos. Sol.-Terr. Phy., 212, 105506, https://doi.org/10.1016/J.JASTP.2020.105506, 2021.

Lindzen, R. S. and Holton, J. R.: A Theory of the Quasi-Biennial Oscillation, J. Atmos. Sci., 25, 1095–1107, https://doi.org/10.1175/1520-0469(1968)025<1095:ATOTQB>2.0.CO;2, 1968.

Liu, H., Tao, C., Jin, H., and Nakamoto, Y.: Circulation and Tides in a Cooler Upper Atmosphere: Dynamical Effects of CO2 Doubling, Geophys. Res. Lett., 47, 1–9, https://doi.org/10.1029/2020GL087413, 2020.

Liu, H., Tao, C., Jin, H., and Abe, T.: Geomagnetic activity effects on CO_2-driven trend in the thermosphere and ionosphere: ideal model experiments with GAIA, J. Geophys. Res.-Space, 126, e2020JA028607, https://doi.org/10.1029/2020JA028607, 2021.

Liu, X., Yue, J., Xu, J., Garcia, R. R., Russell, J. M., Mlynczak, M., Wu, D. L., and Nakamura, T.: Variations of global gravity waves derived from 14 years of SABER temperature observations, J. Geophys. Res., 122, 6231–6249, https://doi.org/10.1002/2017JD026604, 2017.

Luo, J., Hou, J., and Xu, X.: Variations in stratospheric gravity waves derived from temperature observations of multi-gnss radio occultation missions, Remote Sensing, 13, 1–20, https://doi.org/10.3390/rs13234835, 2021.

Manson, A. H., Meek, C. E., Hall, C. M., Nozawa, S., Mitchell, N. J., Pancheva, D., Singer, W., and Hoffmann, P.: Mesopause dynamics from the scandinavian triangle of radars within the PSMOS-DATAR Project, Ann. Geophys., 22, 367–386, https://doi.org/10.5194/angeo-22-367-2004, 2004.

Matzka, J., Stolle, C., Yamazaki, Y., Bronkalla, O., and Morschhauser, A.: The Geomagnetic Kp Index and Derived Indices of Geomagnetic Activity, Space Weather, 19, e2020SW002641, https://doi.org/10.1029/2020SW002641, 2021.

Medvedev, A. S., Klaassen, G. P., and Beagley, S. R.: On the role of an anisotropic gravity wave spectrum in maintaining the circulation of the middle atmosphere, Geophys. Res. Lett., 25, 509–512, https://doi.org/10.1029/98GL50177, 1998.

Mossad, M., Strelnikova, I., Wing, R., and Baumgarten, G.: Assessing Atmospheric Gravity Wave Spectra in the Presence of Observational Gaps, EGUsphere [preprint], https://doi.org/10.5194/egusphere-2023-1598, 2023.

Nozawa, S., Brekke, A., Manson, A., Hall, C. M., Meek, C., Morise, K., Oyama, S., Dobashi, K., and Fujii, R.: A comparison study of the auroral lower thermospheric neutral winds derived by the EISCAT UHF radar and the Tromso medium frequency radar, J. Geophys. Res.-Space, 107, SIA 29-1–SIA 29-20, https://doi.org/10.1029/2000JA007581, 2002.

Offermann, D., Hoffmann, P., Knieling, P., Koppmann, R., Oberheide, J., Riggin, D. M., Tunbridge, V. M., and Steinbrecht, W.: Quasi 2 day waves in the summer mesosphere: Triple structure of amplitudes and long-term development, J. Geophys. Res., 116, D00P02, https://doi.org/10.1029/2010JD015051, 2011.

Offermann, D., Goussev, O., Kalicinsky, C., Koppmann, R., Matthes, K., Schmidt, H., Steinbrecht, W., and Wintel, J.: A case study of multi-annual temperature oscillations in the atmosphere: Middle Europe, J. Atmos. Sol.-Terr. Phy., 135, 1–11, https://doi.org/10.1016/j.jastp.2015.10.003, 2015.

Pedatella, N. M., Liu, H. L., Conte, J. F., Chau, J. L., Hall, C., Jacobi, C., Mitchell, N., and Tsutsumi, M.: Migrating Semidiurnal Tide During the September Equinox Transition in the Northern Hemisphere, J. Geophys. Res.-Atmos., 126, 1–14, https://doi.org/10.1029/2020JD033822, 2021.

Perminov, V., Semenov, A., Pertsev, N., Medvedeva, I., Dalin, P., and Sukhodoev, V.: Multi-year behaviour of the midnight OH^* temperature according to observations at Zvenigorod over 2000–2016, Adv. Space Res., 61, 1901–1908, https://doi.org/10.1016/j.asr.2017.07.020, 2018.

Peters, D. H. and Entzian, G.: Long-term variability of 50 years of standard phase-height measurement at Kühlungsborn, Mecklenburg, Germany, Adv. Space Res., 55, 1764–1774, https://doi.org/10.1016/j.asr.2015.01.021, 2015.

Peters, D. H., Entzian, G., and Keckhut, P.: Mesospheric temperature trends derived from standard phase-height measurements, J. Atmos. Sol.-Terr. Phy., 163, 23–30, https://doi.org/10.1016/j.jastp.2017.04.007, 2017.

Pisoft, P., Sacha, P., Polvani, L. M., Añel, J. A., de la Torre, L., Eichinger, R., Foelsche, U., Huszar, P., Jacobi, C., Karlicky, J., Kuchar, A., Miksovsky, J., Zak, M., and Rieder, H. E.: Stratospheric contraction caused by increasing greenhouse gases, Environ. Res. Lett., 16, 064038, https://doi.org/10.1088/1748-9326/abfe2b, 2021.

Poblet, F. L., Vierinen, J., Avsarkisov, V., Conte, J. F., Charuvil Asokan, H., Jacobi, C., and Chau, J. L.: Horizontal Correlation Functions of Wind Fluctuations in the Mesosphere and Lower Thermosphere, J. Geophys. Res.-Atmos., 128, e2022JD038092, https://doi.org/10.1029/2022JD038092, 2023.

Portnyagin, Y. I., Merzlyakov, E. G., Solovjova, T. V., Jacobi, C., Kürschner, D., Manson, A. H., and Meek, C.: Long-term trends and year-to-year variability of mid-latitude mesosphere/lower thermosphere winds, J. Atmos. Sol.-Terr. Phy., 68, 1890–1901, https://doi.org/10.1016/j.jastp.2006.04.004, 2006.

Qian, L., Burns, A. G., Solomon, S. C., and Wang, W.: Carbon dioxide trends in the mesosphere and lower thermosphere, J. Geophys. Res.-Space, 122, 4474–4488, https://doi.org/10.1002/2016JA023825, 2017.

Reid, I. M., Spargo, A. J., and Woithe, J. M.: Seasonal variations of the nighttime $O(^1S)$ and OH (8-3) airglow intensity at Adelaide, Australia, J. Geophys. Res., 119, 6991–7013, https://doi.org/10.1002/2013JD020906, 2014.

Reid, I. M., McIntosh, D. L., Murphy, D. J., and Vincent, R. A.: Mesospheric radar wind comparisons at high and middle southern latitudes, Earth Planets Space, 70, 1–16, https://doi.org/10.1186/s40623-018-0861-1, 2018.

Renkwitz, T. and Latteck, R.: Variability of virtual layered phenomena in the mesosphere observed with medium frequency radars at 69° N, J. Atmos. Sol.-Terr. Phy., 163, 38–45, https://doi.org/10.1016/j.jastp.2017.05.009, 2017.

Renkwitz, T., Tsutsumi, M., Laskar, F. I., Chau, J. L., and Latteck, R.: On the role of anisotropic MF/HF scattering in mesospheric wind estimation, Earth Planets Space, 70, 158, https://doi.org/10.1186/s40623-018-0927-0, 2018.

Robinson, G. K.: Properties of student's t and of the Behrens-Fisher solution to the two means problem, Ann. Stat., 4, 963–971, https://doi.org/10.1214/aos/1176343594, 1976.

Schminder, R., Kürschner, D., Singer, W., Hoffmann, P., Keuer, D., and Bremer, J.: Representative height-time cross-sections of the upper atmosphere wind field over Central Europe 1990-1996, J. Atmos. Sol.-Terr. Phy., 59, 2177–2184, https://doi.org/10.1016/S1364-6826(97)00062-X, 1997.

Singer, W., Hoffmann, P., Keuer, D., Schminder, R., and Kuerschner, D.: Wind in the middle atmosphere with partial reflection measurements during winter and spring in middle europe, Adv. Space Res., 12, 299–302, https://doi.org/10.1016/0273-1177(92)90483-E, 1992.

Singer, W., Latteck, R., Friedrich, M., Dalin, P., Kirkwood, S., Engler, N., and Holdsworth, D. A.: D-region electron densities obtained by differential absorption and phase measurements with a 3-MHz-Doppler radar, in: 17th ESA Symposium on European Rocket and Balloon Programmes and Related Research, Sandefjord, Norway, 30 May–2 June 2005, 233–238, ISBN 9783540773405, 2005.

Sprenger, K. and Schminder, R.: Solar cycle dependence of winds in the lower ionosphere, J. Atmos. Terr. Phys., 31, 217–221, https://doi.org/10.1016/0021-9169(69)90100-7, 1969.

Stober, G., Kuchar, A., Pokhotelov, D., Liu, H., Liu, H.-L., Schmidt, H., Jacobi, C., Baumgarten, K., Brown, P., Janches, D., Murphy, D., Kozlovsky, A., Lester, M., Belova, E., Kero, J., and Mitchell, N.: Interhemispheric differences of mesosphere–lower thermosphere winds and tides investigated from three whole-atmosphere models and meteor radar observations, Atmos. Chem. Phys., 21, 13855–13902, https://doi.org/10.5194/acp-21-13855-2021, 2021.

Sun, M., Li, Z., Li, J., Lu, J., Gu, C., Zhu, M., and Tian, Y.: Responses of Mesosphere and Lower Thermosphere Temperature to the Geomagnetic Storm on 7–8 September 2017, Universe, 8, 96, https://doi.org/10.3390/universe8020096, 2022.

VanderPlas, J. T.: Understanding the Lomb–Scargle Periodogram, Astrophys. J. Suppl. S., 236, 16, https://doi.org/10.3847/1538-4365/AAB766, 2018.

Vellalassery, A., Baumgarten, G., Grygalashvyly, M., and Lübken, F.-J.: Greenhouse gas effects on the solar cycle response of water vapour and noctilucent clouds, Ann. Geophys., 41, 289–300, https://doi.org/10.5194/angeo-41-289-2023, 2023.

Vincent, R. A., Kovalam, S., Murphy, D. J., Reid, I. M., and Younger, J. P.: Trends and Variability in Vertical Winds in the Southern Hemisphere Summer Polar Mesosphere and Lower Thermosphere, J. Geophys. Res.-Atmos., 124, 11070–11085, https://doi.org/10.1029/2019JD030735, 2019.

Wang, C. and Picaut, J.: Understanding ENSO physics–a review, Geoph. Monog. Series, 147, 21–48, https://doi.org/10.1029/147GM02, 2004.

Warner, C. D., Scaife, A. A., and Butchart, N.: Filtering of parameterized nonorographic gravity waves in the Met Office Unified Model, J. Atmos. Sci., 62, 1831–1848, https://doi.org/10.1175/JAS3450.1, 2005.

Weber, M., Arosio, C., Coldewey-Egbers, M., Fioletov, V. E., Frith, S. M., Wild, J. D., Tourpali, K., Burrows, J. P., and Loyola, D.: Global total ozone recovery trends attributed to ozone-depleting substance (ODS) changes derived from five

merged ozone datasets, Atmos. Chem. Phys., 22, 6843–6859, https://doi.org/10.5194/acp-22-6843-2022, 2022.

Wilhelm, S., Stober, G., and Brown, P.: Climatologies and long-term changes in mesospheric wind and wave measurements based on radar observations at high and mid latitudes, Ann. Geophys., 37, 851–875, https://doi.org/10.5194/angeo-37-851-2019, 2019.

Yiğit, E. and Medvedev, A. S.: Influence of parameterized small-scale gravity waves on the migrating diurnal tide in Earth's thermosphere, J. Geophys. Res.-Space, 122, 4846–4864, https://doi.org/10.1002/2017JA024089, 2017.

Yuan, T., Solomon, S. C., She, C.-Y. Y., Krueger, D. A., and Liu, H.-L. H. L.: The Long-Term Trends of Nocturnal Mesopause Temperature and Altitude Revealed by Na Lidar Observations Between 1990 and 2018 at Midlatitude, J. Geophys. Res.-Atmos., 124, 5970–5980, https://doi.org/10.1029/2018JD029828, 2019.

Yue, J., Russell, J., Jian, Y., Rezac, L., Garcia, R., López-Puertas, M., and Mlynczak, M. G.: Increasing carbon dioxide concentration in the upper atmosphere observed by SABER, Geophys. Res. Lett., 42, 7194–7199, https://doi.org/10.1002/2015GL064696, 2015.

Zechmeister, M. and Kürster, M.: The generalised Lomb-Scargle periodogram, Astron. Astrophys., 496, 577–584, https://doi.org/10.1051/0004-6361:200811296, 2009.

Zhou, B., Xue, X., Yi, W., Ye, H., Zeng, J., Chen, J., Wu, J., Chen, T., and Dou, X.: A comparison of MLT wind between meteor radar chain data and SD-WACCM results, Earth and Planetary Physics, 6, 451–464, https://doi.org/10.26464/epp2022040, 2022.

Appendix C

Jacobi et al. (2023)

Jacobi, C., Kuchar, A., Renkwitz, T., and Jaen, J.: Long-term trends of midlatitude horizontal mesosphere/lower thermosphere winds over four decades, Adv. Radio Sci., 21, 111–121, https://doi.org/10.5194/ars-21-111-2023, 2023.

Adv. Radio Sci., 21, 1–11, 2023
https://doi.org/10.5194/ars-21-1-2023

Advances in Radio Science
Open Access Proceedings

Long-term trends of midlatitude horizontal mesosphere/lower thermosphere winds over four decades

Christoph Jacobi[1], **Ales Kuchar**[1], **Toralf Renkwitz**[2], **and Juliana Jaen**[2]

[1]Institute for Meteorology, Leipzig University, Stephanstr. 3, 04159 Leipzig, Germany
[2]Leibniz-Institute of Atmospheric Physics e.V. at the University Rostock, Schloßstraße 6, 18225 Kühlungsborn, Germany

Correspondence: Christoph Jacobi (jacobi@uni-leipzig.de)

Received: 9 January 2023 – Revised: 5 March 2023 – Accepted: 15 March 2023 – Published:

Abstract. We analyse 43 years of mesosphere/lower thermosphere (MLT) horizontal winds obtained from a joint analysis of low frequency (LF) spaced receiver lower ionospheric drift measurements from late 1978 through 2008 and VHF meteor radar wind observations since summer 2004 at Collm (51.3° N, 13.0° E). Due to limitations of the earlier LF measurements, we restrict ourselves to the analysis of monthly mean winds near 90 km, which represents the meteor peak height as well as mean LF reflection heights in the MLT. We observe mainly positive trends of the zonal prevailing wind throughout the year, while the meridional winds tend to decrease in magnitude in both summer and winter. Furthermore, there is a change in long-term trends around the late 1990s, which is most clearly visible in summer MLT winds. We compare these measurements with long-term partial reflection radar observations of winds at 81–85 km over Juliusruh (54.6° N, 13.4° E) since 1990, and find general qualitative agreement of trends except for summer. The latter can be explained by the different altitudes considered, and by the latitude dependence of the summer mesospheric jet.

1 Introduction

It is well known that anthropogenic influences have a cooling effect on the middle atmosphere, including the mesosphere/lower thermosphere (MLT) which has been shown by observations (She et al., 2019) and modelling (Akmaev, 2002; Bremer and Berger, 2002; Qian et al., 2019; Liu et al., 2020), and which is associated with a shrinking of atmospheric layers from the stratosphere (Pisoft et al., 2021) and mesosphere (Taubenheim et al., 1997; Bremer and Berger, 2002; Peters et al., 2017) to the thermosphere (Emmert et al., 2008; Emmert, 2015). Thermospheric climate change also manifests itself in changes and a decrease in ionospheric layer heights and long-term variability of their plasma parameters (Bremer, 2008; Mielich and Bremer, 2013; Jakowski et al., 2017; Liu et al., 2021). This has been summarized several times (e.g., Beig et al., 2003; Laštovička et al., 2006, 2008; Beig, 2011). The effect of anthropogenic atmospheric composition change on the MLT wind is less clear. From earlier radar observations there is an indication that, at least during the last decades, the zonal winds change towards more westerly ones both in summer and winter, and that the meridional winds show a decrease in magnitude (Bremer et al., 1997; Jacobi et al., 1997, 2015; Hoffmann et al., 2011). However, winds in the MLT are strongly forced by gravity wave breaking, and the gravity waves are in turn filtered by the middle atmosphere mean winds. This means, that the MLT winds are influenced mainly by middle atmospheric mean wind changes. Possible changes in gravity wave sources and the interaction between mean winds and waves play a minor role as has been shown by Smith et al. (2010). Still, besides further modelling effort, analysis of long wind time series are required.

Apart from the long-term cooling and a decrease in layer heights, changes in trends of various middle and upper atmosphere parameters have been reported. One mechanism possibly responsible for trend changes is the ozone reversal after 1995, and decreasing cooling or even recent warming of the middle atmosphere had been attributed to that (Lübken et al., 2013). Trends of other parameters, such as planetary waves or ozone laminae (Jacobi et al., 2008, 2009b) also had breakpoints near the ozone turnaround date, and MLT wind changes were thought to be connected with that. It is, however, also possible that MLT wind trend changes are con-

nected with long-term trends in the lower atmosphere, e.g. increased temperature trends at high latitudes after the 1990s (Wendisch et al., 2023).

Two of the longest MLT radar wind time series are available in Germany, namely at Collm (51.3° N, 13.0° E; Jacobi et al., 1997; Jacobi and Kürschner, 2006; Jacobi et al., 2015) and Juliusruh (54.6° N, 13.4° E; Keuer et al., 2007; Hoffmann et al., 2011; Jaen et al., 2022). Owing to their different observation methods, they refer to slightly different heights in the MLT, and although long-term trends at the individual sites have been determined several times, a direct comparison of long-term changes at these two sites is still missing. Therefore, in this paper, we compare long-term changes of MLT zonal and meridional winds over Collm and Juliusruh based on observations from 1990 to 2021 in order to check whether the derived trends are consistent. The Collm time series extends further back in time, and these data will be presented also.

2 Observations

At Collm, MLT winds had been measured from December 1978 to 2008 by the low frequency (LF) spaced receiver (D1) method using the sky wave of three commercial radio transmitters. Monthly median half-hourly winds have been used to calculate monthly mean zonal and meridional prevailing winds using a regression analysis including mean winds and the semidiurnal tide (Jacobi and Kürschner, 2006). Since the reflection height itself has been measured only after late 1982 (Kürschner and Schminder, 1986; Kürschner et al., 1987), the data are attributed to the mean nighttime LF reflection height of about 90 km (Jacobi et al., 2009a). LF observations at Collm had started even earlier than 1978 (e.g., Sprenger and Schminder, 1967; Jacobi et al., 1997), but these measurements had been performed on single frequencies and they are not used here.

Since 2004 to date, VHF meteor radar observations have been performed at Collm on 36.2 MHz (Jacobi et al., 2007). An upgrade of the radar has been made in 2015/2016, including antenna configuration and peak power increase. Details of the radar configuration can be found, e.g., in Stober et al. (2021). The radar delivers wind observations in the approximate height range of 75 to 105 km, and the height information is provided by an interferometer. Mean height-time cross-sections of zonal and meridional VHF radar winds for the years 2005–2021 are shown in Fig. 1. In winter, zonal winds are westerly and meridional winds are poleward. In summer, zonal winds are easterly in the upper mesosphere, but westerly in the lower thermosphere, while the meridional winds are southward. The year-to-year variability of mean winds is larger in winter than in summer, due to the action of planetary waves and especially sudden stratospheric warmings especially in January and February (e.g., Charlton and Polvani, 2007), which may strongly affect the mesospheric and thermospheric circulation (e.g., Hoffmann et al., 2007; Miyoshi et al., 2015; Shepherd et al., 2020). Meridional winds, which are driven mainly by gravity wave mean flow interaction in the mesosphere, are considerably weaker than the zonal winds. Similar seasonal cycles of MLT winds have been already shown by earlier observations at Collm and at other midlatitude sites (e.g., Manson and Meek, 1984, 1991; Kashcheyev and Oleynikov, 1994; Schminder et al., 1997). In the following analysis, we do not include the height information that is available from the interferometer, and use the VHF winds without the height information. Monthly mean prevailing winds are calculated by a least squares fit of one month of half-hourly mean winds on model winds including the mean (prevailing) wind and the semidiurnal and diurnal tide (Jacobi et al., 2015).

Meteor peak heights are close to 90 km (e.g., Liu et al., 2017) and thus are comparable to the mean LF nighttime reflection heights. Therefore, the LF and VHF wind time series have been combined using a LF D1 speed bias correction and a virtual height correction based on the joint LF/VHF observations from mid 2004 to 2008. The virtual height correction takes into account the group retardation of LF radio waves in the ionospheric D region that leads to too high (virtual) heights. The correction was performed using phase comparisons of the semidiurnal tide (Jacobi, 2011) and resulted in mean nighttime LF real height estimates that are very close to meteor peak heights. The zonal LF and VHF winds during the joint measurements were close to each other (Jacobi et al., 2015). The meridional LF and VHF winds differed, which was partly due to a spaced receiver speed bias particularly strong in meridional winds (Jacobi et al., 2009a). Furthermore, a correction of the bias due to nighttime LF observation gaps was applied to take into account that neglecting the diurnal tide in the LF analysis leads to errors in mean meridional winds especially in summer due to the diurnal tide phase position then. Therefore, a mean meridional wind bias for each month of the year separately was determined and used to correct the LF meridional winds. The analysis method is described by Jacobi et al. (2015). Note that meteor heights tend to decrease with time due to the shrinking of the middle atmosphere (Stober et al., 2014; Lima et al., 2015), but the same is true for the LF nighttime reflection heights (Kürschner and Jacobi, 2003) so that no change in trends will arise from this decrease. Here, we use combined LF/VHF data from December 1978 through May 2022 for a long-term trend annalysis, while a presentation of the seasonal cycle (see section 4 below) is based on data from January 1990 to December 2021. A long-term linear trend comparison between WACCM-X predictions and the Collm dataset for the shorter period of 1980–2014 has also been performed by Qian et al. (2019). They modeled long-term trends and solar cycle variability of mesospheric temperatures and winds. Their simulated wind trends varied greatly with season and location.

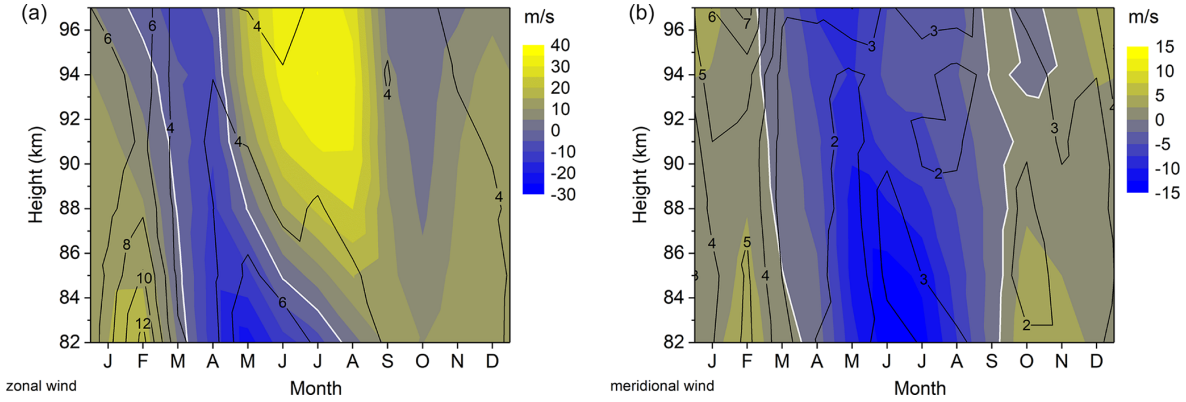

Figure 1. Color coding: 2005–2021 mean monthly mean zonal **(a)** and meridional **(b)** winds over Collm measured by VHF meteor radar. The respective zero lines are given as solid white curves. Contour lines: standard deviations based on the monthly means of each year.

Between 1990 and 2003 a partial reflection (PR) radar was in operation in Juliusruh working with the FMCW (Frequency Modulated Continuous Waves) method at a frequency of 3.18 MHz (e.g., Keuer et al., 2007). This radar has been replaced in spring 2003 by a new modular transmission and reception system (Hoffmann et al., 2010) with distributed power and a new so-called Mills-Cross-Antenna. Now the radar is working with a peak pulse power of 64 kW to date. Other technical parameters are: 27 µs pulse width, 18°-wide 3 dB beam width, height resolution of 4 km, and sampling resolution of 1 km. We use means from observations obtained between 81 and 85 km using the Full Correlation Analysis wind method.

The following analysis is based on measurements from December 1979 to May 2022 for Collm data, and January 1990 to December 2021 for a comparison of Juliusruh and Collm long-term changes. For Juliusruh, we use monthly means calculated from daily data. For Collm, we use regression analyses based on one month of half-hourly mean zonal and meridional winds each. Seasonal mean winds are calculated as averages over three monthly mean winds. Note that the Juliusruh winds refer to the upper mesosphere throughout the year. Collm observations in winter also show mesospheric winds, but in summer the lower thermospheric jet is visible.

3 Long-term trends over Collm and their changes, based on LF/VHF measurements

In Fig. 2 are shown 3-monthly mean zonal and meridional winds over Collm at about 90 km for winter (December–February, DJF), spring (March–May, MAM), summer (June–August, JJA), and autumn (September–November, SON). Linear fits without and with one possible trend breakpoint are also added. Breakpoints have been determined through a piecewise linear fitting. This method selects the most probable piecewise fit model with a priori unknown number of breakpoints (up to five) and autoregressive model of order 0, 1, or 2 by minimizing the Bayesian Information Criterion (BIC). The standard deviation of the breakpoint year is determined using a Monte Carlo method. Details of the breakpoint model are given in Liu et al. (2010). We allow a minimum distance of 5 years between individual breakpoints. Trend breaks are given as solid symbols in Fig. 2, if they are indicated as the most probable solution by the minimum BIC, otherwise they are half-filled. Also shown in Fig. 2 are standard deviations of breakpoints. Uncertainty in determining the breakpoints arises from interannual wind variability in relation to the change of linear trend. For MAM zonal winds, the minimum BIC refers to a fit curve with three breakpoints (black line in Fig. 2), which is also added. However, the related BIC is not so much different from the one for a curve with only one breakpoint. If no solid breakpoint symbol is shown, the most probable fit is a straight line. The linear trend coefficients and years of possible trend breaks are also shown in Table 1, together with the respective BIC and order of the autoregression model in brackets and the linear trend values before and after the respective breakpoint. The linear trends differ somewhat from those presented by Qian et al. (2019). They used only data until 2015, and trends have been derived from a multiple linear regression including trend and solar cycle. The zonal wind trends by Qian et al. (2019) are somewhat stronger than those reported here, which can be explained by either a solar cycle influence or the effect of the recent years, where in Fig. 2 one can see an tendency opposite to the linear long-term trend in all seasons.

Linear trends of zonal winds are positive throughout the year, although in spring they are not significant at the 95 % level according to a t-test. The positive trends indicate a strengthening of the westerly mesospheric jet in winter, and a strengthening of the lower thermospheric jet above the MLT wind reversal in summer as well. The meridional winds decrease in magnitude with time during all seasons, which results in a positive trend in summer. This behaviour is mostly similar to the one reported earlier from shorter intervals of

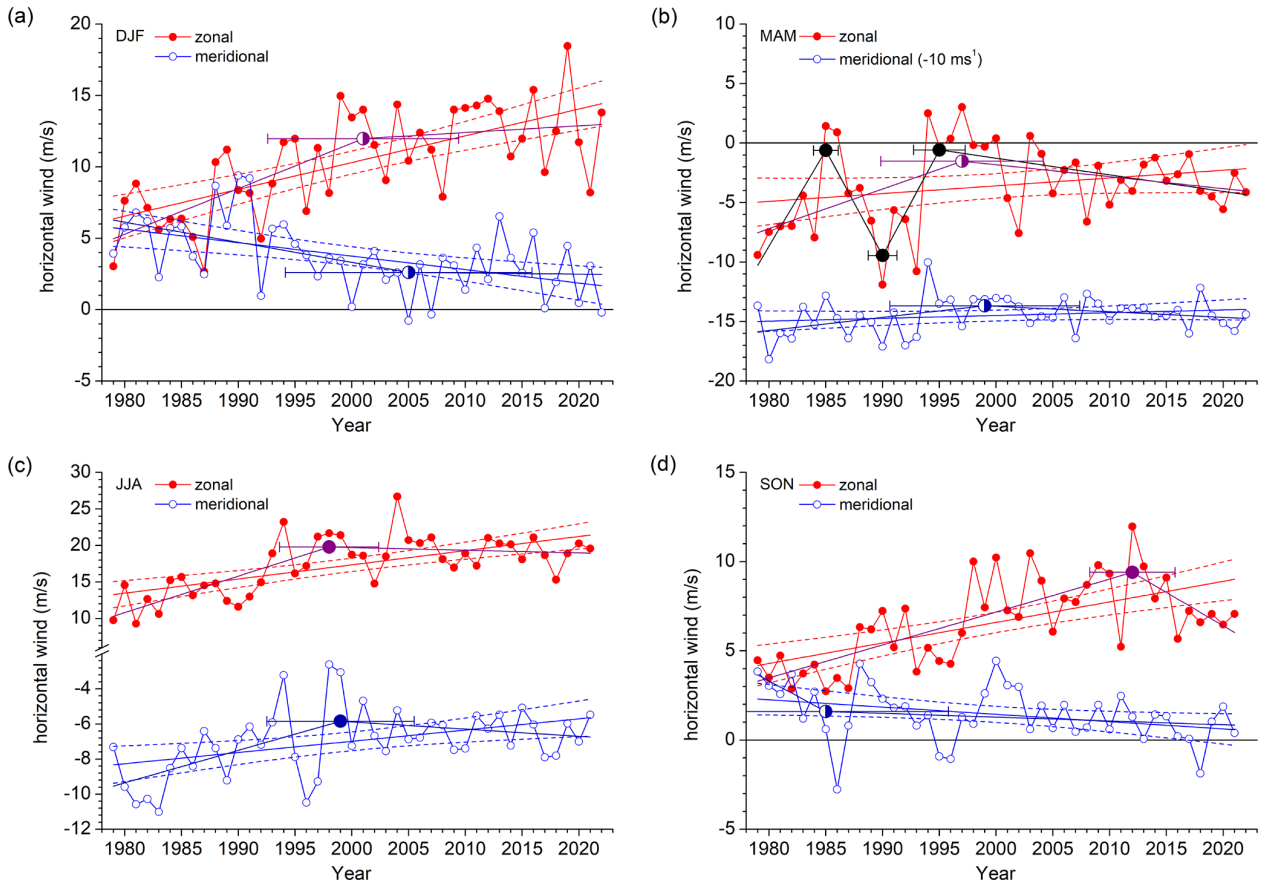

Figure 2. Seasonal mean zonal (red) and meridional (blue) winds over Collm at about 90 km for **(a)** DJF, **(b)** MAM, **(c)** JJA, and **(d)** SON. Linear fits are added with their 95 % confidence intervals. Linear fits with a trend break are also added as purple (zonal wind) and royal blue (meridional wind) curves. Trend breaks are given as solid symbols, if they are indicated by the minimum BIC, otherwise they are half–filled. For MAM zonal winds, the minimum BIC refers to a curve with three breakpoints, which is also added. If no solid breakpoint symbol is given, the minimum BIC curve is the straight linear fit line.

Table 1. Linear trend coefficients (in m s^{-1} yr^{-1}) and their standard errors of horizontal winds over Collm December 1978–May 2022. Significant trends at the 95 % level according to a t-test are given in bold. Also added are years of trend breaks with their standard deviation. Trend break years are given in bold if the fit results in minimum BIC. The respective BIC and order of the autoregression model are given in brackets. For MAM, the break year and BIC are also given for the solution with one breakpoint. The rightmost column shows the linear trends (in m s^{-1} yr^{-1}) before and after the respective breakpoint.

season	component	linear trend	break year	trends before/ after break
DJF	zonal	**0.19 ± 0.03** (91.4/0)	2001 ± 8.4 (93.8/0)	0.32/0.05
	meridonal	**–0.09 ± 0.03** (73.4/0)	2005 ± 10.9 (79.5/0)	−0.14/−0.01
MAM	zonal	0.07 ± 0.04 (112.2/1)	**1985 ± 1.1** (108.5/0)	1.61/−1.72
			1990 ± 1.3	−1.72/1.77
			1995 ± 2.3	1.77/−0.14
			1999 ± 2.3 (112.5/0)	0.33/−0.10
	meridional	0.03 ± 0.02 (41.1/0)	1999 ± 8.4 (43.4/0)	0.11/−0.05
JJA	zonal	**0.19 ± 0.04** (95.2/1)	**1998 ± 4.4** (89.7/0)	0.50/−0.04
	meridional	**0.06 ± 0.02** (53.2/0)	**1999 ± 6.5** (52.7/0)	0.19/−0.04
SON	zonal	**0.12 ± 0.02** (58.7/0)	**2012 ± 3.8** (51.0/0)	0.18/−0.37
	meridional	**–0.04 ± 0.02** (38.0/0)	1985 ± 10.8 (42.2/1)	−0.34/−0.02

Collm data (Jacobi et al., 2015; Qian et al., 2019). Note that Qian et al. (2019) used November–January means for winter, and had performed multiple regression analyses including a solar cycle effect, so that their linear trends differ, especially in winter, where the sign of the trend is different than reported here.

Note that in spring there is large variability in the first half of the observation period. This results in additional breakpoints. This may as well be considered as the signature of a quasi-decadal variation. Actually, during the 1980s and 1990s, the spring zonal winds over Collm are in anticorrelation with solar activity (Jacobi et al., 1997; Jacobi and Kürschner, 2006), but this possible solar cycle effect is not obviously visible in later years, and actually even seems to change its phase, so that there are maximum easterly winds around 1980 and 1990 (solar maximum), but weak easterly winds during the maximum of solar cycle 24 (2014). A quasi-decadal variation is most strongly expressed during May (see Fig. 5 below), but also visible in other seasons, especially in autumn.

Visual inspection of Fig. 2 and the analysis of breakpoints and linear trends before and after them (Table 1) also show that there is a tendency for a decrease in the long-term trend with time, i.e. a change to weaker or even reversed trends. The linear fits including breakpoints show that such a change is significant especially in summer and appears in the late 1990s. During winter, a change of trends is also visible near these dates, taking into account the uncertainty of the breakpoint detection, which is large due to the interannual variability of mean winds partly caused by stratospheric sudden warmings. However, for DJF the fit with one breakpoint is not the most probable solution according to BIC, but this would be a straight line in winter. Similar tendencies are visible for the meridional wind in spring, where a possible breakpoint is seen around the year 1999, but a pure linear trend is more probable. The long-term tendencies in autumn behave differently; there are indications for decreasing zonal winds in the 2nd decade of the 2000s together with strong westerly winds before 2015, which are also observed over Juliusruh (see Fig. 4d below). The reason for this interannual variability is currently not clear. This resulted in minimum BIC for the shown fit model, however, there are also model solutions which show changes in the late 1990s and not in the 2010s (not shown here) that, according to BIC, are even more probably than the pure linear fit. During all other seasons, zonal wind trends after 2000 are small and partly negative.

4 Comparison of Collm LF/VHF and Juliusruh PR winds and their changes

In this section, Collm and Juliusruh long-term wind changes are compared. However, owing to the different observations by LF/VHF and PR, the reference heights used here differ. Therefore, a direct comparison of winds is not performed here, but only winds at 90 and 83 km during 1990–2021 are presented and analysed with respect to their linear trends.

4.1 Seasonal cycles over Collm and Julisuruh

A comparison of the long-term mean seasonal cycle of horizontal winds over Collm and Juliusruh is given in Fig. 3. Here we present data of the years 1990–2021. As in Fig. 1 the zonal winds (left panel) are westerly during winter over both sites. The winter winds very closely agree with each other, which is due to the small vertical wind gradient then (see Fig. 1). In summer, the Juliusruh winds are easterly. Connected with the very strong positive zonal wind shear (Fig.1), however, westerly (positive) zonal winds are visible at 90 km over Collm. The slight latitudinal difference also contributes to this feature, because the easterly summer wind jet extends to greater heights at higher latitudes (e.g., Jaen et al., 2022).

The meridional winds are weaker than the zonal ones. Over Collm, a clear seasonal cycle is visible, with equatorward (southward) winds in summer, and weak poleward (northward) winds in winter. But over Juliusruh, at lower altitudes, the meridional winds do not show such a clear seasonal cycle. An equatorward maximum is visible in June/July but it is weaker than over Collm at higher altitudes. Again, in winter the winds over Collm and Juliusruh differ less strongly than in summer, but still the winter meridional wind magnitudes over Juliusruh are smaller than those over Collm. The differences are clearly an effect of the different altitudes considered since meridional winds are owing to gravity wave mean flow interaction, which is strongly height dependent (e.g., Yiğit and Medvedev, 2015; Lilienthal et al., 2020).

4.2 Comparison of trends over Collm and Julisuruh

Figure 4 shows zonal and meridional wind time series at Collm and Juliusruh, respectively, for four seasons. Linear fits are added based on the data from 1990–2021. The trend coefficients, their standard errors and their confidence intervals (in brackets) are given in Table 2. The Collm winds, respectively, represent part of the dataset that has been shown in Fig. 2. Comparing the Collm trends derived from the full dataset in Table 1 with those after 1990 (Table 2), it is clear that the trends become weaker and mostly insignificant. After the breakpoint, wind trends either become very weak, or reverse (Fig. 2 and Table 1). Thus, the 43 year trends over Collm are mainly caused by the very strong trends in the first half of the dataset and become smaller when one decade of observations in this first half is disregarded. We do not show linear trends with possible breakpoints as the analysis is only performed for the time after 1990, so that breakpoints, if any, would be expected close to the beginning of the time series.

In DJF the zonal wind trends are positive, i.e. towards stronger westerly winds over both sites. Due to the small vertical (see Fig. 1) and meridional gradients (Jacobi et al., 2019) during DJF, the mean values are very close to each

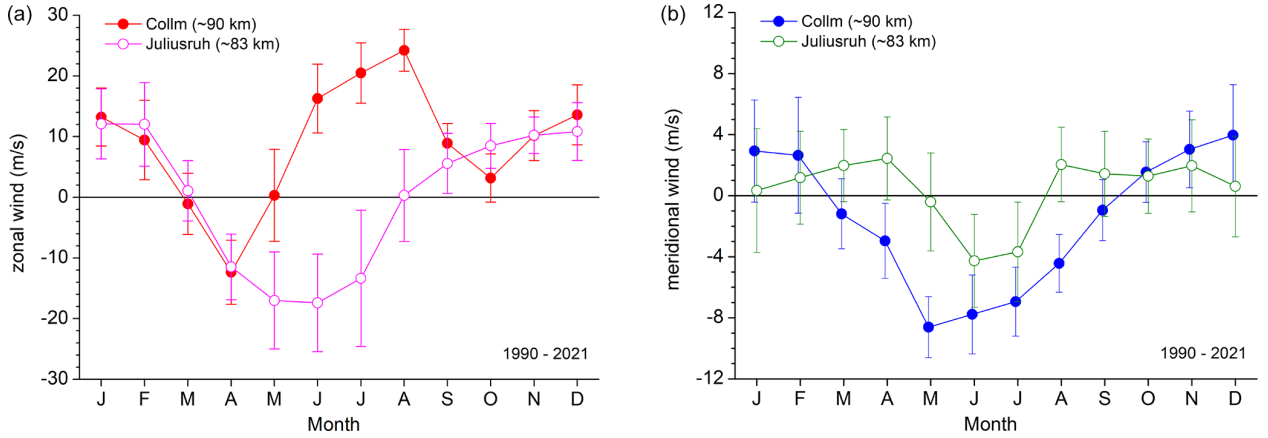

Figure 3. 1990–2021 mean monthly mean zonal **(a)** and meridional **(b)** winds over Collm at about 90 km and Juliusruh at 81–85 km. Error bars show standard deviations based on the monthly means of each year.

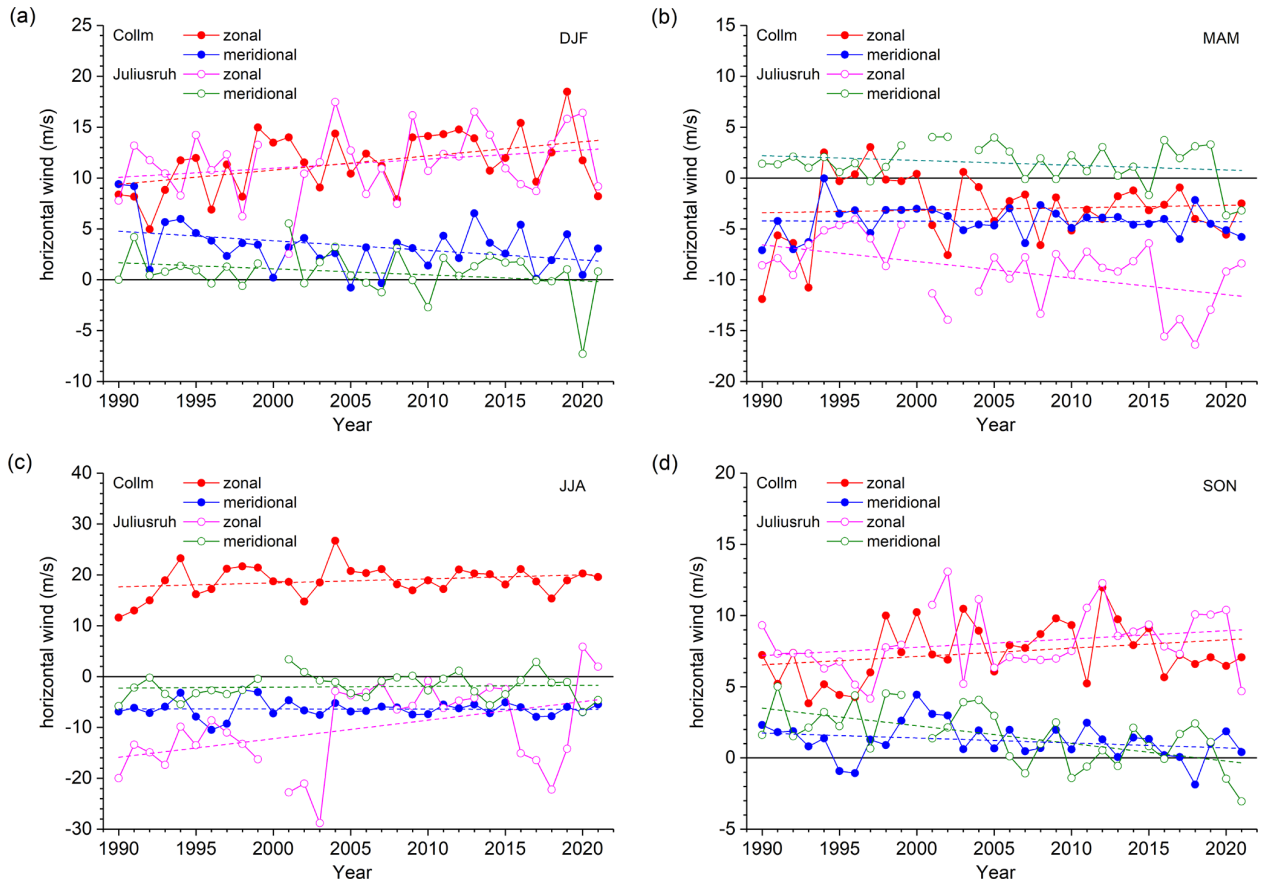

Figure 4. Seasonal mean zonal and meridional winds over Collm at about 90 km and Juliusruh at 81–85 km for **(a)** DJF, **(b)** MAM, **(c)** JJA, and **(d)** SON.

other. The trend is slightly weaker over Juliusruh, so it is not statistically significant. Interannual variability is in the same order of magnitude over both sites, however, maximums and minimums do not always correspond to each other. The meridional winds decrease over both sites, although the linear trend for Juliusruh is weaker and not statistically significant at the 95 % level.

During spring (MAM) there is considerable interannual variability of zonal winds over both sites. Moreover, while during March and April the long-term mean zonal winds are

Table 2. Linear trends and their standard errors of seasonal mean horizontal winds over Collm and Juliusruh. For spring, the March/April mean and May winds are given separatly as well. 95 % confidence intervals are given in brackets. Values are given in m s^{-1} yr^{-1}. Significant trends at the 95 % level according to a t-test are given in bold.

Season	Site	zonal wind	meridional wind
DJF	Collm	**0.14 ± 0.05** (0.03 : 0.25)	**–0.09 ± 0.04** (−0.18 : −0.01)
	Juliusruh	0.09 ± 0.07 (−0.04 : 0.22)	−0.06 ± 0.04 (−0.14 : 0.03)
MAM	Collm	0.02 ± 0.07 (−0.11 : 0.16)	−0.00 ± 0.03 (−0.06 : 0.06)
	Juliusruh	**–0.16 ± 0.06** (−0.28 : −0.05)	−0.05 ± 0.04 (−0.12 : 0.03)
March/April	Collm	0.01 ± 0.06 (−0.11 : 0.13)	+0.00 ± 0.03 (−0.06 : 0.06)
	Juliusruh	**–0.32 ± 0.06** (−0.44 : −0.21)	−0.03 ± 0.04 (−0.11 : 0.06)
May	Collm	0.03 ± 0.11 (−0.20 : 0.26)	−0.01 ± 0.04 (−0.09 : 0.06)
	Juliusruh	0.18 ± 0.14 (−0.12 : 0.47)	−0.08 ± 0.06 (−0.20 : 0.05)
JJA	Collm	0.08 ± 0.06 (−0.04 : 0.19)	−0.00 ± 0.03 (−0.07 : 0.06)
	Juliusruh	**0.36 ± 0.15** (0.06 : 0.66)	0.02 ± 0.05 (−0.08 : 0.12)
SON	Collm	0.06 ± 0.04 (−0.02 : 0.13)	−0.03 ± 0.02 (−0.08 : 0.01)
	Juliusruh	0.06 ± 0.04 (−0.03 : 0.14)	**–0.12 ± 0.03** (−0.19 : −0.06)

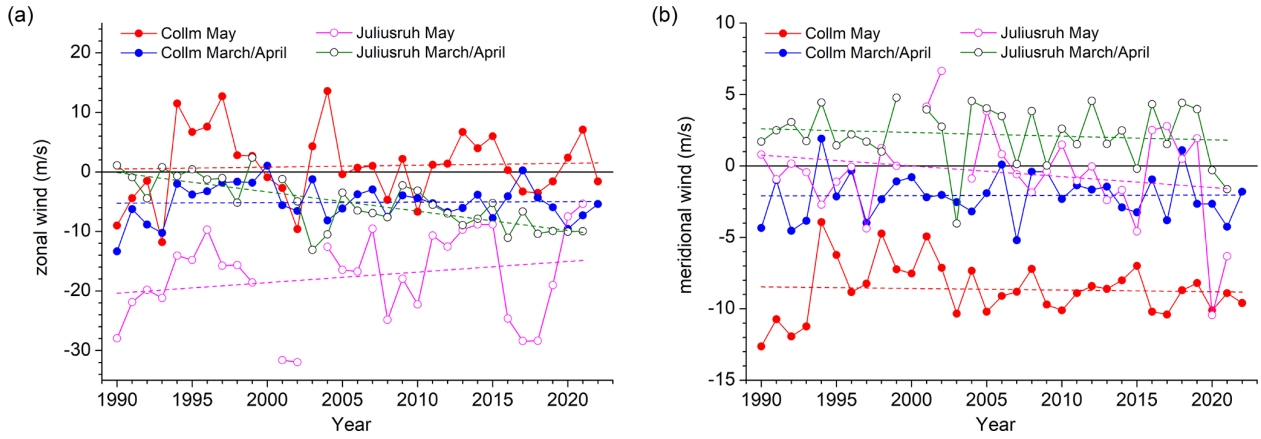

Figure 5. Bimonthly and monthly mean **(a)** zonal and **(b)** meridional winds over Collm at about 90 km and Juliusruh at 81–85 km for March/April and May.

similar over both sites, this is not the case for May with its summer onset (see Fig. 3). Consequently, there are also different long-term trends over the two sites for the zonal wind. We show March/April and May mean winds separately in Fig. 5 with the trend coefficients are also shown in Table 2. Over Juliusruh, the zonal wind trend is negative, while it is negligible over Collm. Note that the latter is due to strongly negative wind values over Collm in the early 1990s and the breakpoint in 1995 (see Table 1), and if the linear trend is calculated from 1995–2021 it becomes negative with the trend at Collm becoming comparable to the Juliusruh one. The Collm zonal wind trends during March/April and May are similar (Fig. 5) however, the May winds are more variable than the March/April ones so that the strong quasi-decadal variability in MAM zonal winds is mainly due to May wind variability, and not owing to winter final stratospheric warming variations. During May, the transition from spring to summer takes place, with the lower thermosphere change to westerlies owing to gravity wave action. There is a strong acceleration of the zonal wind on the order of 20 m s^{-1} per month (see Fig. 1) in May, and a delay in summer beginning (SB) would already have large impact on the May winds. Jaen et al. (2022) shows that the SB may vary by a period on the order of 10 d, which, given the seasonal cycle, lead to a change of 5–10 m s^{-1} for mean May zonal winds. Note that the large decadal/interdecadal variability over both sites at both heights is similar, and the May zonal winds over Collm and Juliusruh are positively correlated with a correlation coefficient of $r = 0.7$.

The meridional wind trends over Collm and Juliusruh are both negative, but insignificant in MAM, and the trend at Collm is extremely weak. This is also the case for March/April and May regarded separately (Fig. 5) .

Summer zonal wind trends are positive at both sites (Fig. 4c and Table 2), which means a weakening of the easterly mesospheric jet but a strengthening of the lower thermospheric westerlies. The meridional wind trends are small at both sites. The positive linear trend over Collm seen in Fig. 2 is due to strong changes in the 1980s and early 1990s, but not to trends in later years.

Autumn (SON) long-term changes qualitatively agree with winter ones. Thus, zonal wind trends are positive, while meridional wind trends are negative. This is true for both Collm and Juliusruh. There is a considerable interannual variability, so linear trends are not significant except for the meridional winds over Juliusruh.

5 Conclusions

The radar MLT wind time series obtained at Juliusruh and Collm range among the longest ones worldwide, so the analysis of their interannual and long-term variability may provide insight into possible effects of climate change on the MLT. Here, we show long-term trends and possible changes in trends over Collm, and compare the long-term linear trends over both sites. Owing to the different observation methods the considered heights differ by several kilometres. Consequently, the summer climatological mean zonal winds are different: while the Juliusruh observations at about 83 km show the upper part of the mesospheric easterlies, the Collm LF/VHF measurements fall into the lower thermospheric westerly jet. During winter, the vertical zonal wind gradient is smaller, and the differences between the two sites are smaller, too.

Long-term trends over Collm and Juliusruh agree qualitatively (in terms of sign), in particular in SON and DJF, but also for JJA, notwithstanding the climatological difference in mean winds. Differences in trends are found for MAM. This may be partly due to a possible trend change in the 1990s, and the strong wind shear in the summer half year, which at least includes May also.

Based on Collm winds, there are indications for a trend change in the late 1990s, which is especially prominent in summer. During winter, although the most probable solution for linear fits is a straight line then, a possible trend change is also visible. Such a change, possibly connected with the ozone turnaround after 1995 or lower atmosphere climate change, has been reported earlier (Jacobi et al., 2015). The update of the Collm time series presented here shows that the wind tendencies after the late 1990s, which mainly show a decrease or even a reversal of the trends before that time, continued during the recent years.

The comparison of Collm and Juliusruh winds in Fig. 4 also shows a considerable variability at time scales of a few years, although the year-to-year variability at the two sites is partly different. Possible mechanisms for such kind of variability may be the influence of lower/middle atmosphere circulation patterns like QBO, NAO, and ENSO. These patterns have been shown to possibly influence the middle atmosphere winds up to the mesosphere (Jacobi and Beckmann, 1999; Sridharan et al., 2010; Ermakova et al., 2019; Koval et al., 2022), but their effect decreases or reverses, respectively, near the mesopause region. The height difference of the wind time series analysed here therefore may be a reason for the different variability at these time scales. The effect of lower atmosphere variability on the MLT therefore should be analysed in more detail in the future, including numerical modelling.

In the literature, a possible solar cycle effect on mean MLT winds has frequently been proposed (Sprenger and Schminder, 1967; Jacobi et al., 1997; Qian et al., 2019). Such a solar cycle may influence trend analyses, if not adequately taken into account (Laštovička et al., 2012; Laštovička and Jelínek, 2019). There are indications that there is a quasi-decadal variability of winds present in the MLT, but on the other hand it seems that this effect is not stable and changes with time. However, given that a solar effect on winds may be quite variable with location and season, and taking into account that at least some of the linear trend estimates change when including solar activity, further analyses are required to carefully analyse the solar activity effect on MLT winds, including its possible modulation with time.

Code availability. The trend break detection software is available on request by Christoph Jacobi as Fortran-90 code.

Data availability. Collm wind data are available on request by Christoph Jacobi. Juliusruh wind data are available on request by Toralf Renkwitz (renkwitz@iap-kborn.de).

Author contributions. CJ initiated the study, provided the Collm wind data and prepared the first draft of the paper. AK contributed to the trend analysis. TR and JJ provided the Juliusruh wind data. All authors actively contributed to the writing of the final version.

Competing interests. The contact author has declared that none of the authors has any competing interests.

Disclaimer. Publisher's note: Copernicus Publications remains neutral with regard to jurisdictional claims in published maps and institutional affiliations.

Special issue statement. This article is part of the special issue "Kleinheubacher Berichte 2022".

Financial support. This research has been supported by the Deutsche Forschungsgemeinschaft (grant nos. PO 2341/2-1 and JA 836/43-1) and the Bundesministerium für Bildung und Forschung (grant no. 01LG 1902A.).

Review statement. This paper was edited by Ralph Latteck and reviewed by two anonymous referees.

References

Akmaev, R.: Modeling the cooling due to CO_2 increases in the mesosphere and lower thermosphere, Phys. Chem. Earth A/B/C, 27, 521–528, https://doi.org/10.1016/S1474-7065(02)00033-5, 2002.

Beig, G.: Long-term trends in the temperature of the mesosphere/lower thermosphere region: 2. Solar response, J. Geophys. Res.-Space, 116, A00H12, https://doi.org/10.1029/2011JA016766, 2011.

Beig, G., Keckhut, P., Lowe, R. P., Roble, R. G., Mlynczak, M. G., Scheer, J., Fomichev, V. I., Offermann, D., French, W. J. R., Shepherd, M. G., Semenov, A. I., Remsberg, E. E., She, C. Y., Lübken, F. J., Bremer, J., Clemesha, B. R., Stegman, J., Sigernes, F., and Fadnavis, S.: Review of mesospheric temperature trends, Rev. Geophys., 41, 1015, https://doi.org/10.1029/2002RG000121, 2003.

Bremer, J.: Long-term trends in the ionospheric E and F1 regions, Ann. Geophys., 26, 1189–1197, https://doi.org/10.5194/angeo-26-1189-2008, 2008.

Bremer, J. and Berger, U.: Mesospheric temperature trends derived from ground-based LF phase-height observations at mid-latitudes: comparison with model simulations, J. Atmos. Sol.-Terr. Phys., 64, 805–816, https://doi.org/10.1016/S1364-6826(02)00073-1, 2002.

Bremer, J., Schminder, R., Greisiger, K., Hoffmann, P., Kürschner, D., and Singer, W.: Solar cycle dependence and long-term trends in the wind field of the mesosphere/lower thermosphere, J. Atmos. Sol.-Terr. Phys., 59, 497–509, https://doi.org/10.1016/S1364-6826(96)00032-6, 1997.

Charlton, A. J. and Polvani, L. M.: A new look at stratospheric sudden warmings. Part I: Climatology and modeling benchmarks, J. Climate, 20, 449–469, https://doi.org/10.1175/JCLI3996.1, 2007.

Emmert, J. T.: Altitude and solar activity dependence of 1967–2005 thermospheric density trends derived from orbital drag, J. Geophys. Res.-Space, 120, 2940–2950, https://doi.org/10.1002/2015JA021047, 2015.

Emmert, J. T., Picone, J. M., and Meier, R. R.: Thermospheric global average density trends, 1967–2007, derived from orbits of 5000 near-Earth objects, Geophys. Res. Lett., 35, L05101, https://doi.org/10.1029/2007GL032809, 2008.

Ermakova, T. S., Aniskina, O. G., Statnaia, I. A., Motsakov, M. A., and Pogoreltsev, A. I.: Simulation of the ENSO influence on the extra-tropical middle atmosphere, Earth Planets Space, 71, 8, https://doi.org/10.1186/s40623-019-0987-9, 2019.

Hoffmann, P., Singer, W., Keuer, D., Hocking, W., Kunze, M., and Murayama, Y.: Latitudinal and longitudinal variability of mesospheric winds and temperatures during stratospheric warming events, J. Atmos. Sol.-Terr. Phys., 69, 2355–2366, https://doi.org/10.1016/j.jastp.2007.06.010, 2007.

Hoffmann, P., Becker, E., Singer, W., and Placke, M.: Seasonal variation of mesospheric waves at northern middle and high latitudes, J. Atmos. Sol.-Terr. Phys., 72, 1068–1079, https://doi.org/10.1016/j.jastp.2010.07.002, 2010.

Hoffmann, P., Rapp, M., Singer, W., and Keuer, D.: Trends of mesospheric gravity waves at northern middle latitudes during summer, J. Geophys. Res.-Atmos., 116, D00P08, https://doi.org/10.1029/2011JD015717, 2011.

Jacobi, C.: Meteor radar measurements of mean winds and tides over Collm (51.3° N, 13° E) and comparison with LF drift measurements 2005–2007, Adv. Radio Sci., 9, 335–341, https://doi.org/10.5194/ars-9-335-2011, 2011.

Jacobi, C. and Beckmann, B.: On the connection between upper atmospheric dynamics and tropospheric parameters: Correlations between mesopause region winds and the North Atlantic Oscillation, Climatic Change, 43, 629–643, https://doi.org/10.1023/A:1005451227975, 1999.

Jacobi, C. and Kürschner, D.: Long-term trends of MLT region winds over Central Europe, Phys. Chem. Earth A/B/C, 31, 16–21, https://doi.org/10.1016/j.pce.2005.01.004, 2006.

Jacobi, C., Schminder, R., Kürschner, D., Bremer, J., Greisiger, K., Hoffmann, P., and Singer, W.: Long-term trends in the mesopause wind field obtained from LF D1 wind measurements at Collm, Germany, Adv. Space Res., 20, 2085–2088, https://doi.org/10.1016/S0273-1177(97)00599-1, 1997.

Jacobi, C., Fröhlich, K., Viehweg, C., Stober, G., and Kürschner, D.: Midlatitude mesosphere/lower thermosphere meridional winds and temperatures measured with meteor radar, Adv. Space Res., 39, 1278–1283, https://doi.org/10.1016/j.asr.2007.01.003, 2007.

Jacobi, C., Hoffmann, P., and Kürschner, D.: Trends in MLT region winds and planetary waves, Collm (52° N, 15° E), Ann. Geophys., 26, 1221–1232, https://doi.org/10.5194/angeo-26-1221-2008, 2008.

Jacobi, C., Arras, C., Kürschner, D., Singer, W., Hoffmann, P., and Keuer, D.: Comparison of mesopause region meteor radar winds, medium frequency radar winds and low frequency drifts over Germany, Adv. Space Res., 43, 247–252, https://doi.org/10.1016/j.asr.2008.05.009, 2009a.

Jacobi, C., Hoffmann, P., Liu, R., Križan, P., Laštovička, J., Merzlyakov, E., Solovjova, T., and Portnyagin, Y.: Midlatitude mesopause region winds and waves and comparison with stratospheric variability, J. Atmos. Sol.-Terr. Phys., 71, 1540–1546, https://doi.org/10.1016/j.jastp.2009.05.004, 2009b.

Jacobi, C., Lilienthal, F., Geißler, C., and Krug, A.: Long-term variability of mid-latitude mesosphere-lower thermosphere winds over Collm (51° N, 13° E), J. Atmos. Sol.-Terr. Phys., 136, 174–186, https://doi.org/10.1016/j.jastp.2015.05.006, 2015.

Jacobi, C., Lilienthal, F., Stober, G., Korotyshkin, D., and Merzlyakov, E.: Mesosphere/lower thermosphere winds measured with nearby SKiYMET meteor radars at Collm and Juliusruh, and comparison with Kazan winds, 2019 Kleinheubach Conference, 23–25 September 2019, Miltenberg, Germany, IEEE, https://ieeexplore.ieee.org/document/8890153 (last access: 15 December 2022), 2019.

Jaen, J., Renkwitz, T., Chau, J. L., He, M., Hoffmann, P., Yamazaki, Y., Jacobi, C., Tsutsumi, M., Matthias, V., and Hall, C.: Long-term studies of mesosphere and lower-thermosphere sum-

mer length definitions based on mean zonal wind features observed for more than one solar cycle at middle and high latitudes in the Northern Hemisphere, Ann. Geophys., 40, 23–35, https://doi.org/10.5194/angeo-40-23-2022, 2022.

Jakowski, N., Hoque, M., Mielich, J., and Hall, C.: Equivalent slab thickness of the ionosphere over Europe as an indicator of long-term temperature changes in the thermosphere, J. Atmos. Sol.-Terr. Phys., 163, 91–102, https://doi.org/10.1016/j.jastp.2017.04.008, 2017.

Kashcheyev, B. and Oleynikov, A.: Dynamic regime of the mesopause–lower thermosphere at mid-latitudes of the northern hemisphere by radio meteor observations, J. Atmos. Sol.-Terr. Phys., 56, 1197–1207, https://doi.org/10.1016/0021-9169(94)90057-4, 1994.

Keuer, D., Hoffmann, P., Singer, W., and Bremer, J.: Long-term variations of the mesospheric wind field at mid-latitudes, Ann. Geophys., 25, 1779–1790, https://doi.org/10.5194/angeo-25-1779-2007, 2007.

Koval, A. V., Gavrilov, N. M., Pogoreltsev, A. I., and Kandieva, K. K.: Dynamical impacts of stratospheric QBO on the global circulation up to the lower thermosphere, J. Geophys. Res.-Atmos., 127, e2021JD036095, https://doi.org/10.1029/2021JD036095, 2022.

Kürschner, D. and Jacobi, C.: Quasi-biennial and decadal variability obtained from long-term measurements of nighttime radio wave reflection heights over Central Europe, Adv. Space Res., 32, 1701–1706, https://doi.org/10.1016/S0273-1177(03)90465-0, 2003.

Kürschner, D. and Schminder, R.: High-atmosphere wind profiles for altitudes between 90 and 110 km obtained from D1 LF measurements over Central Europe in 1983/1984, J. Atmos. Sol.-Terr. Phys., 48, 447–453, https://doi.org/10.1016/0021-9169(86)90121-2, 1986.

Kürschner, D., Schminder, R., Singer, W., and Bremer, J.: Ein neues Verfahren zur Realisierung absoluter Reflexionshöhenmessungen an Raumwellen amplitudenmodulierter Rundfunksender bei Schrägeinfall im Langwellenbereich als Hilfsmittel zur Ableitung von Windprofilen in der oberen Mesopausenregion, Z. Meteorol., 37, 322–332, 1987.

Laštovička, J. and Jelínek, Š.: Problems in calculating long-term trends in the upper atmosphere, J. Atmos. Sol.-Terr. Phys., 189, 80–86, https://doi.org/10.1016/j.jastp.2019.04.011, 2019.

Laštovička, J., Akmaev, R. A., Beig, G., Bremer, J., and Emmert, J. T.: Global Change in the Upper Atmosphere, Science, 314, 1253–1254, https://doi.org/10.1126/science.1135134, 2006.

Laštovička, J., Akmaev, R. A., Beig, G., Bremer, J., Emmert, J. T., Jacobi, C., Jarvis, M. J., Nedoluha, G., Portnyagin, Yu. I., and Ulich, T.: Emerging pattern of global change in the upper atmosphere and ionosphere, Ann. Geophys., 26, 1255–1268, https://doi.org/10.5194/angeo-26-1255-2008, 2008.

Laštovička, J., Solomon, S. C., and Qian, L.: Trends in the neutral and ionized upper atmosphere, Space Sci. Rev., 168, 113–145, https://doi.org/10.1007/s11214-011-9799-3, 2012.

Lilienthal, F., Yiğit, E., Samtleben, N., and Jacobi, C.: Variability of gravity wave effects on the zonal mean circulation and migrating terdiurnal tide as studied with the Middle and Upper Atmosphere Model (MUAM2019) using a nonlinear gravity wave scheme, Front. Astron. Space Sci., 7, 588956, https://doi.org/10.3389/fspas.2020.588956, 2020.

Lima, L., Araújo, L., Alves, E., Batista, P., and Clemesha, B.: Variations in meteor heights at 22.7° S during solar cycle 23, J. Atmos. Sol.-Terr. Phys., 133, 139–144, https://doi.org/10.1016/j.jastp.2015.08.015, 2015.

Liu, H., Tao, C., Jin, H., and Nakamoto, Y.: Circulation and tides in a cooler upper atmosphere: dynamical effects of CO_2 doubling, Geophys. Res. Lett., 47, e2020GL087413, https://doi.org/10.1029/2020GL087413, 2020.

Liu, H., Tao, C., Jin, H., and Abe, T.: Geomagnetic activity effects on CO_2-driven trend in the thermosphere and ionosphere: ideal model experiments with GAIA, J. Geophys. Res.-Space, 126, e2020JA028607, https://doi.org/10.1029/2020JA028607, 2021.

Liu, L., Liu, H., Chen, Y., Le, H., Sun, Y.-Y., Ning, B., Hu, L., and Wan, W.: Variations of the meteor echo heights at Beijing and Mohe, China, J. Geophys. Res.-Space, 122, 1117–1127, https://doi.org/10.1002/2016JA023448, 2017.

Liu, R. Q., Jacobi, C., Hoffmann, P., Stober, G., and Merzlyakov, E. G.: A piecewise linear model for detecting climatic trends and their structural changes with application to mesosphere/lower thermosphere winds over Collm, Germany, J. Geophys. Res.-Atmos., 115, 588956, https://doi.org/10.1029/2010JD014080, 2010.

Lübken, F.-J., Berger, U., and Baumgarten, G.: Temperature trends in the midlatitude summer mesosphere, J. Geophys. Res.-Atmos., 118, 13347–13360, https://doi.org/10.1002/2013JD020576, 2013.

Manson, A. and Meek, C.: Winds and tidal oscillations in the upper middle atmosphere at Saskatoon (52° N, 107° W, $L = 4.3$) during the year June 1982–May 1983, Planet. Space Sci., 32, 1087–1099, https://doi.org/10.1016/0032-0633(84)90134-X, 1984.

Manson, A. H. and Meek, C. E.: Climatologies of mean winds and tides observed by medium frequency radars at Tromsø (70° N) and Saskatoon (52° N) during 1987–1989, Can. J. Phys., 69, 966–975, https://doi.org/10.1139/p91-152, 1991.

Mielich, J. and Bremer, J.: Long-term trends in the ionospheric F2 region with different solar activity indices, Ann. Geophys., 31, 291–303, https://doi.org/10.5194/angeo-31-291-2013, 2013.

Miyoshi, Y., Fujiwara, H., Jin, H., and Shinagawa, H.: Impacts of sudden stratospheric warming on general circulation of the thermosphere, J. Geophys. Res.-Space, 120, 10897–10912, https://doi.org/10.1002/2015JA021894, 2015.

Peters, D. H., Entzian, G., and Keckhut, P.: Mesospheric temperature trends derived from standard phase-height measurements, J. Atmos. Sol.-Terr. Phys., 163, 23–30, https://doi.org/10.1016/j.jastp.2017.04.007, 2017.

Pisoft, P., Sacha, P., Polvani, L. M., Añel, J. A., de la Torre, L., Eichinger, R., Foelsche, U., Huszar, P., Jacobi, C., Karlicky, J., Kuchar, A., Miksovsky, J., Zak, M., and Rieder, H. E.: Stratospheric contraction caused by increasing greenhouse gases, Environ. Res. Lett., 16, 064038, https://doi.org/10.1088/1748-9326/abfe2b, 2021.

Qian, L., Jacobi, C., and McInerney, J.: Trends and solar irradiance effects in the mesosphere, J. Geophys. Res.-Space, 124, 1343–1360, https://doi.org/10.1029/2018JA026367, 2019.

Schminder, R., Kürschner, D., Singer, W., Hoffmann, P., Keuer, D., and Bremer, J.: Representative height-time cross-sections of the upper atmosphere wind field over Central Europe 1990–1996, J. Atmos. Sol.-Terr. Phys., 59, 2177–2184, https://doi.org/10.1016/S1364-6826(97)00062-X, 1997.

She, C.-Y., Berger, U., Yan, Z.-A., Yuan, T., Lübken, F.-J., Krueger, D. A., and Hu, X.: Solar Response and Long-Term Trend of Midlatitude Mesopause Region Temperature Based on 28 Years (1990–2017) of Na Lidar Observations, J. Geophys. Res.-Space, 124, 7140–7156, https://doi.org/10.1029/2019JA026759, 2019.

Shepherd, M. G., Meek, C. E., Hocking, W. K., Hall, C. M., Partamies, N., Sigernes, F., Manson, A. H., and Ward, W. E.: Multi-instrument study of the mesosphere-lower thermosphere dynamics at 80° N during the major SSW in January 2019, J. Atmos. Sol.-Terr. Phys., 210, 105427, https://doi.org/10.1016/j.jastp.2020.105427, 2020.

Smith, A. K., Garcia, R. R., Marsh, D. R., Kinnison, D. E., and Richter, J. H.: Simulations of the response of mesospheric circulation and temperature to the Antarctic ozone hole, Geophys. Res. Lett., 37, L22803, https://doi.org/10.1029/2010GL045255, 2010.

Sprenger, K. and Schminder, R.: Results of ten years' ionospheric drift measurements in the l.f. range, J. Atmos. Sol.-Terr. Phys., 29, 183–199, https://doi.org/10.1016/0021-9169(67)90132-8, 1967.

Sridharan, S., Tsuda, T., and Gurubaran, S.: Long-term tendencies in the mesosphere/lower thermosphere mean winds and tides as observed by medium-frequency radar at Tirunelveli (8.7° N, 77.8° E), J. Geophys. Res.-Atmos., 115, D08109, https://doi.org/10.1029/2008JD011609, 2010.

Stober, G., Matthias, V., Brown, P., and Chau, J. L.: Neutral density variation from specular meteor echo observations spanning one solar cycle, Geophys. Res. Lett., 41, 6919–6925, https://doi.org/10.1002/2014GL061273, 2014.

Stober, G., Kuchar, A., Pokhotelov, D., Liu, H., Liu, H.-L., Schmidt, H., Jacobi, C., Baumgarten, K., Brown, P., Janches, D., Murphy, D., Kozlovsky, A., Lester, M., Belova, E., Kero, J., and Mitchell, N.: Interhemispheric differences of mesosphere–lower thermosphere winds and tides investigated from three whole-atmosphere models and meteor radar observations, Atmos. Chem. Phys., 21, 13855–13902, https://doi.org/10.5194/acp-21-13855-2021, 2021.

Taubenheim, J., Entzian, G., and Berendorf, K.: Long-term decrease of mesospheric temperature, 1963–1995, inferred from radiowave reflection heights, Adv. Space Res., 20, 2059–2063, https://doi.org/10.1016/S0273-1177(97)00596-6, 1997.

Wendisch, M., Brückner, M., Crewell, S., Ehrlich, A., Notholt, J., Lüpkes, C., Macke, A., Burrows, J. P., Rinke, A., Quaas, J., Maturilli, M., Schemann, V., Shupe, M. D., Akansu, E. F., Barrientos-Velasco, C., Bärfuss, K., Blechschmidt, A.-M., Block, K., Bougoudis, I., Bozem, H., Böckmann, C., Bracher, A., Bresson, H., Bretschneider, L., Buschmann, M., Chechin, D. G., Chylik, J., Dahlke, S., Deneke, H., Dethloff, K., Donth, T., Dorn, W., Dupuy, R., Ebell, K., Egerer, U., Engelmann, R., Eppers, O., Gerdes, R., Gierens, R., Gorodetskaya, I. V., Gottschalk, M., Griesche, H., Gryanik, V. M., Handorf, D., Harm-Altstädter, B., Hartmann, J., Hartmann, M., Heinold, B., Herber, A., Herrmann, H., Heygster, G., Höschel, I., Hofmann, Z., Hölemann, J., Hünerbein, A., Jafariserajehlou, S., Jäkel, E., Jacobi, C., Janout, M., Jansen, F., Jourdan, O., Jurányi, Z., Kalesse-Los, H., Kanzow, T., Käthner, R., Kliesch, L. L., Klingebiel, M., Knudsen, E. M., Kovács, T., Körtke, W., Krampe, D., Kretzschmar, J., Kreyling, D., Kulla, B., Kunkel, D., Lampert, A., Lauer, M., Lelli, L., von Lerber, A., Linke, O., Löhnert, U., Lonardi, M., Losa, S. N., Losch, M., Maahn, M., Mech, M., Mei, L., Mertes, S., Metzner, E., Mewes, D., Michaelis, J., Mioche, G., Moser, M., Nakoudi, K., Neggers, R., Neuber, R., Nomokonova, T., Oelker, J., Papakonstantinou-Presvelou, I., Pätzold, F., Pefanis, V., Pohl, C., van Pinxteren, M., Radovan, A., Rhein, M., Rex, M., Richter, A., Risse, N., Ritter, C., Rostosky, P., Rozanov, V. V., Donoso, E. R., Saavedra-Garfias, P., Salzmann, M., Schacht, J., Schäfer, M., Schneider, J., Schnierstein, N., Seifert, P., Seo, S., Siebert, H., Soppa, M. A., Spreen, G., Stachlewska, I. S., Stapf, J., Stratmann, F., Tegen, I., Viceto, C., Voigt, C., Vountas, M., Walbröl, A., Walter, M., Wehner, B., Wex, H., Willmes, S., Zanatta, M., and Zeppenfeld, S.: Atmospheric and Surface Processes, and Feedback Mechanisms Determining Arctic Amplification: A Review of First Results and Prospects of the (AC)3 Project, B. Am. Meteorol. Soc., 104, E208–E242, https://doi.org/10.1175/BAMS-D-21-0218.1, 2023.

Yiğit, E. and Medvedev, A. S.: Internal wave coupling processes in Earth's atmosphere, Adv. Space Res., 55, 983–1003, https://doi.org/10.1016/j.asr.2014.11.020, 2015.

Appendix D

Sivakandan et al. (2023)

Sivakandan, M., Mielich, J., Renkwitz, T., Chau, J. L., Jaen, J., & Laštovička, J.: Long-term variations and residual trends in the E, F, and sporadic E (Es) layer over Juliusruh, Europe, Journal of Geophysical Research: Space Physics, 128, e2022JA031097. https://doi.org/10.1029/2022JA031097, 2023.

JGR Space Physics

RESEARCH ARTICLE
10.1029/2022JA031097

Long-Term Variations and Residual Trends in the E, F, and Sporadic E (Es) Layer Over Juliusruh, Europe

M. Sivakandan[1], J. Mielich[1], T. Renkwitz[1], J. L. Chau[1], J. Jaen[1], and J. Laštovička[2]

[1]Leibniz Institute of Atmospheric Physics at the University of Rostock (IAP), Kühlungsborn, Germany, [2]Institute of Atmospheric Physics Czech Academy of Sciences, Praha, Czechia, Germany

Key Points:

- The amplitude of annual and solar cycle oscillations are predominant in peak frequencies, and altitude of the E-and F-region, respectively
- In the E-region, daytime foEs shows a weak negative trend -2.00 ± 0.61 kHz/yr during 1964–2019
- Day and nighttime F-region critical frequency, and peak height trends are negative. The daytime hmF2 trend is weaker than the nighttime

Supporting Information:

Supporting Information may be found in the online version of this article.

Correspondence to:

M. Sivakandan,
mani@iap-kborn.de

Citation:

Sivakandan, M., Mielich, J., Renkwitz, T., Chau, J. L., Jaen, J., & Laštovička, J. (2023). Long-term variations and residual trends in the E, F, and sporadic E (Es) layer over Juliusruh, Europe. *Journal of Geophysical Research: Space Physics*, *128*, e2022JA031097. https://doi.org/10.1029/2022JA031097

Received 18 OCT 2022
Accepted 23 MAR 2023

Author Contributions:

Conceptualization: M. Sivakandan
Data curation: M. Sivakandan, J. Mielich, T. Renkwitz, J. L. Chau, J. Jaen, J. Laštovička
Formal analysis: M. Sivakandan, J. Mielich
Methodology: M. Sivakandan, J. Mielich, T. Renkwitz
Supervision: J. L. Chau
Writing – original draft: M. Sivakandan

Abstract Using 63 and 56 yr of continuous observations, we investigate the long-term oscillations and residual linear trends, respectively, in the E- and F-region ionosonde measured parameters of frequencies and height over Juliusruh, Europe. Using the Lomb-Scargle periodogram (LSP) long-term variations are estimated before the trend calculation. We found that the amplitude of the annual oscillation is higher than the 11-yr solar cycle variation in the critical frequencies of the daytime E (foE) and Es (foEs) layers. In the F-region, except for daytime hmF2, and nighttime foF2, the amplitude of the 11-yr solar cycle variation is higher than the annual oscillation. The combination of the LSP estimated periods and their corresponding amplitudes and traditional regression analysis are used to construct a model for E- and F-region ionospheric parameters. The modeled estimates are in good agreement with the observations. The trend calculation is derived by applying a least-squares fit analysis to the residuals, subtracting the model from the observation. In the F-region, both day (nighttime) foF2 and hmF2 show negative trends of -4.44 ± 1.78 (-4.30 ± 1.63) kHz/yr and -413 ± 47 (-574 ± 75) m/yr, respectively. The Piecewise linear trend of foF2 provides negative and positive trends in 1964–1996 and 1997–2019, respectively. In the E-region, foEs show a negative trend of -2.00 ± 0.61 kHz/yr. The present investigation suggests that the greenhouse cooling effect and negative trend in the atomic oxygen (O) as well as wind shear variability could be the main drivers for the observed negative trends in the hmF2, foF2, and foEs, respectively.

Plain Language Summary Studies on long-term changes are essential for understanding and quantifying the climate change impact on the Earth's ionosphere if it exists. In this investigation, we used 56 yr of ionosonde-measured E- and F-region parameters like frequencies and altitude of maximum electron concentration for trend estimation. We found a negative trend in the F-region ionospheric peak critical frequency (foF2), and its associated peak altitude (hmF2). More importantly, the nighttime hmF2 trend is slightly higher than the daytime. The foF2 trend is negative from 1964 to 1996 and positive during 1997–2019. The present study suggests that the anthropogenic forcing originated negative trends in the atomic oxygen, and the greenhouse cooling effect could be the driver for the F-region ionospheric trends. In the E-region, foE shows a weak and statistically insignificant positive trend. For the first time, we also report a negative trend in the foEs that could be caused by the wind shear variabilities.

1. Introduction

Long-term changes are one of the challenging and debatable research topics because of the estimation method and the social relevance in the climate change scenario. Studies on the long-term changes in the upper atmosphere yield more attention after Roble and Dickinson (1989). Using a model simulation, they reported that due to the doubling of the carbon dioxide (CO_2) and methane (CH_4) mixing ratios in the mesosphere and thermosphere, temperatures of these regions will cool about 10 K and 50 K, respectively. Motivated by the above investigation Rishbeth (1990) predicted that the greenhouse effect in the ionosphere under the composition changes and cooling mentioned by Roble and Dickinson (1989), the E- and F-region peak heights lower by about 2 km, and 20 km, respectively, however, changes in the electron number density is very small. That study also postulated that a decrease in atmospheric pressure due to the cooling of the stratosphere, mesosphere, and thermosphere caused by the greenhouse effect is responsible for the descent in the ionospheric peak altitudes. At the same time, compensation of effects due to atmospheric composition and temperature changes could inhibit the changes in the plasma density. Using more than 30 yr of ionosonde data, Bremer (1992) studied the ionospheric trends in the mid-latitudes, and his results were qualitatively in good agreement with Rishbeth (1990). Since then, there have been many investigations that looked into the seasonal, latitudinal, and longitudinal variation of trends in the E-

Journal of Geophysical Research: Space Physics 10.1029/2022JA031097

Writing – review & editing: J. Mielich, T. Renkwitz, J. L. Chau, J. Jaen, J. Laštovička

and F-region ionosphere (Bremer, 2008; Bremer et al., 2004; Bremer & Peters, 2008; Danilov, 2008, 2009, 2015; Danilov & Konstantinova, 2020; Laštovička, 2017, 2022; Laštovička et al., 2008, 2012; Mielich & Bremer, 2013; Mikhailov, 2006; Mikhailov & de la Morena, 2003; Mikhailov & Marin, 2001; Prasad et al., 2012). The outcome of these investigations shows that the long-term changes in the foF2 and hmF2 is not uniform, for example, in some of these locations the trend is positive and some other stations show a negative trend (Bremer et al., 2004; Mielich & Bremer, 2013). Most of these studies have postulated that the greenhouse effect (Laštovička, Solomon et al., 2012) and stratospheric ozone distribution changes are prime causes of the observed trends (Bremer & Peters, 2008). In contradiction, Mikhailov and Marin (2001) suggest that the observed trends associated with the geomagnetic activity variations that is, are of natural origin. However, lately using whole atmosphere model simulations Qian et al. (2021) found that trends in the thermosphere were predominantly driven by greenhouse gases, whereas in the F-region critical frequency (foF2), peak altitude (hmF2), and electron temperature (T_e) the role of greenhouse gases and of the secular change of the geomagnetic field were comparable in some regions. However, globally the role of magnetic field change is negligible because locally it is both positive and negative.

Recently, Cnossen (2020) studied the trend in the upper atmospheric neutral temperature, neutral density at 400 km altitude, and hmF2, peak electron density (NmF2) as well as total electron content using the Whole Atmosphere Community Climate Model eXtension (WACCM-X) simulation data from 1950 to 2015. The author found a negative trend in all these parameters and argued that CO_2 is probably the main driver of trends in the thermosphere. However, for high (magnetic) latitudes, the effects of changes in the Earth's magnetic field also appear to be important. Main magnetic field changes are likely responsible for a long-term decrease in Joule heating, which is especially important at low/equatorial latitudes of the American sector. Her simulation also showed that trends associated with main magnetic field changes can be either positive or negative, depending on the location. Patches of negative trends are considerably stronger and larger than patches of positive trends because main magnetic field changes push global mean trends to be more negative than they would be due to the increase in CO_2 concentration alone. In a nutshell, several factors may contribute to the long-term changes or trends in the upper atmosphere Laštovička et al. (2012), namely stratospheric ozone depletion, long-term changes in solar and geomagnetic activity, secular changes in the Earth's magnetic field, long-term changes of atmospheric circulation and atmospheric wave activity, and of mesospheric water vapor concentration. However, one of the prime factors of long-term changes and trends in the foF2 is CO_2 increase in the lower atmosphere and linked global warming (Laštovička, 2022).

Most of the earlier investigations mainly studied the trends in the F and/or E region critical frequencies, and peak altitudes (Bremer & Peters, 2008; Mikhailov, 2006). In the case of sporadic E layers, most of the earlier studies focused on the occurrence characteristics, and seasonal and solar activity dependency, but very few reports are available on the trends in foEs (Abdu et al., 1996; Pezzopane et al., 2015). In the present investigation, we used 63 yr of continuous ionosonde data to estimate the long-term variations in the daytime E region parameters, that is, foE, foEs, and day and nighttime F-region parameters that is, hmF2, and foF2, and 56 yr of data for the trends estimation of the above parameters over Juliusruh, Germany. Instrumentation and methodology are provided in Section 2, and results and discussion are given in Sections 3 and 4, respectively. Finally, Section 5 describes the concluding remarks.

2. Instrumentation and Method

We study the long-term variations and trends in the E- and F-region using ionosonde observations at Juliusruh (54.6°N, 13.4°E) representing a high-mid latitude transition region in northern Germany. Long-period oscillations and trends are investigated using Lomb-Scargle periodogram (LSP), and least-square fitting analysis, respectively. A detailed description of the ionosonde and the methodology are given below.

2.1. Ionosonde

The ionosonde Juliusruh (Mecklenburg Vorpommern) provides one of the longest, and most continuous observations around the globe, and the data are available since July 1957. Thus, in total 63 yr of data are available as of 2020, which are used for the estimation of long-term variations. However, to avoid any artificial negative slope due to the starting year 1957 (solar maximum) and the end year 2020 (solar minimum), only 56 yr of data (five solar cycles) are used to investigate the long-term trends. Therefore, we consider only the years between 1964

Journal of Geophysical Research: Space Physics 10.1029/2022JA031097

and 2019 (both are the solar-minimum years) for the trend estimation. At first, we estimate the hourly median of E- and F-region ionospheric parameters such as h'F, h'Es, foE, foEs, h'F, foF2, hmF1, and hmF2. Then, the monthly median of hourly data is calculated, followed by the daytime and nighttime mean values are estimated by averaging the data during the time interval of 08–14 UT and 21-01 UT, respectively (centered around 11 and 23 UT). Note here that the virtual height h'F is directly observed from the ionograms. However, hmF1 and hmF2 are the real heights that are estimated using Shimazaki's formula as described by Mielich and Bremer (2013). The following technical issues influence the monthly median data and have to be noticed to understand a possible exclusion of some periods or characteristics from the analyzed data set:

1. Until 1990 a high-power ionosonde with a starting frequency of ∼500 kHz was in operation. This allowed a recording of nighttime E layer critical frequencies but led to the scaling of relatively high virtual E layer heights.
2. Between 1990 and 1994, a polish ionosonde of type KOS was in operation.
3. The high and not all the time stable output power of the first Juliusruh ionosondes influenced signal power-sensitive characteristics, like the lowest frequency at which echo traces are observed on the ionogram (fmin) and the blanketing frequency of Es layer (fbEs).
4. Since 1994, so-called Digisondes are in operation. From April–August 1998, during the upgrade from Digisonde portable model (DPS) DPS-1 to DPS-4, a frequency-modulated carrier wave Barry Research Chirp Sounder was the replacement. With ∼3 km distance, the co-located Chirp Sounder receiver was too close to the transmitter to identify the ionospheric reflection in the presence of the ground wave in the ionogram. Daytime frequencies below ∼5 MHz, particularly h'E, foE, h'Es, foEs, and fbEs were affected.
5. The formerly more intensely used commercial medium frequency radio band up to 1.6 MHz led to partly strong interference and/or gaps in the ionograms, which made the scaling more difficult or impossible. In the modern Digisondes, the automatic Radio Frequency Interference Mitigation (RFIM) algorithm may lead to gaps in the ionogram trace in that frequency range.
6. Former ionosondes were not able to distinguish between near vertical and oblique echoes and showed not only vertical but also some partly strong oblique echoes, which were scaled as vertical ones with relatively high virtual heights and with artificially higher values of foEs (Laštovička, Boška et al., 2012). Generally, oblique echoes are mainly the problem for Es due to their cloudy horizontal structure.
7. Modern national and international frequency regulations do not allow continuous transmission over the whole frequency band. A specified restricted frequency list leads to several gaps of some 50 kHz, which affects characteristics close to these restricted frequency bands.
8. Until 1992, different human scalers did the manual scaling of Juliusruh ionograms. After 1993, only one scaler was involved in that task until today. Even, when the manual scaling is done according to the official ionogram scaling rules, each human scaler tends to scale a bit to higher or lower values.
9. Juliusruh monthly medians are processed including the so-called qualitative and descriptive letters. Qualitative letters give information about the uncertainty of the value of up to 20%. In the long-term analysis of this paper, these letters remain unused.

While analyzing the data, we carefully removed the instrumental biases in the data set. For example, to avoid errors in the trend estimation due to the instrumental capability we consider the foE only above 1 MHz because before the 1980s the measurable lower frequency of ionosonde is 0.5 MHz after that it is changed to 1 MHz. It is worth mentioning here that among historical ionosonde data from Europe, the Juliusruh data are those of the best quality (Burešová, 1997).

2.2. Lomb Scargle Periodogram and Trend Analysis

It is essential to remove the short and long-period oscillations before the estimation of the linear trend (Bremer, 1992; Laštovička et al., 2006; Laštovička & Jelínek, 2019). In literature, various solar proxies are used to remove the solar and geomagnetic influences on trend estimation. For example, sunspot number, F10.7, E10.7, Lyman Alpha, and so on. Recently, Laštovička (2019) and Laštovička (2021) showed that the optimum solar proxies are different for different ionospheric parameters. Thus, we used the traditional regression analysis method (as shown in Equation 1) to estimate the trend. However, this method is not suitable to remove the semi-annual, and annual oscillations. Therefore, in addition to the traditional method, we use an additional approach to remove the annual and semi-annual variations on the long-term trend estimation. As a first step, we use the LSP analysis to

Journal of Geophysical Research: Space Physics 10.1029/2022JA031097

Table 1
Linear Residual Trends in E- and F-Region Parameters Using Both Traditional and New Methods

	Linear residual trend (kHz/yr)				Correlation coefficient (r)			
	Daytime		Nighttime		Daytime		Nighttime	
Parameters	Traditional	New	Traditional	New	Traditional	New	Traditional	New
foE	0.22 ± 0.30	0.08 ± 0.42	Nil	Nil	0.976	0.966	Nil	Nil
foEs	-1.64 ± 0.50	-2.00 ± 0.61	Nil	Nil	0.972	0.902	Nil	Nil
foF2	-4.40 ± 1.78	-4.44 ± 1.78	-3.30 ± 1.38	-4.30 ± 1.63	0.991	0.991	0.971	0.972
hmF2[a]	-387 ± 45	-413 ± 47	-557 ± 76	-574 ± 75	0.949	0.950	0.929	0.930

[a]Linear trend unit is in m/yr.

identify the predominant oscillations (VanderPlas, 2018). In the second step, by combining the period and amplitude of the long-period oscillations, and the traditional regression analysis (Bremer, 1992), a model ionosonde parameters X_m are constructed as shown in Equation 2.

$$X_r = a + b.Solar\ proxy \tag{1}$$

$$X_m = X_r(t) + A_i \cdot \sin\left(\frac{2\pi}{P_i}\right)t + B_i \cdot \cos\left(\frac{2\pi}{P_i}\right)t \tag{2}$$

$$Lt = X_{ob} - X_m \tag{3}$$

In the above equations, X_r, X_m, and X_{ob} are regression, modeled, and observed ionosonde parameters, respectively. In Equation 1, a, and b are regression coefficients. We used F10.7 as a solar proxy in the trend analysis. In Equation 2, A_i, B_i, and P_i are the amplitude and period of the ith oscillations (e.g., semi-annual and annual oscillation), respectively, and t is the time series of the data. In general, a part of the above approach in Equation 2 has been used to estimate the trends in the middle and lower atmosphere (Holmen et al., 2016). Since the solar cycle with its period of ∼9–14 yr is one of the predominant oscillations in the data, we used the traditional regression method for better model data construction. The residual values are calculated by subtracting the model values from the observations using Equation 3, followed by the least-square fit analysis used to estimate the slope of the residual values or linear trend for the ionosonde parameters, namely foE, foEs, hmF2, and foF2 with 95% confidence interval. We also compared the new method's estimated residual trends with the traditional one. The residual trend estimated from both these methods is in good agreement (as shown in Table 1).

3. Observations

3.1. Seasonal and Diurnal Variability of E- and F-Region Ionosonde Parameters

To understand the seasonal and diurnal behavior, a climatology with 63 yr of hourly parameter values of the E region (i.e., foEs, foE, h'Es, h'E), is shown in Figures 1a–1d. The critical frequencies foEs and foE show a diurnal variation of maxima and minima during the day and nighttime, respectively. They also exhibit seasonal variations with a maximum in local summer and a minimum during winter. The magnitude of foEs shows a wide/broad maximum peaking around local noon and increasing again toward ∼15:00 UT (see Figure 1a). The foE peaks around local noon all the month. Please note that official local time over Juliusruh is universal time+2 (UT+2) and UT+1 hr during summer and winter, respectively. The diurnal variation of h'Es displays two prominent peaks viz., early morning and evening hours from March to September and only around noon from October to February. The semi-diurnal and diurnal tides could be a controlling factor of the observed two peaks in the h'Es (Pignalberi et al., 2014). The h'E shows two peaks viz., morning and in the evening hours along the year. Moreover, the h'E also shows seasonal variation; summer and winter peaks occur at quite different times (see Figure 1d).

We also studied the seasonal and diurnal behavior, climatology with 63 yr of hourly parameter values of the F-regions (i.e., h'F, foF2, hmF1, and hmF2) are shown in Figures 1e–1h. As expected, the virtual and real heights (h'F and hmF2) are generally lower during the daytime, (especially for h'F) than in the nighttime. The hmF1 is only present in the daytime, particularly during the equinox and summer months. Most frequently, hmF2 is

Journal of Geophysical Research: Space Physics 10.1029/2022JA031097

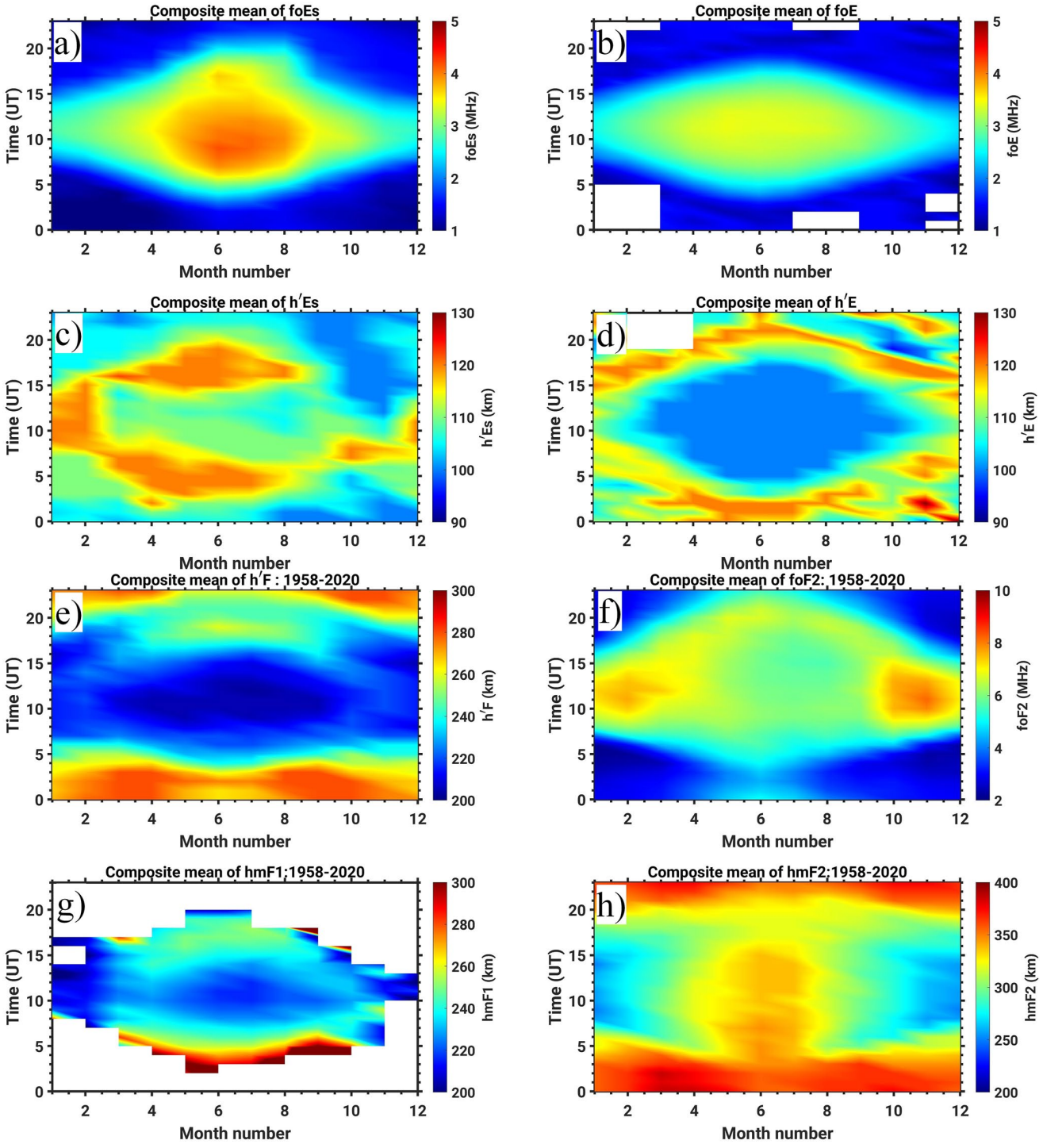

Figure 1. Diurnal and seasonal variability of the composite mean of 63 yr of hourly median E (a–d), and F (e–h) region ionosonde parameters.

located around 350 km during nighttime, and the lowest altitudes of the hmF2 are observed in the winter daytime (~250 km). On the other hand, the foF2 is higher in the winter than in the summer, which coincides with occurring at lower altitudes. The foF2 show two peaks during summer, one is before noon, and the other is at around 20 UT. The seasonal variability of foF2 and hmF2 are consistence with earlier observations (Rao et al., 2014) at mid-latitudes.

Journal of Geophysical Research: Space Physics 10.1029/2022JA031097

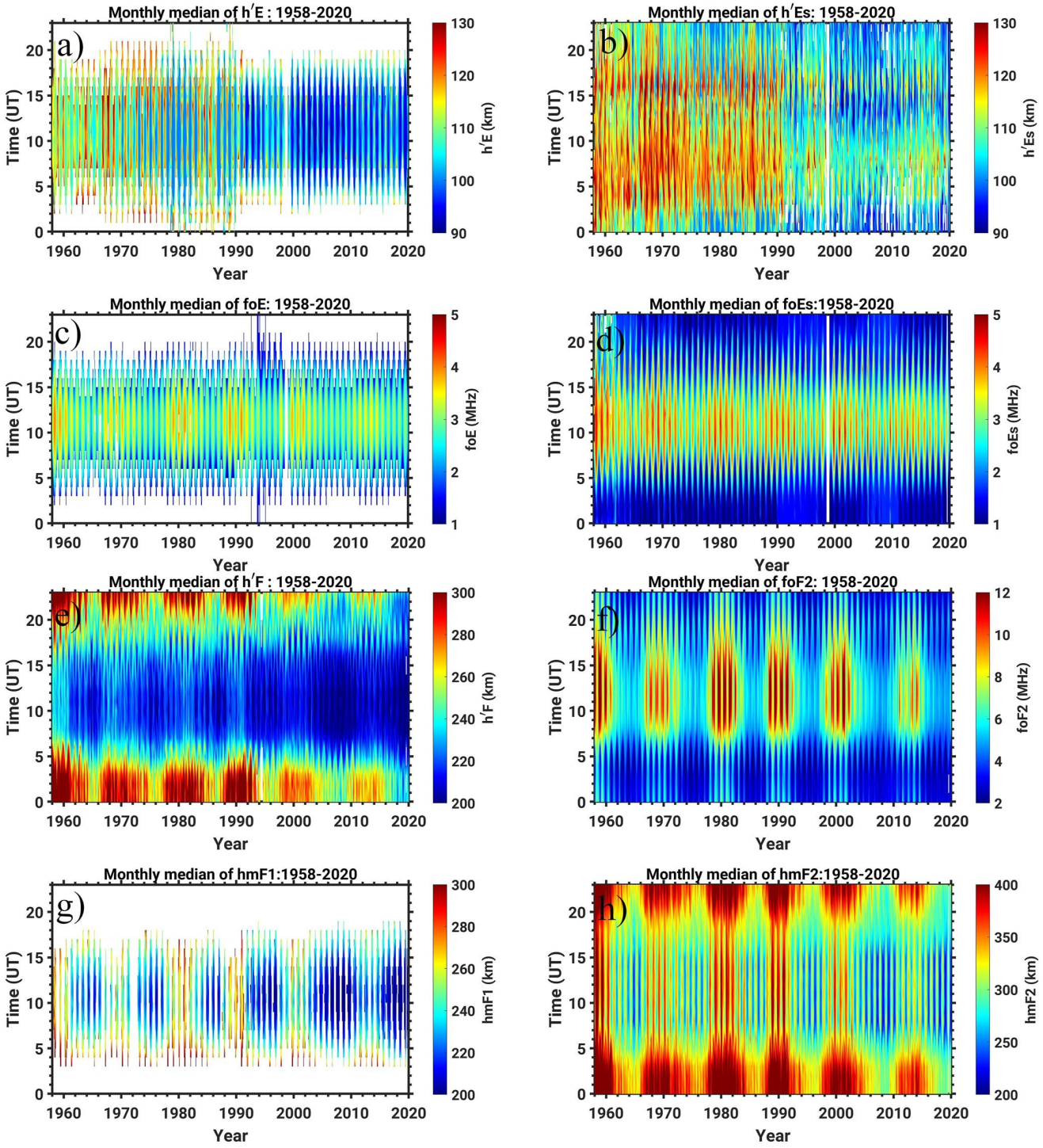

Figure 2. Diurnal variation of the monthly median of hourly E (a–d), and F (e–h) region ionosonde parameters.

3.2. Intra and Inter-Annual Variability of the E- and F-Region Ionosonde Parameters

Figure 2 shows the monthly median of hourly median E- and F-region ionosonde parameters, namely h'E, h'Es, foE, and foEs, from July 1957 to December 2020. The h'E data is available only during the daytime as described in the previous section and does not show any diurnal variation. The distribution of h'Es shows morning and evening time enhancements in all the years, irrespective of height variations before and after 1990. Both the

Journal of Geophysical Research: Space Physics 10.1029/2022JA031097

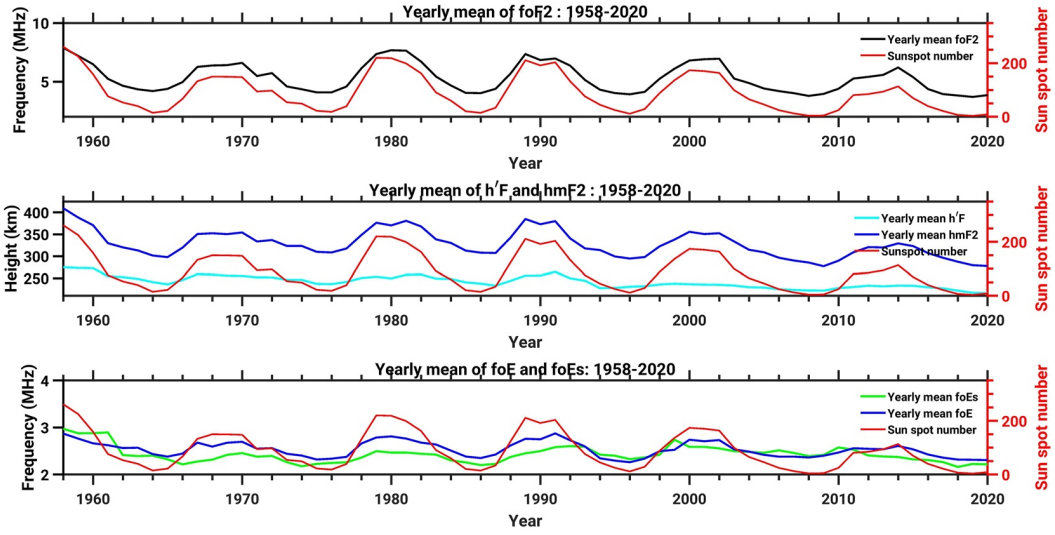

Figure 3. (a) Comparison of an annual mean of foF2 and sunspot number, (b) hmF2 and h'F and sunspot number, and (c) foEs and foE and sunspot number.

h'E and h'Es did not show any solar cycle variation. An important point to be noted here is the high differences in h'E, and h'Es altitudes before and after 1990 (see Figures 2a and 2b). These differences are implications of a high-power ionosonde with a starting frequency of ~500 kHz, which was in operation until 1990. This characteristic allowed a recording of nighttime E layer critical frequencies but led to the scaling of relatively high virtual E layer heights (as mentioned in Section 2.1). Due to these differences, the trend analysis was not performed from these parameters. The magnitude of the foE and foEs show an annual and solar cycle variation as shown in Figures 2c and 2d, and are higher during high solar activity than during lower solar activity years, as it is depicted in Figure 3c. Eventually, during the nighttime echoes from the E region altitudes are not observed for the used frequency range of above 1 MHz.

The diurnal and monthly variations of the h'F are shown in Figure 2e. The h'F is below and above 250 km during the day and nighttime in all the months, respectively. The h'F is very low that is, below 200 km in the daytime of the solar minima years of the last three solar cycles. During the day and nighttime, h'F shows a clear solar cycle variation with higher altitudes during the high solar activity years. Figure 2f shows the diurnal and monthly variations of critical plasma frequency of the F2 (foF2). The foF2 is much higher during the daytime than at nighttime, and the highest frequencies are observed around the local noon. Similarly, the foF2 is higher during the solar maxima years of the solar cycles 19, 21, 22, and 23 than the weaker solar cycles 20 and 24. Diurnal and monthly variations of the hmF1 and hmF2 are shown in Figures 2g and 2h, respectively. The hmF1 altitude is below and above 225 km during solar minima and maxima, respectively, and the echoes from the hmF1 layer are absent during the nighttime irrespective of the solar condition. In the case of hmF2, most often it is below 350 km during the daytime and above 350 km at nighttime. The hmF2 maximum altitudes are located above 400 km during the nighttime of the solar maxima years of the solar cycles 19, 21, and 22.

The annual mean of the E- and F-region parameters viz. foF2 h'F, hmF2, foE, and foEs are shown in Figures 3a–3c to understand the year-to-year and solar cycle variations. In the F-region, foF2 and hmF2 show a strong positive correlation with sunspot number. However, in h'F, the solar cycle dependency is positive but rather feeble. In the E region, foE and foEs display a strong positive correlation till the 23rd solar cycle but weak during the 24th solar cycle. In particular, foEs at the solar minimum year 2008 are higher than at the solar maximum year 2014 (see Figure 3c).

4. Results

4.1. Long-Term Variability and Residual Trends

For the residual trend analysis, we need to perform the LSP analysis to identify the predominant long-period oscillations and their amplitudes for each ionospheric parameter. Using these periods and amplitude of the

Journal of Geophysical Research: Space Physics 10.1029/2022JA031097

estimated oscillations model data are constructed using Equation 1. Obtained long-term variations and trends in the ionosonde parameters are detailed in the following subsections.

4.1.1. Long-Term Variability and Residual Trends in Daytime foE and foEs

Daytime averaged monthly median of foE and foEs and their corresponding LSP are shown in Figures 4a–4d. The overall, daytime mean of foE and foEs is 3.0 ± 0.5 MHz and 3.2 ± 0.6 MHz, respectively. The analysis shows that both of these parameters' annual oscillation is predominant in the E-region followed by the 11 yr solar cycle variation also contributing to the long-term variations. Since the 11 yr of the solar cycle shows a broader range of 9–13 yr, the traditional regression method is used to fit the solar variability. Combining the traditional method, and LSP estimated period and amplitude of the other oscillation (e.g., annual oscillation), a model data is constructed using Equation 1 (detailed in Section 2). A similar analysis is carried out in all other parameters, which are detailed in the following subsections. A comparison of the observation and model estimated foE and foEs from 1958 to 2020 and shown in Figures 4e and 4g, it is obvious from the correlation coefficients (0.966 for foE and 0.902 for foEs) that both are in good agreement with each other. Furthermore, the model values are subtracted from the observational values to deduce the residual variations. By applying the least-square fit on the residual variation the linear slope is estimated and shown in Figures 4f and 4h. As mentioned in Section 2, to avoid the extremes of solar activity at the rim of the time series, the high (the year 1958) and minimum (the year 2019) solar activity effect in the linear slope estimation, we considered only the years from 1964 to 2019 as both these years fall under the low solar activity condition. The foE does not show any significant trend. However, the foEs show a weak negative slope of −2.04 ± 0.61 kHz/yr (±0.61 represents 95% confidence interval). The magnitude of the linear slopes is above the 95% confidence interval. Thus, it is reasonable to assume that the obtained negative trend in the foEs is an outcome of geophysical variation rather than an error or artifact.

4.1.2. Long-Term Variability and Residual Trends in the Day and Nighttime foF2

The monthly medians of day and nighttime averaged foF2 are shown in Figures 5a and 5c, and their corresponding LSP analysis are shown in Figures 5b and 5d, respectively. The 63 yr mean of a day and nighttime foF2 is ∼7 ± 2 MHz and ∼4 ± 1 MHz, respectively. From Figures 5b and 5d, a distinct feature is observed that during the daytime the amplitude of the 11-yr solar cycle variation is more predominant than the annual oscillation. In contrast, the amplitude of the annual oscillation is comparable to or larger than the 11-yr solar cycle variation at nighttime. Figures 5e and 5g display the comparison of observed and modeled foF2 values, the model and observed foF2 show a good correlation of 0.991 and, 0.972, during the day and nighttime respectively. The residual values are estimated by subtracting the model values from the observation, which is shown in Figures 5f and 5h (black curve), in these figures the slope of the least-squares fit is also shown (red dotted line). Interestingly, the day and nighttime foF2 show weak negative slopes of −4.44 ± 1.78 kHz/yr, and −4.30 ± 1.63 kHz/yr. Moreover, the magnitude of the negative trends in the day and nighttime foF2 is statistically significant.

4.1.3. Long-Term Variability and Residual Trends in the Day and Nighttime hmF2

Figures 6a–6d shows the day and nighttime averaged monthly median of hmF2 and their corresponding LSP analysis. The mean altitude of the day and nighttime hmF2 is found at 303 ± 43 km and 363 ± 41 km, respectively. The hmF2 shows the nighttime F2 peak altitude is higher than the daytime. Another interesting observation is that the annual oscillation is more predominant than the 11-yr solar cycle variation during the daytime, whereas for the nighttime hmF2 basically only the 11 yr solar cycle is visible. The observation and model hmF2 values are remarkably in agreement with each other the correlation coefficient is shown in Figures 6e and 6g. The linear residual slope is negative for both day and nighttime with the magnitude of −413 ± 47 m/yr and −574 ± 75 m/yr, however, for both day and nighttime, the estimated slope is well above the 95% confidence interval. From these results, it is clear that the ionospheric peak height shows a descending tendency. Moreover, the rate of descending is nearly the same during the day and nighttime. Overall, day and nighttime E- and F-region linear residual trends estimated in the present study are given in Table 1.

4.2. Trend Estimation Before and After the Year 1996

To investigate if there is any secular trend in different time intervals, we have divided the data into two parts viz 1964–1996 and 1997–2019. This period has been selected for two reasons: (a) We are carrying out the trend

Journal of Geophysical Research: Space Physics 10.1029/2022JA031097

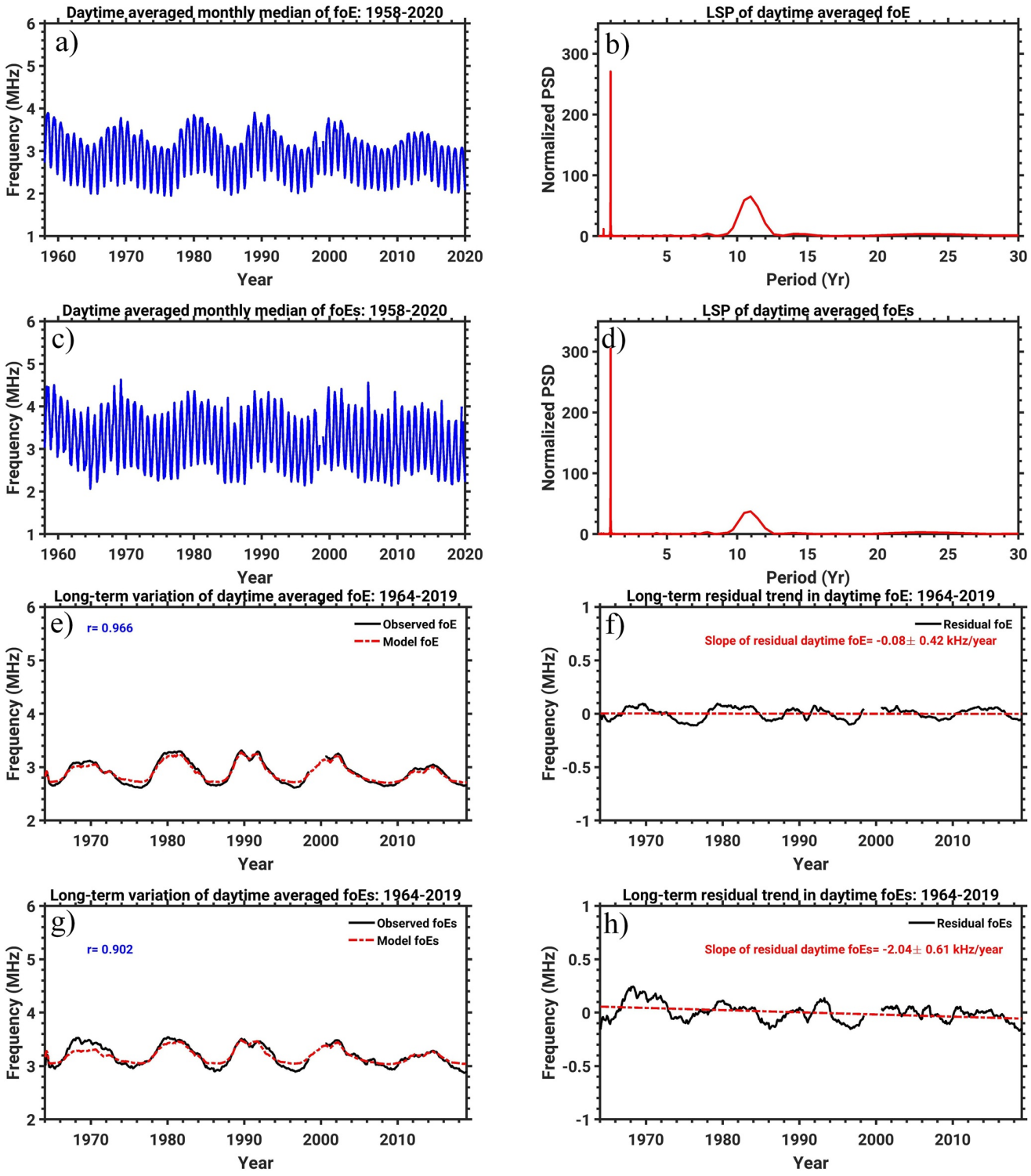

Figure 4. (a & c) Daytime averaged monthly median of foE and foEs and their Lomb-Scargle periodogram (LSP) analysis (b & d), respectively. (e & g) Comparison of observation and model foE and foEs, (f & h) residual (black curve) of the foE and foEs and their linear trends (red dotted line).

analysis of solar minimum and minimum, and (b) To investigate if there are any drastic changes in the last two solar cycles. The estimated trend for foE, foEs, foF2, and hmF2 is listed in Table 2. Since the new and traditional methods' estimated trends are in good agreement, we have shown only the figures for the new method. Figures using the traditional method are attached as Figures S6 and S7 in the Supporting Information S1.

Journal of Geophysical Research: Space Physics 10.1029/2022JA031097

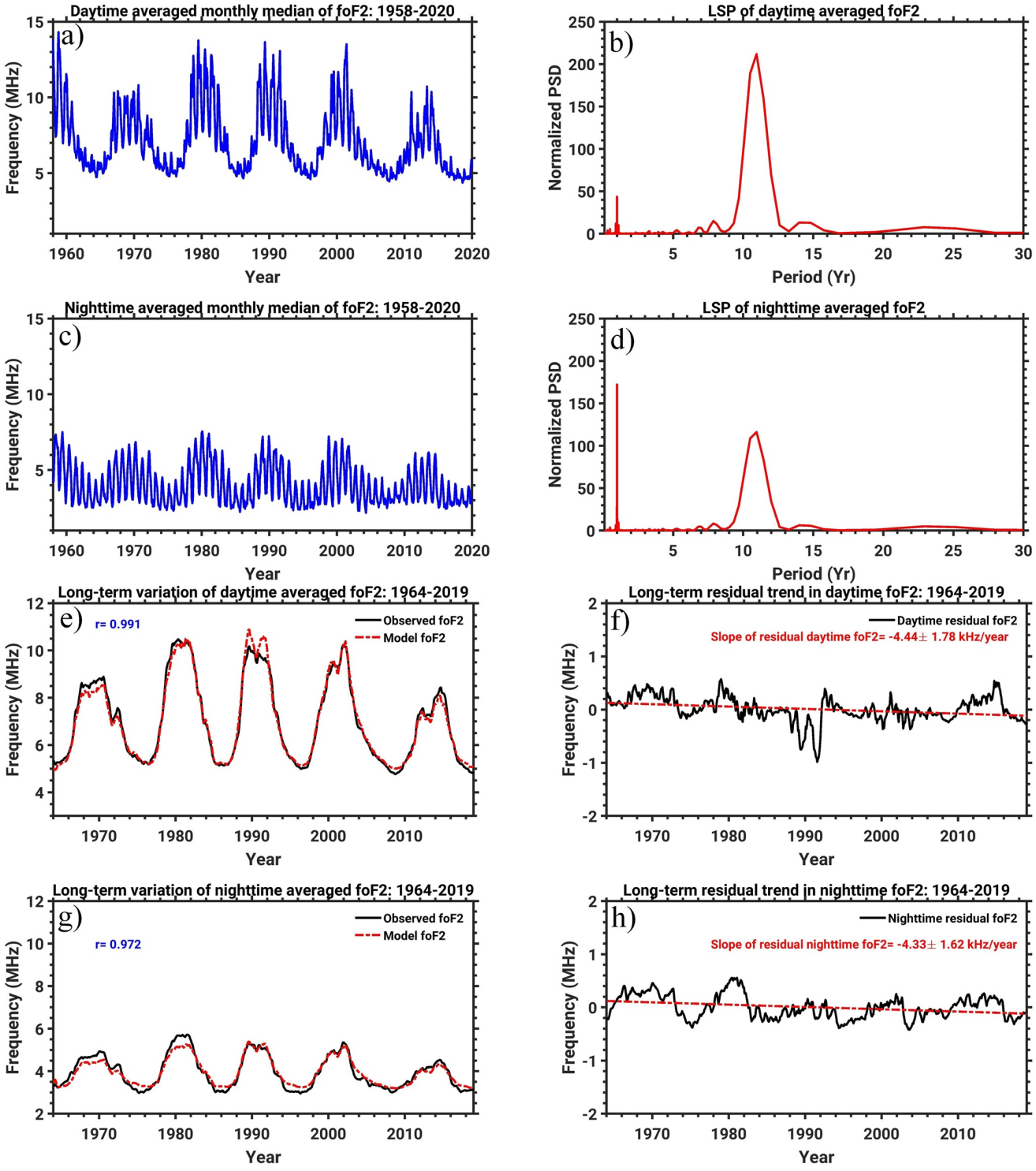

Figure 5. Same as Figure 4 but for day and nighttime foF2.

Long-term variations of daytime foE and foEs (left panel) and their corresponding residual trends (right panel) are shown in Figures 7a–7h for the years before (Figures 7a–7d) and after (Figures 7e–7h) 1996. For both the foE and foEs the residual trend is negative before and after the year 1996. However, for foE magnitude of the slope is below the significant level. The split time series foEs trend is slightly higher than for the whole period.

Journal of Geophysical Research: Space Physics 10.1029/2022JA031097

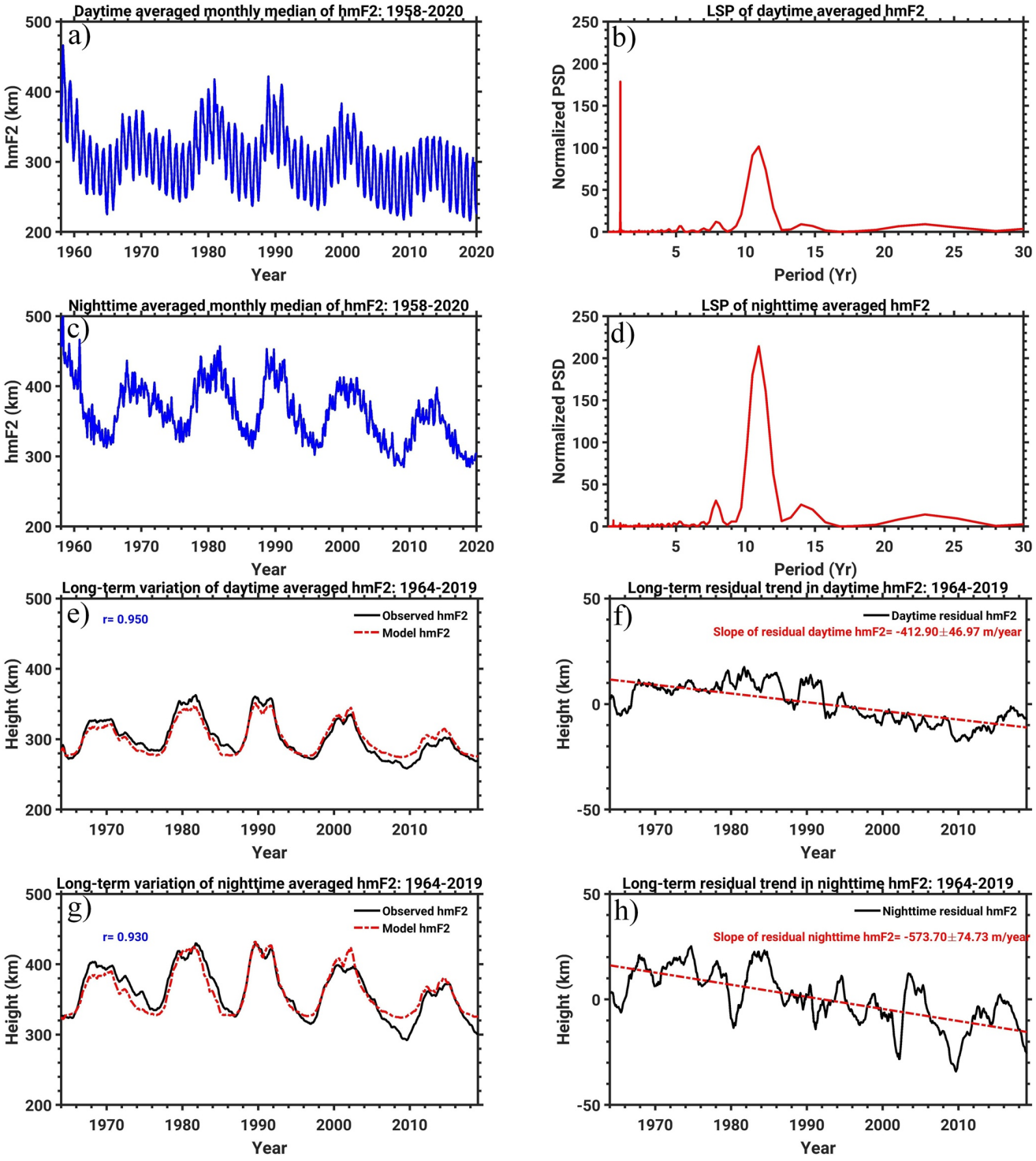

Figure 6. Same as Figure 4 but for day and nighttime hmF2.

Figure 8 denotes the long-term variation of day and nighttime foF2 and their residual trend before (Figures 8a–8d) and after (Figures 8e–8h) the year 1996. Interestingly, the foF2 trend is significantly higher between 1964 and 1996 than in 1997–2019. Moreover, foF2 shows a positive slope during the interval of 1997–2019, however magnitude of the trend is below the significant level. This shows that critical frequency in the F-region has a secular trend and/or piecewise linear trend.

Journal of Geophysical Research: Space Physics 10.1029/2022JA031097

Table 2
Linear Residual Trends in E- and F-Region Parameters Using the New Method During 1964–1995 and 1996–2019

	Linear residual trend (kHz/yr)			
	Daytime		Nighttime	
Parameters	1964–1996	1997–2019	1964–1996	1997–2019
foE	−0.45 ± 1.00	−0.77 ± 1.43	Nil	Nil
foEs	−3.79 ± 1.49	−3.54 ± 1.89	Nil	Nil
foF2	−14.75 ± 3.93	4.60 ± 5.42	−12.98 ± 3.71	0.49 ± 4.78
hmF2[a]	−74 ± 98	−87 ± 114	−455 ± 152	−488 ± 311

[a]Linear trend unit is in m/yr.

The long-term variation of day and nighttime hmF2 and their residual trends are shown in Figures 9a–9h, for the years before (Figures 9a–9d) and after (Figures 9e–9h) 1996. The residual trend is negative for both the day and nighttime of hmF2 as well as before and after the year 1996. Furthermore, the daytime negative slope is weaker than the nighttime for both the interval of 1964–1996 and 1997–2019. Moreover, the magnitude of the daytime slope is below the significant level for both time intervals. The magnitude of the nighttime trend is nearly the same before and after the year 1996. This shows that the residual trend in the hmF2 is a linear decrease from 1964 to 2019.

5. Discussion

In the present study, we used a new approach by combining the traditional method with a new method to estimate the long-term variations and linear residual trends, which will help to better understand their behavior in the E- and F-region over Juliusruh, Germany. From the new approach, we found the following advantages (a) the new method confirms trends from the traditional method, (b) the traditional method shows poor performance to reproduce the semi-annual and annual variations, however, the new approach shows better performance for nighttime foF2, daytime hmF2, foE and foEs (Figures S4 and S5 with a correlation coefficient of model and observation is attached in the Supporting Information S1 and Table S2). During our data analysis, we also found that the magnitude of the linear trend estimation is highly affected by the long-period oscillations (e.g., solar cycle) more than the short-period ones (e.g., semi-annual and annual oscillations). Moreover, the short-period oscillations only affect the significance level. Therefore, it is essential to remove both short and long-period oscillations from the time series data for better trend estimation.

In the F-region, it is expected that the 11-yr solar cycle variation is the prime driver for long-term oscillation. However, the day and nighttime show a different picture, for example, for daytime hmF2 and nighttime foF2, the peak amplitude of the annual oscillation is comparable to or higher than the 11-yr solar cycle. This suggests that while using the foF2 and hmF2 monthly median data for the long-term trend estimations, in addition to the solar cycle variation annual oscillation is also to be removed. The present study day and nighttime foF2 shows a similar negative trend of −4.44 ± 1.78 and −4.33 ± 1.62 kHz/yr, respectively. The magnitude of the estimated trends is in good agreement with earlier investigations (Danilov, 2015; Mielich & Bremer, 2013). There are two main parameters that could cause a trend in the foF2 namely, temperature (T_n) and/or atomic Oxygen (O) concentration. Rishbeth (1990) postulated that the global cooling may not have any significant impact on daytime critical frequency foF2, because the cooling will increase the O/N2 which will cause an increase in the plasma density. On the other hand, the loss coefficient also will increase which causes to decrease in the plasma density, a combination of these two effects will cancel out each other. However, using three ionosonde stations over Europe (including Juliusruh), Danilov (2015) reported a negative trend with a maximum during the daytime and a minimum at nighttime. Furthermore, the earlier investigations also showed that the negative trend is stronger during the winter than in the summer. The magnitude of the negative trend obtained from the present study is nearly equal to the summer daytime trend reported by (Danilov, 2015). According to Mikhailov (2000), the electron density concentration maximum of the F2 layer (N_mF_2) at a fixed pressure level/height is

$$N_mF_2 \propto \left([O]^{0.65}/(T_n)^{0.83}\right) \times ([O]/[N_2])^{0.65} \quad (4)$$

Journal of Geophysical Research: Space Physics 10.1029/2022JA031097

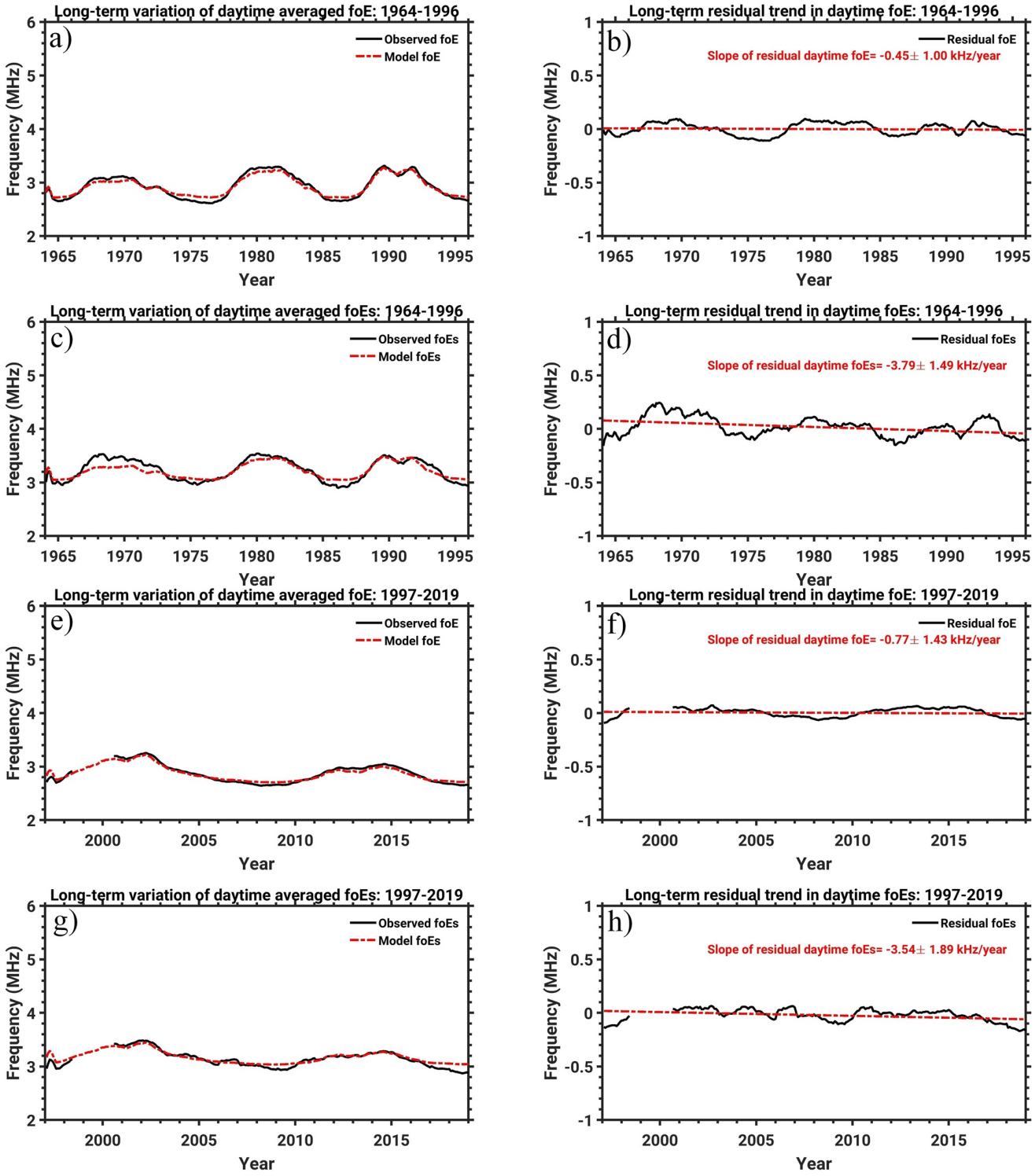

Figure 7. Daytime foE and foEs residual trends before (a–d) and after (e–h) the year 1996.

The F2 layer floats at a constant pressure level (Rishbeth & Edwards, 1989), due to which the second term of the equation mostly would not change. At the same time, changes in the first term can affect the electron density maximum and so in foF2. In fact, a decrease in temperature due to the CO_2 cooling in the upper atmosphere should slightly increase the NmF2, as a result, there should be a positive trend. Instead, the present results indicate

Journal of Geophysical Research: Space Physics 10.1029/2022JA031097

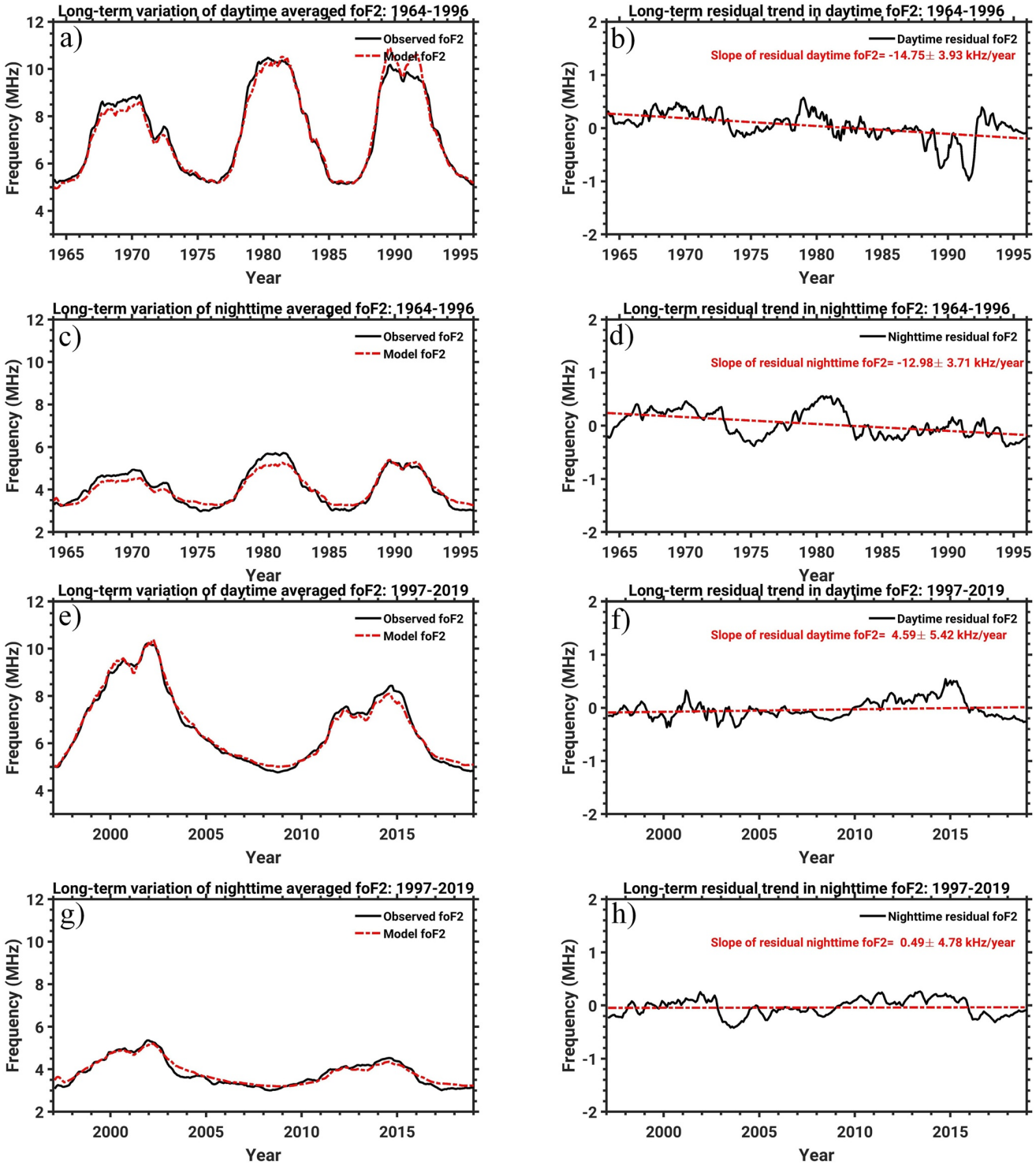

Figure 8. Same as Figure 7 but for day and nighttime foF2.

a weak negative trend in the foF2, This suggests that the noted negative trend may be associated with a decrease in the atomic Oxygen concentration than the neutral temperature. Using mass spectrometer data from 1966 to 1992, Pokhunkov et al. (2009) reported a negative trend in the atomic oxygen concentration at the altitude range of 100–160 km in the northern hemisphere. Furthermore, they also concluded that 15%–20% changes in the negative trend could be caused by the solar forcing and the remaining contribution may be due to anthropogenic changes

Journal of Geophysical Research: Space Physics 10.1029/2022JA031097

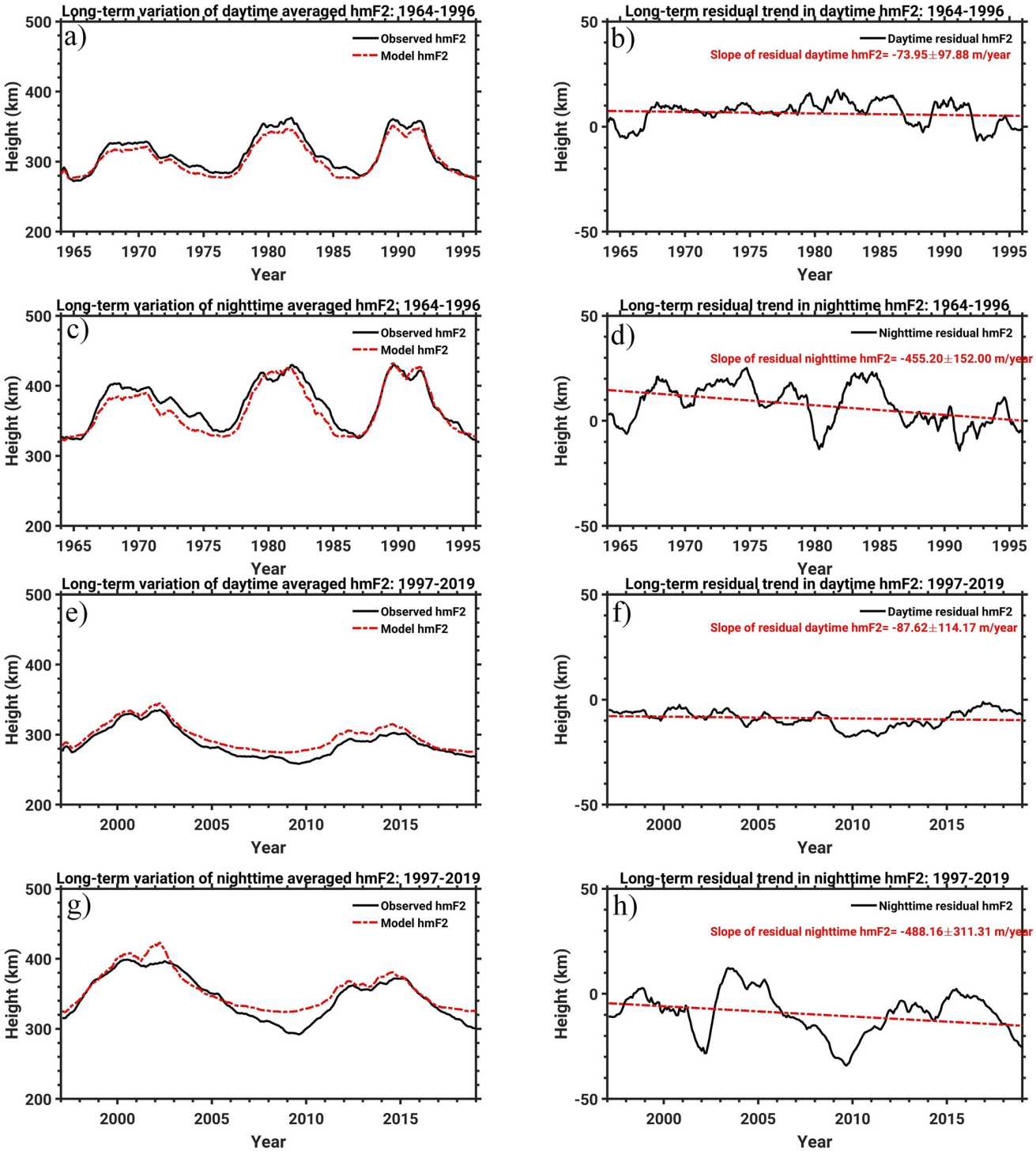

Figure 9. Same as Figure 7 but for day and nighttime hmF2.

originating from the lower atmosphere. This further supports the idea that the changes in the composition are a primary factor for the observed negative trends in the foF2. In addition to the composition, dynamical factors such as neutral meridional wind also could have some role in the trend. For example, using model simulations Qian et al. (2009) also showed a negative and positive trend in the day, and nighttime foF2 respectively, for which they argued the greenhouse effect is the prime driver, and meridional neutral wind dynamics also have a significant

Journal of Geophysical Research: Space Physics 10.1029/2022JA031097

role. In order to investigate the secular trend (if any), we split the whole data into two-time series viz. 1964–1996 and 1997–2019. Interestingly, the negative trend is three times larger than the overall trend during the interval of 1964–1996. The negative trend in atomic oxygen could be the main cause for the negative trend in foF2 during 1964–1996. The magnitude of the residual trend is positive during the interval of 1997–2019, however, they are below the 95% significance level. This positive signature in the residual slope suggests that, unlike the previous interval in the last two decades, the cooling effect could be more dominant than the changes in the compositions.

The residual of day and nighttime hmF2 also shows a decreasing trend of -413 ± 47 and -574 ± 75 m/yr, respectively, during the period of 1964–2019. The magnitude of the present trend during daytime is in good agreement with an earlier investigation by Mielich and Bremer (2013) over Juliusruh. In addition, the present study also indicates that the nighttime trend is slightly higher than the daytime. At daytime, due to the interaction of chemical loss, plasma diffusion, and neutral winds, the height of the E- and F-layer peaks corresponds to a fixed pressure level in the neutral atmosphere. Whereas at nighttime, the E-layer is weak and not observable by ionosonde, and the dynamical processes such as neutral winds and electric fields drive the F2-layer (Rishbeth & Edwards, 1989). Under the steady-state assumption, a ∼50 K decrease in temperature could lower the ionospheric peak altitude (hmF2) by 15 and 20 km at noon and midnight, respectively (Rishbeth, 1990). In the last 56 yr, the hmF2 altitude decreased by 23 and 32 km during the day and nighttime, respectively. The magnitude of the daytime trend is in good agreement with the estimation of Rishbeth (1990), and the nighttime trend is even higher than the expected values. These results suggest that the contraction in the upper atmosphere by the greenhouse effect cooling could be a primary factor for the decreasing trend in the hmF2. Furthermore, we also suggest that during the daytime the insolation might try to compensate for the cooling effect, which could be one of the reasons for the observed difference between the magnitude of daytime and nighttime trend.

The present study shows that the nighttime hmF2 trend is nearly the same in two different intervals of 1964–1996 and 1997–2019. However, the magnitude of the daytime trend decreased significantly and it is below the significance level for both these intervals. This suggests that the cooling of the upper atmosphere is persisting for the last half-century. Overall, these results evidence that the hmF2 trend is linear in nature during the period of 1964–2019.

In addition to the CO_2 cooling, secular changes in the geomagnetic activity are also proposed as a driver for the long-term trend in the F2 layer. During the period of 1965–2020, according to the International Geomagnetic Reference Field model the geomagnetic latitude changed from 54.31°N in 1965 to 54.14°N in 2020, implicating negligible effect in Juliusruh. However, the geomagnetic variations are highly regional dependent that could not explain the noted day and nighttime differences. This arises the question of why the decreasing trend or ionospheric response to the cooling effect during the day and nighttime is different.

In the E-region, the critical frequencies namely, foE and foEs depict robust annual and weak 11-yr solar cycle oscillations. These oscillations could be caused by seasonal and long-term variations of solar heating. Since the nighttime E-layer is weak and not observable by ionosonde, we estimate only the daytime linear residual trend in the foE and foEs. Earlier, Mikhailov (2006) reported a positive trend in foE, and similarly, Bremer and Peters (2008) also showed a positive trend in foE from 1957 to 2002, over Juliusruh. Similarly, the present result also shows a very weak positive trend in both the new and traditional methods, however, the magnitude of the trend is statistically insignificant. Two potential drivers are proposed for the E region plasma density trends in literature, namely (a) decrease of NO in the E region heights (Mikhailov, 2006) and changes in the stratospheric ozone (Bremer & Peters, 2008). In addition, Mikhailov and de la Morena (2003) found foE trends to be geomagnetically controlled before about 1970. Followed by Laštovička (2005) reported that the role of solar and geomagnetic activity decreased from the beginning to the end of the twentieth century. According to Bremer and Peters (2008), the foE trend is in anti-correlation with the O_3. Overall, the E-region parameter trends are very weak and, therefore, very sensitive to various influences.

The daytime foEs show a statistically significant weak negative trend of 2.00 ± 0.61 kHz/yr. In general, the wind shear theory is a well-recognized mechanism for the formation of the Es layer in the mid-latitudes (Mathews, 1998). According to the wind shear theory, ions with significant lifetimes against recombination are accumulated by the westward neutral winds above and eastward or weak westward wind below in the E-region. Studies also have suggested that in the mid-latitudes, the Es-layer occurrence rate strongly depends on the combination of negative wind shears and sporadic meteor deposition in the upper atmosphere (Haldoupis et al., 2007). Furthermore, the wind shear in the mesosphere lower thermosphere is primarily

Journal of Geophysical Research: Space Physics 10.1029/2022JA031097

driven by the tides, particularly diurnal, semidiurnal, terdiurnal, and quarterdiurnal tides in the mid-latitudes, thus the Es layer occurrence also shows a semi-diurnal tidal pattern (Arras et al., 2009; Jacobi & Arras, 2019). A recent study using meteor radar wind observations shows a tendency of stronger eastward and southward directed winds during the last decade (Jacobi et al., 2015) for the mid-latitudes. Thus, we suggest that the weakening of the westward wind in the E-region altitude could suppress the ion accumulations as a consequence the wind shear could be a reason for the obtained negative trend in foEs. Besides, meteor deposition and tidal variability's role in the foEs negative trend is also worth investigating in the future. We also observed that the foEs trend is negative during the period of 1964–1996 and 1997–2019 with magnitudes of -3.79 ± 1.49 and -3.54 ± 1.89, respectively. This suggests that the decreasing trend in the daytime foEs is also linear in nature.

6. Concluding Remarks

The present study investigates the long-term variations and linear residual trends using 63 yr of the E- and F-region ionosonde parameters: foE, foEs, foF2, and hmF2 from Juliusruh. The obtained results and their causes are listed below:

1. Using the LSP analysis the predominant oscillations in the E- and F-region ionosonde parameters are identified.
2. The present analysis exhibit that the annual and solar cycle oscillation has a significant role in the long-term variation in the critical plasma frequencies and altitudes of the F2 layer. The amplitude of the 11-yr solar cycle oscillation is more dominant than the annual oscillation in the daytime foF2, and nighttime hmF2, and the peak amplitude of the annual oscillation is higher than the solar cycle in nighttime foF2 and daytime hmF2. On the other hand, the annual oscillation presides over the 11-yr solar cycle oscillation in the daytime foE and foEs.
3. Using the period and amplitude of the predominant semi-annual and annual oscillations in combination with traditional regression analysis model values of foE and foEs, hmF2, and foF2 are constructed, and these model estimates are comparable with the observation. The residual values are estimated by subtracting the model values from the observation. Then, by applying the least-squares fit analysis long-term trends in the above parameters are calculated. The results obtained from the new method are well consistent with the traditional method.
4. In the F-region, overall the day and nighttime median foF2 shows a weak negative trend of 4.44 ± 1.78 and 4.30 ± 1.63 kHz/yr, respectively. Furthermore, the foF2 also shows a secular trend pattern of a large negative during 1964–1996, and a statistically insignificant but positive slope in the period of 1997–2019, respectively. Thus, we postulate that decreasing trend in the atomic oxygen could be a driver for the observed negative trend, and the large decline in the neutral temperature in the last two decades could be a cause for the noted weak positive trend in the foF2 over Juliusruh.
5. Overall, the day and nighttime median hmF2 show a negative trend of 413 ± 47 and 574 ± 75 m/yr, respectively. Thus, the nighttime hmF2 trend is stronger than in the daytime. Our investigation suggests that the contraction of the upper atmosphere due to the greenhouse effect cooling is the prime driver for the decreasing trend in the hmF2.
6. In the E-region, we found a weak positive slope in the daytime foE, however, its magnitude is below the 95% significance level. On the other hand, the daytime foEs show a negative trend of -2.00 ± 0.61 kHz/yr. We speculate that changes in the neutral wind shear might be a driving mechanism for the noted negative trends in foEs.

Data Availability Statement

The ionosonde data used in this study are openly available at https://www.sws.bom.gov.au/World_Data_Centre/1/3. The sunspot number and daily mean F10.7 data are available at https://lasp.colorado.edu/lisird/data/american_relative_sunspot_number_daily/ and https://lasp.colorado.edu/lisird/data/noaa_radio_flux/.

Acknowledgments
One of the authors, M.S. acknowledges the financial support provided by the Alexander-von-Humboldt Foundation and the research opportunity provided by the Leibniz Institute of Atmospheric Physics (IAP). J.L. acknowledges support from the Czech Science Foundation under Grant 18-01625S. T.R. has been supported by the Deutsche Forschungsgemeinschaft under VACILT project, Grant PO 2341/2-1. J.J. acknowledges the financial support by Federal Ministry of Education and Research (BMBF) Grant 01LG 1902A. One of the authors M.S. acknowledges Dr. D.H.W. Peters for reading the revised draft and for his valuable suggestions. The authors thank two anonymous reviewers for their valuable suggestions and comments which enhanced the quality of the paper. Open access funding enabled and organized by Projekt DEAL.

References

Abdu, M. A., Batista, I. S., Muralikrishna, P., & Sobral, J. H. (1996). Long term trends in sporadic E layers and electric fields over Fortaleza, Brazil. *Geophysical Research Letters*, *23*(7), 757–760. https://doi.org/10.1029/96GL00589

Arras, C., Jacobi, C., & Wickert, J. (2009). Semidiurnal tidal signature in sporadic E occurrence rates derived from GPS radio occultation measurements at higher midlatitudes. *Annales Geophysicae*, *27*(6), 2555–2563. Retrieved from https://angeo.copernicus.org/articles/27/2555/2009/. https://doi.org/10.5194/angeo-27-2555-2009

Bremer, J. (1992). Ionospheric trends in mid-latitudes as a possible indicator of the atmospheric greenhouse effect. *Journal of Atmospheric and Terrestrial Physics*, *54*(11), 1505–1511. https://doi.org/10.1016/0021-9169(92)90157-G

Bremer, J. (2008). Long-term trends in the ionospheric E and F1 regions. *Annales Geophysicae*, *26*(5), 1189–1197. https://doi.org/10.5194/angeo-26-1189-2008

Bremer, J., Alfonsi, L., Bencze, P., Laštovička, J., Mikhailov, A. V., & Rogers, N. (2004). Long-term trends in the ionosphere and upper atmosphere parameters. *Annals of Geophysics*, *47*(2–3 Sup.), 1009–1029. https://doi.org/10.4401/ag-3283

Bremer, J., & Peters, D. (2008). Influence of stratospheric ozone changes on long-term trends in the meso- and lower thermosphere. *Journal of Atmospheric and Solar-Terrestrial Physics*, *70*(11–12), 1473–1481. https://doi.org/10.1016/j.jastp.2008.03.024

Burešová, D. (1997). Results of foF2 data testing with the UNDIV program. *Studia Geophysica et Geodaetica*, *41*(1), 82–87. https://doi.org/10.1023/A:1023392808566

Cnossen, I. (2020). Analysis and attribution of climate change in the upper atmosphere from 1950 to 2015 simulated by WACCM-X. *Journal of Geophysical Research: Space Physics*, *125*(12), e2020JA028623. https://doi.org/10.1029/2020JA028623

Danilov, A. (2008). Long-term trends in the relation between daytime and nighttime values of foF2. *Annales Geophysicae*, *26*(5), 1199–1206. https://doi.org/10.5194/angeo-26-1199-2008

Danilov, A. (2009). Critical frequency foF2 as an indicator of trends in thermospheric dynamics. *Journal of Atmospheric and Solar-Terrestrial Physics*, *71*(13), 1430–1440. https://doi.org/10.1016/j.jastp.2008.04.001

Danilov, A. (2015). Seasonal and diurnal variations in foF2 trends. *Journal of Geophysical Research: Space Physics*, *120*(5), 3868–3882. https://doi.org/10.1002/2014JA020971

Danilov, A. D., & Konstantinova, A. V. (2020). Long-term variations in the parameters of the middle and upper atmosphere and ionosphere (review). *Geomagnetism and Aeronomy*, *60*(4), 397–420. https://doi.org/10.1134/S0016793220040040

Haldoupis, C., Pancheva, D., Singer, W., Meek, C., & MacDougall, J. (2007). An explanation for the seasonal dependence of midlatitude sporadic E layers. *Journal of Geophysical Research*, *112*(6), 1–7. https://doi.org/10.1029/2007JA012322

Holmen, S. E., Hall, C. M., & Tsutsumi, M. (2016). Neutral atmosphere temperature trends and variability at 90km, 70°N, 19°E, 2003-2014. *Atmospheric Chemistry and Physics*, *16*(12), 7853–7866. https://doi.org/10.5194/acp-16-7853-2016

Jacobi, C., & Arras, C. (2019). Tidal wind shear observed by meteor radar and comparison with sporadic E occurrence rates based on GPS radio occultation observations. *Advances in Radio Science*, *17*, 213–224. Retrieved from https://ars.copernicus.org/articles/17/213/2019/. https://doi.org/10.5194/ars-17-213-2019

Jacobi, C., Lilienthal, F., Geißler, C., & Krug, A. (2015). Long-term variability of mid-latitude mesosphere-lower thermosphere winds over Collm (51°N, 13°E). *Journal of Atmospheric and Solar-Terrestrial Physics*, *136*, 174–186. https://doi.org/10.1016/j.jastp.2015.05.006

Laštovička, J. (2005). On the role of solar and geomagnetic activity in long-term trends in the atmosphere–ionosphere system. *Journal of Atmospheric and Solar-Terrestrial Physics*, *67*(1), 83–92. https://doi.org/10.1016/j.jastp.2004.07.019

Laštovička, J. (2017). A review of recent progress in trends in the upper atmosphere. *Journal of Atmospheric and Solar-Terrestrial Physics*, *163*, 2–13. https://doi.org/10.1016/j.jastp.2017.03.009

Laštovička, J. (2019). Is the relation between ionospheric parameters and solar proxies stable? *Geophysical Research Letters*, *46*(24), 14208–14213. https://doi.org/10.1029/2019GL085033

Laštovička, J. (2021). What is the optimum solar proxy for long-term ionospheric investigations? *Advances in Space Research*, *67*(1), 2–8. https://doi.org/10.1016/j.asr.2020.07.025

Laštovička, J. (2022). Long-Term changes in ionospheric climate in terms of foF2. *Atmosphere*, *13*(1), 110. https://doi.org/10.3390/atmos13010110

Laštovička, J., Akmaev, R. A., Beig, G., Bremer, J., Emmert, J. T., Jacobi, C., et al. (2008). Emerging pattern of global change in the upper atmosphere and ionosphere. *Annales Geophysicae*, *26*(5), 1255–1268. https://doi.org/10.5194/angeo-26-1255-2008

Laštovička, J., Boška, J., Burešová, D., & Kouba, D. (2012). High historical values of foEs-reality or artefact? *Journal of Atmospheric and Solar-Terrestrial Physics*, *74*, 51–54. https://doi.org/10.1016/j.jastp.2011.10.008

Laštovička, J., & Jelínek, Š. (2019). Problems in calculating long-term trends in the upper atmosphere. *Journal of Atmospheric and Solar-Terrestrial Physics*, *189*(10), 80–86. https://doi.org/10.1016/j.jastp.2019.04.011

Laštovička, J., Mikhailov, A. V., Ulich, T., Bremer, J., Elias, A. G., Ortiz de Adler, N., et al. (2006). Long-term trends in foF2: A comparison of various methods. *Journal of Atmospheric and Solar-Terrestrial Physics*, *68*(17), 1854–1870. https://doi.org/10.1016/j.jastp.2006.02.009

Laštovička, J., Solomon, S. C., & Qian, L. (2012). Trends in the neutral and ionized upper atmosphere. *Space Science Reviews*, *168*(1–4), 113–145. https://doi.org/10.1007/s11214-011-9799-3

Mathews, J. (1998). Sporadic E: Current views and recent progress. *Journal of Atmospheric and Solar-Terrestrial Physics*, *60*(4), 413–435. https://doi.org/10.1016/S1364-6826(97)00043-6

Mielich, J., & Bremer, J. (2013). Long-term trends in the ionospheric F2 region with different solar activity indices. *Annales Geophysicae*, *31*(2), 291–303. https://doi.org/10.5194/angeo-31-291-2013

Mikhailov, A. V. (2000). Ionospheric f2-layer storms. *Fisica de la Tierra*, *12*, 223–262.

Mikhailov, A. V. (2006). Trends in the ionospheric E-region. *Physics and Chemistry of the Earth*, *31*(1–3), 22–33. https://doi.org/10.1016/j.pce.2005.02.005

Mikhailov, A. V., & de la Morena, B. A. (2003). Long-term trends of *f*oE and geomagnetic activity variations. *Annales Geophysicae*, *21*(3), 751–760. https://doi.org/10.5194/angeo-21-751-2003

Mikhailov, A. V., & Marin, D. (2001). An interpretation of the foF2 and hmF2 long-term trends in the framework of the geomagnetic control concept. *Annales Geophysicae*, *19*(7), 733–748. https://doi.org/10.5194/angeo-19-733-2001

Pezzopane, M., Pignalberi, A., & Pietrella, M. (2015). On the influence of solar activity on the mid-latitude sporadic E layer. *Journal of Space Weather and Space Climate*, *5*, A31. https://doi.org/10.1051/swsc/2015031

Pignalberi, A., Pezzopane, M., & Zuccheretti, E. (2014). Sporadic E layer at mid-latitudes: Average properties and influence of atmospheric tides. *Annales Geophysicae*, *32*(11), 1427–1440. Retrieved from https://angeo.copernicus.org/articles/32/1427/2014/. https://doi.org/10.5194/angeo-32-1427-2014

Journal of Geophysical Research: Space Physics 10.1029/2022JA031097

Pokhunkov, A. A., Rybin, V. V., & Tulinov, G. F. (2009). Quantitative characteristics of long-term changes in parameters of the upper atmosphere of the Earth over the 1966–1992 period. *Cosmic Research*, *47*(6), 480–490. https://doi.org/10.1134/S0010952509060045

Prasad, S. N., Prasad, D. S., Venkatesh, K., Niranjan, K., & Rama Rao, P. V. (2012). Diurnal and seasonal variations in sporadic E-layer (Es layer) occurrences over equatorial, low and mid latitude stations - A comparative study. *Indian Journal of Radio and Space Physics*, *41*(1), 26–38.

Qian, L., Burns, A. G., Solomon, S. C., & Roble, R. G. (2009). The effect of carbon dioxide cooling on trends in the F2-layer ionosphere. *Journal of Atmospheric and Solar-Terrestrial Physics*, *71*(14–15), 1592–1601. https://doi.org/10.1016/j.jastp.2009.03.006

Qian, L., McInerney, J. M., Solomon, S. S., Liu, H., & Burns, A. G. (2021). Climate changes in the upper atmosphere: Contributions by the changing greenhouse gas concentrations and Earth's magnetic field from the 1960s to 2010s. *Journal of Geophysical Research: Space Physics*, *126*(3), e2020JA029067. https://doi.org/10.1029/2020JA029067

Rao, S., Sharma, S., Galav, P., & Pandey, R. (2014). Variation of monthly mean foF2 and hmF2 over a mid-latitude station during the period 1997–2006. *Advances in Space Research*, *53*(5), 744–751. Retrieved from https://www.sciencedirect.com/science/article/pii/S0273117713008156. https://doi.org/10.1016/j.asr.2013.12.018

Rishbeth, H. (1990). A greenhouse effect in the ionosphere? *Planetary and Space Science*, *38*(7), 945–948. https://doi.org/10.1016/0032-0633(90)90061-T

Rishbeth, H., & Edwards, R. (1989). The isobaric F2-layer. *Journal of Atmospheric and Terrestrial Physics*, *51*(4), 321–338. https://doi.org/10.1016/0021-9169(89)90083-4

Roble, R. G., & Dickinson, R. E. (1989). How will changes in carbon dioxide and methane modify the mean structure of the mesosphere and thermosphere? *Geophysical Research Letters*, *16*(12), 1441–1444. https://doi.org/10.1029/GL016i012p01441

VanderPlas, J. T. (2018). Understanding the Lomb–Scargle periodogram. *The Astrophysical Journal Supplement Series*, *236*(1), 16. https://doi.org/10.3847/1538-4365/aab766

Appendix E

Renkwitz et al. (2023)

Renkwitz, T., Sivakandan, M., Jaen, J., and Singer, W.: Ground-based noontime D-region electron density climatology over northern Norway, Atmos. Chem. Phys., 23, 10823–10834, https://doi.org/10.5194/acp-23-10823-2023, 2023.

Atmos. Chem. Phys., 23, 10823–10834, 2023
https://doi.org/10.5194/acp-23-10823-2023

Atmospheric Chemistry and Physics
Open Access
EGU

Ground-based noontime D-region electron density climatology over northern Norway

Toralf Renkwitz[1], Mani Sivakandan[1,2], Juliana Jaen[1], and Werner Singer[1]

[1]Leibniz Institute of Atmospheric Physics at the University of Rostock,
Schloss-Str. 6, 18225 Kühlungsborn, Germany
[2]Faculty of Mathematics and Natural Sciences, University of Rostock, 18051 Rostock, Germany

Correspondence: Toralf Renkwitz (renkwitz@iap-kborn.de)

Received: 24 April 2023 – Discussion started: 25 April 2023
Revised: 24 July 2023 – Accepted: 31 July 2023 – Published: 4 October 2023

Abstract. The bottom part of the Earth's ionosphere is the so-called D region, which is typically less dense than the upper regions. Despite the comparably lower electron density, the ionization state of the D region has a significant influence on signal absorption for propagating lower to medium radio frequencies. We present local noon climatologies of electron densities in the upper middle atmosphere (50–90 km) at high latitudes as observed by an active radar experiment. The radar measurements cover 9 years (2014–2022) from the solar maximum of cycle 24 to the beginning of cycle 25. Reliable electron densities are derived by employing signal processing, applying interferometry methods, and applying the Faraday-International Reference Ionosphere (FIRI) model. For all years a consistent spring–fall asymmetry of the electron density pattern with a gradual increase during summer as well as a sharp decrease at the beginning of October was found. These findings are consistent with very low frequency (VLF) studies showing equivalent signatures for nearby propagation paths. It is suggested that the meridional circulation associated with downwelling in winter could cause enhanced electron densities through NO transport. However, this mechanism can not explain the reduction in electron density in early October.

1 Introduction

The lower part of the ionosphere is called the D region and generally refers to altitudes below 100 km (Mitra, 1968). The ionization of nitric oxide (NO) and meta-stable oxygen molecules (O_2) in this region's electron concentration is mainly controlled by the Lyman-alpha line and UV radiation, respectively. It is also a region where cluster ions are prevalent. The D region also co-exists with the mesosphere, which is the most dynamic region of the Earth's atmosphere, where temperature decreases with altitude and most of the wave breaking occurs. Diurnal variation in the D-region electron density is primarily controlled by the changes in the solar zenith angle. Unlike in the E and F regions, ions and electron motion in the D region is mainly driven by the neutral winds because the collision frequency is higher than the gyro-frequency (< 80 km). Therefore, the variability in the D region is not only driven by solar radiation but also significantly affected by neutral atmospheric dynamics. For example, the so-called D-region winter anomaly (i.e., enhancement in the electron density during winter) is proposed to be caused by the atmosphere–ionosphere coupling process through the planetary wave, temperature, and composition changes by vertical and meridional transport. Changes in the D-region electron concentration impede the long-distance propagation of high-frequency (HF) radio waves through absorption. Thus, understanding and quantification of the D-region electron density variability and its causative mechanisms are essential.

Continuous observation of the D region is very challenging because of the low electron abundance. There are very few direct observational techniques such as sounding rockets (Mechtly, 1974), incoherent scatter radar (Chau and Woodman, 2005; Baumann et al., 2022), very low frequency (VLF) methods (Worthington and Cohen, 2021), and partial-reflection radars or medium-frequency (MF) radars (Belrose,

1970; Igarashi et al., 2000; Singer et al., 2008) that are effectively used to measure the D-region electron density (see. e.g., Friedrich and Rapp, 2009, for a review). Among them, the rocketborne in situ measurements (Faraday experiment) are highly accurate (capable of detecting even low electron density), but the data availability is comparably sparse because the launching costs are high. Using the available EISCAT radar data and rocket measurements, Friedrich et al. (2004) present the quiet auroral ionosphere and its neutral background. Particularly for the representation of the D region only a limited number of rocket measurements could be used.

In addition to the direct measurements, indirect information on the middle atmosphere ionization state can be obtained by proxies such as riometer absorption, which measures the reduction in incident galactic radio noise relative to a quiet-day curve (Friedrich et al., 2002). The quiet-day curve is typically derived from the previous interference-free days (see, e.g., Moro et al., 2012; Renkwitz et al., 2011). The observed absorption is an integrative parameter attributed to the electron density at altitudes between 80–90 km due to collisions between free electrons and neutrals. During polar cap absorption, the 55-ion Sodankylä model was applied in the inversion of the raw densities measured by the ultra-high-frequency (UHF) EISCAT radar, and that provided some realistic estimates of the actual electron density in the D region (del Pozo et al., 1999). Recently, long-distance subionospheric VLF radio wave observation was also used as an indirect method to investigate the long-term climate change in the D region (Clilverd et al., 2017).

Apart from observations, based on the available data sets and Chapman's theory, there are some statistical (McNamara, 1979), empirical (Friedrich and Torkar, 1992; McKinnell and Friedrich, 2007; Friedrich et al., 2018a), semi-empirical (Friedrich and Torkar, 2001), physical, chemical, and theoretical models (Burns et al., 1991; Verronen et al., 2016; Zhu et al., 2023) that also exist in the literature, and they can reasonably well reproduce the quiet-time lower ionosphere. For example, incorporating several hundred rocket profiles, Friedrich and Torkar (2001) and Friedrich et al. (2018a) developed an empirical model called the Faraday-International Reference Ionosphere (FIRI) model. IMAZ is a neural-network-based empirical model for the lower ionosphere in the auroral zone (McKinnell and Friedrich, 2007) developed for the International Reference Ionosphere (IRI) global model community. Combining two chemical models, namely the Mitra–Rowe simplified 6-ion model and a 35-ion model developed at the Sodankylä Geophysical Observatory, Burns et al. (1991) developed a D- and E-region chemical model called Sodankylä Ion and neutral Chemistry (SIC) model. Later on, Verronen et al. (2005) pointed out that the SIC model could correctly estimate the ionization and electron densities during solar proton events (SPEs) in October–November 2003. A comparative study of electron densities observed from the VLF and rocket measurement with the OASIS (Originally Austrian Study of the IonoSphere) model showed that below 68–70 km the model data agree well with observations. However, above 68–70 km the OASIS model fails to reproduce the observation (Siskind et al., 2018). Overall, the models can be used as a climatological mean representative of the D region; when it comes to the observational dynamical changes, their reliability is questionable at least below 80 km because of the limited availability of the D-region observational data.

As mentioned earlier, the diurnal and seasonal variation in the D-region electron density is primarily caused by the variable solar zenith angle; the Lyman-alpha radiation; and by minor species, notably NO. In addition, D-region electron density also shows an asymmetrical behavior that can not be explained by the solar variation. For example, recently Baumann et al. (2022) reported the electron density is higher during sunset than sunrise. They postulate that the change in the recombination rates is a plausible reason for this observed asymmetry. Similarly, earlier investigations showed enhancement in the D-region electron density during winter (winter anomaly; Offermann, 1979a, b). In winter's absence of sunlight or a reduction in solar radiation, solar EPP (energetic particle precipitation) could be a primary cause of the observed winter anomaly. However, the winter anomaly is also observed in the absence of EPP, so-called "meteorological types" of winter anomaly (Offermann, 1980). There are several mechanisms proposed for the formation of the meteorological types of winter anomaly: changes in the NO due to the transport process associated with atmospheric planetary waves and sudden stratospheric warming events (Kawahira, 1985). Though there are several case studies and periodic campaigns carried out to explore the D-region electron density variations and their causative mechanisms, we are still unable to address the seasonal variation in D-region studies by continuous observations.

A recent study by Macotela et al. (2021) reported that during the fall equinox, there is an increase in the noontime mean amplitude of VLF radio waves in high and middle latitudes not relate to the solar zenith angle (SZA; see Fig. 3); they called this a fall effect. They showed that during that time a decrease in the background temperature and an increase in the semi-diurnal tide (S2) amplitude are observed. Thus, they postulate that the changes in the collision frequency associated with the background temperature could be a prime reason for the observed increase in the noontime VLF amplitude. It is well known that the VLF radio waves are drastically affected by the D-region electron density; however, Macotela et al. (2021) did not consider the electron density role (if any) in the fall effect. Therefore, this study focuses on exploring the altitudinal and seasonal variation in noontime electron density using partial-reflection radar observations from 2014 to 2022 at a high-latitude location.

In the following sections, we will introduce the instrument used in this study, followed by a brief description of the ex-

periment and methods to derive electron densities in Sect. 2. This includes the advances we recently made in the processing and outlier removal by, e.g., applying the FIRI model as a quiet reference. It also includes the detection of EPP and splits the radar data into quiet and solar, geomagnetically active periods. In Sect. 3 the results, namely the annual noontime electron density profiles including the 9-year climatology, are presented. Furthermore, we discuss the specific features found and the probable connections to other phenomena. Finally, we conclude our findings in Sect. 4.

1.1 The Saura radar

The Saura radar is a modular partial-reflection radar built in 2002 on the island of Andøya (69° N, 16° E). The radar operates at 3.17 MHz, and due to the proximity to the medium frequencies, it is often referred to as an MF radar. The specialty of this instrument is the comparably large Mills Cross antenna array spreading over roughly 1×1 km (see Fig. 1). Each dipole antenna forming the sketched crossed dipoles is connected to an individual phase-controlled transceiver module capable of 2 kW peak power. This configuration allows for the emission of circularly polarized pulsed radio waves and beamforming for different pointing directions, which makes it unique for this frequency range.

One major scientific target of this instrument is the measurement of winds in the lower ionosphere, namely the D region. Such measurements are widely performed by a Doppler beam swinging (DBS) experiment, measuring the radial velocity components for distinct vertical and four oblique beam-pointing directions. The horizontal resolution for DBS is typically less than 10 km at 80 km altitude.

Alternatively, full correlation analysis (FCA; e.g., Briggs, 1984) can be applied and is especially advantageous for higher-altitude imaging Doppler interferometry (IDI; e.g., Palmer et al., 1995; Roper and Brosnahan, 1997); see Renkwitz et al. (2018) for more details and its application with the Saura radar. For the last few years the Saura radar wind measurements have been performed with a resolution of at best 4 min, and the same cadence is applicable for electron density measurements. However, larger windows of up to 12 min are often used to reduce the uncertainty.

The latest upgrades to the radar included the introduction of pulse code capability and the addition of three digital receiver channels to improve the signal-to-noise ratio and strengthen interferometric methods.

2 Electron density experiment description

Two methods may be used with sufficiently large MF radars to deduce electron densities in the D region, making use of observing the wave absorption and Faraday rotation. They are normally referred as differential phase experiments (DPEs) and differential amplitude experiments (DAEs), analyzing the radar echoes from alternating transmission of both

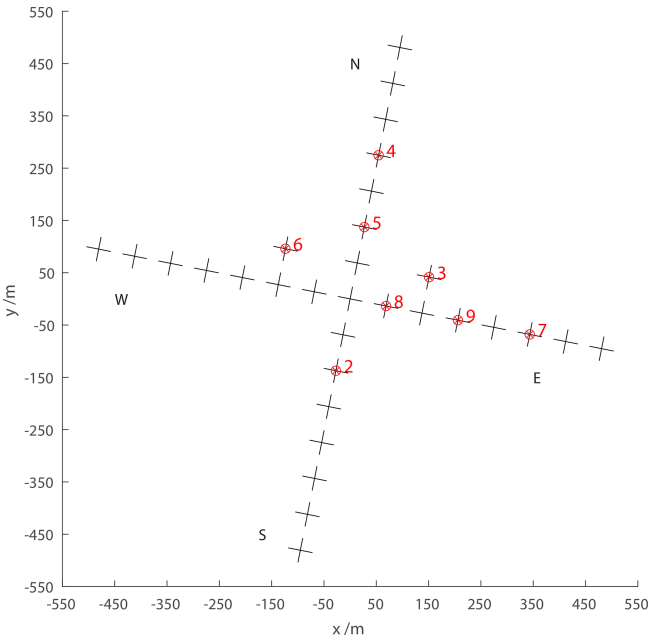

Figure 1. Sketch of the Saura radar antenna array; marked antennas are connected to individual receiver channels used for interferometry.

magneto-ionic modes. These techniques were described by, e.g., Sen and Wyller (1960), Belrose (1970), Budden (1983), and more recently Vuthaluru (2003) and were also applied by, e.g., Grant et al. (2004), Osepian et al. (2008), or Liu et al. (2020) and Zhu et al. (2023) to the MAI and Kunming radar systems.

Equation (1) describes the relation of the amplitude ratio A_x/A_o to the ratio of reflection coefficients R_x/R_o for the height interval Δh for DAEs, in which k_x and k_o are the absorption indices and are related to the imaginary part of the complex refractive indices by a factor ω/c for both magneto-ionic modes. For DPEs the differential phases of the two modes and the reflection coefficients are compared and normalized by the real part of the refractive indices, μ_x and μ_o, per height interval (Eq. 2):

$$N_{\mathrm{DAE}}(h) = \frac{\Delta(\ln R_x/R_o) - \Delta(ln\, A_x/A_o)}{2(k_x - k_o)\Delta h}, \tag{1}$$

$$N_{\mathrm{DPE}}(h) = \frac{\Delta(\phi R_x - \phi R_o) - \Delta(\phi A_x - \phi A_o)}{2(\mu_x - \mu_o)\Delta h}. \tag{2}$$

For this study, we restrict where we apply the high-latitude approximation of the Sen–Wyller refractive index to DPEs after Flood (1980). For the Saura radar, equivalent experiments have been carried out not only by Singer et al. (2008, 2011) and Renkwitz et al. (2021) but also, e.g., with the Buckland Park radar by Holdsworth et al. (2002). The pressure and temperature profiles are taken from CIRA-86

Table 1. Saura experiment parameters.

	vert-ox	sd-07ox-4c
Beam directions	$\theta = 0°, \phi = 0°$	$\theta = 0°, \phi = 0°$ $\theta = 6.7°, \phi = 56.2,$ 146.2, 236.2, 326.2°
Code	single pulse	4 bit complementary
Range resolution	1000 m	1000 m
Pulse repetition	75/30 Hz	100/30 Hz
Runtime	215 s	235 s

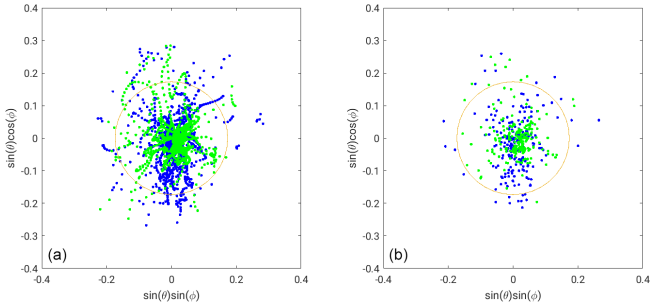

Figure 2. Example of derived angle-of-arrival (AOA) positions for O and X mode, depicted in blue and green, respectively. **(a)** Original resolution. **(b)** With 1 s integration time. The orange circle marks the selected 10° area of interest.

for consistency because, e.g., rocketborne falling-sphere experiments did not cover the winter period. Lübken (1999) found the deviations from CIRA-86 to be within about ±5 % for altitudes below 80 km. We tend to rely on CIRA-86 as we also work on comparable experiments for the middle-latitude station Juliusruh (54.6° N, 13.4° E) for which no rocketborne data exist. For the magnetic field, $51\,800 \times 10^{-9}$ T after IGRF-13 (International Geomagnetic Reference Field; Alken et al., 2021) and $\theta = 11.9°$ are used for the radar location.

Electron densities have been derived from two different experiments that have probed the atmosphere with alternating circular polarization, matching both magneto-ionic components (ordinary, extraordinary). The vert-ox experiment is an uncoded vertical-only experiment, whereas the sd-07ox-4c experiment is a 4 bit complementary-code Doppler beam swinging (DBS) experiment probing five different directions primarily intended for wind measurements (see Table 1 for more experiment details). The experiments have durations of 215 and 235 s for the vertical-only and DBS experiments, respectively, which cover multiples of the typical correlation time of the observed structures. The shorter runtime of the vertical experiment is chosen to allow a short high-range monitor experiment, which is not used here. Thus for most of the measurements, almost continuous sampling is maintained without larger gaps. The pulse repetition frequency is adapted for day and night measurements in order to prevent clutter from multiple ionosphere–ground reflections. The lower number of data points in the DBS experiment per beam-pointing direction is partly compensated for by the 4 bit complementary code. This pulse coding improves the signal-to-noise ratio as the averaged transmitted power increases, and received power from random noise and interference is reduced as it does not match the code. After decoding the multi-beam DBS experiment, we only analyze the vertical measurements for electron density estimations. Equivalent-electron-density measurements with the Saura radar have lately also been used to investigate, e.g., so-called polar mesosphere winter echoes (PMWEs) and study their occurrence (Renkwitz et al., 2021). Furthermore, Saura electron density profiles have been partly validated by rocketborne in situ measurements during a PMWE campaign (Strelnikov et al., 2021; Staszak et al., 2021).

2.1 Amendment of the electron density estimates

The typically observed rather large variability in electron density profiles gives rise to multiple potential sources within the probed volume. Assuming a 6° wide transmit beam, the illuminated area corresponds to a diameter of ≈ 8.5 km at 80 km altitude, neglecting side lobes. The horizontal variability in gradients in the electron density for this size is likely caused by the presence and superposition of propagating small-scale waves. Since the earlier electron density measurements with the Saura radar (Singer et al., 2011), the fundamental technique has been combined with additional signal processing methods and interferometry.

First, we split the complex times series into four blocks; then the correlation length of the detected echoes for each block and range is derived. The correlation length is used to apply a sufficient amount of coherent integration to reduce the variability in the raw data in order to stabilize the angle-of-arrival (AOA) estimates.

To improve the individual electron density estimates for each experiment run, we remove radar echoes that are received most likely through the side lobes of the antenna array. Given the sparse character of the Mills Cross-like antenna layout, imperfections in the radiation pattern, namely side lobes along the axes of the antenna array, exist. For situations when much larger electron density gradients exist in the orientation of these side lobes rather than in the nominal main beam-pointing direction, echoes from these unwanted directions are received and will impair the results.

Therefore, we apply interferometric methods to discriminate the location of the scattering structures. For localizing the scattering structures, we generally make use of four individual antennas, marked in Fig. 1 as receiver channels 3–6. With this arrangement, six individual and non-redundant baselines can be used for AOA estimates, covering up to 25° given its shortest baselines of 1.48λ (≈ 140 m) (see, e.g., Renkwitz et al., 2018; Renkwitz and Latteck, 2019). The same arrangement and basic methodology were already applied using IDI to make use of the ionospheric inhomogene-

ity for Saura wind measurements (see Renkwitz et al., 2018). The required phase information of the receiving channels is estimated based on AOA statistics for all beam positions for the course of months.

An example of derived instantaneous AOA positions for a single vertical sounding experiment of less than 4 min runtime is shown in Fig. 2 for a range of 89 km from the radar. Two scenarios are shown, the native resolution and after applying an integration of 1s before solving for AOA. From that plot, it is obvious that many positions are still outside the marked 10° area of interest. Furthermore, as the radar echoes are measured in range gates, basically a position on the spherical shell, it will result in vertical smearing without proper conversion and selection. For each of the four time series blocks, the AOA positions are used to potentially discard the derived differential phase between the ordinary and extraordinary wave for the same chunks.

Another important point is a suitable unwrapping of the differential phases. Even though a progressively increasing radial phase difference is expected with increasing electron density over altitude, we also allow for minor negative estimated phases to cope with measurement errors. Larger negative phases, however, are interpreted as positive phase wraps. Note that a reduction in electron density may occur for electron bite-out situations during the charging of ice particles in the summer mesosphere (Rapp et al., 2003; Rapp and Lübken, 2004; Friedrich et al., 2011). Note that these scenarios should not affect the altitudes below 80 km that are mostly investigated.

The first cleaning of the data is done by removing isolated data points, like potential erroneous data at the lowermost captured altitudes. Additionally, outliers based on the typically observed variability in values adjacent in time and altitude are flagged.

In the next step, we aim to reject suspicious electron density profiles that show excessively small or large values. For this, we use FIRI (Friedrich et al., 2018b) profiles that are selected for the nearest latitude (60°) as well as solar flux and then interpolated for the day of year (DOY) and solar zenith angle (SZA; see Fig. 3). The interpolated FIRI local noontime electron densities for low-solar-flux conditions (sfu = 90) are depicted in Fig. 4. We are aware FIRI is not explicitly meant to be representative of polar latitudes, but we apply the profiles as a coarse reference for geomagnetic quiet times.

For the evaluation of the Saura electron density profiles for quiet conditions, we allow for deviations between 1/10 of and 4 times the reference profile. The same methodology is used for geomagnetically disturbed times, but we allow for much larger densities (100 times the FIRI profile). For the main target of this study, namely deriving daily noon averages, we average the remaining profiles for both scenarios between 09:00–13:00 UT.

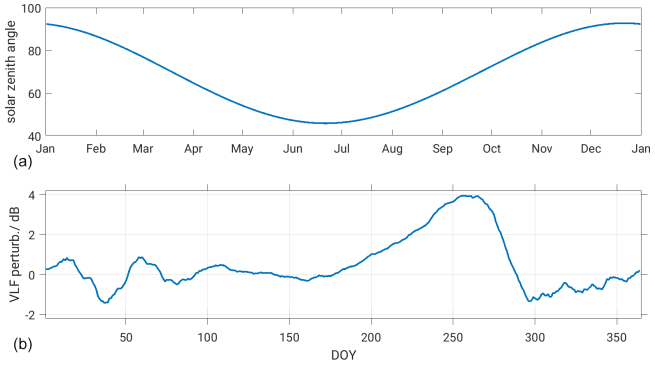

Figure 3. **(a)** Daily noon solar zenith angle for the Saura location. **(b)** Detected mean VLF amplitude perturbations for the transmitter Cutler (USA, NAA) and receiver Sodankylä (Finland, SOD), after Macotela et al. (2021).

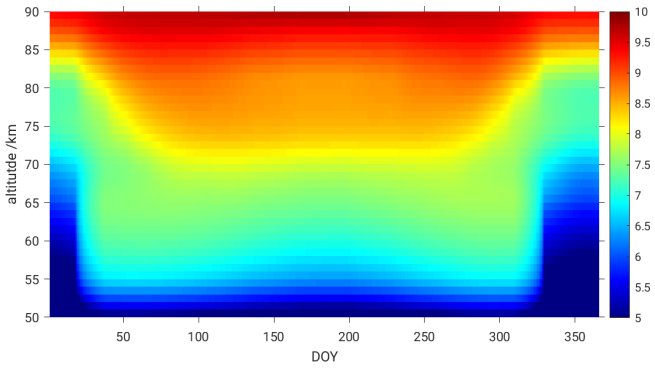

Figure 4. Electron densities as derived from FIRI for 60° N during low-solar-flux conditions (sfu = 90), interpolated for the SZA at noontime for each DOY. The color bar represents densities as $\log_{10}(n_e)\,\mathrm{m}^{-3}$.

2.2 Discrimination between quiet and disturbed conditions

As already mentioned, enhanced solar and geomagnetic activity will alter the current state of the lowermost ionospheric layer until it settles down and recombination is completed. For our purpose of deriving climatologies for not only quiet but also disturbed conditions, these different conditions need to be separated. One obvious and frequently used way to evaluate the geomagnetic conditions is to use proxies derived from, e.g., magnetometer data like K or Hpo indices or riometer data. Often, these parameters are then analyzed in combination for multiple locations. Depending on the distribution of these locations, the proxies might be more relevant for mid-latitudes and as planetary indices. Additionally to this and solar radiation like F10.7 and F30 flux, solar wind parameters are useful to describe the current influx. Particle detectors on board GOES and POES satellites and comparable instrumentations may also discriminate between certain energy bands of precipitating particles.

Fortunately, the Saura radar itself is very sensitive to electron density enhancements occurring in the radar's field of view; see Renkwitz and Latteck (2017). Significantly enhanced electron densities, e.g., caused by EPP, form virtually isolated layers in the echo power profiles as the radar signal is strongly absorbed for the altitudes above. The first observations of such virtual layers have been reported and named ILMEs (isolated lower mesospheric echoes; Hall et al., 2006) and have been widely attributed to events of precipitating protons during solar flares. The time series of such isolated layers for the years 2003 to 2022 as detected by Saura (extended data set by Renkwitz and Latteck, 2017) is used in the following to flag disturbed conditions and treat the electron density data for both scenarios separately.

Based on the ILME detections using the Saura radar, periods of EPP events are flagged and thus excluded from further processing of the quiet periods' profiles. To prevent contamination from undetected events and to cover the recombination time, we use a window of ±1 h around the individual EPP detections. In the next step, the daily noon medians for all data and quiet times only are calculated for each altitude from all valid measurements during the period of 09:00–13:00 UT, and they are stored for the corresponding DOY.

An example of a successful differentiation for both disturbed and quiet ionospheric conditions and corresponding annual noon electron densities is shown for the year 2019 in Fig. 5. In the upper panel, all valid data including active periods (e.g., EPP and SPEs) are shown, where enhanced electron densities are clearly visible around March–April and September–October for altitudes of 60–70 km. Such enhancements near the equinoxes are commonly related to the Russell–McPherron cycle (Russell and McPherron, 1973). The visible vertically aligned gaps are caused by the rejection of long-lasting EPP events rather than observational gaps. The bottom panel depicts the quiet-time (excluding EPP and SPEs) D-region electron densities during the year 2019. Interestingly, even after removing the geomagnetic-disturbance effect, the enhancement in the electron density during the spring and fall equinox is prominent; the probable cause and effect of these enhancements will be discussed in the following.

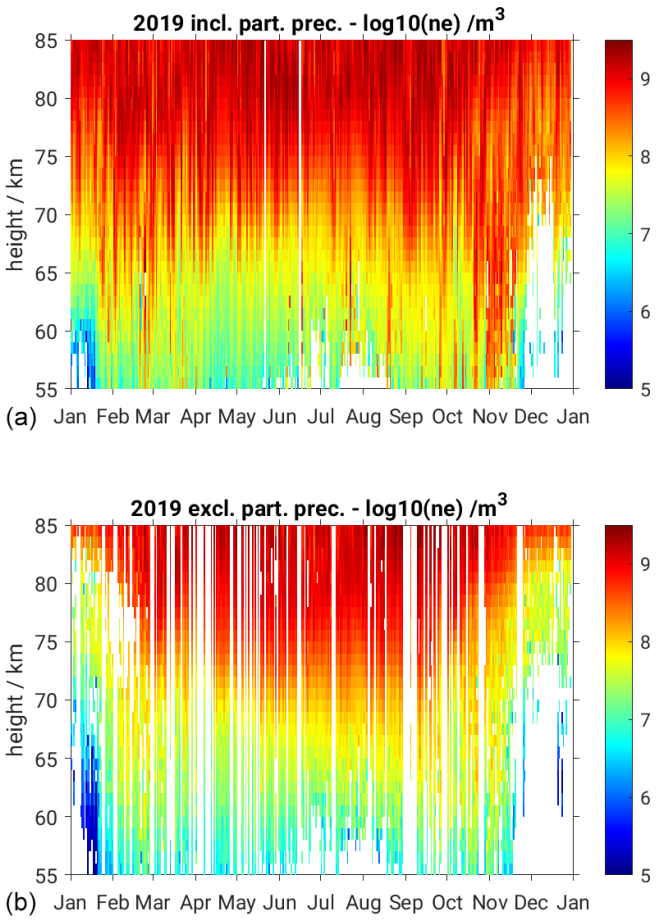

Figure 5. Observed Saura electron densities during 2019, for all conditions **(a)** and excluding active periods **(b)**.

3 Analysis and discussion

The composite means of 9 years (2014–2022) of electron densities during geomagnetically disturbed and quiet conditions are provided in Fig. 6, top and bottom panels, respectively. The general picture of the electron densities in the lower ionosphere is governed by the dominating incident solar radiation. As an indicator of incident radiation, not only the flux of UV (Lyman-alpha line and X-rays in the case of solar flares) but also the solar zenith angle (SZA) are used. Assuming a rather constant flux and a symmetrical SZA for spring and fall (see Fig. 3), a symmetric electron density is also expected, neglecting other contributing factors like dynamics. This assumed symmetry of spring and fall electron densities is not observed in our data, but increasing D-region electron densities below 75 km altitude from spring towards fall are shown for 2019 in Fig. 5.

It has to be noted that 2019 was characterized by generally extremely low solar and geomagnetic activity and might therefore represent an extreme case. Therefore we also applied the same methods to years of enhanced solar activity, from 2014 (the maximum of solar cycle 24) until the end of 2022 (onset of solar cycle 25). The analysis covers a total of 9 consecutive years since the last major radar upgrade, spanning a rather poor solar maximum to extreme solar-minimum conditions, represented by monthly smoothed solar sunspot numbers of 130 down to 0 and a corresponding 10.7 cm solar flux of 150 to 67 sfu (see NOAA, 2023).

For all data of each year, the 2-hourly solar flux is used to derive FIRI profiles that are then employed to reject obvious outliers from the radar measurements. For a climatological picture, we calculated median electron densities for each DOY over all years, which is shown for both, all and

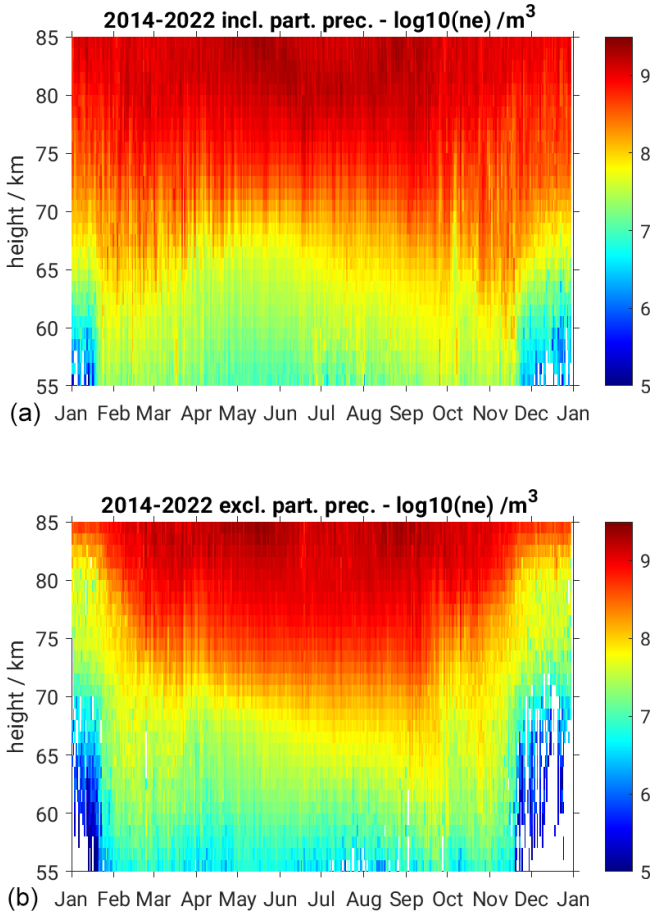

Figure 6. Climatology of electron density including **(a)** and excluding **(b)** particle precipitation events for the years 2014–2022.

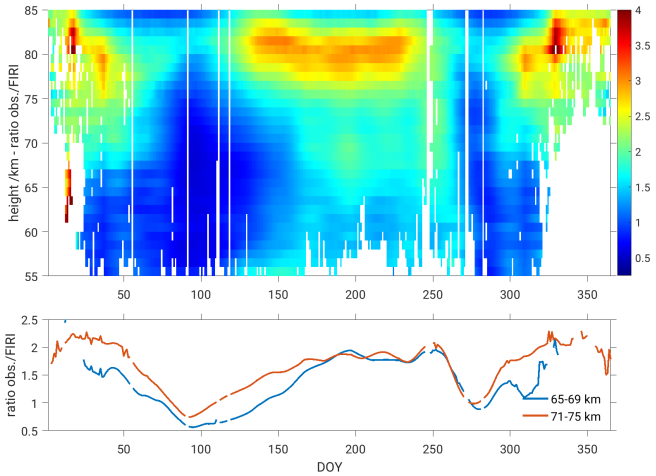

Figure 7. Linear ratio of observed median electron densities after 30 d smoothing to FIRI. Bottom: median ratio for the altitude bins 65–69 km and 71–75 km.

quiet, conditions in Fig. 6. Even though we are averaging over fairly different solar and geomagnetic conditions, the general asymmetry which was already found for the year 2019 prevails also for this climatology. For a constant number electron density of 100 electrons cm^{-3}, an almost linear slope from the beginning of April to the end of September is visible for 72 to 66 km, respectively. Such a slope was already visible for the 2019 data shown in Fig. 5.

Noteworthily, in February and March as well as in September and November, enhanced electron densities are visible below 65 km altitude. One plausible cause for these enhancements might be undetected EPP events creating a bias in the medians shown. However, enhancements are also seen in the FIRI output for altitudes as low as 55 km from April to November (see Fig. 4). Furthermore, there might be dynamics-driven causes for the observed variability as it is in a rather unstable period with its proximity to sudden stratospheric warmings (SSWs) during winter.

Note that the abrupt changes at the end of January and November appear artificial and are likely caused by the FIRI reference applied to reject too large values of the measurements. The mentioned period actually describes the time of lowest SZA, when the sun is basically below the horizon the whole day, and represents the most challenging scenario to derive reliable electron densities. One obvious reason for this is the generally very low ionization and steep gradient near 85 km altitude (cf. Fig. 4) that does not allow for much range for radar measurements, keeping in mind a minimum range resolution of 1 km. The upper panel of Fig. 6 depicts the median of all valid data including EPP events. Enhancements around the equinoxes are visible, especially during the winter period. Even though the frequency of strong and long-lasting events is rather low in wintertime, their contribution may still be significant as they typically occur near noontime.

The ratio of observed quiet-time median electron densities smoothed with a 30 d window to the very SZA-symmetric FIRI is shown in Fig. 7. Data covered by less than 4 years of quiet-time observations are blanked as they may not be representative (see EPP around the equinoxes). For altitudes above 75 km, the pattern appears symmetric to the SZA. Specifically interesting are the altitudes near 70 km, which show enhanced densities from June to mid-September.

As we initially highlighted, the focus of this study is on the asymmetry between spring and fall as previous studies indicated such behavior in the detected VLF amplitudes of long-distance transmissions (Macotela et al., 2021; see bottom panel of Fig. 3). This asymmetry of spring and fall is also clearly visible in the electron density measurements as depicted in the bottom panel of Fig. 7.

Generally, the period from the end of summer and middle of fall is a rather dynamical time of the year, for which we will introduce some presumably related observations. Macotela et al. (2021) argued that changes in the temperature and semi-diurnal tidal amplitude (see Conte et al., 2018) could be a cause for the fall effect. However, their study did

not include electron density's role in the observed fall effect (if any). It should be noted that the VLF amplitude is highly influenced by the electron density gradient in the D-region ionosphere (Silber and Price, 2017). Thus, the present results suggest that in addition to the dynamical effects, enhancement in the electron density could also contribute to the observed fall effect in the VLF amplitude. Iimura et al. (2021) investigated the quasi-2 d wave (Q2DW) structure for multiple latitudes using ground-based and satellite measurements. Notably, they found enhanced Q2DW activity during summertime between 75–95 km altitude for 60° N. This enhancement fades towards the zonal wind reversal (DOY 260), which is also coincident with the decrease in the semidiurnal tides. Another interesting result also noted in our electron density profiles is that, at the beginning of October, a rather sharp and sudden decrease in electron densities is visible, which can be related to the so-called October effect (Pancheva and Mukhtarov, 1996). A challenging aspect of the present result is what could be the source of these electron density enhancements (reduction) during the fall (October) conditions. One of our current understandings and hypotheses is that, during the late summer and fall period, downwelling occurs at mesospheric altitudes as part of mean meridional circulations. Such downwelling will transport more NO from the lower thermosphere to the observed altitudes, and planetary wave circulations transport NO-rich air equatorward to mid-latitudes, where it is ionized to produce high electron densities through ionization (Garcia et al., 1987). The meridional wind climatology of the radar's position for the same years is shown in Fig. 8, including a 16 d smoothing window and rejecting sparse data. For the period of observed electron density enhancements (April to September), the meridional wind magnitude is continuously very small. However, from October to April, intensified northward winds dominate below 75 km altitude. If the meridional circulation associated with downwelling is the cause of the enhanced electron densities, then one should observe the high electron densities in October as well. Thus, it gives an indication that there could be some other process also involved in the noted changes in the electron densities during the fall conditions. Coincidentally, Conte et al. (2018) reported a decrease in the S2 amplitude during October for middle and high latitudes. During this period, a very pronounced and consistent feature occurs in the mesosphere, namely the zonal wind reversal (see, e.g., Keuer et al., 2007; Hoffmann et al., 2010; Jaen et al., 2022). This raises the questions of whether the changes in the S2 amplitude and zonal wind reversal have any impact on the D-region electron density and, if so, how?

For a better interannual analysis, the median electron densities for 65–69 km and 71–75 km over DOY are shown separately for each year in Fig. 9 after smoothing with a 30 d window. The annual asymmetry is seen for both altitude bins but is very pronounced for the lower altitudes, where an increase by a factor of at least 3 is seen from day 100 to 250.

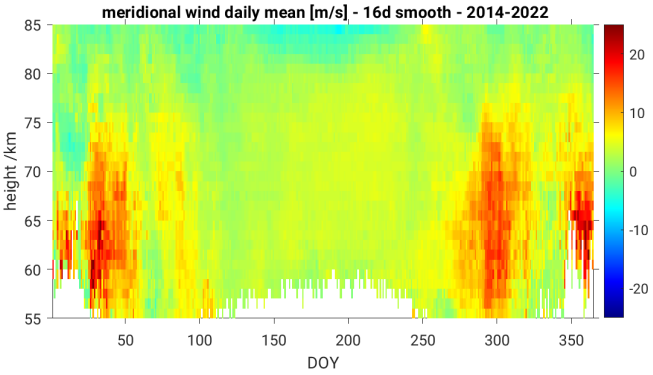

Figure 8. Climatology of Saura meridional winds (2014–2022) showing low magnitudes below 80 km during summer months.

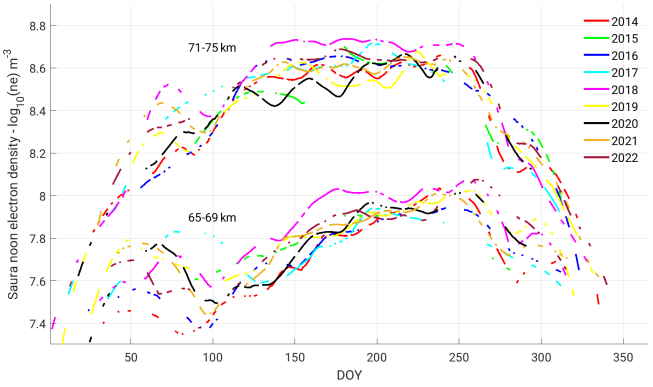

Figure 9. Averaged electron densities for the altitude bins 65–69 km and 71–75 km including a 30 d smoothing. The gaps each year correspond to periods of enhanced geomagnetic activity which are excluded, equivalent to Fig. 5.

The sudden decrease in electron density occurs around day 265 but differs by about 10 d between the higher- and lower-altitude bins. The exact timing of both the increase around day 110 and the decrease around day 250 shows comparably little variability throughout the years for the higher-altitude window, whereas it seems less stable for the lower altitudes, with spreads of 20 d, giving rise to potentially larger sensitivity to other phenomena like dynamics. An important point here is that the fall effect is present in all the years with minor year-to-year variations in the onset time, irrespective of solar activity.

Despite the general increase for the lower altitudes from DOY 100 to 250 for most of the years, especially for 2018, an early rampant behavior until DOY 170 and a rather continuous noon electron density level until DOY 270 are seen. A similar peculiarity is prominent for the upper-altitude bin. Given 2018 was a year with extremely low solar activity, the annual development of electron densities found seems rather surprising. Basically, the opposite is seen for 2014, near the solar maximum of cycle 24, where low electron densities in spring and a steady increase until DOY 250 are observed.

The tendency for somewhat larger electron densities below 70 km altitude during low solar flux, 70 sfu for the solar minimum and 150 sfu for the 2014 solar maximum, is also visible in FIRI, while the contrary is found for the altitudes above. In the previous study of Macotela et al. (2021), the majority of the year 2018 did not show any significant deviation from other years. However, slightly enhanced VLF amplitudes were seen for the second week of October. Noteworthily, these detected amplitudes are derived for the propagation path between the most northeastern part of the USA (Cutler, ME) and northern Finland (Sodankylä). Thus, the electron density profiles of the entire path need to be taken into consideration, and the local Saura profile might have only little influence. Thus, more local phenomena could have caused the observed higher electron densities in 2018. However, these need further investigation to explore the exact reason.

4 Conclusions and outlook

In this study, we present local noontime climatologies of electron density in the middle atmosphere at high latitudes not only for solar and geomagnetically quiet periods but also including disturbed periods. The data were derived by active high-frequency radar experiments exploiting the phase information of radar echoes that correspond to Faraday rotation caused by electron density in the Earth's magnetic field. To improve the long-established methods, we applied further signal processing as well as interferometry techniques. The latter is used to reject radar echoes from far off the beam-pointing direction. We furthermore involved the FIRI model output to exclude obvious outliers from further processing, which proved to be very useful for SZA below 90°. Geomagnetically active periods including EPP events as well as SPEs were detected with the radar, and these periods were treated separately from the quiet times. Finally, local noontime electron density profiles were derived for both situations.

We found a clear asymmetry between spring and fall, which is not explainable by the SZA, nor is it visible in the ionospheric models. However, recent VLF experiments have shown a comparable asymmetry in detected VLF amplitudes. Furthermore, we found a consistent and steep decrease in electron densities around DOY 265.

Our current understanding is that downwelling is associated with the meridional circulation during the fall and winter seasons and could be responsible for the enhanced electron density through the transport of NO from the lower thermosphere, while the enhanced meridional winds and tidal activity at the lower altitudes might explain the sudden reduction in the electron density during the first week of October. During the late summer and fall periods, a temperature reduction and an increase in semi-diurnal tide could also play a significant role in the observed electron density changes.

The pattern of asymmetric spring–fall and a steep decrease in October was found for all 9 years of data analyzed in this study, while the interannual variability is restricted to a few days, which might be surveyed in more detail at a later point.

We plan to investigate the peculiarities found, like the enhanced densities of 2018, in more depth in a successive study, where we aim to incorporate both methods, absorption and phase rotation measurements, and incorporate additional modeling efforts. Furthermore, we plan to extend the measurements to the technologically rather similar, but smaller, radar system in Juliusruh at middle latitudes, which in the past has mostly been used for the study of dynamics (see, e.g., Hoffmann et al., 2010; Jaen et al., 2022).

Data availability. The data needed to reproduce the electron density figures including the observations are shared through https://doi.org/10.22000/993 (Renkwitz, 2023).

Author contributions. TR had the main responsibility of the radar experiment, its data analysis, and the writing of the article. SM and JJ helped to develop the concept, interpret data, and discuss results. WS contributed to the fundamental electron density analysis and discussions of results. All authors read, corrected, and agreed to the submitted version of the manuscript.

Competing interests. The contact author has declared that none of the authors has any competing interests.

Disclaimer. Publisher's note: Copernicus Publications remains neutral with regard to jurisdictional claims in published maps and institutional affiliations.

Acknowledgements. We appreciate suggestions by Jorge L. Chau and the support of the Andøya Space Center for Saura radar operations.

Financial support. This research has been supported by the Deutsches Zentrum für Luft- und Raumfahrt (AMELIE project (grant no. D/921/67286532)), the Deutsche Forschungsgemeinschaft (VACILT project (grant no. PO 2341/2-1)), and the Bundesministerium für Bildung und Forschung (TIMA-2 project in the frame of ROMIC-II (grant no. 01 LG 1902A)).

The publication of this article was funded by the Open Access Fund of the Leibniz Association.

Review statement. This paper was edited by John Plane and reviewed by Martin Friedrich and one anonymous referee.

References

Alken, P., Thébault, E., Beggan, C. D., Amit, H., ubert, J., Baerenzung, J., Bondar, T. N., Brown, W. J., aliff, S., Chambodut, A., Chulliat, A., Cox, G. A., Finlay, C. C., Fournier, A., Gillet, N., Grayver, A., Hammer, M. D., Holschneider, M., Huder, L., Hulot, G., Jager, T., Kloss, C., Korte, M., Kuang, W., Kuvshinov, A., Langlais, B., Léger, J.-M., Lesur, V., Livermore, P. W., Lowes, F. J., Macmillan, S., Magnes, W., Mandea, M., Marsal, S., Matzka, J., Metman, M. C., Minami, T., Morschhauser, A., Mound, J. E., Nair, M., Nakano, S., Olsen, N., Pavón-Carrasco, F. J., Petrov, V. G., Ropp, G., Rother, M., Sabaka, T. J., Sanchez, S., Saturnino, D., Schnepf, N. R., Shen, X., Stolle, C., Tangborn, A., Tøffner-Clausen, L., Toh, H., Torta, J. M., Varner, J., Vervelidou, F., Vigneron, P., Wardinski, I., Wicht, J., Woods, A., Yang, Y., Zeren, Z., and Zhou, B.: International Geomagnetic Reference Field: the thirteenth generation, Earth Planet. Space, 73, 49, https://doi.org/10.1186/s40623-020-01288-x, 2021.

Baumann, C., Kero, A., Raizada, S., Rapp, M., Sulzer, M. P., Verronen, P. T., and Vierinen, J.: Arecibo measurements of D-region electron densities during sunset and sunrise: implications for atmospheric composition, Ann. Geophys., 40, 519–530, https://doi.org/10.5194/angeo-40-519-2022, 2022.

Belrose, J. S.: Radio wave probing of the ionosphere by the partial reflection of radio waves (from heights below 100 km), J. Atmos. Terrest. Phys., 32, 567–596, https://doi.org/10.1016/0021-9169(70)90209-6, 1970.

Briggs, B. H.: The analysis of spaced sensor records by correlation techniques, MAP Handbook, 13, 166–186, 1984.

Budden, K.: Approximations in magnetoionic theory, J. Atmos. Terrest. Phys., 45, 213–218, https://doi.org/10.1016/S0021-9169(83)80043-9, 1983.

Burns, C., Turunen, E., Matveinen, H., Ranta, H., and Hargreaves, J.: Chemical modelling of the quiet summer D-andE-regions using EISCAT electron density profiles, J. Atmosp. Terrest. Phys., 53, 115–134, https://doi.org/10.1016/0021-9169(91)90026-4, 1991.

Chau, J. L. and Woodman, R. F.: D and E region incoherent scatter radar density measurements over Jicamarca, J. Geophys. Res.-Space Phys., 110, A12314, https://doi.org/10.1029/2005JA011438, 2005.

Clilverd, M. A., Duthie, R., Rodger, C. J., Hardman, R. L., and Yearby, K. H.: Long-term climate change in the D-region, Sci. Rep., 7, 16683, https://doi.org/10.1038/s41598-017-16891-4, 2017.

Conte, J. F., Chau, J. L., Laskar, F. I., Stober, G., Schmidt, H., and Brown, P.: Semidiurnal solar tide differences between fall and spring transition times in the Northern Hemisphere, Ann. Geophys., 36, 999–1008, https://doi.org/10.5194/angeo-36-999-2018, 2018.

del Pozo, C. F., Turunen, E., and Ulich, T.: Negative ions in the auroral mesosphere during a PCA event around sunset, Ann. Geophys., 17, 782–793, https://doi.org/10.1007/s00585-999-0782-1, 1999.

Flood, W. A.: A D region mid- and high-latitude approximation to the Sen-Wyller refractive index equations, Radio Sci., 15, 797–799, https://doi.org/10.1029/RS015i004p00797, 1980.

Friedrich, M. and Rapp, M.: News from the Lower Ionosphere: A Review of Recent Developments, Surv. Geophys., 30, 525–559, https://doi.org/10.1007/s10712-009-9074-2, 2009.

Friedrich, M. and Torkar, K. M.: An empirical model of the nonauroral D Region, Radio Sci., 27, 945–953, https://doi.org/10.1029/92RS01929, 1992.

Friedrich, M. and Torkar, K. M.: FIRI: A semiempirical model of the lower ionosphere, J. Geophys. Res-.Space Phys., 106, 21409–21418, https://doi.org/10.1029/2001JA900070, 2001.

Friedrich, M., Harrich, M., Torkar, K., and Stauning, P.: Quantitative measurements with wide-beam riometers, J. Atmos. Solar-Terrest. Phys., 64, 359–365, 2002.

Friedrich, M., Harrich, M., Steiner, R., Torkar, K., and Lübken, F.-J.: The quiet auroral ionosphere and its neutral background, Adv. Space Res., 33, 943–948, https://doi.org/10.1016/j.asr.2003.08.006, 2004.

Friedrich, M., Rapp, M., Plane, J. M., and Torkar, K. M.: Bite-outs and other depletions of mesospheric electrons, J. Atmos. Solar-Terrest. Phys., 73, 2201–2211, https://doi.org/10.1016/j.jastp.2010.10.018, 2011.

Friedrich, M., Pock, C., and Torkar, K.: FIRI-2018, an Updated Empirical Model of the Lower Ionosphere, J. Geophys. Res.-Space Phys., 123, 6737–6751, https://doi.org/10.1029/2018JA025437, 2018a.

Friedrich, M., Pock, C., and Torkar, K.: FIRI-2018, an Updated Empirical Model of the Lower Ionosphere, J. Geophys. Res.-Space Phys., 123, 6737–6751, https://doi.org/10.1029/2018JA025437, 2018b.

Garcia, R. R., Solomon, S., Avery, S. K., and Reid, G. C.: Transport of nitric oxide and the D region winter anomaly, J. Geophys. Res.-Atmos., 92, 977–994, https://doi.org/10.1029/JD092iD01p00977, 1987.

Grant, J., Grainger, R., Lawrence, B., Fraser, G., von Biel, H., Heuff, D., and Plank, G.: Retrieval of mesospheric electron densities using an optimal estimation inverse method, J. Atmos. Solar-Terrest. Phys., 66, 381–392, https://doi.org/10.1016/j.jastp.2003.12.006, 2004.

Hall, C. M., Manson, A. H., Meek, C. E., and Nozawa, S.: Isolated lower mesospheric echoes seen by medium frequency radar at 70° N, 19° E, Atmos. Chem. Phys., 6, 5307–5314, https://doi.org/10.5194/acp-6-5307-2006, 2006.

Hoffmann, P., Becker, E., Singer, W., and Placke, M.: Seasonal variation of mesospheric waves at northern middle and high latitudes, J. Atmos. Solar-Terrest. Phys., 72, 1068–1079, https://doi.org/10.1016/j.jastp.2010.07.002, 2010.

Holdsworth, D., Vuthaluru, R., Reid, I. M., and Vincent, R. A.: Differential absorption measurements of mesospheric and lower thermospheric electron densities using the Buckland Park MF radar, J. Atmos. Solar-Terrest. Phys., 64, 2029–2042, https://doi.org/10.1016/S1364-6826(02)00232-8, 2002.

Igarashi, K., Murayama, Y., Nagayama, M., and Kawana, S.: D-region electron density measurements by MF radar in the middle and high latitudes, Adv. Space Res., 25, 25–32, https://doi.org/10.1016/S0273-1177(99)00893-5, 2000.

Iimura, H., Fritts, D. C., Lieberman, R. S., Janches, D., Mitchell, N. J., Franke, S. J., Singer, W., Hocking, W. K., Taylor, M. J., and Moffat-Griffin, T.: Climatology of quasi-2-day wave structure and variability at middle latitudes in the northern and south-

ern hemispheres, J. Atmos. Solar-Terrest. Phys., 221, 105690, https://doi.org/10.1016/j.jastp.2021.105690, 2021.

Jaen, J., Renkwitz, T., Chau, J. L., He, M., Hoffmann, P., Yamazaki, Y., Jacobi, C., Tsutsumi, M., Matthias, V., and Hall, C.: Long-term studies of mesosphere and lower-thermosphere summer length definitions based on mean zonal wind features observed for more than one solar cycle at middle and high latitudes in the Northern Hemisphere, Ann. Geophys., 40, 23–35, https://doi.org/10.5194/angeo-40-23-2022, 2022.

Kawahira, K.: The D region winter anomaly at high and middle latitudes induced by planetary waves, Radio Sci., 20, 795–802, https://doi.org/10.1029/RS020i004p00795, 1985.

Keuer, D., Hoffmann, P., Singer, W., and Bremer, J.: Long-term variations of the mesospheric wind field at mid-latitudes, Ann. Geophys., 25, 1779–1790, https://doi.org/10.5194/angeo-25-1779-2007, 2007.

Liu, T., Yang, G., Zhao, Z., Liu, Y., Zhou, C., Jiang, C., Ni, B., Hu, Y., and Zhu, P.: Design of Multifunctional Mesosphere-Ionosphere Sounding System and Preliminary Results, Sensors, 20, 2664, https://doi.org/10.3390/s20092664, 2020.

Lübken, F.-J.: Thermal structure of the Arctic summer mesosphere, J. Geophys. Res.-Atmos., 104, 9135–9149, https://doi.org/10.1029/1999JD900076, 1999.

Macotela, E. L., Clilverd, M., Renkwitz, T., Chau, J., Manninen, J., and Banys, D.: Spring-Fall Asymmetry in VLF Amplitudes Recorded in the North Atlantic Region: The Fall-Effect, Geophys. Res. Lett., 48, e2021GL094581, https://doi.org/10.1029/2021GL094581, 2021.

McKinnell, L.-A. and Friedrich, M.: A neural network-based ionospheric model for the auroral zone, J. Atmos. Solar-Terrest. Phys., 69, 1459–1470, https://doi.org/10.1016/j.jastp.2007.05.003, 2007.

McNamara, L. F.: Statistical model of the D region, Radio Sci., 14, 1165–1173, https://doi.org/10.1029/RS014i006p01165, 1979.

Mechtly, E. A.: Accuracy of rocket measurements of lower ionosphere electron concentrations, Radio Sci., 9, 373–378, https://doi.org/10.1029/RS009i003p00373, 1974.

Mitra, A.: A review of D-region processes in non-polar latitudes, J. Atmos. Terrest. Phys., 30, 1065–1114, https://doi.org/10.1016/S0021-9169(68)80001-7, 1968.

Moro, J., Denardini, C. M., Correia, E., Abdu, M. A., Schuch, N. J., and Makita, K.: A comparison of two different techniques for deriving the quiet day curve from SARINET riometer data, Ann. Geophys., 30, 1159–1168, https://doi.org/10.5194/angeo-30-1159-2012, 2012.

NOAA: Space weather conditions – solar cycle progression, https://www.swpc.noaa.gov/products/solar-cycle-progression (last access: 15 August 2023), 2023.

Offermann, D.: An integrated GBR campaign for the study of the D-region winter anomaly in western Europe 1975/76, J. Atmos. Terrest. Phys., 41, 1047–1050, https://doi.org/10.1016/0021-9169(79)90080-1, 1979a.

Offermann, D.: Recent advances in the study of the D-region winter anomaly, J. Atmos. Terrest. Phys., 41, 735–752, https://doi.org/10.1016/0021-9169(79)90121-1, 1979b.

Offermann, D.: A Winter Anomaly Campaign in Western Europe, Philos. T. R. Soc. A, 296, 261–268, 1980.

Osepian, A., Tereschenko, V., Dalin, P., and Kirkwood, S.: The role of atomic oxygen concentration in the ionization balance of the lower ionosphere during solar proton events, Ann. Geophys., 26, 131–143, https://doi.org/10.5194/angeo-26-131-2008, 2008.

Palmer, R. D., Huang, X., Fukao, S., Yamamoto, M., and Nakamura, T.: High-resolution wind profiling using combined spatial and frequency domain interferometry, Radio Sci., 30, 1665–1679, https://doi.org/10.1029/95RS02594, 1995.

Pancheva, D. V. and Mukhtarov, P. Y.: Modelling of the electron density height profiles in the mid-latitude ionospheric D-region, Annals of Geophysics, http://hdl.handle.net/2122/1713 (last access: 10 July 2023), 1996.

Rapp, M. and Lübken, F.-J.: Polar mesosphere summer echoes (PMSE): Review of observations and current understanding, Atmos. Chem. Phys., 4, 2601–2633, https://doi.org/10.5194/acp-4-2601-2004, 2004.

Rapp, M., Lübken, F.-J., and Blix, T.: The role of charged ice particles for the creation of PMSE: A review of recent developments, Adv. Space Res., 31, 2033–2043, https://doi.org/10.1016/S0273-1177(03)00226-6, 2003.

Renkwitz, T.: RenkwitzACP2023. Leibniz Institute of Atmospheric Physics at the University of Rostock, RADAR [data set], https://doi.org/10.22000/993, 2023.

Renkwitz, T. and Latteck, R.: Variability of virtual layered phenomena in the mesosphere observed with medium frequency radars at 69° N, J. Atmos. Solar-Terrest. Phys., 163, 38–45, https://doi.org/10.1016/j.jastp.2017.05.009, 2017.

Renkwitz, T. and Latteck, R.: Angle of Arrival study of atmospheric high frequency radar echoes, in: 2019 6th International Conference on Space Science and Communication (IconSpace), 230–234, https://doi.org/10.1109/IconSpace.2019.8905934, 2019.

Renkwitz, T., Singer, W., Latteck, R., and Rapp, M.: Multi beam observations of cosmic radio noise using a VHF radar with beam forming by a Butler matrix, Adv. Radio Sci., 9, 1–9, https://doi.org/10.5194/ars-9-349-2011, 2011.

Renkwitz, T., Tsutsumi, M., Laskar, F. I., Chau, J. L., and Latteck, R.: On the role of anisotropic MF/HF scattering in mesospheric wind estimation, Earth, Planet. Space, 70, 158, https://doi.org/10.1186/s40623-018-0927-0, 2018.

Renkwitz, T., Latteck, R., Strelnikova, I., Johnsen, M. G., and Chau, J. L.: Characterization of polar mesospheric VHF radar echoes during solar minimum winter 2019/2020. Part I: Ionisation, J. Atmos. Solar-Terrest. Phys., 221, 105684, https://doi.org/10.1016/j.jastp.2021.105684, 2021.

Roper, R. G. and Brosnahan, J. W.: Imaging Doppler interferometry and the measurement of atmospheric turbulence, Radio Sci., 32, 1137–1148, https://doi.org/10.1029/97RS00089, 1997.

Russell, C. T. and McPherron, R. L.: Semiannual variation of geomagnetic activity, J. Geophys. Res., 78, 92, https://doi.org/10.1029/JA078i001p00092, 1973.

Sen, H. K. and Wyller, A. A.: On the generalization of the Appleton-Hartree magnetoionic formulas, J. Geophys. Res. (1896–1977), 65, 3931–3950, https://doi.org/10.1029/JZ065i012p03931, 1960.

Silber, I. and Price, C.: On the Use of VLF Narrowband Measurements to Study the Lower Ionosphere and the Mesosphere–Lower Thermosphere, Surv. Geophys., 38, 407–441, https://doi.org/10.1007/s10712-016-9396-9, 2017.

Singer, W., Latteck, R., and Holdsworth, D. A.: A new narrow beam Doppler radar at 3 MHz for studies of the high-

latitude middle atmosphere, Adv. Space Res., 41, 1488–1494, https://doi.org/10.1016/j.asr.2007.10.006, 2008.

Singer, W., Latteck, R., Friedrich, M., Wakabayashi, M., and Rapp, M.: Seasonal and solar activity variability of D-region electron density at 69° N, J. Atmos. Solar-Terrest. Phys., 73, 925–935, https://doi.org/10.1016/j.jastp.2010.09.012, 2011.

Siskind, D. E., Zawdie, K. A., Sassi, F., Drob, D. P., and Friedrich, M.: An Intercomparison of VLF and Sounding Rocket Techniques for Measuring the Daytime D Region Ionosphere: Theoretical Implications, J. Geophys. Res.-Space Phys., 123, 8688–8697, https://doi.org/10.1029/2018JA025807, 2018.

Staszak, T., Strelnikov, B., Latteck, R., Renkwitz, T., Friedrich, M., Baumgarten, G., and Lübken, F.-J.: Turbulence generated small-scale structures as PMWE formation mechanism: Results from a rocket campaign, J. Atmos. Solar-Terrest. Phys., 217, 105559, https://doi.org/10.1016/j.jastp.2021.105559, 2021.

Strelnikov, B., Staszak, T., Latteck, R., Renkwitz, T., Strelnikova, I., Lübken, F.-J., Baumgarten, G., Fiedler, J., Chau, J. L., Stude, J., Rapp, M., Friedrich, M., Gumbel, J., Hedin, J., Belova, E., Hörschgen-Eggers, M., Giono, G., Hörner, I., Löhle, S., Eberhart, M., and Fasoulas, S.: Sounding rocket project "PMWE" for investigation of polar mesosphere winter echoes, J. Atmos. Solar-Terrest. Phys., 218, 105596, https://doi.org/10.1016/j.jastp.2021.105596, 2021.

Verronen, P. T., Seppälä, A., Clilverd, M. A., Rodger, C. J., Kyrölä, E., Enell, C.-F., Ulich, T., and Turunen, E.: Diurnal variation of ozone depletion during the October-November 2003 solar proton events, J. Geophys. Res.-Space Phys., 110, A09S32, https://doi.org/10.1029/2004JA010932, 2005.

Verronen, P. T., Andersson, M. E., Marsh, D. R., Kovács, T., and Plane, J. M. C.: WACCM-D—Whole Atmosphere Community Climate Model with D-region ion chemistry, J. Adv. Model. Earth Syst., 8, 954–975, https://doi.org/10.1002/2015MS000592, 2016.

Vuthaluru, R.: MF radar observations of D-region electron densities at Adelaide, PhD thesis, University Adelaide, 2003.

Worthington, E. R. and Cohen, M. B.: The Estimation of D-Region Electron Densities From Trans-Ionospheric Very Low Frequency Signals, J. Geophys. Res.-Space Phys., 126, e2021JA029256, https://doi.org/10.1029/2021JA029256, 2021.

Zhu, M., Xu, T., Sun, S., Zhou, C., Hu, Y., Ge, S., Li, N., Deng, Z., Zhang, Y., and Liu, X.: Physical Model of D-Region Ionosphere and Preliminary Comparison with IRI and Data of MF Radar at Kunming, Atmosphere, 14, 235, https://doi.org/10.3390/atmos14020235, 2023.

Contribution to the Manuscripts

Individual contributions of the PhD candidate to the manuscripts submitted in this cumulative thesis are listed below.

In Jaen et al. (2022), the candidate was involved in the conceptualization and performed the majority of the data analyses including the implementation of the PCA, with the provided wind data. The candidate was responsible for drawing up the discussion and conclusion of the paper that was shared with the advisors. The candidate developed all the figures, wrote the manuscript, and had help writing the subsection of instruments. The candidate was also responsible for the submission of the manuscript and addressing all of the reviewers' comments during the review process. Approximately 85% of the work was made by the PhD candidate.

In Jaen et al. (2023), the candidate was involved in the conceptualization and performed all of the data analyses. The candidate also had a major share in discussing the results and drawing conclusions. The candidate developed all the figures and wrote the manuscript. The candidate was also responsible for the submission of the manuscript and addressing all of the reviewers' comments during the review process. Approximately 85% of the work was made by the PhD candidate.

In Jacobi et al. (2023), the candidate played a minor part in discussing the concept and results. The candidate also provided a preliminary version of the Juliusruh MF radar data. The candidate contributed to the discussion of the differences between Collm and Juliusruh radar data differences while being a minor part of the text, editing, and review process of the manuscript. Approximately 20% of the work was made by the PhD candidate.

In Sivakandan et al. (2023), the candidate was involved in the trend calculations and significance testing and was involved in the interpretation of some of the results. The candidate contributed to the manuscript's text at an advanced stage, connecting it to the dynamics of the E layer. The candidate provided minor assistance during the review process. Approximately 30% of the work was made by the PhD candidate.

In Renkwitz et al. (2023), the candidate was a minor part of the formulation of the concept and discussions and assisted in connecting the results of the paper to the dynamics of MLT. The candidate had minor comments on the text of the manuscript and minor assistance during the review process. Approximately 10% of the work was made by the PhD candidate.

Declaration of Authorship

I, Juliana JAEN, herewith, declare the following:

- The opportunity for this PhD project was not communicated to me commercially. In particular, I have not engaged any organization that, for money, seeks supervisors for the drawing up of dissertations or that performs entirely or partially on my behalf the duties incumbent upon me regarding the examinations.
- I hereby declare under oath that I have completed the work submitted here independently and have composed it without outside assistance. Furthermore, I have not used anything other than the resources and sources stated and where I have taken sections from these works in terms of content or text, I have identified this appropriately.

Signed: _____

Date: _____